# MICROFLUIDIC CELL CULTURE ARRAYS FOR CLONAL EXPANSION AND CHARACTERIZATION OF MAMMALIAN CELLS

by

Véronique Lecault

B.A.Sc., University of Ottawa, 2006
B.Sc. (Honours), University of Ottawa, 2006

A THESIS SUBMITTED IN PARTIAL FULFILLMENT OF THE REQUIREMENTS FOR THE DEGREE OF

DOCTOR OF PHILOSOPHY

in

THE FACULTY OF GRADUATE STUDIES

(Chemical and Biological Engineering)

THE UNIVERSITY OF BRITISH COLUMBIA

(Vancouver)

December 2012

# Abstract

Single-cell culture provides a unique means to reveal the heterogeneity within mammalian cell populations. Advances in multilayer soft lithography have enabled the development of high-throughput nanoliter-volume cell culture platforms with integrated and programmable fluidic control to precisely modulate the microenvironment. Coupled with time-lapse imaging, these microfluidic systems allow hundreds of single cells to be monitored simultaneously while providing analytical advantages to characterize each clone. However, there are many challenges associated with the miniaturization of mammalian cell cultures and even greater difficulties for non-adherent cell types. This work shows how microfluidic devices and their control system can be designed to gently trap suspension cells and enable robust clonal expansion. Mouse hematopoietic stem cell (HSC) populations were chosen for their sensitivity and stringent cell culture requirements to demonstrate that normal cell growth and function could be sustained in the microfluidic system. Using microfluidic clonal analysis and image processing it was observed that cells from HSC-enriched populations had highly heterogeneous growth profiles. Automated medium exchange and temporal stimulation were then exploited to show that a high Steel factor (SF) concentration was needed for survival of primary HSCs specifically at the time of exit from quiescence. The ability to perform live immunostaining was combined with genealogical tracing to identify distinct characteristics, such as long cell cycle times and frequent asynchrony of daughter cells, associated with HSC clones exhibiting persistent endothelial protein C receptor expression (EPCR) after *in vitro* culture. Finally, the flexibility of this microfluidic system was demonstrated with the culture of Chinese hamster ovary (CHO) cells, the most widely used suspension-adapted mammalian cell type for the production of therapeutic recombinant proteins. In this system,

the high cell density and the rapid concentration of cell-secreted products in nanoliter-volume chambers were exploited to measure the amount of secreted monoclonal antibodies from single cells and to increase their cloning efficiency. The ability to recover clones from the microfluidic system has allowed the selection and expansion of high-producing cell lines. This thesis demonstrates the potential and adaptability of high-throughput microfluidic single-cell culture systems for both research and therapeutic applications.

# Preface

A version of sections 1.2.2 and 1.2.3, presented in Chapter 1, has been published as a review article in *Current Opinion in Chemical Biology*:

- Lecault, V., White, A.K., Singhal, A., Hansen, C.L. Microfluidic single cell analysis: from promise to practice. *Current Opinion in Chemical Biology*, 16(3-4), 381-390 (2012).

I drafted the sections used in this thesis and worked with my colleagues, Adam White and Anupam Singhal, who wrote other sections of the manuscript and shared equal authorship with me. The entire manuscript was reviewed as a team and the article received significant input and editing by Dr. Carl Hansen (Centre for High-Throughput Biology, University of British Columbia, Vancouver, Canada) before its publication.

A version of Chapter 2 was published in the journal *Nature Methods* as described below:

- Lecault, V., VanInsberghe, M., Sekulovic, S., Knapp, D., Wohrer, S., Bowden, W., Viel, F., McLaughlin, T., Jarandehei, A., Miller, M.,, Falconnet, D., White, A.K., Kent, D., Copley, M., Taghipour, F., Eaves, C.J., Humphries, R.K., Piret, J.M., Hansen, C.L. High-throughput analysis of single hematopoietic stem cell proliferation in perfusion microfluidic cell culture arrays. *Nature Methods*, 8(7), 581-586 (2011).

This work is the result of a collaborative project with members from 4 different research groups: Dr. Carl Hansen, Dr. James Piret (Michael Smith Laboratories, University of British Columbia, Vancouver, Canada), Dr. Connie Eaves and Dr. Keith Humphries (both from the Terry Fox Laboratory, BC Cancer Agency, Vancouver, Canada). I primarily prepared the manuscript with significant intellectual input from the principal investigators mentioned

above and I generated all the figures except when mentioned otherwise below.

I designed the experiments with input from Drs. James Piret, Carl Hansen, Connie Eaves and Keith Humphries and members of their laboratory. Adam White and Didier Falconnet helped in the early development of cell culture devices. I designed the microfluidic devices presented in this work with intellectual input from Carl Hansen and help from two co-op students, Thomas McLaughlin and William Bowden, for fabrication. I performed all microscale experiments and maintained macroscale cultures with ND13 cells with the exception of the experiment presented in Fig. 2.11, which was performed by Michelle Miller. Sanja Sekulovic, David Knapp, Stephan Wohrer, David Kent or Michael Copley sorted primary murine HSCs for microfluidic experiments and maintained them in culture when necessary. Sanja Sekulovic performed the *in vivo* reconstitution assays presented in Fig. 2.13a-c. Flow simulation studies presented in Figs. 2.3b-d and 2.4d were generated by Asafeh Jarandehei with supervision from Drs. Fariborz Taghipour (Department of Chemical and Biological Engineering, University of British Columbia, Vancouver, Canada) and James Piret.

I developed the majority of image acquisition scripts with input from Michael VanInsberghe and William Bowden. The image analysis scripts presented in Fig. 2.8 were primarily written by Michael VanInsberghe. Francis Viel, a student from Université Laval (Quebec City, Canada) who joined the laboratory of Dr. Carl Hansen for a summer term, developed the enhanced bifocal image analysis algorithm presented in Fig. 2.17. I received help from Michael VanInsberghe, William Bowden and Francis Viel for image and data analysis, and David Knapp performed the Cox proportional analysis presented in Table 2.1.

A version of Fig. 2.14 presented in Chapter 2 was published in *Blood* as a figure in the following article:

- Sekulovic, S., Gasparetto, M., Lecault, V., Hoesli, C.A., Kent, D.G., Rosten, P., Wan, A., Brookes, C., Hansen, C.L., Piret, J.M., Smith, C., Eaves, C.J., Humphries, R.K. Ontogeny stage-independent and large magnitude clonal expansion in vitro of hematopoietic stem cells stimulated by an engineered NUP98-HOX fusion transcription factor. *Blood*, 18(16), 4366-4376 (2011).

Sanja Sekulovic designed the experiments, purified the cells and transduced them. I performed the microfluidic cell culture experiments, analyzed the cell growth kinetics with help from Francis Viel and I generated the figures.

Chapter 3 is a version of a manuscript that will be submitted for publication. David Knapp and I designed the experiments with input from Drs. Carl Hansen, Connie Eaves, James Piret and Keith Humphries. David Knapp sorted HSCs and performed *in vivo* repopulating assays. William Bowden fabricated the devices and I performed all microfluidic experiments. Francis Viel developed the genealogical tracing algorithm, which was further perfected by William Bowden who also built the graphical user interface for manual curation. I wrote the majority of the scripts for data analysis and generated all the figures. I primarily wrote the manuscript with input from David Knapp, William Bowden as well as Drs. James Piret, Connie Eaves and Carl Hansen.

Chapter 4 is also a version of a manuscript to be submitted for publication. This work was done in collaboration with Anjali Verma and her supervisors, Joe Orlando and Christopher Martin (EMD Millipore, Bedford, USA). I designed all experiments with input from Anjali Verma, James Piret and Carl Hansen. Anjali Verma prepared the CHO cell pool and analyzed the titers for all samples. She also performed the clone selection experiment using limiting dilution presented in Figs. 4.8b, 4.14 and 4.15. Except for the

experiment mentioned above, I maintained all cultures from single cells to shake flasks. William Bowden and I fabricated the devices and I did all microfluidic experiments. William Bowden developed the scripts and graphical user interface to measure the bead and cell fluorescence intensities. Anupam Singhal shared his expertise to develop the bead immunocapture assay. I generated all the figures and primarily wrote the manuscript with input from William Bowden, Anjali Verma, Anupam Singhal as well as Drs. James Piret and Carl Hansen.

The animal procedures presented in this work met the Canadian Council on Animal Care requirements and received specific project and protocol approval from the UBC Animal Care Committee (Animal Care Certificate Number: A11-0080).

# Table of Contents

# List of Tables

# List of Figures

# List of Abbreviations

| | |
|---|---|
| AML | Acute myeloid leukemia |
| CAFC | Cobblestone area-forming cell |
| CFC | Colony-forming cell |
| CHO | Chinese hamster ovary |
| CI | Confidence interval |
| CLP | Common lymphoid progenitor |
| CMP | Common myeloid progenitor |
| CRU | Competitive repopulating unit |
| CV | Coefficient of variation |
| DHFR | Dehydrofolate reductase |
| DMEM | Dubelcco's modified Eagle medium |
| DNA | Deoxyribonucleic acid |
| ELISA | Enzyme-linked immunosorbent assay |
| ELISPOT | Enzyme-linked immunosorbent spot |
| ESC | Embryonic stem cell |
| E-SLAM | $CD45^{+}CD48^{-}EPCR^{+}CD150^{+}$ |
| EGFP | Enhanced green fluorescent protein |
| EYFP | Enhanced yellow fluorescent protein |
| FACS | Fluorescence-activated cell sorting |
| FBS | Fetal bovine serum |
| FITC | Fluorescein isothiocyanate |
| G-CSF | Granulocyte-colony stimulating factor |
| GFP | Green fluorescent protein |
| GM | Granulocytes-monocytes |
| GS | Glutamine synthase |
| GUI | Graphical user interface |
| HOX | Homeobox |
| HSC | Hematopoietic stem cell |

| | |
|---|---|
| IFN | Interferon |
| IL | Interleukin |
| IVC | Integral of viable cell concentration |
| JNK | c-Jun N-terminal kinase |
| Lin | Lineage |
| LT-CIC | Long-term culture-initiating cell |
| mAb | Monoclonal antibody |
| MAPK | Mitogen-activated protein kinase |
| MSL | Multilayer soft lithography |
| MSX | Methionine sulfoximine |
| MTX | Methotrexate |
| NA10hd | NUP98-HOXA10 homeodomain |
| ND13 | NUP98-HOXD13 |
| NUP98 | Nucleoporin 98 |
| NF | Nuclear factor |
| PCR | Polymerase chain reaction |
| PDMS | Polydimethylsiloxane |
| PE | Phycoerythrin |
| PTFE | Polytetrafluoroethylene |
| RNA | Ribonucleic acid |
| RT-qPCR | Reverse transcription quantitative polymerase chain reaction |
| SF | Steel factor |
| SLAM | Signaling lymphocyte activation molecule |
| SP | Side population |
| SPR | Specific productivity |
| TNF | Tumor necrosis factor |
| TGF | Transforming growth factor |
| t-PA | Tissue plasminogen activator |
| WBC | White blood cell |

# List of Symbols

| Symbol | Description | Units |
|---|---|---|
| $C$ | Viable cell concentration | cells $ml^{-1}$ |
| $c_{Ab}$ | Antibody concentration | $\mu g\ ml^{-1}$ |
| $I$ | Bead fluorescence intensity | dimensionless |
| $I_{max}$ | Maximum bead fluorescence intensity | dimensionless |
| $K$ | Equilibrium constant | $ml\ \mu g^{-1}$ |
| $P$ | Poisson probability | dimensionless |
| $t$ | Time | days |
| $\mu_c$ | Average number of cells per chamber | cells |
| $x$ | Number of cells per chamber | cells |

# Acknowledgements

I would first like to thank my co-supervisors, Dr. James Piret and Dr. Carl Hansen, who have both been fantastic advisors throughout my program. Jamie, thank you for your optimism, thoughtfulness and for giving me so many opportunities to enrich my graduate experience. Working with you was a privilege and I will forever be grateful for giving me the chance to discover Vancouver. Carl, thank you for sharing your ambition and vision throughout this journey. You have inspired me to surpass myself and go beyond what I thought was ever possible.

I also wish to thank my collaborator and committee member, Dr. Connie Eaves, who has been a role model and an inspiration. She has shared her passion for understanding complex biology with an unmatched level of dedication and I have learned tremendously from her. Also sincere thanks to Dr. Christina Gyenge for gladly accepting to be part of my committee and Dr. Keith Humphries for his invaluable input since the very beginning of this project.

I also wish to thank Dr. Jules Thibault for teaching me the basics of engineering with passion and for introducing me to my doctoral supervisor. I discovered my love for research in his laboratory and would not be where I am today without this experience. As well, thanks to Dr. Jean Caillé, my mentor and friend, for seeing the potential in me when I was a junior undergraduate student and for giving me the opportunity to enter the biotechnology world. Jean, your support, encouragement and advice throughout the years have been invaluable.

Thanks to Marta Szabat, Corinne Hoesli, Pascal Beauchesne, Nicolas Caron and all my colleagues from the Piret lab for the insightful scientific discussions. Also thanks to Mario Jardon, Soroush Nasseri and Navid

Ghaffari for helping me find my way into this new CHO world and for sharing their expertise, knowledge and shaking incubator with me. Special thanks to Chris Sherwood for making the Piret lab a wonderful place to work and for introducing me to the underwater world of the Pacific Coast. I sincerely thank the four exceptional students who have worked with me: Michael VanInsberghe, Thomas McLaughlin, Francis Viel and William Bowden. With their enthusiasm and eagerness to learn, they have all contributed enormously to this project. Equal thanks to my colleagues in the Hansen lab. Adam White, thank you for being such a cheerful friend and labmate from the very beginning. We shared many successes and failures together, including the excitement of the first cell division and the disappointments from repeated cell death. Your presence along the way and your contagious giggle brought optimism and fun into this journey. I hope we will have the opportunity to work together again. I would also like to thank Didier Falconnet, for his expertise and initial input in the project, as well as his continuous efforts to understand my French. Special thanks to Darek Sikorski for sharing the challenges of mammalian cell culture and Anupam Singhal for his input in the cell line selection project. Thanks to Carmen de Hoog, for her witty comments and for ensuring the smooth operations of the laboratory. Also, special thanks to Hans Zahn, the exceptional engineer who has saved the lives of many cells by building "The Box".

Thanks to the fantastic collaborators from the Terry Fox Laboratory: Sanja Sekulovic, Michelle Miller, David Knapp, Michael Copley, Michael O'Connor, Stefan Wohrer, Ivan Sloma, Florian Kuchenbauer and Claudia Benz, with a special mention to David Kent for his useful advice on many topics and for introducing me to Let's Talk Science. As well, thanks to Holly Prentice for initiating the collaboration on cell line selection, and Anjali Verma from EMD Millipore for her contribution in turning this initial idea into a successful project. I also acknowledge NSERC, MSFHR and CIHR for

supporting my research endeavours and I wish to share my appreciation to the Stem Cell Network and its members for improving my graduate experience in many ways.

Thanks to Samantha Benton and all the Let's Talk Science team. It has been a pleasure working with such passionate individuals. You have made my life incredibly more fulfilling. I wish to sincerely thank all Let's Talk Science supporters and UBC volunteers without whom this science outreach program would not be possible. Special thanks to the dynamic inaugural StemCellTalks Vancouver Team: Maisam Makarem, Ben Paylor and Michael Copley. I had tremendous fun working with you and I am glad I met you along the way.

Thanks to my dear friends Dominique, Denis and Émilie, for their continuous support despite the miles separating us. Thank you Alex, for reminding me to always celebrate our successes, big or small, and for listening to my stories about the same article for so many years. Thank you Caroline and Serge for your attentive ear, your understanding of the graduate student life and for the great moments we have shared together. And thank you Joost, for your love and support in this past year and for bringing me into the wind or atop a cliff whenever I needed to free my mind.

Finally, thanks to my loving family for being so wonderful, with a special mention to Ald for all the great laughs. Thanks to my grandparents for their love, help and inspiration, in body or spirit, throughout this journey. Thank you Mélanie, my sister and friend, for coming to visit so often and for always being there for me. I am glad to finally join you in the ranks of doctors. Last but not least, thank you Francine and Michel, my loving parents, for your support and all the sacrifices you made to take me where I am. You have always encouraged me to follow my dreams and gave me everything I needed to succeed. I could not have done this without you.

*To my mom and dad,*
*for their utmost love and support*
*every step along the way*

*À mes très chers parents,*
*pour leur amour inconditionnel et leur support*
*tout au long de mon cheminement*

# CHAPTER 1 Introduction

## 1.1 Thesis Overview

Nature provides a number of examples where individual entities from a population show different behaviors and functions. For instance, identical twins share the same genetic information and often look alike. However, they are different individuals with distinct personalities, characters and reactions, some of which are innate and others shaped by the external factors affecting their lives. Honeybees all have yellow and black stripes, but they can be divided into sub-groups that hold different functions for the proper maintenance of the hive. One rare but essential bee, the queen, is responsible for laying thousands of eggs and ensuring the perpetuity of the colony. At the cellular scale, populations with similar phenotypes can also contain various subsets of cells that are functionally different[1-3]. Clonal populations often exhibit heterogeneous behaviors and genetic diversity, a phenomenon particularly prevalent in cancers[4,5] and clonally derived cell lines[6]. The analysis of bulk populations may obscure this heterogeneity and prevent the identification of characteristics associated with rare but important cells.

While the scientific community has long recognized the need for single-cell analysis to tackle this problem, the sensitivity and throughput required to perform such measurements has not been readily available. The emergence of new technologies in the past decade has greatly facilitated the study of single cells. In particular, multilayer soft lithography (MSL) have enabled precise control and handling of picoliter-scale volumes via integrated fluidic systems of micro-pumps, micro-valves, and micro-mixers. These scalable microfluidic systems require less reagents and allow often-unprecedented throughput to be reached in a relatively cost-effective fashion. In addition, the miniaturization of fluid handling can provide unique

analytical advantages by concentrating products to be analyzed and by limiting non-specific interactions[7].

Microfluidic features are particularly appealing for the study of live populations of cells. Appropriately sized culture platforms can be built in transparent material, allowing individual cells to be monitored under the microscope as their everyday moves are recorded on camera. One can observe their behaviors and responses in real-time as elements are added or removed from the system. Although the suitability of microfluidics to sustain mammalian cell culture has been explored for multiple cell types[8], prior to this work it had not yet been developed into a robust technology for studying sensitive non-adherent mammalian cells. In addition, the analytical advantages provided by miniaturization have generally been underexploited for cell culture applications. This thesis describes how the scalability and flexibility of microfluidic technology can be used for the *in vitro* characterization and culture of suspension mammalian cells at the clonal level. The current chapter reviews microfluidic technologies for single-cell analysis and mammalian cell culture. It then introduces two important biological systems, hematopoietic stem cells (HSCs) and Chinese hamster ovary (CHO) cells, studied in this thesis to demonstrate the applications of the technology.

Chapter 2 focuses on technology development and describes the design features of a robust microfluidic system for suspension cell culture. The technology is first tested on HSC-enriched populations, arguably one of the hardest cells to cultivate *in vitro*, and is then used to obtain new insights into the biology of primary murine HSCs.

Chapter 3 demonstrates how the same technology combined with high-resolution time-lapse imaging, live immunostaining and semi-automated image processing can be exploited to identify *in vitro* phenotypes of clones

having *in vivo* repopulating potential. Genealogical tracing of single cells and their progeny is used to gain a better understanding of the growth characteristics of primary murine HSCs.

Chapter 4 demonstrates the flexibility of the system and the benefits of concentrating cells in nanoliter-volumes by adapting the technology for another application: the production of recombinant monoclonal antibodies (mAbs). A microfluidic single-cell protein secretion assay is combined with clonal culture of CHO cells to enable rapid cell line selection.

Finally, Chapter 5 concludes this thesis by explaining the significance of this work, summarizing the key elements needed to achieve robust microfluidic cell culture and recommending directions for future studies.

## 1.2 Microfluidic Technologies

### 1.2.1 Multilayer Soft Lithography

Miniaturization is a powerful approach to reach higher levels of throughput without increasing the requirements for space and resources. For example, the integration of electronic circuits has led to massive technological advances in the development of portable electronic devices such as laptop computers, smart phones, tablets and music players. The miniaturization of fluidic systems can be achieved by photolithography, the same method already used for the fabrication of small electronic devices. Briefly, a photoresist layer of desired height is spun onto a silicon wafer, and then exposed to ultraviolet light through a high-resolution mask containing the desired features. Microstructures are revealed upon soaking in a development solution[9]. This technique has been proven useful for many microfluidic applications, but it has a limited ability for integrating fluid flow

controls and functionalizing the surface[10]. Furthermore, the opaqueness of the silicon substrate is not always suitable for imaging purposes.

In the late 90's, George Whitesides and his group showed that polydimethylsiloxane (PDMS), a silicone elastomer, could replicate features from silicon wafers with high precision[10,11]. Replica molding with PDMS enabled low cost production of multiple chips from a single silicon master[8,10,12], making this technology suitable for the fabrication of disposable devices. In addition, the flexibility, transparency, gas permeability and biocompatibility of PDMS[13-15] provided desirable features for a wide range of applications. Shortly afterwards, Stephen Quake and his group demonstrated that the elastomeric properties of the material could be exploited to integrate complex systems of pumps, valves and mixers by means of multilayer soft lithography (MSL)[16,17]. This was achieved by using a thin and flexible membrane of PDMS separating intersecting control and flow channels. Application of positive pressure in control channels induced a deflection of the membrane, thereby closing proximal flow channels. Since then, thousands of these valves have been integrated in microfluidic devices to enable precise fluid handling. In the past decade, the use of MSL has exploded, leading to a plethora of applications in the fields of biology, biochemistry, engineering, material sciences, physics and chemistry[12,15,18].

### 1.2.2 Microfluidics for Single-Cell Analysis

The recurring challenge in single-cell analysis is to simultaneously achieve the sensitivity, precision, throughput and economy needed to detect and study complex subpopulations of cells. Microfluidic formats are ideally suited to addressing these problems by providing reduced reagent costs, high effective template concentrations, scalability, ease of automation, improved cell handling and multi-step integration (**Table 1.1**).

Microfluidic single-cell technologies and the diversity of their applications have been well reviewed[7,19,20]. The availability of a commercial microfluidic platform (Dynamic Array™, Fluidigm) enabling multiplexed gene expression analysis on large numbers of samples has led to a number of new biological discoveries. Important advances have been made in fields where dissecting the heterogeneity of populations is particularly relevant such as developmental biology[21,22], cancer[23,24] and stem cell science[3,25-28]. For instance, multiplexed gene analysis of single cells from purified long-term HSC populations combined with information theory have led to the identification of distinct subpopulations of cells[28]. As well, single-cell expression analysis of normal and malignant colon cells has shown that tumor heterogeneity is largely due to multilineage differentiation[23]. There is a rising interest towards elucidating clonal diversity at the genome level to obtain a better understanding of tumor evolution in cancer[29]. Microfluidic approaches to genotype individual chromosomes paired with new sequencing technologies have brought new tools to study these heterogeneous systems[30]. The combination of microfluidics and sequencing also has advantages for whole genome amplification and has already been used to obtain genetic profiles of known and unknown species from complex environments[31,32].

In addition to facilitating multiplexed genetic analysis of single cells, microfluidic devices provide numerous advantages to the study of live cells. For instance, using a fluorescent protein fusion library in *Escherichia Coli*, Taniguchi and colleagues have measured protein abundance in individual cells and have shown a lack of correlation between protein and mRNA levels[33]. Reducing cell culture volumes by several orders of magnitude leads to the rapid concentration of secreted molecules from cells and fast diffusion times, resulting in increased sensitivity. This feature has been exploited in a method called microengraving, which consists of using a functionalized glass cover over a microwell array to capture secreted proteins from single cells[34,35].

Microfluidic devices have also been employed to rapidly capture secreted antibodies from single hybridoma cells on beads and to measure their binding kinetics[36]. With a different method, the Heath group has patterned antibody capture arrays inside microfluidic devices to detect cytokine secretion from cytotoxic T lymphocytes activated in response to a tumor[37,38]. An alternative approach have used microfluidic devices for the high-throughput analysis of secreted proteins from single cells by encapsulating them in emulsions consisting of sub-nanoliter aqueous droplets in oil[39,40]. Microfluidic droplet generation is also being developed for drug screening applications by measuring viability of encapsulated single cells exposed to different chemical compositions[41].

The combination of microfluidic flow control, precise cell immobilization, fluorescent protein reporters, and image processing has been used to access several experimental regimes that are difficult or impossible to implement in bulk cultures: the study of cell signaling under stable and precisely defined spatial gradients[42], the frequency analysis of signaling response under oscillating stimulation conditions[43,44] and the high-throughput analysis of network response under combined chemical and genetic perturbations[45,46]. Time-course experiments that track individual cells through time are critical to understand the mechanisms of response heterogeneity, including effects of cell cycle, cell age and genealogical relationships. In addition to quantitative measures of clonal growth and survival, genealogical analysis, allowing for the reconstruction of the "family tree" in each clone, provides a rich phenotype for understanding cellular decision-making and retrospectively assessing the heterogeneity of the starting cell populations. These features have been exploited to study the response of archetypical protein signaling networks in yeast, most notably the pheromone and HOG mitogen activated protein kinase (MAPK) networks. For instance, Falconnet *et al.* have found that non-uniform gene expression

and phenotypic responses observed at intermediate concentrations of pheromone were not random, but rather correlated with genealogical relationships, illustrating how non-genetic heritable traits may influence the critical threshold for cellular decision making[46]. The generation of division pedigrees from a large number of single cells can be assisted by microfluidic designs that confine clones in a limited space[46,47]. In one example, microfluidic chambers were used to grow yeast colonies in linear chambers, hence facilitating the assignment of mother-daughter relationships. Time-lapse imaging has revealed that bursts of heat shock protein expression were synchronized between a cell and its immediate progeny[47].

As a high-precision alternative to optical analysis of cellular growth, the Manalis group has developed an innovative approach that directly measures the mass of single cells using microfabricated cantilevers with integrated flow channels. This technique was used to study mammalian cell size regulation[48,49] and to show that precise measurement of cellular density could be used to distinguish infected or thalessimic erythrocytes from healthy ones, as well as drug-treated lymphocytes from non-treated ones[50]. Although this system has not yet been adapted to high-throughput formats, it provides an excellent illustration of how microfluidic approaches can enable previously inaccessible measurements with unmatched precision for understanding cellular heterogeneity. As analysis of populations at the single-cell level generally involves the study of a large number of cells, there is room for the development of better automation tools to track cell growth and generate cellular genealogies in a fast and high-throughput fashion.

### 1.2.3 Microfluidic Mammalian Cell Culture

High-throughput approaches are extremely powerful to characterize single mammalian cells and to study the complex and highly dynamic

interactions that govern their growth and behavior. Microwell arrays using various substrates such as hydrogels, silicon, photoresist, PDMS or glass have been used to trap and analyze single suspension cells[51-54], to confine adherent and non-adherent clones into small areas for cell tracking[55-57] and to study the interactions between different cell types by colocalization[58]. Some approaches have employed surface patterning of microwells to more precisely dissect and mimic the factors present in the *in vivo* microenvironment[59,60]. The cell trapping mechanisms in these large-volume microwell arrays generally allow medium exchange but lack the flexibility of enclosed programmable microfluidic systems that allow for precise spatio-temporal control of culture conditions. For instance, Tay and colleagues have exploited temporally varying and automated fluid control in a microfluidic cell culture device to demonstrate that single 3T3 mouse fibroblast cells respond to tumor necrosis factor (TNF)-α in a digital manner; that is, lower numbers of cells responded to lower doses of TNF-α even though the amplitude of transcription factor nuclear factor (NF)-κB remained high[61]. Pulse stimulation studies showed that prior exposure to TNF-α played a role in subsequent cellular responses, indicating that this pathway is not a purely stochastic system. Cheong and colleagues took advantage of microfluidic parallelization to reconstruct signaling kinetics using endpoint staining of fixed cells at different time points after stimulation, thereby enabling the detection of multiple proteins on each cell[62]. With this method, it was shown that c-Jun N-terminal kinase (JNK) signaling exhibited a binary switch-like response after anisomycin stimulation in HeLa cells[63].

Several groups have reported the study of embryonic or mesenchymal stem cells in microfluidic devices[64-68]. Albrecht *et al.* have used histone H2B-EGFP and tubulin-EYFP to facilitate tracking of mitotic events in murine embryonic stem cells (ESCs) and have observed an apparent synchronization of division events across the microfluidic device[67]. Others have used perfusion

microfluidic systems to study the effect autocrine and paracrine signaling on ESCs self-renewal and differentiation[66,69,70]. Tumarkin and colleagues have employed a variant of this approach to study cellular paracrine signaling by co-encapsulating cells in microfluidic-generated agarose beads, and demonstrating that cell survival could be modulated by the ratio of MBA2 interleukin (IL)-3 secreting cells to M07e factor-dependent cells[71].

Despite this progress, applications to mammalian systems have been slower to develop than those aimed at analyzing yeast and bacterial cell responses[43,45,72,73]. A majority of reports on mammalian cell culture in microfluidic devices have been limited to short-term experiments performed in relatively large volumes with high perfusion rates[56,62,74-77]. In many cases, the same studies could have been done in macroscale cultures and did not exploit the unique analytical advantages of microfluidics. **Table 1.2** summarizes the reports of microfluidic PDMS devices to cultivate mammalian cells. Devices with chamber volumes greater than 10 μl were excluded from this summary as these volumes approach standard macroscale 384-well plate cultures. Aside from a few exceptions[68,75,78], these reports tend to omit growth rate comparisons with conventional cultures or when addressed, microfluidic cultures exhibit slower growth rates[79-82] and deviations from normal phenotypes[83]. This lesser ability to exploit microfluidics to its full potential can be mainly attributed to greater technical challenges associated with controlling the more stringent mammalian cell culture requirements in these devices. For example, gas permeability of PDMS is an important asset in cell culture to avoid oxygen limitations[84,85]. However, vapor permeation results in high rates of evaporation[86-88], which can in turn lead to significant osmolarity shifts that have been shown to influence mammalian cell metabolism[89], growth[90] and embryo development[91-93]. These problems are amplified due to the extreme PDMS surface area to medium volume ratio of microscale culture chambers[94,95]. As chamber

volumes decrease the cell culture medium becomes increasingly susceptible to environmental variations. To achieve robust cell culture, evaporation effects can often be minimized by keeping humidity close to saturation in the surrounding environment and by using large chambers or high perfusion. Medium exchange also serves to avoid nutrient limitations, control pH and wash away possibly toxic compounds secreted by the cells or leaching from incompletely cured PDMS[13,80,96]. However, some cell types do not thrive under high perfusion rates as they need the conditioning from other cells[97] and therefore perfusion should be used when medium exchange is needed but not as a means to overcome evaporation or other PDMS effects. It has been shown that PDMS can absorb small hydrophobic molecules such as rhodamine or oestrogen[98-100]. It is not clear whether this phenomenon generally affects cultures since albumin likely carries small hydrophobic molecules at the low concentrations naturally found in serum[101]. However, it could become problematic for studies where medium has to be supplemented by drug molecules or hormones at higher concentrations. It is also possible that some components may be depleted by adsorption on the wall. Culture medium generally contain a high concentration of albumin that is readily adsorbed on PDMS[102]. Therefore, priming the device with culture medium should mitigate adsorption effects during experiments.

Standard microfluidic devices do not enable immobilization of suspension cells for perfusion, which explains in part the lack of reports on long-term mammalian suspension cell culture. HSC culture in enclosed microfluidic devices has not been demonstrated prior to this work. Likewise, adherent CHO cells have been cultured in microfluidic devices[103-105], but there has not been any report using suspension-adapted cell lines. The development of solutions to minimize PDMS effects combined with gentle cell trapping mechanisms for medium exchange are essential to enable the culture of suspension cells in microfluidic systems.

## 1.3 Hematopoietic Stem Cells

### 1.3.1 The Hematopoietic System

During development, hematopoiesis begins in the yolk sac of the embryo, then proceeds to the aortic region to reach the fetal liver and finally the bone marrow[106]. Adult HSCs reside primarily in the bone marrow but can also be found at a lower frequency in peripheral and cord blood. Traditionally, HSCs have been defined as cells capable of producing all blood cell types and dividing into one or more cells also possessing unrestricted differentiation potential, referred to as self-renewal[107]. The classic model of hematopoiesis classifies committed hematopoietic cells into a myeloid compartment originating from common myeloid progenitor (CMP) cells that generate platelets, erythrocytes and phagocytes (macrophages and granulocytes), and a lymphoid compartment originating from common lymphoid progenitors (CLP) that generate lymphocytes (B cells, T cells and NK cells)[108]. This classic model implies that CLPs have already lost their ability to give rise to myeloid cells and, conversely, that CMPs cannot produce lymphoid cells. Further lineage restriction is depicted by binary and irreversible decisions. This model has been derived mainly from functional readouts of the types of progeny that could be produced by a cell, providing a stepwise description of the differentiation processes. Its validity has been challenged in both murine and human systems, notably from the observations that myeloid cells could be produced from T cell progenitors that could no longer give rise to B cells and that some progenitor cells could generate lymphocytes and myeloid cells but not erythrocytes or megakaryocytes[109,110]. The emergence of new techniques to dissect the molecular mechanisms responsible for the irreversible loss of multilineage potential during differentiation has allowed the classic model of hematopoiesis to evolve[106]. More recent models suggest that differentiation occurs much more dynamically, with a progressive specification of hematopoietic lineages[111,112]. Mathematical models have been

proposed where lineage specification arises from a competition between different lineage propensities, and where lineage commitment is acquired following a succession of intrinsic decision steps that can be influenced by external cues[113,114]. These intrisinc decisions can be mediated by numerous mechanisms such as chromatin remodeling[115], transcription factors regulating the expression of specific genes[116,117] as well as post-transcriptional[118] and post-translational modifications[119] altering the stability of transcripts and proteins. Tools to monitor gene expression in response to external stimuli at the single-cell level could be highly valuable to understand the relationship between intrinsic differentiation programs and the cell microenvironment.

### 1.3.2 Regulation of Stem Cell Fate Decisions

For over 50 years, the ability of HSCs to self-renew and differentiate into specialized blood cells has been exploited clinically. While the potential of HSCs in cancer treatment and gene therapy has been demonstrated multiple times[120-123], the complex mechanisms regulating stem cell fate remain unclear. For either clinical or research applications, there are many situations where symmetric self-renewal and therefore expansion of HSCs would be beneficial. HSC expansion naturally occurs *in vivo* during development[124] or after a myelotoxic treatment like chemotherapy[125,126]. However, it has been challenging to replicate *in vitro* the niche conditions enabling symmetric self-renewal. The combination of factors inside a cell and external cues from the environment can dictate choices between self-renewal or differentiation. Soluble factors and cell surface-associated cytokines provided by endosteal osteoblasts and surrounding stromal cells in the bone marrow have been extensively reviewed[127-129]. Growth factors such as Flt-3 ligand, IL-3, IL-6, Steel factor (SF) and granulocyte-colony stimulating factor

(G-CSF) have been identified as influencing fate decisions of HSCs[130]. Efforts to optimize culture conditions by adjusting cytokines combinations and concentrations[55,131-134] or by adding ligands to activate key pathways involved in self-renewal such as Notch and Wnt have yielded improved expansion[59,135], but the overall increase in stem cell activity remains modest.

Several transcription factors and cell cycle-related genes have been identified as regulators of self-renewal[136,137]. Some of these regulators are genes from the homeobox (HOX) family. Strategies to expand HSCs *in vitro* include the transduction of HSCs with nucleoporin98-homeobox fusion genes (NUP98-HOX). HOX genes, either native or fused with NUP98, have been frequently observed in both acute myeloid leukemia (AML) and chronic myeloid leukemia (CML) patients[138]. In primitive murine cells, expression of the leukogenomic protein Nup98-HOXD13 (ND13) blocks differentiation, thereby enabling *in vitro* expansion of a myeloid progenitor-enriched population with short-term *in vivo* repopulating activity[139]. On its own, ND13 has a low propensity for *in vivo* leukemic conversion. However, when combined with other genetic events such as overexpression of the Meis1 gene, it rapidly induces leukemic progression to AML[139,140]. Successful expansion ranging from 1,000- to 10,000-fold over input of highly polyclonal cells has been achieved by overexpressing these proteins[140,141]. Interestingly, the fusion of HOXA10 homeodomain with NUP98 (NA10hd) has enabled *in vitro* stem cell expansion without causing leukemia when cells were transplanted into irradiated mice[142]. This makes for a good model to study stem cell expansion since these cells have a remarkable proliferation advantage compared to non-transduced cells. However, the exact mechanism by which NA10hd leads to stem cell expansion is not well understood.

### 1.3.3 Characterization of Murine HSCs

The throughput and availability of fluorescence-activated cell sorting (FACS) has led to the identification of markers related to HSC activity, thereby allowing enrichment of stem cells while maintaining the ability to perform subsequent experiments. In the case of primitive HSCs, expression of markers such as c-Kit, Sca-1 and CD34 have been correlated with stem cell activity[143]. Cell sorting has often been combined with the absence of other markers (e.g. $lin^{-/lo}$, Flk-$2^{-}$, Thy-$1^{lo}$)[144-146]. Other approaches to further purify stem cells have been developed by selecting the side population (SP) arising from Hoescht dye exclusion[147]. In the best cases, only 20 to 35% of purified murine cells yields reconstitution in irradiated mice[108,148]. Better sorting strategies based on signaling lymphocyte activation molecule (SLAM) family receptors have been developed to enrich HSC populations with purity levels as high as 50%[149-151]. There is now clear evidence that not all cells with engraftment potential are identical[152-154]. Long-term HSCs have the ability to generate both myeloid and lymphoid lineages for multiple transplants. In contrast, a distinct subset of short-term HSCs is lymphoid-biased and lacks durable self-renewal potential[151,155]. The stem cell definition continues to evolve as better markers and phenotypes become available to characterize the heterogeneity within the HSC compartment.

Given the absence of reliable surrogate phenotypic markers for HSCs, the preferred assays to quantify stem and progenitor cells have been based on functional analysis. Several reviews have compared the different *in vivo* and *in vitro* assays to identify HSCs[156-158]. Briefly, *in vitro* assays requiring stromal cells to support stem cell development such as the cobblestone-area-forming cell (CAFC) assay and the long-term culture-initiating cell assay (LT-CIC) have been correlated to the *in vivo* frequency of primitive stem cells[159,160]. Committed progenitor cells can be quantified and characterized based on colony-forming cells (CFCs) in semi-solid methylcellulose media.

These assays require sufficient dilution to ensure that emerging colonies are derived from single cells. The gold standard to determine stem cell activity is the *in vivo* competitive repopulating unit (CRU) assay that evaluates the fraction of stem cells capable of reconstituting the hematopoietic system (typically >1% of peripheral blood cell lineages) in sub-lethally irradiated mice at 16 weeks post-transplantation[161,162]. This assay tests the functional capability of stem cells including self-renewal and differentiation into myeloid and lymphoid progenitors. A new technique now allows the identification of stem cell progeny generated *in vivo* in a high-throughput fashion using clonal barcoding and sequencing[163]. These methods only provide a retrospective characterization, thereby making it impossible to work with a stem cell after its CRU activity has been confirmed.

### 1.3.4 Single-Cell Tracking and Time-Lapse Imaging

Studies aiming at understanding HSC biology are hindered by many challenges: the difficulty of purifying rare stem cells from other hematopoietic cells, the laborious maintenance and characterization of the cultures, the high reagent costs associated with HSC growth factor dependence, the limited ability to maintain potency *in vitro*, and the lack of rapid, non-destructive assays to determine stem cell activity. Researchers are left with heterogeneous populations of hematopoietic cells where specific information about stem cell properties is lost in average measurements. Therefore, single-cell studies provide major advantages to assess the heterogeneity in hematopoietic populations.

One approach to assess HSC population heterogeneity is to follow single cells through time. The analysis of such clonal populations have revealed high heterogeneity in clone sizes, even after multiple serial replating[164]. Assays are usually performed in 96-well plates, require

substantial volumes of costly medium and are extremely time-consuming when tracking of cell divisions is performed manually. Before high time-resolution imaging became easily accessible, dilution of membrane-bound dyes has provided a means to assess the number of cell divisions[165]. These experiments have revealed, for instance, that quiescent behavior and slow cycling correlates with higher potency[166-169] and that daughter cells separated after the first cell divisions can adopt different fates[170,171]. Laborious but insightful clonal studies can be done also to assess cytokine mechanisms[171,172]. For instance, Kent *et al.* have shown that low Steel factor (SF) concentrations can alter HSC integrity and transcription factor profiles within 8 to 16 h of culture[171].

High-frequency live-cell tracking offers the possibility to discover new phenotypes associated with HSCs. Digital imaging coupled with the increasing storage capacity of computers and microscope automation has made time-lapse imaging a powerful tool for live-cell growth kinetics studies. Commercial high-content screening platforms provide automated time-lapse imaging in 96 or 384-well plate format. These platforms are useful tools for the simultaneous analysis of multiple reporter genes and the screening of different culture conditions. However, the relatively large areas of the flat-bottom wells are not well suited to monitor single suspension cells and these platforms are generally restricted to static conditions[173]. Some groups have chosen instead to couple microwell arrays with custom time-lapse imaging systems to discover new features of HSCs. For instance, Dykstra *et al.* have shown that the absence of uropodia combined with longer cell cycles in clonal populations originating from primary murine HSCs cultured in silicone microwells is correlated with increased stem cell activity[55]. Lutolf and colleagues have monitored the growth of single HSCs in hydrogel microwell arrays to study the effect of soluble and tethered proteins on division kinetics and have found that Wnt3 and N-cadherin could stimulate stem cell self-

renewal[59]. Recently, the Roeder group has reported large microwells with functionalized microcavities to study the genealogies of human hematopoietic stem and progenitor cell populations[174]. They showed that transient exposure to a different biomimetic environment can alter the synchrony of divisions.

Functional assays assume that the output reflects the capacity of a cell to generate progeny independently of intrinsic fluctuations that may affect cell fate at the time of the assay. As such, there is an increasing focus to understand the molecular mechanisms responsible for self-renewal and differentiation. The combination of time-lapse imaging with fluorescent reporters and immunostaining can provide insights into the molecular events dictating cell fate. The current challenges in live-cell imaging reside mainly in the automation of genealogical tracing and in the development of reporters to enable the quantitative analysis of molecules in a high-throughput fashion. Tools have been developed to facilitate cell tracking and gene expression analysis. However, in the reports to date these methods ultimately rely on manual editing[174-179]. The Schroeder group has combined a genealogical tracing tool with a set of reporter genes to demonstrate the instructive nature of cytokines for the differentiation of single progenitor cells into granulocytes and monocytes using time-lapse imaging[179]. However, this conclusion may not apply to all cytokines and cell types, and a permissive nature where only cells with a specific lineage propensity would survive in a given set of conditions should not be ruled out.

Conceptually, a stem cell can generate two stem cells, thereby leading to an expansion of their number, divide symmetrically into two cells committed to differentiation or divide asymmetrically to produce a daughter cell identical to the mother stem cell and another cell committed to differentiation. Fate determinants during asymmetric divisions can come from both external factors, such as the niche, and intrinsic variations between daughter cells. It can be difficult to assess the fate symmetry or lack

thereof between two daugthers cells. However, it is possible to study characteristics that can differ between daughter cells such as repopulation patterns, gene expression, protein segregation, cell cycle time, proliferative capacity and death. Even though they may not necessarily be indicators of asymmetric fate, such analyses can provide insights on the interplay between the different molecular players involved in self-renewal and differentiation. For instance, the asymmetric segregation of Numb has been observed by immunocytochemistry in 44% of HSCs obtained from Notch reporter mice[180]. Numb is an inhibitor of the Notch pathway that is known to have an important role in HSCs self-renewal. On average populations, overexpression of Numb was found to inhibit Notch reporter activity and to be associated with differentiated cells, suggesting that cells obtaining Numb during asymmetric division are more likely to acquire a differentiated fate[181]. Giebel *et al*. have demonstrated that the lipid raft markers CD53, CD62L, CD63 and CD71 segregate asymmetrically in approximately 20% of cord blood stem cells. These proteins could be used to enrich stem cells in combination with the surrogate stem cell marker CD133 but it was not possible to determine whether segregation correlated with different fates since all assays were performed on fixed cells[182]. The probability of observing mitotic events on fixed cells is small and therefore live imaging studies are much more powerful. To overcome this challenge, the Sauvageau group overexpressed two fluorescently labeled proteins, Numb and Ap2a2, in mouse HSCs. They found many instances of Ap2a2 asymmetric segregation, suggesting that this protein plays an important role in fate decisions[183]. Another strategy is to use labeled antibodies at low concentrations to track the evolution of surface markers through time. Combined with genealogical tracing, this method has been used to visualize blood formation from the haemogenic enthothelium[175]. This technique can lead to important biological insights but should be used with care as the prolonged exposure to antibodies and fluorescence can potentially influence stem cell behavior.

HSCs are one of the most challenging cell types to culture in microfluidic devices due to their dependence on cytokines, their scarcity and their suspension nature that makes medium exchange for maintenance difficult. The necessity to recover the cultivated cells for subsequent phenotypic or functional analysis is also a challenge. Microfluidic reports to study hematopoietic cells have thus mostly been limited to short term signaling or apoptosis experiments requiring less than 2 h of culture in relatively large chambers[184-186]. Despite these challenges, microfluidic devices have great potential for the high-throughput analysis of single HSC cultures. If properly designed, these systems could enable automated and parallel growth kinetic analysis of hundreds to thousands of single cells. Moreover, temporally varying cytokine stimulation could reveal new insights on HSC requirements for survival and proliferation. In addition, rapid medium exchange could allow live immunostaining of surface markers and, coupled with high frequency imaging of the clonal progeny, offer the possibility to link growth kinetics to *in vitro* phenotypic variations.

## 1.4 Chinese Hamster Ovary Cells

### 1.4.1 Recombinant Protein Production in CHO Cells

The first CHO cell line was derived in the late fifties from Chinese hamster ovaries by Theodore Puck[187]. Multiple variants such as CHO-K1 and CHO-S cells were later produced from the original cell line. CHO cells were initially used for a variety of applications including mutagenesis studies to isolate mutants with particular nutritional requirements. For instance, cells lacking the dihydrofolate reductase (DHFR) gene were found to be auxotrophs for glycine, a purine and thymidine[188]. This has been a useful selection system for cells expressing exogenous proteins. CHO cells eventually became the mammalian host line of choice for therapeutic

recombinant protein production, generally preferred to bacterial or yeast systems for the production of more complex proteins because of their capacity to perform post-translational modifications, in particular adding glycoforms that make proteins bioactive and compatible with humans[189].

CHO cell lines are well characterized and can be modified to integrate selection and gene amplification systems. Despite originating from tissue, CHO cells are readily adapted to suspension culture in serum-free media, an important feature for large-scale bioreactor production. In 1987, human tissue plasminogen activator (t-PA) became the first approved protein to be produced in CHO cells[190,191]. Many other products followed, demonstrating the safety of the CHO cell host[189]. The productivity of CHO cells was modest at first but a combination of media optimization, process development and cell engineering now yields titers up ~10 g $l^{-1}$ [192,193]. The recombinant protein market exceeded 50 billions in 2010[194] and more than 70% of therapeutic recombinant proteins are now produced in CHO cells[189]. The more recent increase of mAbs use for therapeutic purposes has been the major contributor to the growth of this field. Major biologics produced in CHO cells include Humira (Abbott), Avastin (Genentech) and Herceptin (Genentech), primarily used to treat rheumatoid arthritis, colorectal cancer and metastatic breast cancer, respectively. In 2010, together these three drugs have generated 7.4 billion in US sales[194]. CHO cells are expected to remain the most important platform for the production of mAbs, with many in clinical trials including biosimilars as patents approach expiry[195,196].

### 1.4.2 Cell Line Generation for mAb Production

Once the sequence of an antibody of interest is identified, the genes are typically inserted into a plasmid expression vector, along with regulatory elements used to drive transcription and enhance stabilization or translation

of the transcripts[197]. Methods such as calcium-phosphate precipitation, electroporation, lipofection and retroviral transfection are generally employed for transfection[197]. A selection gene such as glutamine synthase (GS) is also inserted into the vector to enable transfected cell selection in glutamine-free medium[198]. A GS inhibitor, methionine sulfoximide (MSX), is added to further increase selection pressure. Alternatively, DHFR can be used to select for transfected cells. A folic acid analogue that blocks DHFR activity, methotrexate (MTX), can be added to the culture at increasing concentrations to amplify the vector copy numbers and thereby also the recombinant protein production[188,189].

The site of random integration can dramatically influence the level of gene transcription. Hence, several gene expression systems have been engineered to improve productivity such as by the addition of chromatin opening elements in the vector to provide increased access to the gene[197,199] or by the insertion of elements that block chromatin-mediated repression[200]. In recent years, site-specific integration methods such as zinc-finger endonucleases and targeted genome editing have been developed to minimize variations due to the insertion site[201,202]. Targeted gene insertion in one hot spot can yield more homogeneous populations and facilitate clone selection. Related cell line engineering strategies can also improve cell survival or product quality, for example by adding genes to block apoptotic pathways or to modulate protein glycolysation[203,204].

Genetic instability decreases product yields and can affect the quality of biological products[205]. The factors responsible for production instability can be at genomic, transcriptional, post-transcriptional, translational, post-translational processing or secretion levels[206]. DNA rearrangements can lead to the dissociation of the antibody sequence from the promoter. It has been reported that MTX selection leads to homologous recombination and translocation that in turn can decrease production stability[207-209]. Epigenetic

changes such as methylation can also affect the binding of transcription factors and lead to decreased productivity levels[210,211]. As well, the proximity of transgenes to telomeric regions has been shown to influence productivity and stability[212]. Cell line instability can significantly impact the profitability of a therapeutic mAb by delaying or even compromising regulatory approval as months of cell line and process development efforts are wasted. The analysis of clonal heterogeneity can be used to predict instability by identifying low producing cell subpopulations before they impact the overall productivity[213]. For instance, single-cell quantitative PCR has revealed that stable clones contained homogeneous transgene copy numbers while clones prone to losing productivity had much more heterogeneous distributions[214]. As well, the analysis of intracellular mAb content on fixed cells by flow cytometry has shown that bimodal distributions containing a minority of cells with low protein content could be detected early in unstable clones[215].

### 1.4.3 Cell Line Selection Methods

The next step in the development pipeline of a new mAb following transfection and selection is the generation of clones with both high productivity and growth rates. Cloning is required to derive a cell line with more reproducible behavior and to maximize the product homogeneity[216]. The traditional method for selecting cell lines is by limiting dilution in multiwell plates. For traditional cell line generation, around 200-300 clones are cultivated for at least 2 weeks in 96-well plates until their productivity can be detected, such as by an enzyme-linked immunosorbent spot (ELISPOT) assay[217]. The highest producing clones can be transferred to a 24-well plate, then to larger culture dishes before being scaled up to batch shake flask cultures if their titer ranks sufficiently high. This process is often repeated to ensure clonality of the cell line. The top performing 10 clones are generally

assayed in fed-batch cultures at this stage[217] and concurrently analyzed for product quality and stability. A few clones (≤3) are moved to bioreactor evaluation before the top performing clone is selected for large-scale production[216,218]. A summary of a traditional cell line selection process is shown in **Fig. 1.1**.

The method described above is time-consuming, work-intensive and takes multiple months[216]. Large robotic systems (e.g. Cello, TAP Biosystems) are available to perform automated limiting dilution with high throughput but their cost is prohibitive for most laboratories[219,220]. Therefore, alternative approaches have been developed to accelerate and increase the throughput of the process. FACS can be employed to directly deposit single cells into wells, thereby eliminating the need for sub-cloning[216,221]. Further integration of FACS capabilities have evolved to measure single-cell productivity[221,222]. One approach is to introduce gene reporters into vectors to quantify expression levels and then enrich for high producers[223-225]. However, reporter levels may not be indicative of the recombinant protein secretion and the introduction of fluorescent reporters can reduce productivity in addition to not always being desirable for therapeutic applications[222,226]. Another approach is to stain for surface-bound mAb and then enrich for brighter cells by flow cytometry[227]. This method has a very high throughput but the relationship between surface-bound and secreted mAb varies between systems as the antibody is quickly dissociated from the cells[228]. Therefore, several techniques have been developed using semi-solid matrices to keep secreted antibodies in the vicinity of the cells. For instance, one way is to encapsulate cells into agarose microbeads and then to stain for the captured mAbs[229]. However, this technique poses challenges due to the low encapsulation efficiency needed to isolate single cells as well as the additional equipment required to make and analyze the microbeads. Another method is to capture the secreted antibody directly on producing cells using a cell surface affinity matrix[230,231]. Cells are

biotinylated and conjugated to a capture antibody before being placed into a viscous medium that limits protein diffusion. Secreted mAbs are thereby captured directly on the cells, which can then be sorted using fluorescently labeled antibodies. This method has been available for over a decade but has not been widely adopted by the industry, perhaps because the benefits do not justify the complication of functionalizing the cells and because the process can be difficult with fragile cell types[220]. A more user-friendly platform, CellXPress (Intrexon), captures mAbs on a protein G-coated surface and uses a laser to eliminate low producers until only one high-producing colony is left in a well[232]. This automated system has high throughput but can possibly damage the cells during laser irradiation[220]. A related commercially available platform, ClonePix (Molecular Devices), has used labeled protein A in the vicinity of high-producing clones cultivated in semi-solid medium. These two systems avoid the potential stress of FACS sorting on the cells and have the advantage of providing clone tracking and automated recovery. However, it has been shown that while ClonePix can enrich for high producers, the fluorescence intensity does not correlate well with clone productivity after expansion, requiring further downstream analysis to distinguish top producers[233].

**Table 1.2** summarizes the attributes of each cell line selection method for identifying production clones. The diversity of these methods and their shortcomings illustrates how the challenges have not been clearly overcome. Reports have shown that productivity in static cultures often do not match the productivity in suspension bioreactor cultures[217]. CHO cells do not thrive at the diluted seeding concentration required to generate clones. When the initial screening is performed on clones, the productivity measurement is a function of both the integral of viable cell concentration (IVC) and the cell specific productivity (SPR). Results can be misleading if cells do not proliferate at the same rate in static cultures compared to bioreactor cultures.

In addition to the physical difference of suspension cultures, the variation in the clonal results can be due to media conditioning, media adaptation, oxygenation, cellular interactions and/or loss of productivity over time. These discrepancies from suspension cultures can be further exacerbated when semi-solid medium is used. Overall, whereas low-performing clones can be eliminated early in the process, considerable time and resources can nonetheless be wasted on clones that end up exhibiting poor performance in large-scale cultures. Thus, there are strong incentives to develop improved technologies to rapidly measure secreted antibodies in conditions that can mimic bioreactor cultures, in a high-throughput fashion and at a reasonable cost. Microfluidic technologies can provide significant advantages to perform single-cell secretion assays due to the increased effective cell density in nanoliter volumes and the rapid accumulation of the secreted product to high concentrations. Combined with clonal cell culture, there is an opportunity to develop powerful cell line selection tools to circumvent some of the challenges of currently available technologies.

## 1.5 Thesis Objectives

This thesis aims at bridging an important gap between proof-of-concept development of microfluidic technologies and their actual use for single-cell culture applications in a biological setting. The overall objective of this research project was to develop a microfluidic cell culture system to facilitate the *in vitro* characterization of single mammalian suspension cells and their clonal progeny, and then to demonstrate the use of the technology by investigating the heterogeneity of biologically relevant cellular systems.

More specifically, the first aim was to solve common challenges characteristic of microfluidic cell culture and to build a robust microfluidic platform suitable for the high-throughput perfusion culture of suspension cell

types. The realization of this goal is demonstrated in Chapter 2, notably by the ability to sustain robust clonal proliferation of mammalian cells while maintaining functional activity of HSCs after recovery.

In order to greatly increase the accessible information on cellular behavior and exploit the analytical advantages of microfluidics, the next aim was to develop a high-throughput image acquisition and image processing system for the monitoring of single cells and the genealogical analysis of their progeny from time-lapse experiments. The third aim was to then use these tools to investigate the diversity in cell cycle entry, division kinetics, surface marker profiling, differentiation and death fates within HSC-enriched populations under static and temporally changing culture conditions, as demonstrated in Chapters 2 and 3.

The final aim of the thesis, presented in Chapter 4, was to demonstrate the flexibility and adaptability of the platform for a different but also relevant cellular system. This goal was achieved by developing a rapid single-cell protein secretion assay and combining it with microfluidic clonal culture for the selection of high mAb-producing CHO cell lines, a key step in the development of biotechnology products. This project has contributed important technological advances for the microfluidic culture and analysis of mammalian cells while demonstrating their value by addressing relevant biological questions.

**Table 1.1 Advantages of microfluidics for single-cell analysis**

| Application | Challenges with traditional methods | Advantages of microfluidics |
|---|---|---|
| Single-cell RT-qPCR | Limited abundance of starting template | Concentration enhancement in small volumes |
| | Cost and throughput required for analysis of large numbers of cells and target genes | Parallelization, automation and economy of scale |
| Single-cell genomics | Amplification bias and sensitivity | Improved reaction bias and sensitivity in nl volumes and reduced contaminant DNA |
| | Isolating individual cells | Integrated microfluidic cell sorting and processing |
| Single-cell measurements of intracellular proteins | Movement of living cells | Confinement of live cells in microfluidic structures |
| | Low amount of signal | Integrated single-cell handling for direct lysate analysis |
| Single-cell measurements of secreted proteins | Small amounts of secreted products from single cells | Concentration enhancement in small volumes |
| | Difficult to co-localize multiple cells in defined chemical environments | Ease of confinement in droplets or microchambers |
| Signaling studies | Mostly limited to static conditions | Easy temporal stimulation |
| | Inability to rapidly exchange conditions on suspension cells | Laminar flow and proper design enabling cell sequestration |
| Live-cell imaging | Difficulties of tracking cells through multiple frames | Confinement of clones facilitating cell tracking |

## Table 1.2 Culture of mammalian cells in PDMS microfluidic devices

| Cell type | Number of chambers | Chamber volume | Perfusion | Duration of culture | Quantitative growth rate comparison to macroscale control | Reference |
|---|---|---|---|---|---|---|
| Fibroblasts, endothelial cells, hESCs | 1 | 2,000 nl | continuous and sporadic (1-2 ml $h^{-1}$, every 2-4 h) | 7 days | normal | [78] |
| Human liver C3A, rat bone marrow, human lung epithelial A549 | 1 | 600 nl | continuous (0.03 ml $h^{-1}$) | 3 days | N/A | [234] |
| Epithelial breast cancer (MCF-7) | 1 | 500 nl | no perfusion | 4 h | N/A | [235] |
| Mouse embryonic fibroblasts, mESCs | 1 | 5,100 nl | continuous (10 nl $min^{-1}$) | 5 days | N/A | [236] |
| CHO-K1 | 1 | N/A | every 3 days | 7 days | N/A | [104] |
| β-TC-6 | 1 | 2,000 nl | continuous (0-6 µl $min^{-1}$) | 48 h | reduced in microscale | [79] |
| Human LS173T carcinoma cells (spheroids) | 1 | 3,700 nl | continuous (3 µl $min^{-1}$) | 43 h | N/A | [237] |
| HEPG2, MCF7, primary hepatocytes, primary bone marrow mesenchymal stem cells | 1 | 600 nl | continuous (0.02-0.1 ml $h^{-1}$) | 72 h | N/A | [65] |
| Embryonic bodies | 1 | N/A | no perfusion | 3 days | N/A | [238] |
| Mouse myoblasts (C2C12) | 1 | N/A | continuous (0.0005 – 0.22 µl $s^{-1}$) | 14 h | N/A | [84] |
| Fibroblast cell line, CHO cells and hepatocytes | 1 | 10-100 nl | continuous (5-50 nl $min^{-1}$) | 5 days | N/A | [239] |
| Primary rat dermal fibroblasts | 1 | 300 nl | continuous (0.05 µl $min^{-1}$) | 24 h | normal | [240] |
| GH3, PC12 cells | 3 | 600 nl | sporadic (every 8 h) | 48 h | N/A | [241] |
| Human epidermal keratinocytes (HEK) | 4 | N/A | continuous (0.025-0.4 µl $min^{-1}$) | 72 h | no growth in microscale | [242] |
| mESCs | 5 | 4,500 nl | continuous (0.01-1 µl $min^{-1}$) | 60 h | N/A | [66] |
| mESCs | 6 | 4,062.5 nl | continuous (33 µl $h^{-1}$) | 6 days | reduced in microscale | [69,70] |
| NIH 3T3, HeLa, B16 | 6 | 150 nl | continuous (0.1-4 nl $s^{-1}$) | 5 days | N/A | [243] |
| hESCs | 6 | 150 nl | sporadic (every 12 h) | 6 days | reduced in microscale but not significantly | [68] |
| Mouse fibroblasts (3T3) | 8 | N/A | no perfusion | 4 h | N/A | [244] |
| Rat primary hippocampal neurons | 16 | 11-69 nl | continuous (gravity) | 7 days | reduced in microscale | [80] |
| mESCs, murine embryonic fibroblasts | 16 | 565 nl | continuous (0.1 µl $h^{-1}$) | 5 days | N/A | [245] |
| Human lung carcinoma (A549) | 25 | 230 nl | sporadic (every 24 h, 1.2 µl $min^{-1}$) | 24 h | reduced in microscale | [82] |
| Rat bone marrow stromal cells | 30 | 100 nl | continuous (0.1 ml $min^{-1}$) | 11 days | N/A | [246] |
| NIH-3T3, A549 human lung alveolar cells, HeLa cells | 32 | N/A | sporadic (varies) | 6 h | N/A | [62,63] |

**Table 1.2 Culture of mammalian cells in PDMS microfluidic devices (continuation)**

| Cell type | Number of chambers | Chamber volume | Perfusion | Duration of culture | Quantitative growth rate comparison to macroscale control | Reference |
|---|---|---|---|---|---|---|
| CHO-K1 | 36 | N/A | no perfusion | 24 h | N/A | [105] |
| NIH 3T3, CHO and NRK | 45 | 6 nl | sporadic (every 4 h) | 4 days | N/A | [97] |
| Primary rat hepatocytes and fibroblasts (3T3-J2) | 64 | 1,200 nl | continuous (1 μl $min^{-1}$) | 32 days | N/A | [247] |
| HeLa, SY5Y human neuroblastoma, NIH-3T3, HepG2 and BAEC primary cells | 64 | 3-10 nl | continuous (0.2-0.4 μl $min^{-1}$) | 7 days | normal | [75] |
| 3T3 mouse fibroblasts | 96 | 40 nl | sporadic (varies) | 36 h | N/A | [61] |
| Human bone marrow mesenchymal stem cells | 96 | 40 nl | sporadic (every hour) | 7 days | N/A | [74] |
| PtK2, HeLa, MEF cells, mESCs | 96 | 3.7-7.4 nl | continuous (1 μl $h^{-1}$) | 60 h | N/A | [67] |
| Human carcinoma (HeLa) | 100 | 31 nl | continuous (0.13 μl $min^{-1}$) | 8 days | N/A | [248] |
| HeLa | 360 | 1-25 nl | continuous (0.1 μl $min^{-1}$) | 11 days | reduced in microscale | [81] |
| ALB/3T3, HeLa and bovine endothelial cells | 576 | 5 nl | no perfusion | 24 h | N/A | [76] |
| Endothelial cells | 672 | 500 nl | N/A | 1-3 days | N/A | [249] |

**Table 1.3 Summary of major cell line selection methods**

| Selection method | Throughput | Measurement of secreted antibody | Productivity measurement independent of growth rate | Suspension culture | Potential stress on cells | Seeding density | Sub-cloning required |
|---|---|---|---|---|---|---|---|
| **Limiting dilution** | Low | Yes | No | Yes | No | Low | Yes |
| **FACS single-cell deposition** | Medium | Yes | No | Yes | Yes | Low | No |
| **Fluorescent reporters** | High | No | Yes | Yes | Yes | Low | No |
| **Surface staining** | High | No | Yes | Yes | Yes | Low | No |
| **Matrix-based assays** | High | Yes | Yes | Yes | Yes | Low | No |
| **Gel microdrop** | Medium | Yes | Yes | No | Yes | Low | Yes |
| **CellXpress (Intrexon)** | High | Yes | Yes | No | Yes | Medium | No |
| **ClonePix (Molecular Devices)** | High | Yes | No | No | No | Medium | Yes |
| **Cello (TAP BioSystems)** | High | Yes | No | Yes | No | Low | Yes |

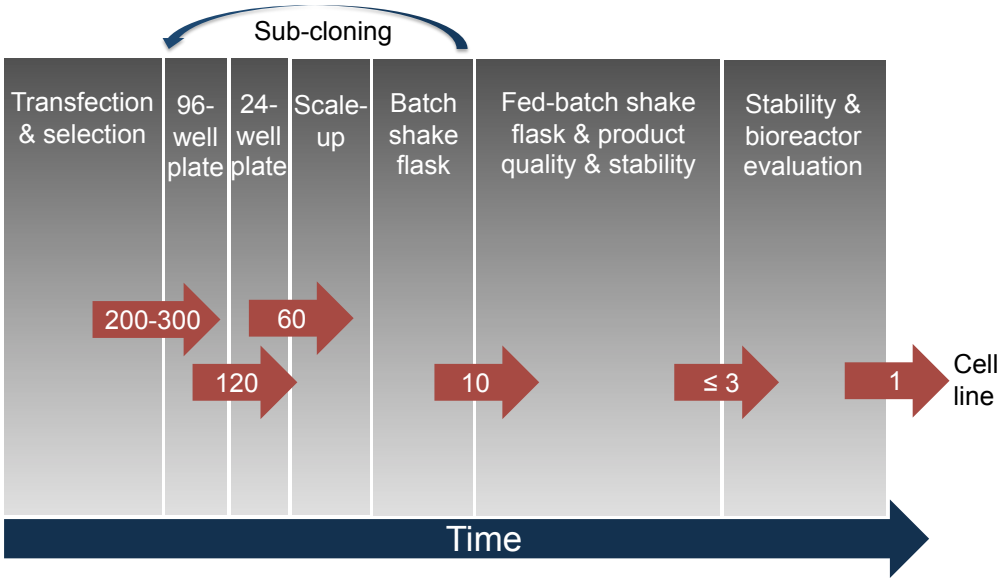


**Figure 1.1 Schematic representation of a traditional cell line generation process**

Cells are first transfected with a vector containing the transgene and are cultivated under selective conditions to eliminate non-transformed cells. Around 200-300 cells are screened in 96-well plates and the top 120 producers are transferred to a 24-well plate where the supernatant can be measured[217]. Top 60 performers are scaled up to batch shake flask cultures and sub-cloned if necessary. The productivity and product quality of the top 10 clones is measured in fed-batch cultures with stability studies performed in parallel. A small number of cell lines (≤ 3) is selected for bioreactor evaluation until the production cell line is chosen[218]. The entire process can take multiple months.

# CHAPTER 2 Microfluidic Cell Culture Arrays for High-Throughput Analysis of Clone Proliferation

The variable responses of individual or rare cells are often obscured by averaged measurements of large populations, which in turn make it difficult to distinguish intrinsically determined cell fate decisions from cell microenvironment effects. These problems are exacerbated in studies of primitive normal and malignant cell populations both because of current limitations in available cell purification protocols[151,155,250] and the inherently stochastic nature of self-renewal and differentiation processes[251,252]. New technologies for investigating the heterogeneity of responses at the single-cell level under well-defined chemical environments are therefore of great interest. This chapter describes the design, development and validation of a microfluidic cell culture platform with multiple functionalities for the high-throughput analysis of single HSCs.

## 2.1 Introduction

The need for scalable analysis of single cells is particularly acute in the investigation of HSC behavior. Analyses of clonal cultures established from single HSCs have previously provided many novel insights that highlight the power of this approach. These include experiments demonstrating that quiescence and delayed cell cycle entry correlate with higher self-renewal potency[55,166], that asymmetric cell divisions are features of HSCs with long-term hematopoietic activity[164,171] and that the probability of HSCs executing self-renewal divisions *in vitro* is regulated by the types and concentrations of growth factors to which they are exposed[171,172,253]. The study of HSCs using automated time-lapse imaging and, in some cases, micropatterned substrates, has enabled increased time resolution and the identification of

new phenotypes associated with particular biological behaviors[55,59,175,177,178]. These latter approaches indicate the great potential of higher throughput microculture systems and encourage the development of more advanced features including variable schedules of medium exchange and the parallelization of multiple experiments per run.

Integrated microfluidic systems provide many potential advantages for live-cell microscopy-based tracking studies. These advantages include low reagent consumption, precise temporal control over growth conditions, and an ability to work with, but not be limited to, small numbers of input cells. While these advantages have been well explored to analyze yeast and bacterial cell responses[43,45,72], applications to mammalian cells are less developed. Although fluid and cell handling capabilities have been well established[8,254,255], there have been relatively few reports of the application of programmable microfluidic systems to the analysis of mammalian cells in suspension culture[62,74-77]. This is due primarily to the greater difficulties encountered in obtaining robust growth of mammalian cells in microfluidic devices. For example, prior to this work microfluidic analyses of cytokine-responses of hematopoietic cells have been limited to measurements of signaling or apoptosis endpoints requiring less than 2 h of culture[184-186].

Major technical hurdles in available microfluidic devices that this work addresses include dehydration problems, immobilization of non-adherent cells during medium exchanges, and recovery of the cultivated cells for subsequent phenotypic or functional analysis. Previous mammalian microfluidic culture systems have been largely restricted to experiments with adherent cells incubated for short periods of time (hours) in relatively large volumes of medium[78,256] and/or maintained under high perfusion rates[67,257-259]. Aside from a few notable exceptions[68,75], longer-term microfluidic mammalian cell culture reports have exhibited reduced growth rates and even deviations from normal phenotypes[83]. Here we describe a simple

microfluidic cell culture design that solves these problems to obtain growth rate performance that replicates standard macrocultures while exploiting the high-throughput potential of microfluidic systems for single or clonal cell analysis. The utility of these devices is illustrated by investigating HSC proliferation control.

## 2.2 Materials and Methods

### 2.2.1 Microfluidic Cell Culture Array Fabrication

Devices were made entirely out of PDMS (Sylgard 184, Dow Corning). The chamber, control and membrane layers were assembled using multilayer soft lithography techniques[16,17] and the iso-osmotic bath and cover layers were integrated by PDMS stamping[260]. Chips were covalently bound to glass slides by oxygen plasma treatment. Devices were left at 80 $^{o}$C for at least 5 days and autoclaved prior to use for cell culture to ensure aseptic conditions and to drive the curing reaction to completion. Detailed protocols for mold and device fabrication are provided in **Appendix A** and **Appendix B** respectively.

### 2.2.2 Microfluidic Cell Culture

Microfluidic devices were placed inside a custom environmental chamber (Live Cell Instrument, Chamlide). The temperature was maintained at 37 $^{o}$C with 5% $CO_2$ in humidified air. Humidity levels approaching saturation were maintained by the addition of two 3-cm Petri dishes filled with water inside the microscope incubator. The iso-osmotic bath and the device were filled with medium 24 h prior to cell loading to obtain an equilibrium with the environment. Positive pressure was maintained by

gravity in the iso-osmotic bath by connecting a 3-ml syringe filled with medium to the bath, thus preventing the formation of gas bubbles that could alter imaging. The content of the bath was replaced prior to cell loading but was not exchanged during the experiment. Cells were concentrated to $2 \times 10^6$ cells $ml^{-1}$, transferred to a polytetrafluoroethylene (PTFE) tubing (Cole-Parmer) and plugged into the device via a stainless steel pin. The channels were flushed with medium and cells were pumped into the device at a rate of 1 $\mu l\ min^{-1}$. Initially loaded cells were allowed to settle down into the chambers, and then more cells were introduced until an adequate density was reached. In order to prevent gas bubbles from forming inside the device, an inlet pressure of 4 pound per square inch (p.s.i.) and an outlet pressure of 1 p.s.i. were maintained at all times. When activated, pumps and valves were pressurized at 35 p.s.i. For cultures of ND13 and NA10 cells, filtered Dulbecco's modified Eagle medium (DMEM) with 15% fetal bovine serum (FBS), 1.6 $\mu g\ ml^{-1}$ puromycin, 100 ng $ml^{-1}$ murine SF, 10 ng $ml^{-1}$ human interleukin (IL)-6 and 6 ng $ml^{-1}$ murine IL-3 (cytokines all from STEMCELL Technologies) was exchanged by replacing fourfold the volume of the chip after 24, 36, 48, 54, 60, 66 and 72 h of culture. Integrated micropumps and microvalves were automatically controlled by custom scripts (LabVIEW, National Instruments). Primary $CD45^+CD48^-EPCR^+CD150^+$ (E-SLAM) cells were isolated as described in the literature[151] and cultivated in Iscove modified Dulbecco medium supplemented with 10 mg $ml^{-1}$ bovine serum albumin, 10 $\mu g\ ml^{-1}$ insulin, and 200 $\mu g\ ml^{-1}$ transferrin, 40 $\mu g\ ml^{-1}$ low-density lipoproteins, 100 U $ml^{-1}$ penicillin, 100 $\mu g\ ml^{-1}$ streptomycin, 2 mM glutamine (all from STEMCELL Technologies), $10^{-4}$ M β-mercaptoethanol (Sigma) plus 20 ng $ml^{-1}$ IL-11 (Genetics Institute) and SF, as indicated. Medium was exchanged every 2 h with pumping for 15 min for each condition to ensure that any medium remaining from a previous condition would be washed out of the array. Images were taken every 12 min in 2 focal planes. The assessment of cell survival and early division times (first and second)

was performed manually by looking at the videos while the individual growth curves for each clone were generated using the image analysis algorithms described below.

### 2.2.3 Image Acquisition

The environmental chamber and the microfluidic devices were mounted onto an inverted microscope (Axiovert 200, Carl Zeiss). Bright field images were acquired with a 20× objective and a CCD camera (Orca ER, Hamamatsu) connected to a computer. The microfluidic cell culture array was automatically scanned with a motorized stage (ProScan II, Prior Scientific) with temporal resolution ranging from 5 min to 6 h depending on the experiment.

### 2.2.4 Alignment and Autofocus

Chamber alignment and autofocus scripts were implemented to acquire homogeneous images, which in turn improved the efficiency of cell segmentation. Each of the image frame contained 4 chambers. The coordinates of the 4 corners of the array were first determined manually and then coordinates for the entire grid were automatically calculated by extrapolation based on the device geometry. To adjust for small, local device distortions introduced during fabrication, each image frame was automatically aligned and focused. For each image frame, both row and column average pixel intensities were calculated. The dark edges of the chambers produced reproducible valleys in these profiles. The locations of these valleys were then found and used to calculate the shift needed in order to align the wells to the image. Once cells were loaded, the images were focused by minimizing the variance of the intensity of the pixels within each

chamber. A constant offset was then applied to each focus position to increase the accuracy of the cell segmentation algorithm. These scripts were implemented in LabVIEW (National Instruments).

### 2.2.5 Image Analysis

Cell segmentation scripts were written in MATLAB (MathWorks). Segmentation was accomplished through 3 main steps: well segmentation, cell-containing region segmentation and single-cell isolation. First, the individual chambers were segmented from the image background. This step of the segmentation was accomplished by applying a bandpass filter and then creating a binary image through an automatically determined threshold. The resulting binary image was then enhanced by removing objects touching the image borders and suppressing noise by eliminating small objects. Finally, the wells were segmented from the rest of the background by filling in the holes created by the edges of the wells. Next, the regions containing cells were separated from the rest of the wells. This was achieved by first applying a local standard deviation filter to enhance high contrast regions. The noise in the filter response was then suppressed by removing small regions and the resulting image was converted into a binary image through an empirically determined threshold. Holes were then filled in to create the final region mask. To segment the individual cells from the rest of the group, a local standard deviation filter and a bandpass filter were applied sequentially to the image. A top-hat filter was then used to enhance the edges and the bounded regions were subsequently filled. The resulting image was then converted to a binary image using an automatically determined threshold and further enhanced by removing small objects. The remaining number of objects was used for the automated cell count.

For experiments requiring a high count accuracy, for instance to generate growth curves of primary HSCs, we developed an enhanced cell segmentation algorithm based on sets of images taken at 2 different focal points (~50 μm apart). One image remained slightly above focus while the other was taken below the focal plane for use in segmentation. After segmenting the well as described above, the portion of the image that was hidden by edge shadows was identified by comparing the intensity of the region inside the perimeter to the global mean intensity of the well. The shadow was removed by calculating a brightness gradient mask around the obstructed region, combining it with the well mask, and applying it to the original image. Next, the high contrast image was used to identify the center of cells which appeared as high intensity spots by applying a brightness threshold. The centers were then dilated to achieve accurate cell size representation. The focused image was used to identify cell boundaries. The image intensity was inverted and sharpened using a negative Laplacian filter to enhance the cell edges. The sharpened image was then subtracted from the original, leaving only the cell contours and well. A bandpass size filter was then applied to remove objects that did not correspond to cell perimeters. The mask containing the cell contours was combined with the cell center mask and the image was dilated. A watershed cut algorithm was then applied to separate adjacent cells that may have been connected during the dilation and filling processes. Finally, the segmented image was compared to an initial image without cells and objects common to both were removed.

### 2.2.6 Live Cell Immunostaining

For live cell immunostaining, the microscope incubator was turned off and the main body containing the microfluidic device was placed on ice. For each step, at least 25 μl (fourfold the volume of the entire array) was pumped

into the array. The device was filled with blocking solution for 20 min. The biotinylated antibody cocktail (anti-B220-, Gr-1-, and Mac-1-biotin) was pumped into the device, incubated on ice for 40 min and then flushed with a solution of Hank's balanced salt solution supplemented with 2% fetal bovine serum (2% FBS-Hanks). A phycoerythrin (PE)-Texas-Red-streptavidin solution was then pumped into the device, incubated on ice for another 40 min and flushed again with 2% FBS-Hanks until all background fluorescence had disappeared. The array was then filled with fresh medium and placed on the microscope for imaging. Bright field and fluorescent images (exposure time, 1 s) were taken for the entire array.

### 2.2.7 Cell Recovery

Micropipettes were pulled from glass capillaries to a tip diameter ranging between 80 to 140 μm. At the end of an experiment, the cover layer was delaminated from the chip, and selected colonies were recovered by piercing the membrane with a micropipette. To recover the entire cell content from the microfluidic device, the chip was flipped upside down and flushed with medium by pumping backwards at a rate of 1 μl $min^{-1}$. Cells were then recovered from the PTFE tube and placed in a suspension culture plate for further analysis. To assess the efficiency of recovery, the plate was centrifuged for 5 min at 400*g*, the cells were allowed to settle for 1 h and then manually counted using an inverted microscope.

### 2.2.8 Macroscale Cultures

ND13 cells[140] were cultured in the same medium as in the microfluidic device (see above). Cells were passaged every 2-3 days and kept in culture for at most 60 days post-transduction. Control growth curves were generated

using an automated cell counter (Cedex, Roche Innovatis). For single-cell control cultures, cells were diluted to a concentration of 5 cells $ml^{-1}$, and distributed into 200 µl of medium per well in U-shaped 96-well plates. The cells were centrifuged at 400*g* for 5 min and allowed to settle for an additional hour in the incubator. Wells observed to contain single cells at the start of the experiment were counted manually every 12 h. For the colony-forming cell (CFC) assays, cells were incubated for 14 days following suspension in methylcellulose (MethoCult 3484, STEMCELL Technologies), after which the number of colonies obtained was manually counted under a microscope.

### 2.2.9 *In Vivo* Hematopoietic Reconstitution Assays

50 E-SLAM cells (containing ~25 HSCs) were isolated from *C57Bl/6Ly-Pep3b* mice to be transduced with a *NUP98-HOXA10hd* retroviral vector and then cultivated for 11 days as previously described[141]. On day 11, the cells were harvested and split equally between cultures in a 96-well dish (control) or a microfluidic array for a further 3 days of culture. Cells were harvested from both conditions, and then fractions representing 1/1,520$^{th}$ or 1/15,200$^{th}$ of the starting cells (estimated as a limiting dose of HSCs assuming a minimum of 60-fold or 600-fold expansion during the culture period respectively) were transplanted into lethally irradiated (810 cGy of x-rays) *C57Bl/6-C2J* mice along with 100,000 bone marrow helper cells. Six weeks, and 3 and 5 months later, peripheral blood samples obtained from each recipient were analyzed for evidence of donor-derived ($GFP^+$) lymphoid and/or myeloid cells as follows. Erythrocytes were lysed with ammonium chloride (STEMCELL Technologies) and leukocytes were suspended in 2% FBS-Hank's (STEMCELL Technologies) and then incubated with a combination of PE-labeled anti-Gr-1/Mac-1, perCP-Cy5.5-labeled anti-

B220 and APC-labeled anti-CD4/CD8 (BD Pharmingen). Flow cytometric analysis was then performed on a FACSAria (Becton-Dickinson).

### 2.2.10 Statistical Analysis

Error bars were calculated using standard deviation of the mean. Relative risk and 95% confidence intervals for the Cox proportional hazard model were calculated using the 'coxph' function from the R package 'survival' with tied times of death being handled using the Efron approximation.

## 2.3 Results

### 2.3.1 Microfluidic Device Design

We have created a 1,600 chamber-array system constructed from PDMS. Each chamber in our device had a volume of 4.1 nl and an integrated system of microvalves[11,16,17] was used to enable precise control and exchange of media (**Fig. 2.1**). PDMS has the advantage of being a transparent and biocompatible silicone elastomer[261] with a high gas permeability that makes the exchange of oxygen and carbon dioxide highly efficient. However, this property also allows rapid transport of water vapor, causing dehydration[262,263], a problem that is further aggravated by the high surface-to-volume ratio characteristic of nano-volume culture chambers. In addition, small hydrophobic molecules can be exchanged between the medium and the elastomeric material, leading to a possible depletion of medium components over time[96,263,264]. Thus, the material properties of available microfluidic culture devices typically promote changes in the composition of the medium that can produce spurious biological responses, reduced growth rates and

even death in the time frames relevant to the assessment of the cell responses of interest.

To circumvent these problems, we incorporated an integrated iso-osmotic bath into the device design, an approach previously applied to the optimization of protein crystallization[265,266]. This was achieved by fabricating the nano-volume chambers and control structures under a 150 μm thick PDMS membrane that separates the culture chambers from an iso-osmotic bath consisting of a macroscopic chamber filled with medium (~1 ml) enclosed by a gas-permeable PDMS cover layer (**Figs. 2.2a,b**). The high volume ratio of the iso-osmotic bath to the culture volume (~200), the low surface-to-volume ratio of the iso-osmotic bath and the near-saturation humidity provided by the microscope incubator together maintained the desired osmotic strength in each microculture chamber over many days. Assuming a relative humidity of 90% in the microscope incubator, we calculated the water losses from the bath to be in the order of ~1% over the course of a 5-day experiment (**Appendix C**). Continuous exchange through the membrane also kept PDMS-permeable medium components in equilibrium and the large volume of the iso-osmotic bath served as a means to reduce the effect of potentially toxic molecule leaching from the PDMS to the culture chambers[96].

### 2.3.2 Cell Immobilization

This microfluidic cell culture system also provides an important advantage over conventional 96-well plate or microwell-based imaging systems by allowing for media perfusion without disturbing cell positions. This capability can be exploited when dynamic medium exchange or immunolabeling of cells in the device is required either during or at the end of an experiment[62,74]. Although mechanical trapping has been proposed as a strategy for immobilizing cells[45,186,267], these methods are poorly suited for

non-adherent mammalian cells that can be deformed to pass through small openings and also can be deleteriously affected by mechanical stress. Our device employs a non-perturbing cell capture mechanism that uses gravity to trap cells as previously reported for well-based cultures[55,59,268-270]. Here we use a design in which the cell culture chambers are inverted with flow channels running over the top of cubic volumes having dimensions of 160 μm × 160 μm × 160 μm (**Fig 2.3a**). This allows laminar flow to deliver cells to the chambers and then ensure that the cells are not disturbed by subsequent perfusion of the device. During cell loading or medium exchange processes, the large volume expansion from the flow channels (≤13 μm × 100 μm) to the chambers (160 μm × 160 μm) results in a rapid reduction of the flow velocity with minimal values near the bottom of the culture chambers (**Fig. 2.3b**). Cells are loaded into the array using the microfabricated peristaltic pump (**Fig. 2.1**) at an overall flow rate of 1 μl $min^{-1}$. This flow rate corresponds to a maximum velocity of ~1 mm $sec^{-1}$ (**Fig. 2.3c**) with shear stresses of <0.3 Pa (**Fig. 2.3d**); i.e., below levels that elicit a physiological response[271]. During loading, cells essentially follow the streamlines at the top of the chambers and thus pass through the array without having time to settle into the chambers. Once the array is filled with cells, the pumping is stopped. The cells then settle to the bottom of the chambers and hence become sequestered away from the flow streamlines. As desired, this loading process can be repeated to achieve more concentrated loading. For example, loading efficiencies of 10-30% of 1,600 chambers enable 160-480 cells to be distributed as single cells in chambers for clonal analyses. Cell distribution across the array is generally uniform and can be modulated by changing the loading speed, the cell density, and the number of loading cycles. In the case of larger arrays (described below), the inclusion of upstream valves allows for direct control over the total number of cells loaded in each array region.

Medium exchange through the array is performed at a flow rate of 2 μl $min^{-1}$ without any observable disturbance of the spatial positions of cells (**Figs. 2.4a,b**). This provides an important advantage for tracking individual cells through time or for monitoring the growth of individual clones. The capability to immobilize non-adherent cells is demonstrated in **Figure 2.4c** where frequent imaging (every 5 min) was used to track the progeny of 3 individual input primitive hematopoietic cells (from the ND13 line described below) while replacing the medium every 6 h. The chamber geometry prevented appreciable shear stress from the perfusion flow with shear stresses calculated to be only up to ~$10^{-4}$ Pa at a distance of one cell diameter from the chamber bottom (**Fig. 2.4d**). From the images obtained, cell genealogical trees spanning a period of 60 h could thus be generated.

Despite the low flow rates, the small length-scale of the chambers allows for efficient exchange of nutrients, growth factors and metabolites through a combination of convection and diffusion. For larger molecules such as cytokines (D~$10^{-10}$ $m^2$ $sec^{-1}$)[272], this diffusion time is approximated by $\tau \sim x^2/D$ where x is one half the chamber height (80 μm), giving exchange times of ~1 min. These exchange times are significantly shorter than the 10-15 min periods used for medium perfusion. Tests with fluorescent dye showed that replacing fourfold the total volume of the array was sufficient to replace the medium from the device (**Fig. 2.4e**).

### 2.3.3 Recovery of Cells After Culture

Cell recovery is often desirable to enable subsequent assays to be performed on the progeny of the input cells. This is particularly important for assessing HSC responses where retention of *in vivo* hematopoietic reconstituting activity must be demonstrated. Our cell immobilization method allows for cells to be recovered from the entire array by simply

inverting the device, causing the cells to settle into the higher flow rate regions of the chambers (**Fig. 2.3c**). Cells are then collected as a pooled population by flushing back through the input port. This recovery method is simple and efficient, allowing for the harvesting of approximately 90% of the cells with losses mainly attributable to non-specific adherence of cells on the chamber surfaces. To recover the contents of selected individual chambers, the layer of PDMS covering the osmotic bath may be removed (**Fig. 2.5a**) and the contents of the desired chamber aspirated after piercing the overlaying membrane with a micropipette (**Fig. 2.5b**). This method was found to be remarkably reliable and easy, allowing more than 90% of the cells in single chambers to be harvested as determined by cell counts before and after recovery (**Figs. 2.5c,d**).

### 2.3.4 Microfluidic Culture of Single Hematopoietic Cells

To evaluate the utility of our device for supporting the growth of single primitive hematopoietic cells, we first compared the growth rate of a preleukemic murine cell line (ND13)[140,141] in the microfluidic device and in conventional cultures. These were set up in 24-well plates seeded with 150,000 cells $ml^{-1}$, 96-well plates seeded with single cells (in 200 μl), and microfluidic cell culture arrays with or without the integrated iso-osmotic bath. The growth kinetics of individual clones inside the device were monitored by time-lapse imaging (e.g. **Fig. 2.6a**)**.** In the presence of the iso-osmotic bath the population doubling time averaged over all chambers loaded with single cells faithfully reproduced the bulk exponential growth rate seen in the 24-well plates, indicating comparable conditions had been achieved. This was also the same as the average growth rate obtained in the 96-well single-cell cultures (**Fig. 2.6b**). In contrast, in devices that lacked the iso-osmotic bath, cell survival and division were both severely compromised (e.g.

**Fig. 2.6b**) despite humidity control in the microscope incubator and the initiation of medium exchanges 24 hours after starting the experiment.

A single cell in a 4 nl isolated chamber is at an effective concentration ~2.5 × $10^5$ cells $ml^{-1}$. At confluence, a chamber contains ~150 cells, corresponding to a concentration of ~4 × $10^7$ cells $ml^{-1}$. This concentration greatly exceeds the limits of what can be sustained in conventional batch cultures. As could be expected, cultures exhibited a strongly inverse correlation between the number of cells inoculated into each isolated chamber and the duration over which cell growth was maintained in the absence of perfusion (**Fig 2.6c**). Thus, medium exchange is required for the long-term culture (days) of proliferating mammalian hematopoietic cells in nanolitre volumes with a progressively increasing rate of medium exchange to accommodate the exponential growth rates obtained. For single-cell cultures of ND13 cells, we found that medium exchanges at 24, 36, 48, 54, 60, 66 and 72 h were sufficient to avoid conditions that led to decreased growth rates (due to nutrient limitations and/or build-up of growth-inhibiting metabolites). The growth of both ND13 cells and the progeny of primary HSCs could be sustained well past confluency by exchanging the medium every 2 h, and this ultimately resulted in much more densely packed 3-dimensional cultures (~ $10^8$ cells $ml^{-1}$).

We next undertook a similar experiment using freshly isolated $CD45^+$ $CD48^-EPCR^+CD150^+$ (E-SLAM) adult mouse bone marrow cells that are approximately 50% pure HSCs[8]. Time course measurements of the proliferation of these cells and their clonal progeny over 5 days showed that the kinetics of 3 successive divisions were comparable to those obtained in macroscale cultures[55,171] (**Fig. 2.7**). Together these results establish the ability of the microfluidic system to support similar rates of growth of both genetically engineered and primary normal HSCs as when these cells are cultivated in conventional systems.

### 2.3.5 Assessment of Growth Heterogeneity in Cell Populations

To manage the large number of images generated per experiment, we developed a custom image analysis software program able to automatically count the cells at each time point in individual chambers (**Fig. 2.8a**). The resulting automated cell count was generally in agreement with the manual quantification of the cells. At higher cell numbers, however, the chamber edge shadow would interfere with the cells near the border, thereby resulting in a slight underestimate of cell numbers using the image algorithm (**Fig. 2.8b**). We used time-lapse imaging and automated image analysis to generate individual growth curves for 243 single ND13 cells over a period of 72 h (**Fig. 2.9a**). After that time, the fastest growing clones became multilayered and too large for further tracking by image analysis. Although the average doubling time for all cells was 16.8 h, we observed substantial heterogeneity in the growth characteristics of individual clones. 52% of the input cells either did not divide or produced progeny that died before the end of the experiment. This widespread death was offset by the rapid proliferation of other cells that divided as frequently as every 12 hours, but with large variability between clones (**Fig. 2.9b**). These variable clone size expansion rates were also observed for ND13 cells generating clones in the 96-well plates (**Fig. 2.9b**).

To further investigate the cellular basis of this heterogeneity, we first immunostained the input ND13 cells for their expression of 3 lineage (lin) markers (Gr-1, Mac-1, and B-220) and then compared the clonal growth kinetics after 72 h of those that were initially positive ($lin^+$, differentiated) and those that were initially negative ($lin^-$, primitive) (from images taken every 5 min). We also used the perfusion capabilities to perform a second lineage staining of the clones present at the end of the experiment. This showed that most of the $lin^+$ cells did not produce colonies (**Fig. 2.10a**), replicating the failure of $lin^+$ cells to form colonies in 96-well cultures. In

contrast, the $lin^-$ cells produced clones efficiently but these were of different sizes and included different phenotypes (**Fig. 2.10b**). Some of the $lin^-$ cells gave rise to exclusively $lin^+$ or $lin^-$ clones. Others contained a mixture of phenotypes (**Fig. 2.10c**). This finding suggests that ND13 cells maintain a population of $lin^-$ clonogenic progenitor cells that produce both more of themselves (i.e., $lin^-$ cells) as well as more mature non-clonogenic $lin^+$ cells. Further support for this model was obtained by isolating $lin^-$ cells by FACS, expanding them in macroscale cultures and then demonstrating after 12 days that a new $lin^+$ population had again been produced (**Fig. 2.11**).

### 2.3.6 Preservation of Functional Properties of Primitive Cells

As a first assessment of the biological state of cells cultivated in our microfluidic system, we evaluated the progenitor population of ND13 cells using a standard semi-solid colony-forming cell (CFC) assay in which the cells are suspended in a viscous methylcellulose-containing medium. Unseparated ND13 cells were first cultivated in the microfluidic device for 72 h and then approximately 720 cells from 5 chambers (corresponding to 11 starting cell equivalents) were recovered and plated into triplicate CFC assays. Parallel methylcellulose assays were set up with the progeny of 11 starting cell equivalents generated in conventional macrocultures. The number of colonies obtained from each source was similar, further demonstrating the ability of the microfluidic device to support an equivalent expansion of ND13 cells with sustained progenitor activity (**Fig. 2.12**).

To test the ability of our microfluidic cell culture device to support self-renewal divisions of primitive hematopoietic cells with long-term *in vivo* reconstituting potential, we examined the growth of mouse bone marrow cells transduced with a NUP98-HOXA10 homeodomain (NA10hd) fusion gene.

This strategy potently stimulates the expansion of HSCs *in vitro* without any signs of leukemic transformation[139,141]. To obtain these cells, we first isolated E-SLAM cells from adult mouse bone marrow (~50% pure HSCs) and then transduced the cells with a NA10hd-encoding retroviral vector. The transduced cells were then expanded for 11 days in a macroscale culture. At the end of this period, replicate aliquots were transferred either to the microfluidic array or a control macroscale vessel and cultivated for an additional 60 h. The cells from each of these two cultures were recovered and decreasing fractions of the same starting equivalent cell numbers injected into groups of 6 irradiated mice each. The total number of cells obtained from the microfluidic chambers and the control macrocultures were similar (**Fig. 2.13a**). All mice showed comparable reconstitution levels by the transplanted cells for >16 weeks post-transplantation, indicative of an overall >600-fold expansion of HSC numbers as compared to the HSC content of the cells initially transduced (**Fig. 2.13b**). Reconstitution of both the myeloid and lymphoid compartments was also equivalent for both sources of expanded HSCs (**Fig. 2.13c**). Notably, the expanding NA10hd HSC population contained a greater proportion of fast growing cells compared to the ND13 cells (**Fig. 2.13d**), consistent with the most primitive nature of NA10hd cells.

### 2.3.7 Growth Kinetics of NA10hd-Transduced Cells

The important *in vitro* expansion characteristic of NA10hd-transduced HSCs can be due to an increase in HSC symmetric self-renewal, a decrease in HSC death, an increase in cell cycle time or a combination of all the above. These events can be hard to distinguish from one another as transformed populations initially contain a mixture of both transduced and non-transduced cells that eventually become dominated by NA10hd-expressing cells several days post-transduction. We used the microfluidic array to

examine the growth kinetics of NA10hd-transduced cells at the single-cell level in early days following transduction. It was possible to retrospectively identify which cells had been successfully transduced by analyzing the GFP fluorescence of each clone at the end of the culture (e.g. **Fig 2.14a**). We first looked at the first division of mouse HSCs that had been transduced with a lentiviral vector. NA10hd-transduced cells showed a faster entry into cell cycle than their non-transduced counterpart. However, a similar behavior was observed in the control population transduced with a Tomato vector (**Fig. 2.14b**), which suggests that lentiviral vectors preferentially infect cells that have a faster entry into cell cycle. Thus, NA10hd-GFP-transduced cells were compared to GFP-transduced cells in the subsequent experiment. We asked whether the marked *in vitro* expansion induced by NA10hd in mHSCs transduced with a retroviral vector could be attributed to a decrease in cell cycle time. The division kinetics of NA10hd-GFP and GFP-transduced single cells was tracked in the microfluidic array 2 days following transduction and there was no significant difference in cycling transit times between the two populations (P-values = 0.27 and 0.48 for the second and third divisions respectively) (**Fig. 2.14c**). Both populations also had similar survival rates (90.2% and 90.9% of single cells for the NA10hd-GFP and GFP control populations respectively). Together these results suggest that the growth advantage of NA10hd-transduced cells is not due to faster cycling or reduced death, but rather to an increase in stem cell self-renewal that over time leads to sustained proliferation.

### 2.3.8 HSCs Response to Temporally Varied SF Stimulation

Steel factor (SF) is a cytokine critical for promoting HSC self-renewal *in vitro*[134] and *in vivo*[273]. Previous work has shown that *in vitro* exposure of HSCs to low concentrations of SF (1 ng $ml^{-1}$) leads to rapid loss of HSC

functionality and later delayed proliferation and death compared to culture in higher concentrations (300 ng $ml^{-1}$)[171]. However, the reversibility of the effect of low SF concentrations on subsequent HSC survival and proliferation is not known. To address this question we used the capabilities of the microfluidic system to test how long quiescent adult HSCs could be exposed to a low SF concentration before rescue by exposure to a high concentration was no longer possible. In order to compare the responses of groups of single HSCs exposed to multiple conditions in parallel, we introduced a modification to the original microfluidic system. This modified system was enlarged to contain 6,144 individual chambers and these were provided with multiple additional inlets and flow control valves to examine many temporally varying conditions simultaneously (**Fig. 2.15**). This allowed us to study 6 different conditions in which primary mouse HSCs (E-SLAM isolates of adult mouse bone marrow) were exposed to 20 ng $ml^{-1}$ of IL-11 plus either 1 ng $ml^{-1}$ SF for the first 8, 16, 24 or 48 h followed by 300 ng $ml^{-1}$ SF for the remainder of the experiment, or constant SF concentrations of 1 ng $ml^{-1}$ or 300 ng $ml^{-1}$ for the entire 12-day experiment (**Fig. 2.16a**). The experiment was repeated twice yielding 5 days of imaging data for a total of 769 single E-SLAM cells cultivated in the device. By day 5, the fastest growing clones reached confluence and we could no longer quantitatively monitor their size. The growth rates of all clones were compared to the results for the constant high SF concentration. As a control, we grew the same cells in conventional macrocultures in 20 ng $ml^{-1}$ IL-11 plus either 1 or 300 ng $ml^{-1}$ SF and these yielded the same growth kinetics as in the microfluidic device. A Cox proportional hazard analysis of the cell survival over time, defined as the fraction of starting cells that remained viable or gave rise to clones, showed no significant difference ($P$ value > 0.1) in survival when the cells were rescued from 1 ng $ml^{-1}$ SF exposure within the first 16 h of culture (**Table 1.1**). However, more prolonged initial exposure to 1 ng $ml^{-1}$ SF led to a rapid decrease in viability between 16 and 24 h and, after that time, the cells could no longer be rescued

by exposure to 300 ng $ml^{-1}$ SF (**Fig. 2.16b**). Interestingly, most dividing cells completed a first mitosis between 24 and 60 h of culture for all conditions and the SF concentration did not affect these cell division kinetics (**Fig. 2.16c**). Analysis of the second division showed comparable kinetics, with more than 80% of the clones remaining viable after a first division regardless of the SF concentration to which they had been initially exposed. To generate individual growth curves of primary cells with higher accuracy, we developed a cell count algorithm based on images taken at 2 different focal points. This enhanced bifocal algorithm gave high accuracy cell counts with excellent correspondence to cell counts determined by manual counting (**Figs. 2.17a,b**). Individual growth curves showed similar growth kinetics patterns regardless of the conditions cells had been exposed to (**Fig. 2.18**). Thus, although a high SF concentration influenced the viability of HSCs as they exited quiescence, it did not directly impact the subsequent division kinetics of cells that had completed a first division.

## 2.4 Discussion

Microfluidic technology combines the advantages of dynamic control of the culture medium, high-throughput experimental designs and automation of image data acquisition. This creates new opportunities for applying the power of clonal analysis to investigations of population responses to multiple extracellular cues that vary in nature and schedule of exposure. Despite increasing improvements in microfluidic technologies, device development to achieve conditions that can support the sustained growth characteristics and biological responses of non-adherent mammalian cells obtained in traditional cultures have not been reported. The device described here introduces several novel design features that are generally applicable to investigate heterogeneous populations of mammalian cells that have stringent medium

requirements. These features include the incorporation of an iso-osmotic bath to control unwanted permeation and dehydration effects, the use of high aspect ratio wells to contain and immobilize non-adherent cells during perfusion, and the use of a reverse perfusion strategy to recover the cells for subsequent analysis or, using selective aspiration, to recover clones of interest.

Using this system, we demonstrate for the first time the successful culture in microfluidic devices of cytokine-dependent hematopoietic cells with expansion and enhanced HSC function consistent with observations in conventional cultures having volumes that are larger by more than 4 orders of magnitude. When compared to previous microfluidic culture of suspension cells, our device provides the highest number of chambers, the longest demonstration of sustained culture, the smallest reported chamber volumes, and the first application to investigate responses of highly purified primary HSCs. The combination of throughput and small chamber volume is particularly attractive for the analysis of such rare cell types or minority subpopulations at high effective cell concentrations. Scalable nanoliter volume cultures could also allow for the investigation of autocrine signaling by single cells using integrated valves to isolate chambers of different volumes during culture. This strategy should thus have the potential to increase the plating efficiency of cell types with unknown requirements and/or impractically high minimum input cell densities. Similarly, the analysis of different cell seeding densities or the co-culture of different cell types at limiting dilution could be used to directly investigate the cell-cell influences of secreted factors. It is also worth noting that with sufficient medium exchange, we were able to produce and maintain densely packed 3-dimensional cell populations, offering new opportunities for the study of HSCs under conditions that may more closely resemble the *in vivo* stem cell niche.

A combination of time-lapse imaging with programmable medium exchanges that do not disturb the spatial position of cells offers unique abilities for measuring the responses of single non-adherent cells to dynamically changing medium conditions. Here we apply this feature to gain new and unanticipated insights about the role of SF exposure in regulating cell survival with both temporal precision and single-cell resolution. Our results show that SF plays a critical role in regulating the survival of cytokine-activated HSCs within a small window between 16 and 24 h of being placed *in vitro,* without affecting the early division kinetics of the cells that survive. These findings suggest that SF may be involved in an early regulatory checkpoint when HSCs exit $G_0$ to enter $G_1$. It has been reported that fetal liver HSCs, which are already cycling, respond to lower SF concentrations *in vitro* compared to quiescent adult bone marrow HSCs[274]. The comparable division kinetics of cycling cells regardless of SF concentration is consistent with this observation.

The ability to replace the culture medium without disturbing cells is essential to avoid nutrient limitations that occur in longer-term experiments, especially at such small culture volumes where even a few cells rapidly grow to high concentrations. In the future, we anticipate it will be possible to further couple emerging image processing tools for the identification of new morphologically defined phenotypes[275] and to track different progeny types identified by specific markers or fluorescent reporters[175]. The added advantages of high throughput and automated medium exchange control will be powerful assets for undertaking previously impossible investigations of the mechanisms controlling cell fate choices and genealogical relationships of rare cell types responding to environmental cues.

Although not unique to microfluidic systems, the throughput and automation of our system also allows for more detailed studies of colony growth and variability that would be impractical using traditional culture

methods. The results presented here provide multiple examples of how macroscale culture performance can be matched in these devices as well as a robust demonstration of how the system can be readily modified to expand the size and complexity of experimental designs to be performed. A recurring theme in both normal and transformed populations is that only a small fraction of the cells is responsible for the long-term maintenance of the overall population. The technology described here can be easily adapted to investigate many such cell types/organisms as well as modified for other applications including drug-response screens, culture optimization, cell characterization and clone selection.

**Table 2.1 Cox proportional hazard analysis of primary HSC survival**

| Condition | *n* | Relative risk (95% CI) | *P* value |
|---|---|---|---|
| High [SF] (300 ng ml$^{-1}$) | 294 | 1.00 | – |
| 8 h in low [SF] | 107 | 0.82 (0.64-1.06) | 0.13 |
| 16 h in low [SF] | 76 | 1.03 (0.78-1.36) | 0.84 |
| 24 h in low [SF] | 24 | 1.27 (0.81-1.99) | 0.29 |
| 48 h in low [SF] | 79 | 1.78 (1.37-2.31) | <0.0001 |
| Low [SF] (1ng ml$^{-1}$) | 189 | 1.53 (1.25-1.86) | <0.0001 |

Relative risks and *P* values were calculated based on the high [SF] condition
CI, confidence interval
–, not applicable

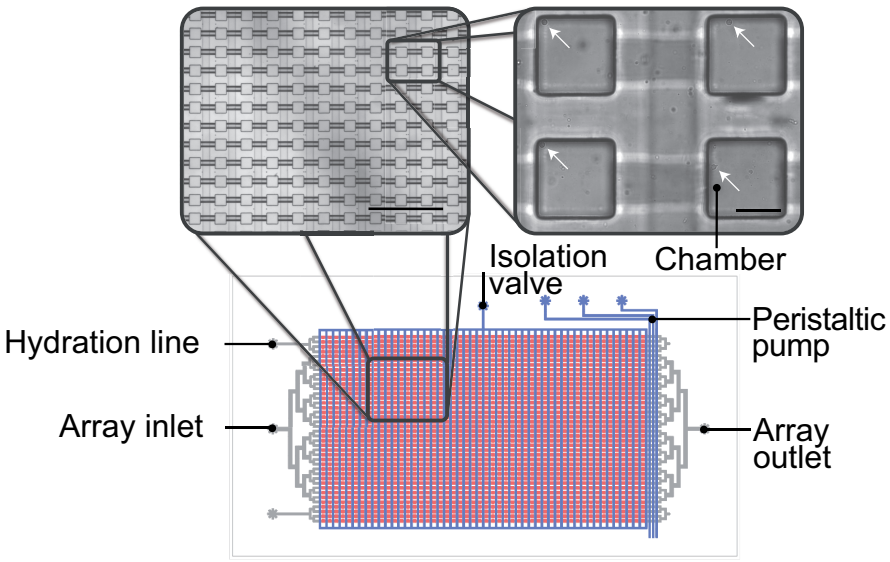


**Figure 2.1 Microfluidic cell culture array**

The cell culture layer contains 1,600 chambers (pink) connected by flow channels (grey). Hydration lines are located on each side of the array to minimize edge effects. The control lines (blue) consist of an isolation valve and a peristaltic pump to control cell loading and perfusion rates. Scale bars, 1 mm (left) and 100 μm (right).

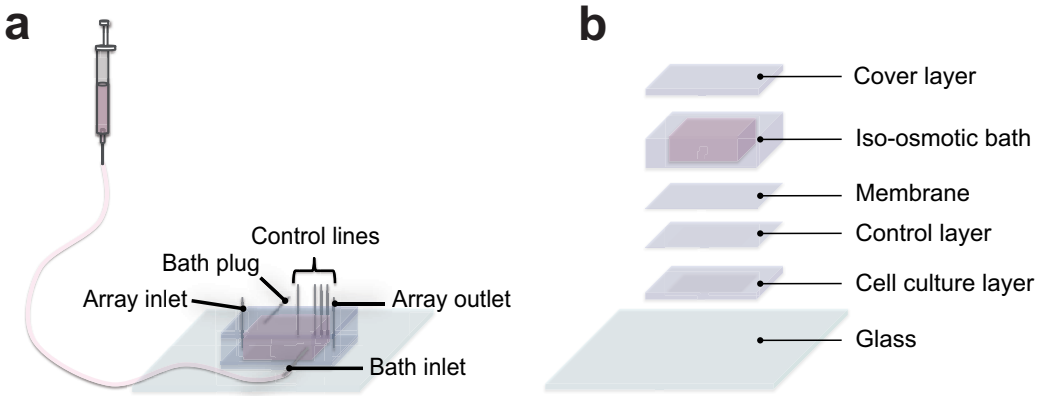


**Figure 2.2 Iso-osmotic bath in microfluidic cell culture device**

(**a**) The integrated iso-osmotic bath was filled with medium to prevent evaporation and maintain constant osmolarity inside the chambers. When necessary, the bath content was replaced by removing the plug and introducing fresh medium from the syringe. Positive pressure was maintained by the syringe to prevent the formation of air bubbles. The array inlet and outlet were pressurized by air and the control lines were connected to solenoid actuators. (**b**) Devices were fabricated using PDMS, a transparent and gas permeable polymer. The cell culture layer, control layer and membrane were bound to each other by multilayer soft lithography. The membrane and cover layer enclosing the iso-osmotic bath were assembled by PDMS stamping.

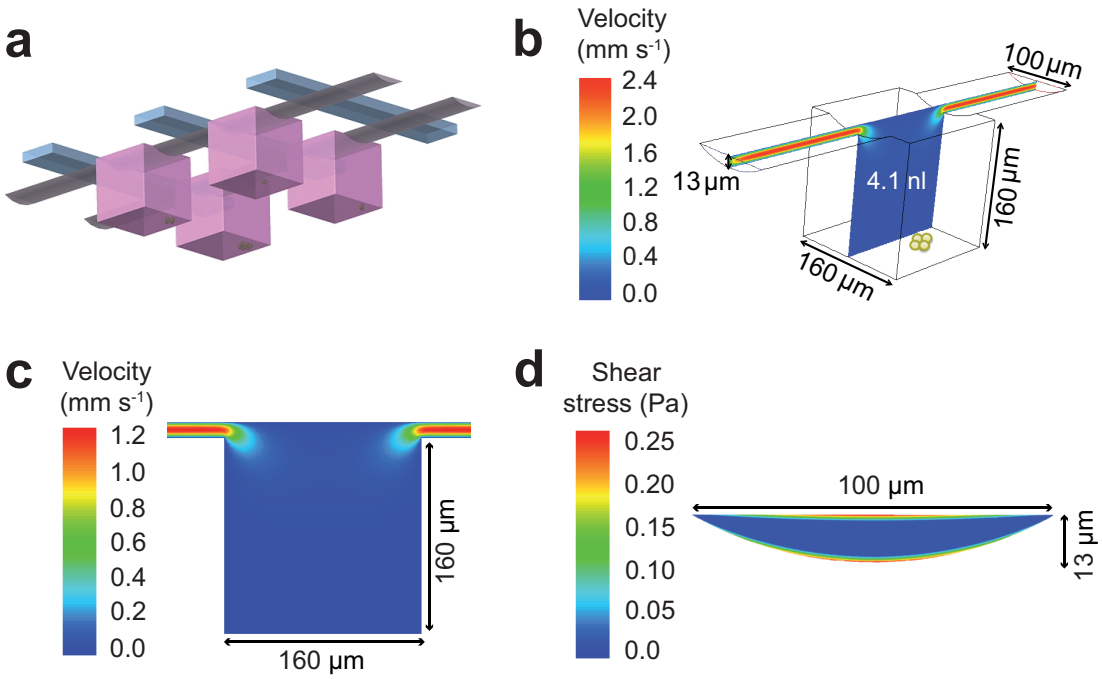


**Figure 2.3 Flow simulations during medium exchange and cell loading**

(**a**) Suspension cells settle down to the bottom of each chamber (pink) by gravity. Control lines (blue) are located above the flow channels (grey) (**b**) Numerical simulation of flow profile through a culture chamber shows that chambers are deep enough to ensure that cell spatial positions are not altered during medium exchange. Each chamber is 160 µm deep and 4.1 nl in volume. (**c**) The velocity magnitude (m $s^{-1}$) during cell loading is modeled for a total flow rate of 1 µl $min^{-1}$. The maximum velocity in the flow channels does not exceed $1.2 \times 10^{-3}$ m $s^{-1}$. (**d**) For the same conditions, the shear stress (Pa) on the flow channel walls is modeled. The maximum shear stress exerted on the cells is 0.26 Pa.

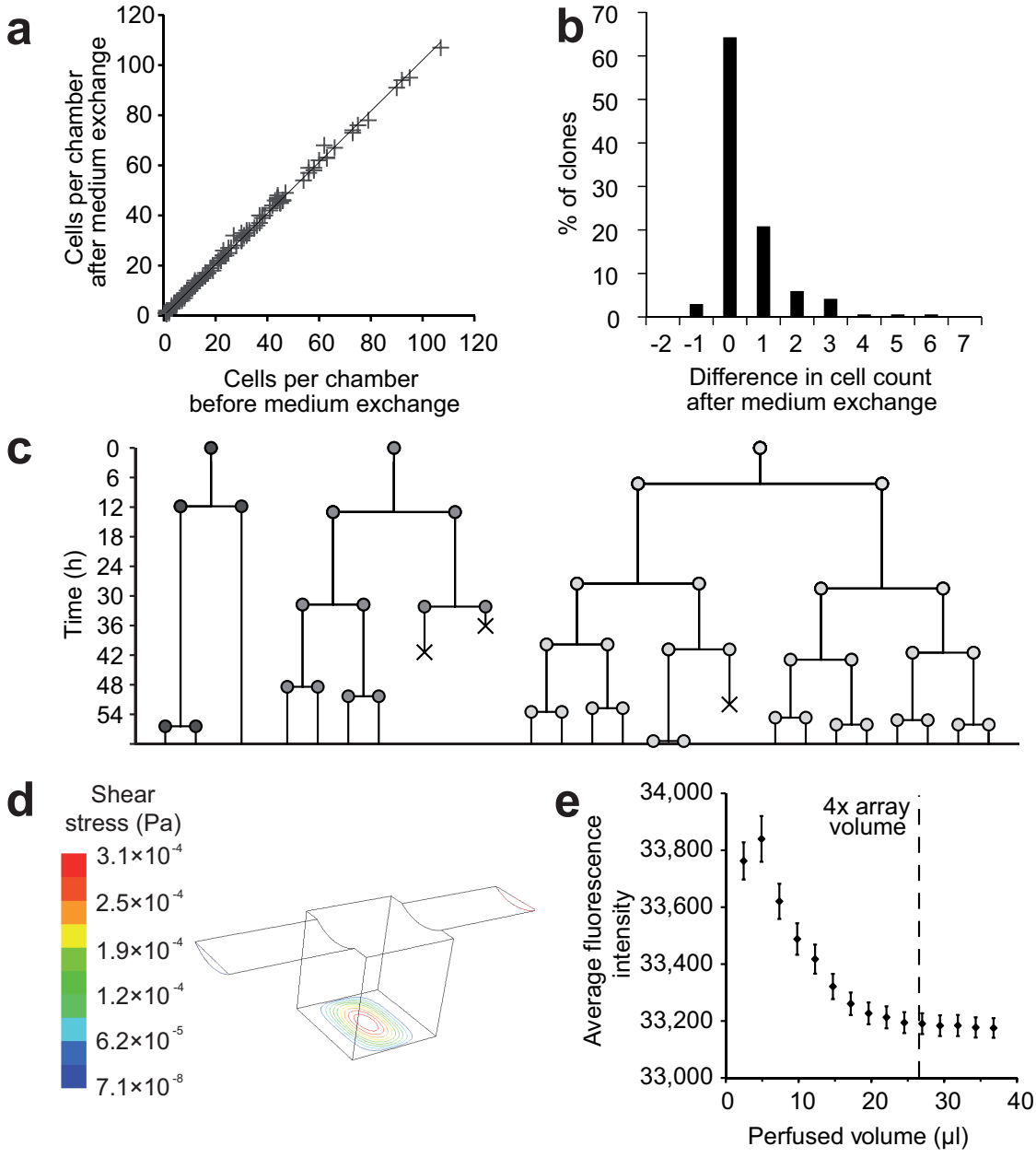
a
Cells per chamber after medium exchange
Cells per chamber before medium exchange
b
% of clones
Difference in cell count after medium exchange
c
Time (h)
d
Shear stress (Pa)
3.1×10-4
2.5×10-4
1.9×10-4
1.2×10-4
6.2×10-5
7.1×10-8
e
Average fluorescence intensity
4x array volume
Perfused volume (µl)

**Figure 2.4 Cell immobilization during medium exchange**

(**a**) Manual cell counts (ND13 cells) in individual chambers before and after medium exchange (2 μl $min^{-1}$ for 10 min) remained similar (slope = 1.02, $R^2$ = 0.998). (**b**) Variations in clone size after medium exchange. The time between both image sets was approximately 15 min (5 min acquisition + 10 min perfusion). In this timeframe, it is frequent to see cells divide or die. Small differences are due to cell death or division and not to the addition or loss of cells. (**c**) Cell immobilization allows lineage tracing of individual ND13 clones without disturbance from the medium exchange process. Cells were imaged every 5 min and medium was exchanged every 6 h. Genalogical pedigrees of 3 clones were built by manual inspection of the videos. (**d**) The shear exerted on the cells while at the bottom of the chamber during medium exchange is calculated for a total flow rate of 2 μl $min^{-1}$. The maximum shear stress does not exceed $3.1 \times 10^{-4}$ Pa. (**e**) The microfluidic cell culture array was loaded with medium supplemented with PE-TexasRed-streptavidin and the inlet was replaced by medium only. Pictures of the last 3 columns of the array were taken during perfusion and fluorescence intensity was quantified using Image J. This experiment shows that perfusing fourfold the volume of the array (26 μl) is sufficient for medium exchange. Each data point represents the average of 9 wells and error bars represent the standard deviation.

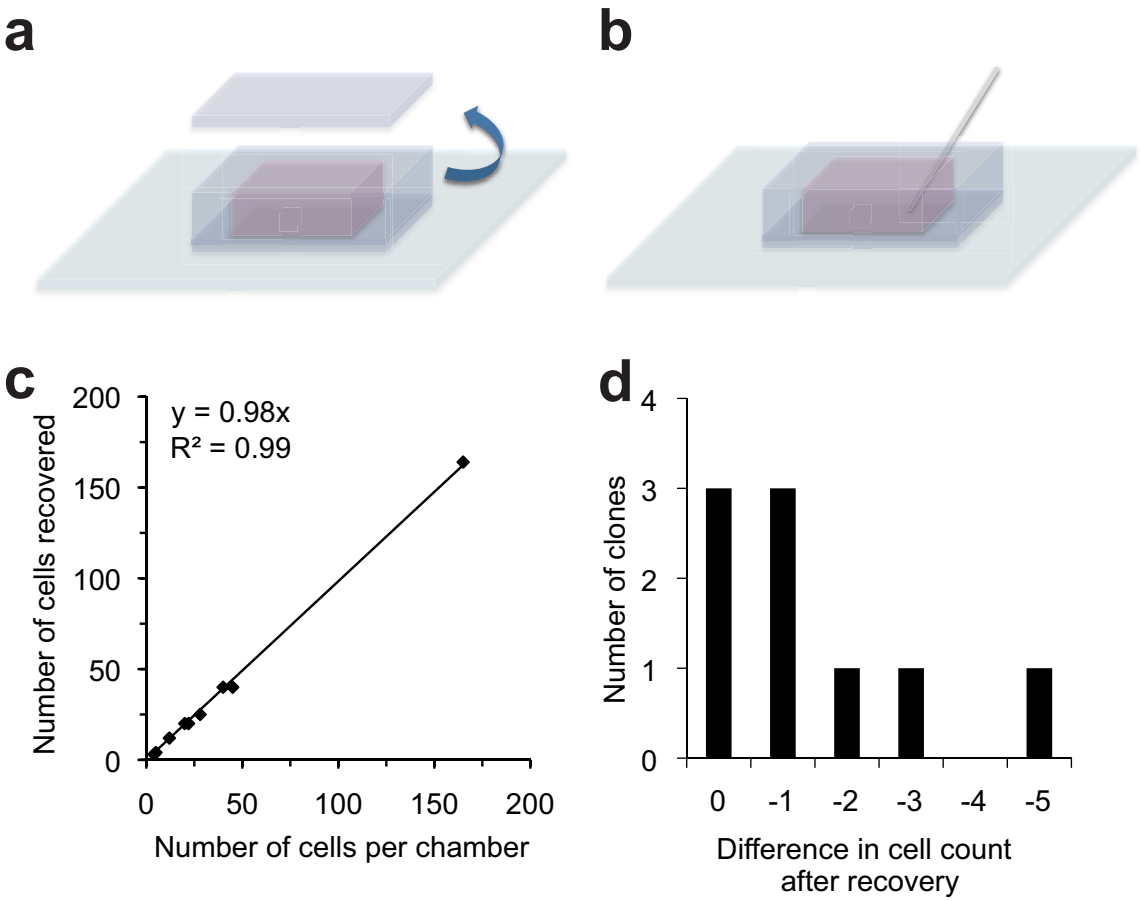


**Figure 2.5 Recovery of selected clones**

(**a**) Individual clones can be recovered from individual chambers by delaminating the cover layer of the device and (**b**) transpiercing the membrane with a micropipette. (**c**) The efficiency of recovery was measured by counting the number of cells in individual chambers and recounting the number of cells that were successfully transferred in a well. On average, 91% of the cells from individual colonies of different sizes could be recovered. (**d**) Cell losses from recovery ranged from 0 to 5 cells per clone.

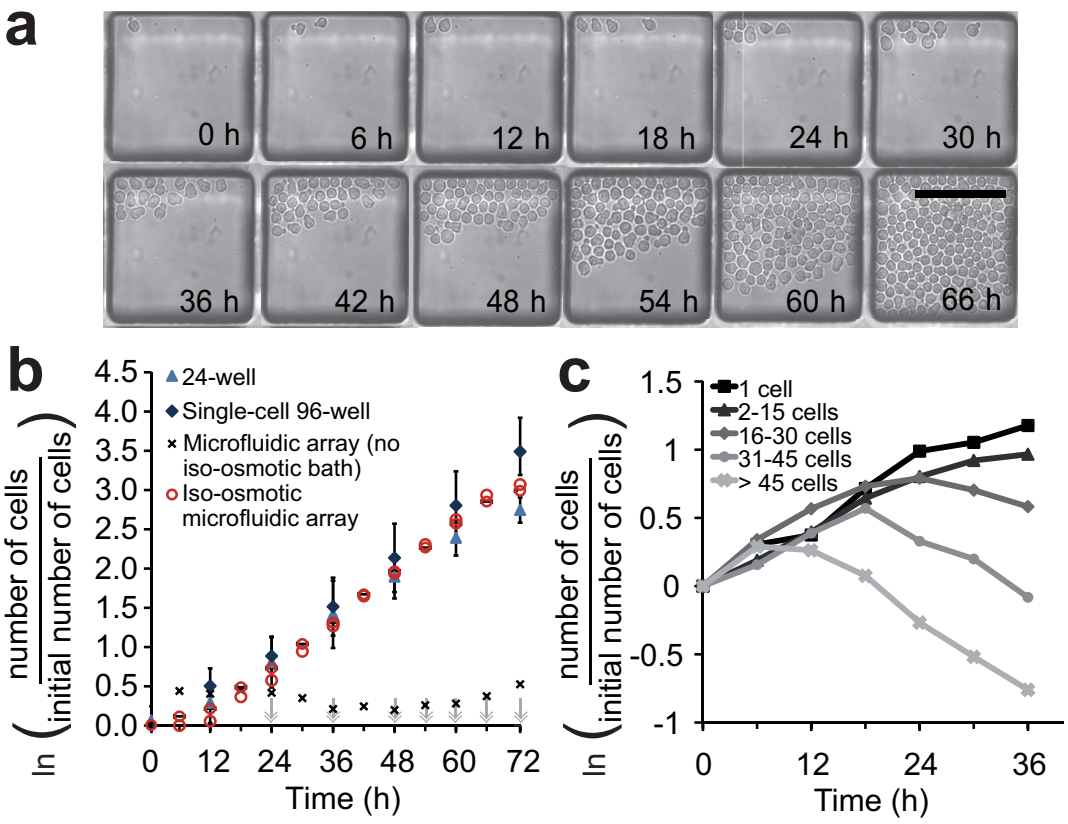


**Figure 2.6 Robust clonal culture of ND13 cells in the perfusion microfluidic cell culture array**

(**a**) Time-lapse imaging of clonal ND13 cell expansion in a chamber. Cells were automatically imaged every 6 h. Scale bar, 100μm. (**b**) Average clonal cell growth rates of ND13 cells in the microfluidic cell culture array ($n$ = 2 experiments) were the same as those in macroscale dish cultures ($n$ = 3 experiments) and single cells plated in 96-well plates ($n$ = 3 experiments). The culture medium was refreshed with increasing frequency (arrows) in the microscale experiment. The absence of an iso-osmotic bath rapidly altered cell growth. (**c**) Cell death in the absence of medium exchange was inversely correlated to the initial number of cells per chamber. Nanoliter-volume chambers at different seeding density were isolated with no medium feeding and no iso-osmotic bath in batch mode.

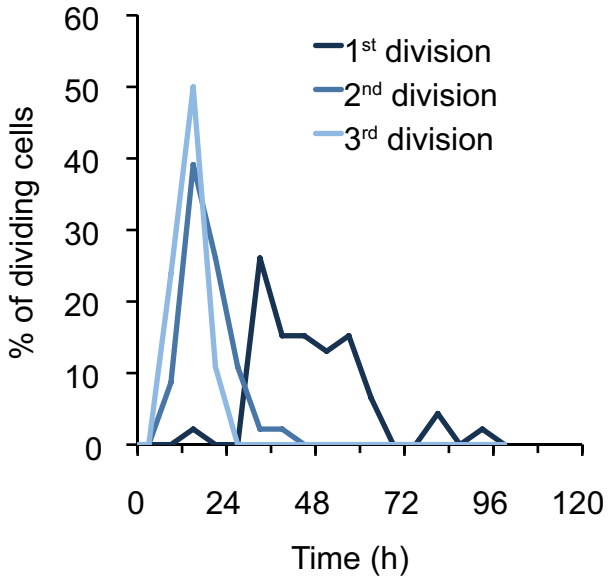


**Figure 2.7 Robust clonal culture of primary HSCs in the perfusion microfluidic cell culture array**

Highly purified murine HSCs E-SLAM were cultured in serum-free media supplemented with 300 ng $ml^{-1}$ SF and 20 ng $ml^{-1}$ IL-11 in the microfluidic cell culture array. Single cells were imaged every 4 min and the times for the first, second and third divisions were identified by manual inspections of the videos ($n$ = 46 cells).

**a**

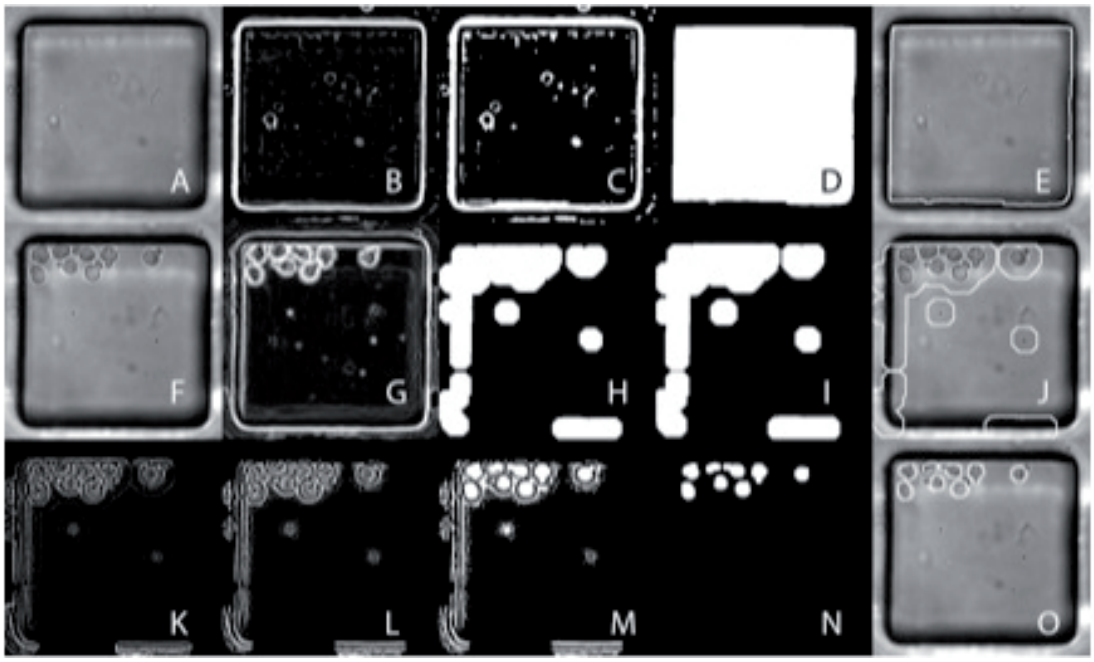
A
B
C
D
E
F
G
H
I
J
K
L
M
N
O

**b**

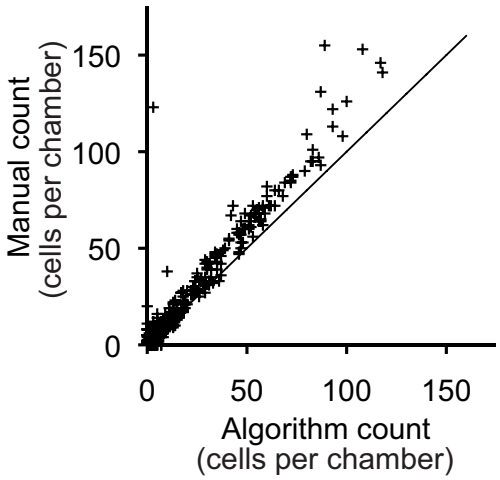
Manual count
(cells per chamber)
150
100
50
0
0
50
100
150
Algorithm count
(cells per chamber)

**Figure 2.8 Automated image analysis algorithm for cell quantification**

(**a**) Cells segmentation scripts were written in MATLAB (MathWorks). Segmentation was accomplished through three main steps: chamber segmentation (A-E), cell-containing region segmentation (F-J), and then single-cell isolation (K-O). First, the individual chambers (A) were segmented from the image background. This step of the segmentation was accomplished by applying a bandpass filter (B) and then creating a binary image through an automatically determined threshold (C). The resulting binary image was enhanced by removing objects touching the image borders and suppressing noise by removing small objects (D). The chambers were segmented from the rest of the background by filling in the holes created by the edges of the chambers. Next, the regions containing cells were separated from the rest of the chamber. This was achieved by first applying a local standard deviation filter to enhance the highly variable regions (G). The noise in the filter response was then suppressed by removing small regions, and the result was converted into a binary image through an empirically determined threshold (H). Any holes in the resulting image were then filled in to create the final region mask (I). To segment the individual cells from the rest of the group, a local standard deviation filter followed by a bandpass filter were applied to the image (K). A top-hat filter was then used to enhance the edges (L), and the bounded regions were subsequently filled (M). This result was then converted to a binary image using an automatically determined threshold, and further enhanced by removing small objects (N). (**b**) Comparison between automated and manual cell counts. The straight line represents the 1:1 slope. Deviations at higher cell numbers were caused by the shadow around the edges some chambers, which was corrected in the enhanced bifocal algorithm.

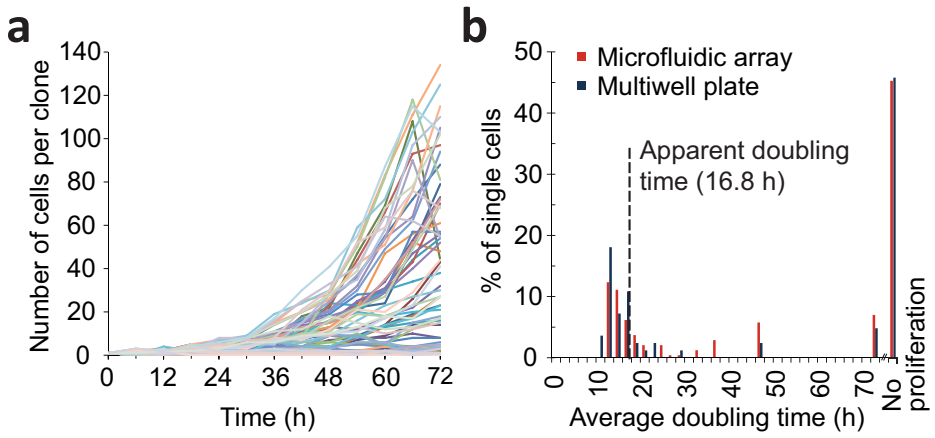


**Figure 2.9 Growth rate heterogeneity within ND13 cell populations**

(**a**) Individual ND13 clones showed highly variable growth curves. The apparent decline in cell counts for large clones at the end of the experiment was due to cells growing in multiple layers, leading to undercounting by image analysis. (**b**) Analysis of ND13 clonal average doubling times after 72 h in culture revealed a highly heterogeneous population where only a small fraction of fast-growing cells contributed to the overall population growth rate and 52% of the cells did not divide or died. Similar distributions were obtained in microscale and macroscale cultures.

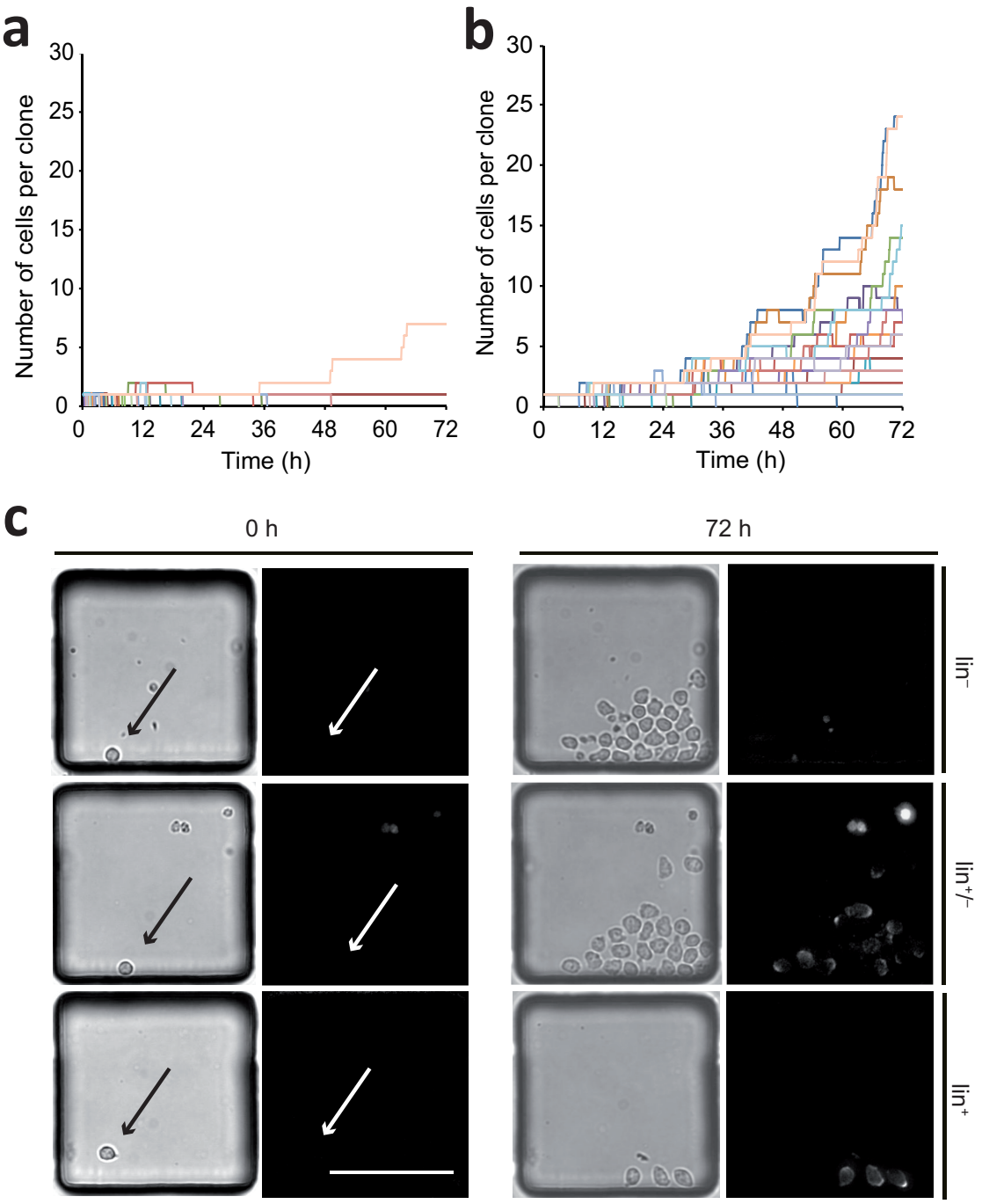
a
b
c
Number of cells per clone
Time (h)
0 h
72 h
lin⁻
lin⁺/⁻
lin⁺

**Figure 2.10 Clonal heterogeneity of primitive and mature subpopulations of ND13 cells**

(**a**) Time-lapse analysis of clones followed by immunostaining showed that the majority of $lin^+$ cells either died or did not give rise to colonies. Colored lines represent individual growth curves from single cells. (**b**) Individual growth curves as represented by colored lines showed that $lin^-$ cells gave rise to clones of highly heterogeneous sizes. (**c**) Perfusion enabled live immunostaining to assess heterogeneity within small clonal populations, as shown for ND13 clones stained for lin markers (B220, Gr-1 and Mac-1) after 72 h inside the microfluidic array. $Lin^-$ cells gave rise to $lin^-$ progeny, $lin^{+/-}$ progeny or entirely $lin^+$ progeny. Scale bar, 100 μm.

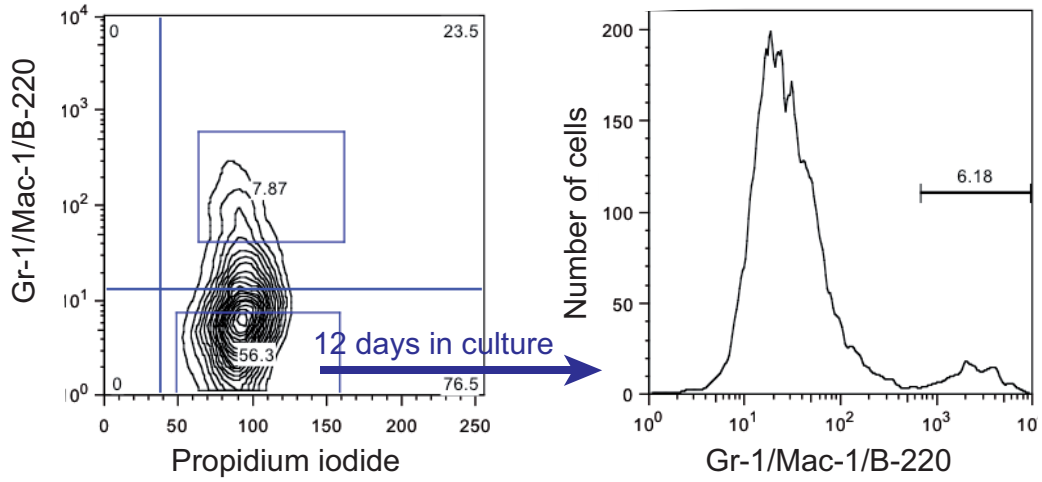


**Figure 2.11 Transient differentiation from ND13 lineage negative cells**

A mature myeloid population was derived from lineage negative ND13 cells. ND13 cells were stained for Gr-1, Mac-1 and B220 and sorted by flow cytometry. The lin$^-$ fraction was cultured for 9 days and gave rise to a new lin$^+$ population.

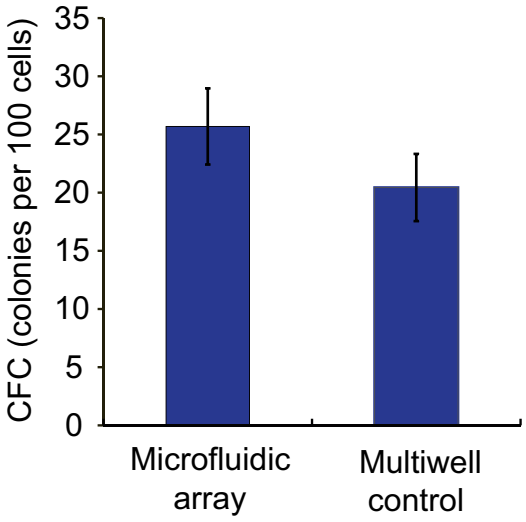


**Figure 2.12 Maintenance of progenitor content as measured by colony-forming cell assays**

ND13 cells were cultivated in the microfluidic device for 72 h and then approximately 720 cells from 5 chambers (corresponding to 11 starting cell equivalents) were recovered and plated into triplicate colony-forming cell (CFC) assays. Parallel methylcellulose assays were performed with the progeny of 11 starting cell equivalents generated in conventional macro-cultures. The progenitor content of the ND13 cells was comparable between microfluidic culture (25.7 ± 3.3 CFC, mean ± s.d., $n$ = 3) and control (20.4 ± 2.9 CFC, mean ± s.d., $n$ = 3).

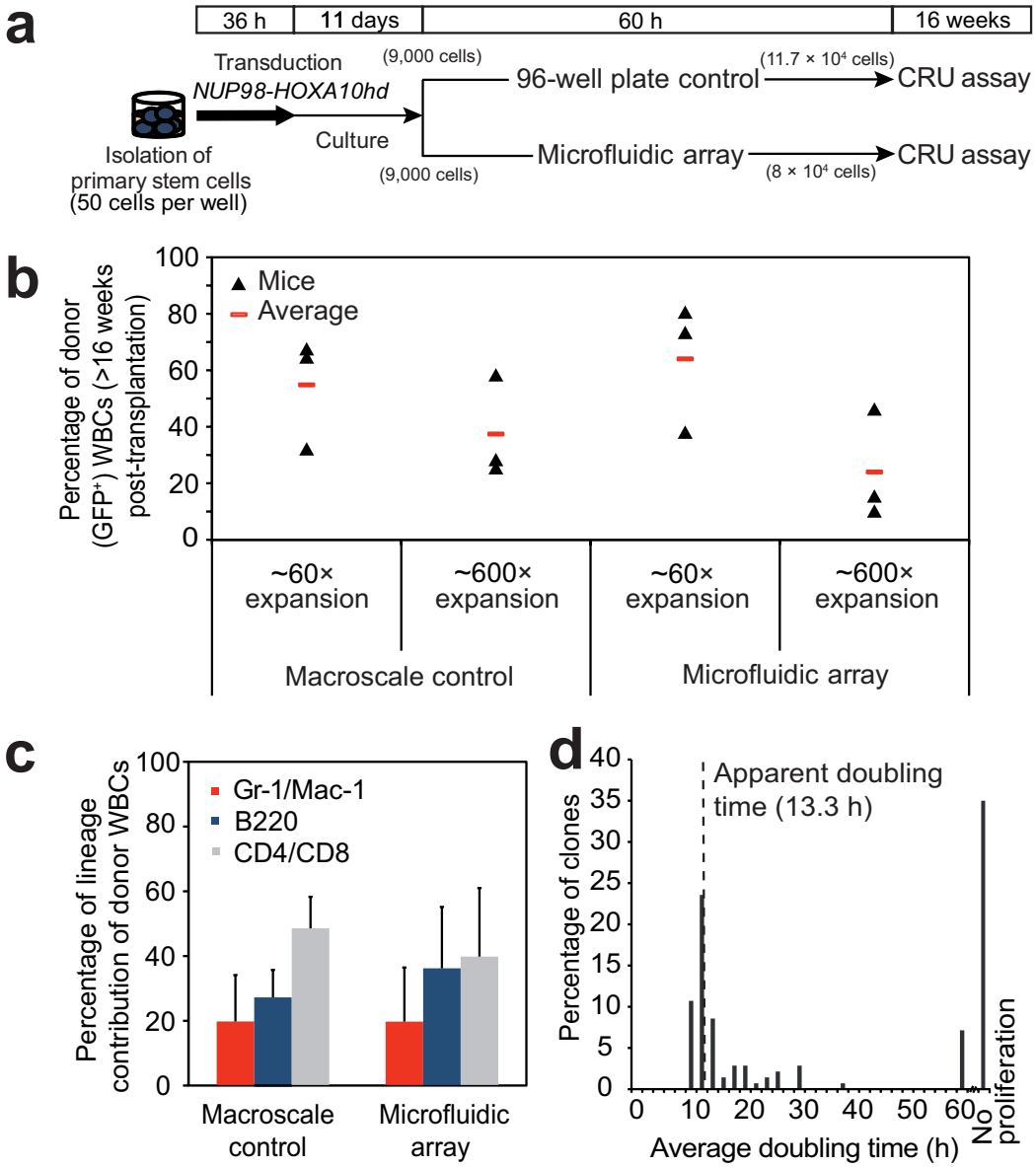
a
36 h
11 days
60 h
16 weeks
Transduction
NUP98-HOXA10hd
(9,000 cells)
96-well plate control
(11.7 × 10⁴ cells)
CRU assay
Isolation of primary stem cells (50 cells per well)
Culture
(9,000 cells)
Microfluidic array
(8 × 10⁴ cells)
CRU assay
b
Percentage of donor (GFP⁺) WBCs (>16 weeks post-transplantation)
Mice
Average
~60× expansion
~600× expansion
~60× expansion
~600× expansion
Macroscale control
Microfluidic array
c
Percentage of lineage contribution of donor WBCs
Gr-1/Mac-1
B220
CD4/CD8
Macroscale control
Microfluidic array
d
Percentage of clones
Apparent doubling time (13.3 h)
Average doubling time (h)
No proliferation

**Figure 2.13 Maintenance of HSC activity in hematopoietic populations cultivated in the microfluidic array**

(**a**) Primary HSCs were transduced with NA10hd, cultured for 11 days, and then introduced into a microfluidic array or a macroscale culture and incubated for 60 h. The entire contents of the device were recovered and the cells were used for *in vivo* competitive repopulating unit (CRU) assays. The same number of starting cell equivalents was injected into each mouse. (**b**) NA10hd-transduced cells maintained functional HSC activity after being cultivated in the microfluidic array and were able to reconstitute the blood-forming system of irradiated mice as measured by peripheral blood analysis of white blood cells (WBCs) 16 weeks post-transplantation ($P$ values = 0.624 and 0.432 for 60× for 600× expansion respectively). (**c**) HSCs cultured in the microfluidic array ($n$ = 6 mice) or control multiwell plate ($n$ = 6 mice) maintained the ability to produce both myeloid and lymphoid lineages 16 weeks after transplantation. **(d)** Distribution of clonal average doubling times for NA10hd cells after 60 h in culture.

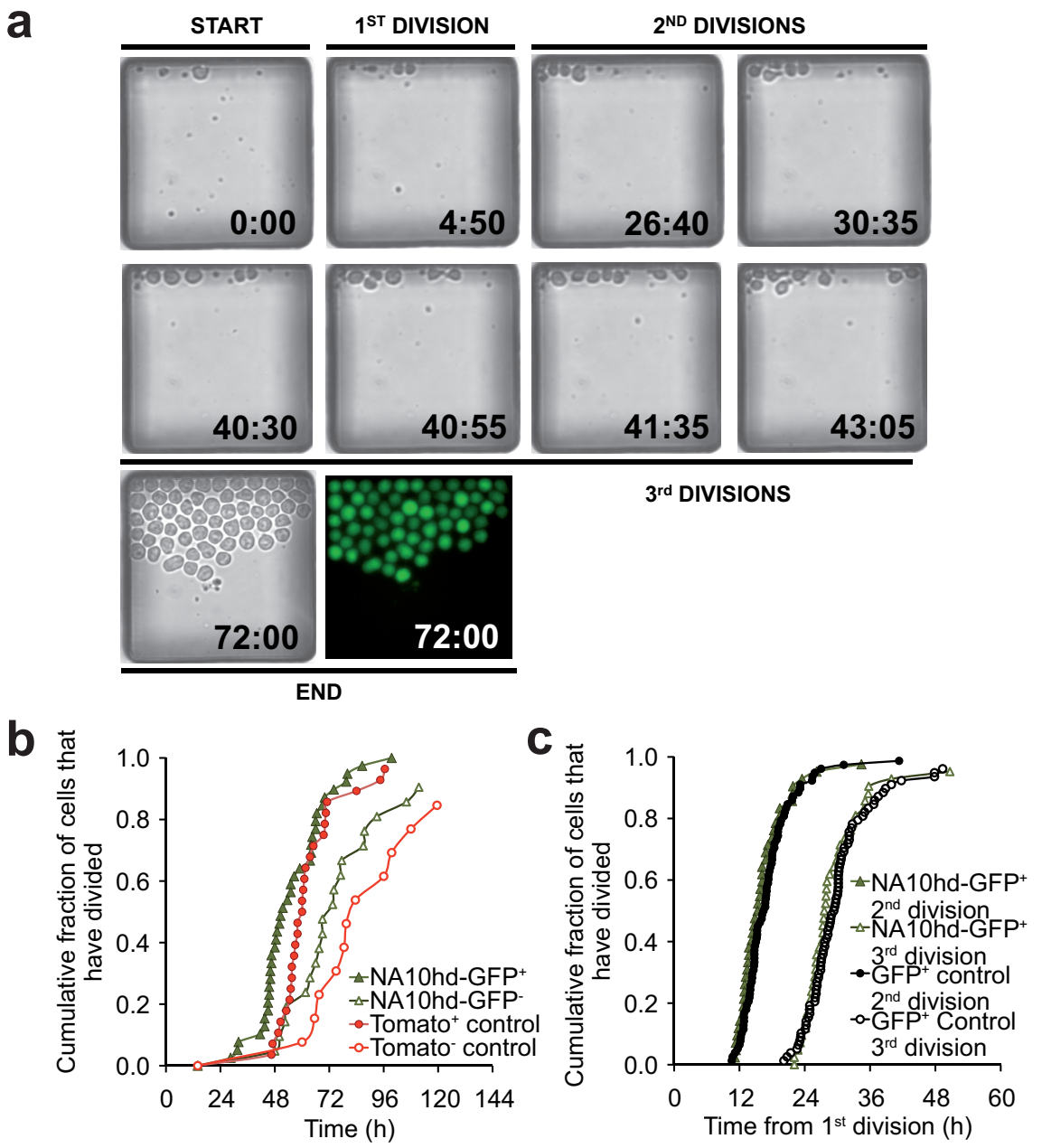


**Figure 2.14 Growth kinetics of NA10hd-transduced mHSCs**

(**a**) Time-lapse imaging of a single HSC transduced with NA10hd-GFP. Times of first, second and third divisions are pictured (hours). A fluorescent image was taken at the end of the culture to confirm expression of the vector. (**b**) Division kinetics of mHSCs transduced with NA10hd ($n$ = 39 GFP$^+$ cells and $n$ = 21 non-transduced cells) or Tomato control ($n$ = 28 Tomato$^+$ and $n$ = 13 non-transduced cells) as they enter cell cycle. The lentiviral vector preferentially infects cells with earlier entry into cell cycle. (**c**) Cell cycle transit times of mHSCs transduced with NA10hd ($n$ = 41 cells) or GFP control ($n$ = 77 cells) using a retroviral vector are comparable.

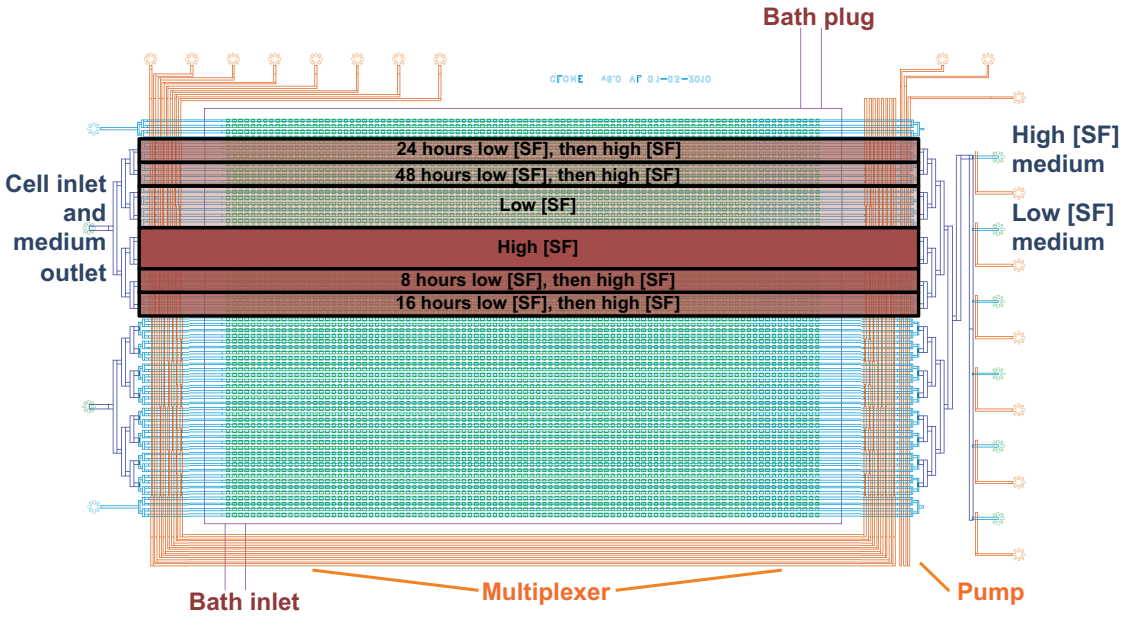


**Figure 2.15 Microfluidic cell culture array for temporal stimulation and parallelization of experiments**

This microfluidic cell culture array contains 6,144 chambers and can support up to 8 different conditions simultaneously. Two populations of cells can be loaded from the left side of the array using the pump located downstream of the array. The multiplexer can be used to direct cells in specific rows and obtain a more even distribution of cells across the different conditions. Up to 6 different reagents can be loaded from the right side of the array. Only the top half of the array was used to study murine HSCs due to the relatively small cell numbers. The 6 different conditions were distributed across the array as shown. Medium was automatically exchanged every 2 h for each condition.

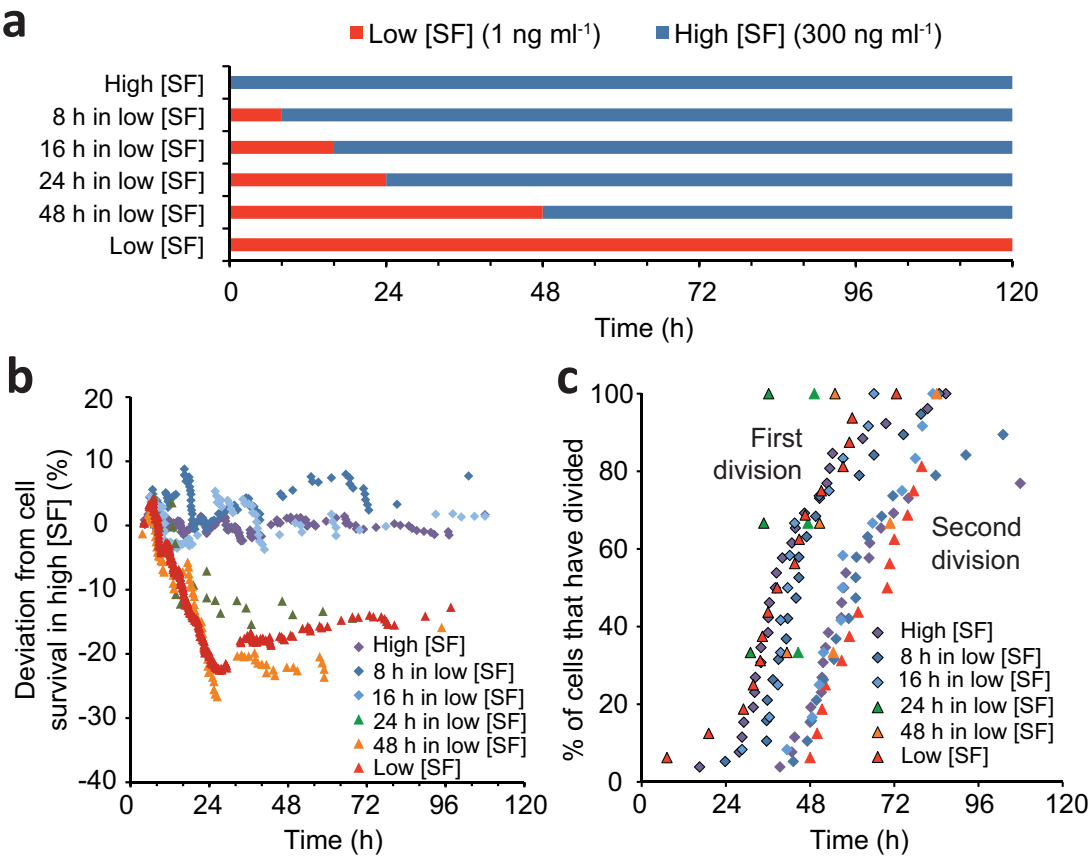


**Figure 2.16 Culture of primary murine HSCs under dynamic conditions in microfluidic cell culture arrays**

(**a**) Quiescent adult mouse HSCs (E-SLAM cells) were exposed to 20 ng ml$^{-1}$ IL-11 plus low SF (1 ng ml$^{-1}$) for 8, 16, 24 or 48 h before switching to addition of high SF (300 ng ml$^{-1}$). Controls cells were maintained continuously in 1 or 300 ng ml$^{-1}$ SF. Cells were cultured in a device containing 6,144 chambers and medium was exchanged every 2 h for all conditions. (**b**) HSCs exposed to 1 ng ml$^{-1}$ SF for up to 16 h could be rescued by transfer to 300 ng ml$^{-1}$ SF without affecting their subsequent viability. Most cell death in the 1 ng ml$^{-1}$ SF condition occured between 16 and 24 h after initiation of the culture. Cells were imaged every 12 min and survival curves were normalized to a third-order polynomial fit for the high SF condition (300 ng ml$^{-1}$). (**c**) Cumulative division kinetics of cycling primary HSCs (excluding dead and quiescent cells) in static and dynamically changing *in vitro* conditions for the first (black outline) and second divisions.

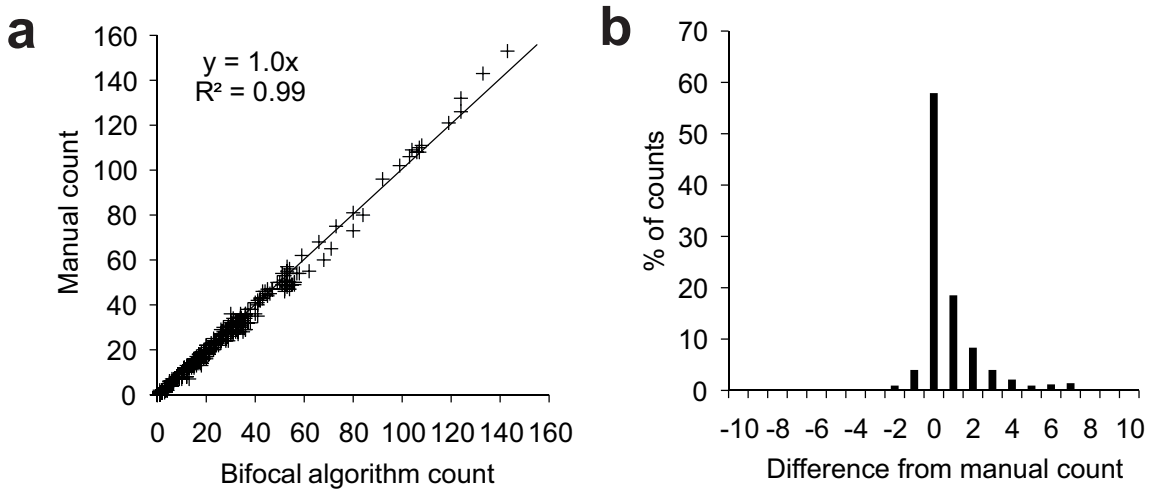


**Figure 2.17 Bifocal image analysis algorithm**

(**a**) Comparison between automated and manual cell counts. The straight line corresponds to a linear least square regression. (**b**) Absolute differences between the algorithm and manual counts.

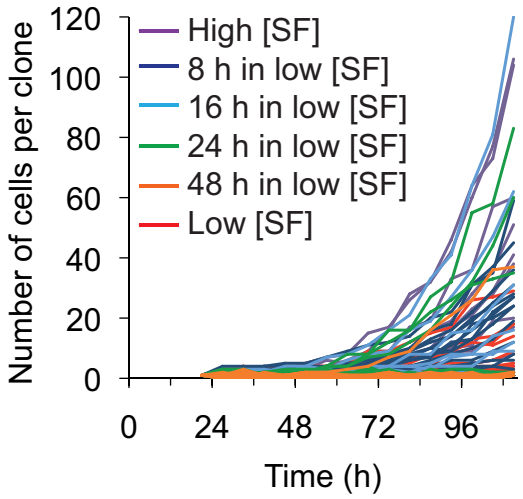


**Figure 2.18 Individual growth curves of primary murine HSCs under different SF exposure conditions**

Growth curves were generated using the enhanced bifocal image analysis algorithm. The analysis was started after 21 h to allow small quiescent cells to reach a suitable size for detection by image analysis.

# CHAPTER 3 Analysis of Genealogical Pedigrees to Assess Clonal Heterogeneity

In the previous chapter it was established that the microfluidic cell culture system had the necessary robustness to study the growth and survival of rare HSCs in temporally varying conditions. The current chapter presents a different application of the technology whereby the image acquisition capabilities of the system are brought to higher temporal resolution and combined with powerful image analysis algorithms to track cells over time. The genealogical pedigrees of single HSCs and their progeny coupled with live immunostaining and clone recovery are used to obtain new insights on HSC characteristics and division patterns *in vitro*.

## 3.1 Introduction

In-depth cell cycle and division kinetics analyses can lead to a better understanding of the mechanisms regulating HSC self-renewal and differentiation. The benefits of tracking single cells and their progeny through time has been well documented[276-278] and clonal analysis has already provided important insights on the division kinetics of both murine and human HSC populations[59,164,165,169,174,253,279]. However, the identification of *in vitro* characteristics specific to HSCs is complicated by the presence of abundant progenitor cells in purified populations. While several combinations of surface markers have been identified to enrich for stem cells, none have been found to be exclusively associated with HSCs. The more recent use of endothelial protein C receptor (EPCR) combined with SLAM family receptors has enabled purities of up to ~50% to be obtained in the mouse system[151]. The $EPCR^-$ fraction is devoid of any stem cell activity but not all $EPCR^+$ cells exhibit *in vivo* repopulating activity[280]. The level of

heterogeneity in purified populations is further augmented by the presence of HSC subtypes with different responses and *in vivo* repopulation patterns[153,154,281]. The assessment of stem cell activity using *in vivo* competitive repopulating unit (CRU) assays requires several months, after which the cells are no longer available for further characterization. An alternative is to cultivate HSCs on stromal cells for several weeks to reveal long-term colony-initiating cells (LT-CIC)[282]. However, this assay is also only retrospective, involves differentiation of the cells and is less specific than *in vivo* CRU assays. More recently, short-term cultures combined with the identification of genealogical phenotypes such as slower division and small clone size have been used to increase the probability of successful clonal transplantation[55,283]. These methods of enrichment demonstrate the potential of *in vitro* clonal characterization as a tool for the identification of HSC properties.

The availability of time-lapse imaging systems with high computational power now allows multiple cells to be monitored with high temporal resolution, hence making the generation of genealogical pedigrees possible. However, continuous tracking of several cells after multiple divisions rapidly becomes prohibitively laborious and difficult to perform reliably. As such, algorithms have been developed to facilitate tracing of genealogical pedigrees. Such analyses require very high accuracy with little room for cell tracking errors. Different levels of automation have been demonstrated but the accurate generation of genealogical pedigrees ultimately relies on human-assisted input[174,179,284]. Tracking large number of cells after multiple divisions becomes difficult as cells from different clones crowd the area and move from one imaging frame to another, thereby increasing the probabilities of tracking errors. To mitigate this problem, some have used microwells to confine clones and facilitate manual genealogical tracing[47,55,56]. In this study, we exploit the microfluidic cell culture system

presented in Chapter 2 to clonally expand single HSCs in nanoliter-volume chambers and to continuously monitor their progeny. We have developed a custom tracking algorithm to automatically generate genealogical pedigrees along with a graphical user interface (GUI) that allows for rapid manual curation when needed. We combine two features of the microfluidic cell culture array, clonal expansion and live immunostaining, to distinguish HSCs clones based on the persistence of EPCR after short-term culture and then use genealogical pedigrees for improved characterization of the *in vitro* growth behavior of HSCs.

## 3.2 Materials and Methods

### 3.2.1 Purification of HSCs

Adult bone marrow was extracted from the pelvis, femurs and tibia of 8-21 week old C57Bl/6J (B6) mice, subjected to a 10 min red blood cell lysis on ice by $NH_4Cl$ (STEMCELL Technologies) and blocked with rat serum (Sigma-Aldrich) and anti-mouse CD16/32 antibody (clone 2.4G2; Becton Dickinson). Cells were then stained using rat anti-mouse antibodies for CD48 (APC, clone HM48-1, Biolegend), CD150 (PE-Cy7, clone TC15-12F12.2, Biolegend), CD45 (FITC, clone 30-F11, eBioscience) and EPCR (PE, clone RMEPCR1560, STEMCELL Technologies). $CD45^+CD48^-EPCR^+CD150^+$ (E-SLAM cells, ~ 50% HSCs) cells were then double sorted using an Influx cell sorter (BD Biosciences). Cells were maintained overnight in conditioned medium from the UG26-1B6 cell line supplemented with 100 ng $ml^{-1}$ recombinant mouse SF and 20 ng $ml^{-1}$ recombinant human IL-11 (both from STEMCELL Technologies) prior to loading into the microfluidic device. Cells were cultivated in the conditioned media described above for all experiments.

### 3.2.2 Microfluidic Cell Culture

The microfluidic device presented in Chapter 2 (1,600 chambers) was primed with conditioned medium from the UG26-1B6 cell line supplemented with 100 ng $ml^{-1}$ recombinant mouse SF and 20 ng $ml^{-1}$ recombinant human IL-11 (both from STEMCELL Technologies) and incubated for 2 days prior to cell loading. The bath was filled with phenol red-free DMEM (Gibco, Life Technologies). Purified HSCs were introduced into the microfluidic device as described in Chapter 2. After loading, the array was scanned and 47 frames containing wells with single cells were selected for genealogical tracing. The number of frames was limited by the speed of image acquisition. Two bright field images, one above and one below focus, were acquired every 2 min for each frame for 5 days. Medium was automatically exchanged every 4 h by pumping fourfold the volume of the device at 2 ul $min^{-1}$.

### 3.2.3 Live Immunostaining

At the end of the experiment, cells were incubated with a blocking solution of rat serum (Sigma-Aldrich) and anti-mouse CD16/32 antibody diluted with equal parts of culture medium for 10 min. Cells were then incubated with a solution of anti-EPCR-biotin diluted in culture medium for 20 min, then washed with culture medium and incubated with culture medium containing streptavidin-PE-Texas Red for 10 min. Cells were washed again with phenol red-free DMEM (Gibco, Life Technologies) until background fluorescence was no longer detectable. A set of bright field and fluorescent images was acquired for every frame. All steps were performed in the microincubator at 37 $^{o}C$ to maintain focus and cell viability. Bright field and fluorescent images (1 s exposure) were taken for each frame. Culture medium was reintroduced in the array immediately after image acquisition. Cells were segmented as described below and a mask of the cells was made.

Fluorescent images were flat field-corrected based on frames containing empty wells. The cell mask was then multiplied with the fluorescent image and the average fluorescence intensity of each cell was calculated as the total pixel intensity of the cell divided by its projected area. The average intensity of a clone was calculated as the sum of the average cell intensities divided by the number of cells.

### 3.2.4 *In Vivo* Reconstitution Assay

Clones were recovered with a pulled glass micropipette in suspension U-shaped 96-well plates containing 200 µl of culture medium supplemented with 100 U $ml^{-1}$ of penicillin and 100 mg $ml^{-1}$ of streptomycin. Harvested colonies were transplanted intravenously into congenic, sublethally irradiated (4 Gy) W41/W41 recipients. Peripheral blood was collected from transplanted animals 8 and 16 weeks post-transplantation, red blood cell lysed (10 min exposure to $NH_4Cl$ on ice), blocked with rat serum and anti-mouse CD16/32, and stained for CD45.2 (FITC, clone 104, eBiosciences), CD45.1 (APC, clone A20, eBiosciences) in addition to either Mac-1 (PE, clone M1/70, BD) and Ly6G (PE, clone 1A8, BD), CD19 (PE, clone eBio1D3, eBioscience), or CD3ε (PE, clone 145-2C11, Biolegend). Positive clones were defined as those capable of contributing >1% of circulating white blood cells (WBCs) at 16 weeks post-transplantation with durable self-renewing clones defined as those that additionally contributed ≥1% to the myeloid WBCs at this time point.

### 3.2.5 Genealogical Tracing Algorithm

Custom scripts for genealogical tracing and data analysis were all written in Matlab (MathWorks). The generation of genealogical pedigrees

required two major steps: (1) the identification of cells in an image frame and (2) the tracking of cells across frames in time. The cell segmentation algorithm was based on two images separated by a focal offset (~50 μm). The first image, taken slightly above the focal plane, was used to find cell boundaries. These were identified using the Sobel Operator, a commonly used tool in image processing to detect edges by computing gradients to identify regions of abrupt intensity changes. The second image was taken below the focal plane, where cells appeared as bright spots due to diffraction, and was used to find cell centroids. An empirically determined brightness threshold was applied to create a mask by setting pixels above the threshold to one and those below to zero. The objects in the mask were then dilated to better represent the actual size of the cells. The edge and centroid masks were combined and holes were filled. The edge mask was then subtracted to separate connected cells and to remove pixels on the cell boundary. A final watershed cut was performed to separate any remaining cell clusters and a size threshold was applied to remove small debris. The segmentation algorithm took approximately 0.15 s per frame to complete using an Intel Core duo CPU (2.53 GHz), including loading the image and saving the segmented mask.

After segmentation, cells were tracked across adjacent frames in time. The centroid position of each cell was recorded in every image. The Euclidian distance between a cell centroid in one frame to all other centroids in the following frame was calculated and stored in a matrix. This step was repeated for all cells to complete a distance matrix. In the matrix, each row represented the distance from a specific cell in the current frame to all the cells in the next frame. Tracking across adjacent frames was achieved by assigning a cell match across two frames that minimized the total distance traveled by all cells between the frames. This standard optimization problem

was solved in polynomial time using the Hungarian algorithm. After matching was found, the cell size and position were recorded to determine growth rates and motility. The algorithm contained mechanisms to automatically correct for segmentation errors. For instance, if a cell was missing for less than 10 time points, its label could be reassigned when it reappeared. Objects that were too far away in the previous frame to be a cell were not assigned labels. The tracking algorithm was able also to identify cell division and death. Cell divisions were recognized by two features: a decrease in eccentricity as the cell became more circular in preparation for division and a rapid decrease in area after division. When these conditions were met, the two nearest cells with approximately the same area were recorded as daughters and added to the genealogical pedigree. Cell death was identified by a sharp decrease in cell size, a lack of motility and darkening of the cell interior.

The algorithm had a 50% probability of making a mistake before the $4^{th}$ division. Causes of errors included debris falsely labeled as cells, cells not segmented properly, cells obscured by the well wall shadows and highly motile cells incorrectly tracked. To achieve much more reliable genealogical tracing, we developed a graphical user interface (GUI) to correct these errors. The GUI cycled through the frames while highlighting and labeling cells in each image for the user. The user could pause on a frame and either switch labels or modify the segmentation by adding, deleting or splitting cells. The cell tracking assignment algorithm then recalculated label matches given the user changes and updated the genealogical pedigree accordingly. Parameters including division times, death times, cell motility, relationship to mother and cell-projected area were saved for each cell at different time points and later used for data analysis.

## 3.3 Results

### 3.3.1 Persistence of EPCR as a Prospective Indicator of Clonal Repopulating Activity

Since HSCs are known to be absent from $EPCR^-$ populations, we asked whether cell fate could be revealed after a short period of *in vitro* culture by analyzing the persistence of this surface marker in clonal progeny. E-SLAM ($CD45^+CD48^-EPCR^+CD150^+$) cells were purified and cultivated from single cells in the microfluidic array for 5 days in conditions promoting stem cell self-renewal using conditioned media from stromal cells supplemented with cytokines (300 ng $ml^{-1}$ SF and 20 ng $ml^{-1}$ IL-11). Only colonies arising from single cells, referred to as clones, were considered in the analysis. In total 71 clones were cultivated and imaged every 2 min, corresponding to the tracking of 1,880 cells. Only one clone did not produce viable progeny as both cells died after the first division. At the end of the experiment, live immunostaining was performed to identify the clones that had conserved EPCR expression (e.g. **Fig. 3.1**). Out of the 70 viable clones, 18 were recovered and injected into mice for *in vivo* reconstitution assays (**Fig. 3.2a**). The average EPCR fluorescence intensity of each clone was measured at the end of the culture. As expected, all clones that had lost EPCR expression failed to engraft in irradiated mice (**Fig. 3.2b**). Remarkably, aside from one exception, all clones that had maintained EPCR expression above an empirically determined clone average intensity threshold (**Fig. 3.3a**) also had *in vivo* reconstituting ability. Interestingly, the only clone that showed myeloid-biased engraftment associated with durable self-renewal was also the clone with the highest average EPCR fluorescence intensity (**Table 3.1**). We then looked at the intensity of each cell within clones (**Fig. 3.3a**). Since clones that had lost EPCR expression generally contained a larger number of cells (**Fig. 3.3b)**, only a minority (21%) of the entire cell population at the end of the culture was $EPCR^+$ (**Fig. 3.4a**). However, more than half of the clones

showed persistent EPCR expression (53%) (**Fig. 3.4b**), a ratio comparable to the purities generally obtained from E-SLAM cells[151]. This data demonstrates the importance of single-cell and clonal analysis in order to distinguish important phenotypes that could be masked in average population measurements.

### 3.3.2 *In Vitro* Phenotypic Characterization of HSCs from Genealogical Pedigrees

We separated the clones into $EPCR^+$ and $EPCR^-$ groups based on their average EPCR intensity relative to the threshold. Some cells above the threshold could be found in $EPCR^-$ clones and conversely, $EPCR^+$ clones could contain cells below the threshold. Since the persistence of EPCR was a good predictor of repopulating activity based on the clonal average after 5 days of culture, we looked for genealogical characteristics that could differ between the two clonal populations. To achieve this, we developed an automated genealogical tracing algorithm that could track single cells and their progeny. The algorithm performed automated segmentation and was able to track cells throughout culture, identify division and death events and generate genealogical pedigrees for each clone. A graphical user interface allowing for manual editing of segmentation and cell labeling was also developed to manually correct any mistake incurred by the algorithm. An example of analyzed time-lapse images and the associated genealogical pedigree is presented in **Figs. 3.5a** and **3.5b** respectively. Genealogical pedigrees of all analyzed clones can be found in **Appendix D**. The probability of death for each new cell was comparably low in both populations (3.75% and 2.55% for $EPCR^+$ and $EPCR^-$ populations respectively), suggesting the presence of a permissive cell culture environment.

We first investigated the differences in division kinetics between the $EPCR^+$ and $EPCR^-$ groups of clones. Clones that had maintained EPCR expression had a slightly delayed entry in cell cycle compared to the $EPCR^-$ group and a marked increase in cell cycle time between the first and second divisions (**Fig. 3.6**). This delayed division kinetics was propagated to subsequent divisions even though differences in cell cycle times were less pronounced. Cells from the $EPCR^+$ population exhibited significantly longer first ($P$ value < 0.05), second ($P$ value < 0.0001) and third ($P$ value < 0.01) division times compared to those in the $EPCR^-$ population. As well, the cell cycle time of all cells that had divided during the experiment was significantly shorter ($P$ value < $10^{-18}$) in the $EPCR^-$ population (25.0 ± 13.2 h) compared to the $EPCR^+$ population (41.0 ± 19.1 h) (**Fig. 3.7**). These results were consistent with previous observations that have reported slower division rates for mouse HSCs[55,283].

We then analyzed the relationship between mother and daughter pairs for the first and second divisions. Interestingly, cells from $EPCR^-$ clones followed a distinct pattern whereby the first daughter cells had shorter cell cycle times than their mother exiting quiescence (**Fig. 3.8a**) but also a shorter cycle time than their daughter progeny (**Fig. 3.8b**). The few cells that did not follow this pattern had a sibling that did. In contrast, the $EPCR^+$ population exhibited much more heterogeneous patterns for cell cycle times between the first and second generations (**Fig. 3.8c**) as well as between the second and third generations (**Fig. 3.8d**). The average difference in cell cycle time between the daughter cells and their mother after the first division was significantly different ($P$ value < 0.001) between the $EPCR^-$ (−4.5 ± 13.3 h) and $EPCR^+$ populations (10.7 ± 26.8 h).

We then looked at the synchrony between all siblings for each population. After the first division, $EPCR^-$ clones exhibited highly

synchronous behavior, with 78.1% of daughter pairs having less than 5 h difference in their cell cycle time (**Fig. 3.9a**). In contrast, only 54.2% of the cells in the EPCR$^+$ population divided synchronously (≤5 h difference) after the first division (**Fig 3.9b**). We found a similar trend for all the daughter pairs generated in the experiment (**Fig. 3.9c,d**). A majority of daughter pairs divided synchronously in EPCR$^-$ clones (81.0%) (**Fig. 3.10**) and asynchronous divisions only occurred in cells with longer cell cycle times with important differences between siblings. This behavior differed from the EPCR$^+$ population where only 50% of daughter pairs were synchronous. On average, the differences between cell cycle times of daughter pairs were significantly larger (*P* value = 0.002) in EPCR$^+$ clones (8.7 ± 9.6 h, mean ± s.d.) compared to EPCR$^-$ clones (4.6 ± 8.8 h, mean ± s.d.) (**Fig. 3.10**).

### 3.3.3 Analysis of Cell Size Growth Rates

In order to better understand the mechanisms behind longer cell cycle times, we tracked cell size based on the projected area throughout the cell cycle. The growth profiles of 9 cells with the longest lifespan in both EPCR$^-$ (**Fig. 3.11**) and EPCR$^+$ (**Fig. 3.12**) populations were examined. Interestingly, a common pattern was observed in both populations where cells would grow minimally and even decrease in size before a period of rapid cell size growth in the 25-40 h preceding division. We looked at cells with cell cycle times ranging from 20 h to 60 h and found a similar behavior for cells with a lifespan greater than 40 h while cells with cell cycle times smaller than 40 h went directly into the cell size growth phase (**Fig. 3.13** and **Fig. 3.14**). These results suggest that rather than growing at a slower pace, slow dividing cells have the propensity to enter a "quiescent" state where there is little or no increase in cell size. We then looked at the 9 cells with the shortest cell cycle time in both populations and noticed that the EPCR$^-$ population (**Fig. 3.15**)

contained cells with both shorter cell cycle times and greater cell size growth rates than cells in the $EPCR^+$ population (**Fig. 3.16**). When we measured the average projected area of each cell in the hour preceding division, we found that faster cycling in $EPCR^-$ clones was associated with larger cells (**Fig. 3.17a**). Short cycling times were generally accompanied by higher cell size growth rates (e.g. **Fig. 3.15**), which in turn led to larger cells prior to division. The average cell size growth rate was twofold greater for the fast cycling cells in the $EPCR^-$ population ($22.7 \pm 3.4$ $\mu m^2$ $h^{-1}$) than in the $EPCR^+$ population ($11.2 \pm 3.3$ $\mu m^2$ $h^{-1}$). This population of large cells with rapid proliferation was only prominent in the $EPCR^-$ population and not in the $EPCR^+$ population (**Fig. 3.17b**), which suggests that this particular phenotype may be associated with differentiating cells. When we looked at the cell size for each generation of cells, we found that cells reached a relatively constant size for the first 3 generations, and then started to gradually increase in size for subsequent generations (**Figs. 3.17c,d**). $EPCR^+$ clones never reached more than 5 complete generations, which may explain why they did not contain cells with this particular phenotype.

## 3.4 Discussion

The combination of short-term culture with live cell surface marker immunostaining at the clonal level has led to the identification of a phenotype closely associated with *in vivo* repopulating activity. Assuming that a clone with *in vivo* repopulating potential after *in vitro* culture must have originated from a stem cell, it was possible to retrospectively determine the fate of the initial mother cell based on the analysis of the average EPCR fluorescence intensity of its clonal progeny. It is conceivable that clones without *in vivo* repopulating potential could have been derived from HSCs that became differentiated over time. However, the high proportion of clones

with stem cell activity, comparable to the purities obtained with freshly isolated cells from this population, suggests that such an event is infrequent under the conditions studied. Clones may have a higher probability of engraftment than single cells if self-renewal events lead to HSC expansion. However, cycling cells may also fail to engraft if they are in the S/$G_2$/M phase at the time of injection[250,285,286], which may explain why one clone with high EPCR intensity (containing 3 cells only) did not engraft. Our results did not provide a clear distinction between long-term and short-term repopulating cells. More experiments are needed to confirm whether the level of EPCR intensity can be an indicator of durable self-renewal. Multiplexing the assay with other surface markers such as CD150 could perhaps also help to predict the *in vivo* repopulation patterns of the cells. It has been shown that long-term HSCs respond differently to transforming growth factor (TGF)-β than short-term HSCs[154]. The differential response to cytokine exposure, coupled with the microfluidic characterization techniques described herein, could be another avenue to investigate the factors responsible for the heterogeneity of the stem cell compartment.

The separation of cells into $EPCR^+$ and $EPCR^-$ populations combined with in-depth analysis of genealogical pedigrees has revealed different characteristics between the two populations. Since all cells were cultivated with frequent medium exchange, the differences in division kinetics and growth phenotypes were likely intrinsically generated. While we observed a common pattern of division kinetics in $EPCR^-$ clones, $EPCR^+$ clones had much more heterogeneous profiles than progenitor populations. This diversity is consistent with the high *in vivo* functional heterogeneity in the HSC compartment[151,153,154]. However, the asynchronous behavior that we observed in HSC populations was different from the previously reported high synchrony between daughter cells pairs[55]. Clones in our system were monitored for a longer period, thereby allowing the inclusion of cells with

longer lifespan in the analysis. The use of conditioned medium may have allowed a higher proportion of cells to self-renew and exhibit a different behavior. It is possible also that the more abundant and synchronous population of committed cells in the previous study had concealed the asynchronous behaviour of repopulating cells. The analysis of *in vitro* persistence of EPCR to identify clones with repopulating potential has revealed subtle HSC phenotypes that otherwise would have been masked in population measurements. Our data included instances where daughter cells had unequal levels of EPCR. However, it is not clear whether this was due to asymmetric segregation of EPCR during division or subsequent differential expression. This could be answered by performing daily live immunostaining or by using low concentrations of anti-EPCR labeled antibody in the culture medium combined with frequent fluorescence imaging[175]. While the later method has the advantage of allowing for continuous monitoring, phototoxicity and permanent binding to the targets, often receptors, can potentially affect cell metabolism. Other groups have instead performed immunostaining on fixed cells to monitor asymmetric segregation[180,183,287]. However, the probability of catching division events at the fixation stage can be very low, especially for small populations of cells with long cell cycle times. The use fluorescent reporters would greatly increase the extent of information that can be extracted from cellular genealogies[180].

The unique propensity of HSCs to return to a quiescent state compared to committed cells has been suggested by others[288]. The absence of cell size growth observed with long cell cycle times supports this hypothesis. The $EPCR^+$ population contained a higher proportion of slow cycling cells, and therefore more cells having the capacity to enter this "quiescent" state where there was no size increase. Further experimentation is needed to determine whether cells in this phase are indeed going back to $G_0$. This could be

achieved by tracking cells for at least one division and then staining fixed cells for the intracellular expression of a proliferation marker such Ki-67, which is present in active cell cycle phases ($G_1$,S,$G_2$/M) but not quiescent cells ($G_o$)[289]. It could be possible also to transduce HSCs with a fluorescence-ubiquitination cell cycle indicator (fucci) vector in order to identify cell cycle phases throughout cell growth curves[290]. We have shown that cell size growth analysis of single cells can reveal important information on the relationship between cell cycle regulation and stem cell fate and have found that differentiated cells were larger than primitive cells. The decrease in cell size that was observed for some cells may be an artifact of the variations in cell shape affecting the projected area or an indication of biological events such as secretion or autophagy. A more detailed analysis of cellular morphologies as was demonstrated for neural stem cells could perhaps leads to the identification of more characteristics associated with HSCs[291]. While undeniably useful, image analysis can only provide an approximation of cell size. New technologies enabling absolute measurement of cell mass and growth at the single-cell level using microfluidic cantilevers[49] could be particularly appropriate to obtain accurate measurements of cell growth in HSCs populations[292].

We have shown that with the right image processing tools, continuous cell tracking and genealogical tracing can reveal unique characteristics of cellular behavior that cannot be observed otherwise. In addition to surface marker analysis, microfluidic technologies could further increase the data content that can be extracted from these experiments by the integration of genomic analysis, transcript quantification, intracellular protein analysis and measurement of protein secretion at the clonal level.

**Table 3.1** ***In vivo*** **repopulating activity of recovered clones**

| Clone rank | Average EPCR intensity | % donor-derived WBCs at 16 weeks post-transplantation | % donor-derived GM of total GM cells |
|---|---|---|---|
| 1 | 1117.5 | 30.73 | 80.50 |
| 2 | 1070.8 | 0.06 | 0.11 |
| 4 | 982.3 | 1.61 | 0.04 |
| 5 | 942.0 | 7.71 | 0.08 |
| 11 | 834.5 | 31.50 | 0.97 |
| 17 | 685.0 | 10.38 | 0.33 |
| 22 | 619.6 | 3.90 | 0.25 |
| 35 | 474.7 | 6.48 | 0.10 |
| 36 | 469.0 | 4.73 | 0.65 |
| 41 | 410.4 | 0.09 | 0.18 |
| 47 | 391.9 | 0.08 | 0.28 |
| 58** | 360.4 | 0.03 | 0.05 |
| 59* | 358.9 | 0.03 | 0.05 |
| 65* | 344.8 | 0.03 | 0.05 |
| 66** | 339.9 | 0.03 | 0.05 |
| 67** | 335.3 | 0.03 | 0.05 |
| 68** | 335.2 | 0.03 | 0.05 |
| 69* | 328.8 | 0.03 | 0.05 |

*These clones were pooled and injected in the same mouse
**These clones were pooled and injected in the same mouse
WBC: White blood cell
GM: Granulocytes-monocytes
B/T: B cells/T cells

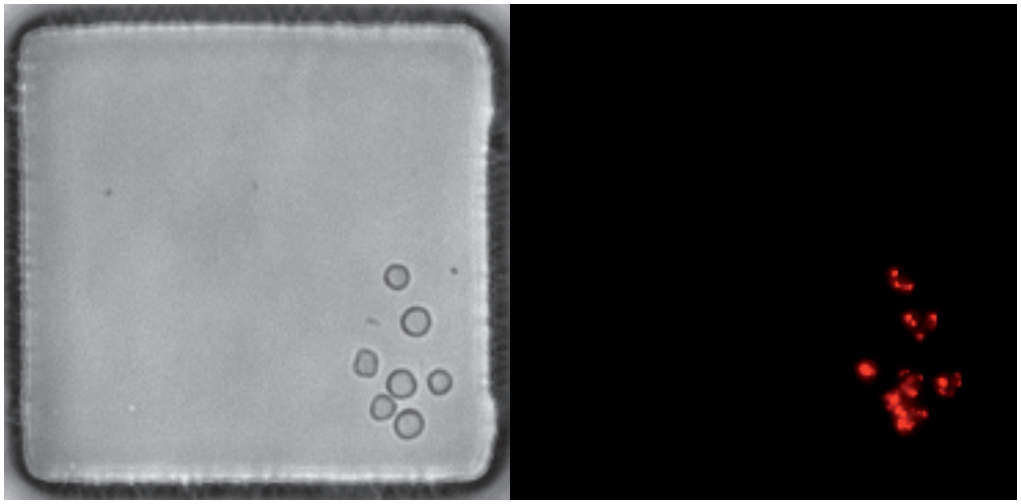

**Figure 3.1 Immunostaining of EPCR on live clones**

Example of EPCR immunostaining of a clone originating from a single E-SLAM cell after 5 days of culture in the microfluidic device. Bright field (left) and fluorescent (right) images are presented. Red false color was applied to the fluorescent image for better visualization. Capping was observed on cells since the staining procedure was performed at 37 °C.

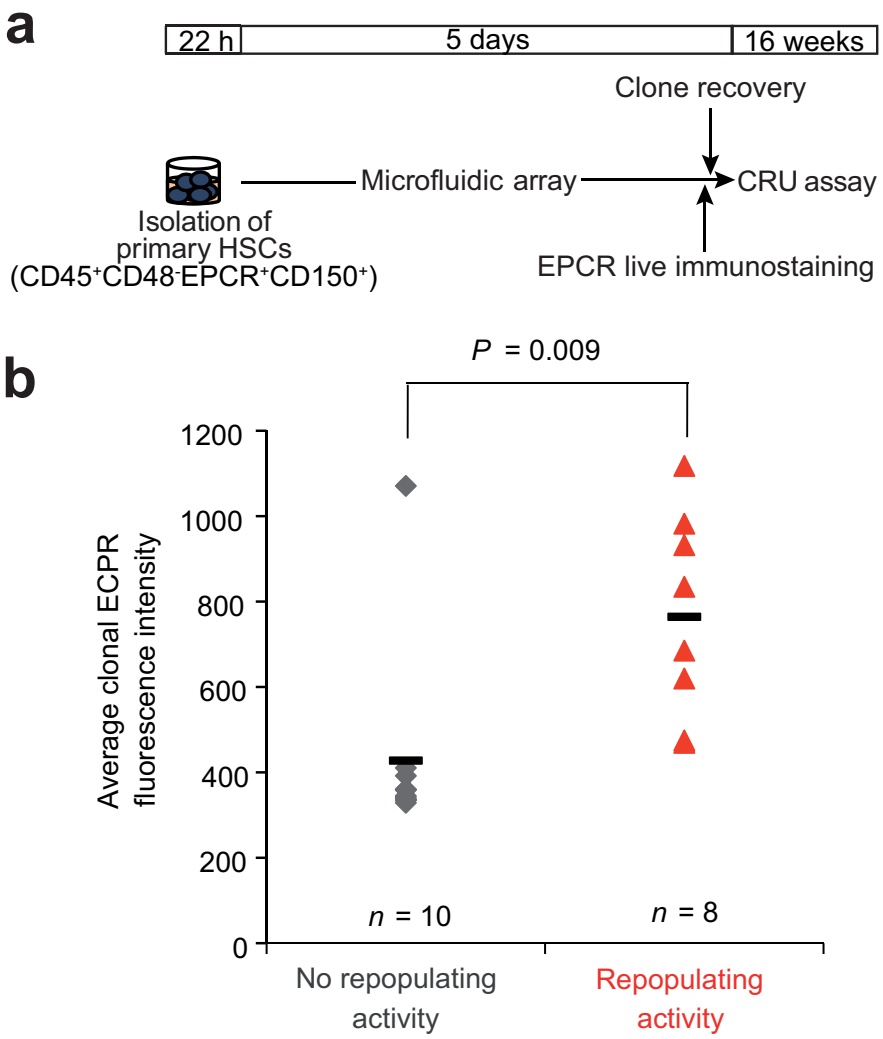


**Figure 3.2 *In vivo* repopulating activity of cultivated clones based on EPCR expression**

(**a**) Schematic of the experimental design. E-SLAM cells were purified and introduced in the microfluidic device after a short overnight culture. Time-lapse imaging of 71 single cells was started after 22 h for 5 continuous days in the microfluidic cell culture array. Clones were then stained for EPCR and selected clones were recovered for *in vivo* CRU assays. (**b**) Repopulating activity of harvested clones based on the average EPCR fluorescence intensity of cells in each clones.

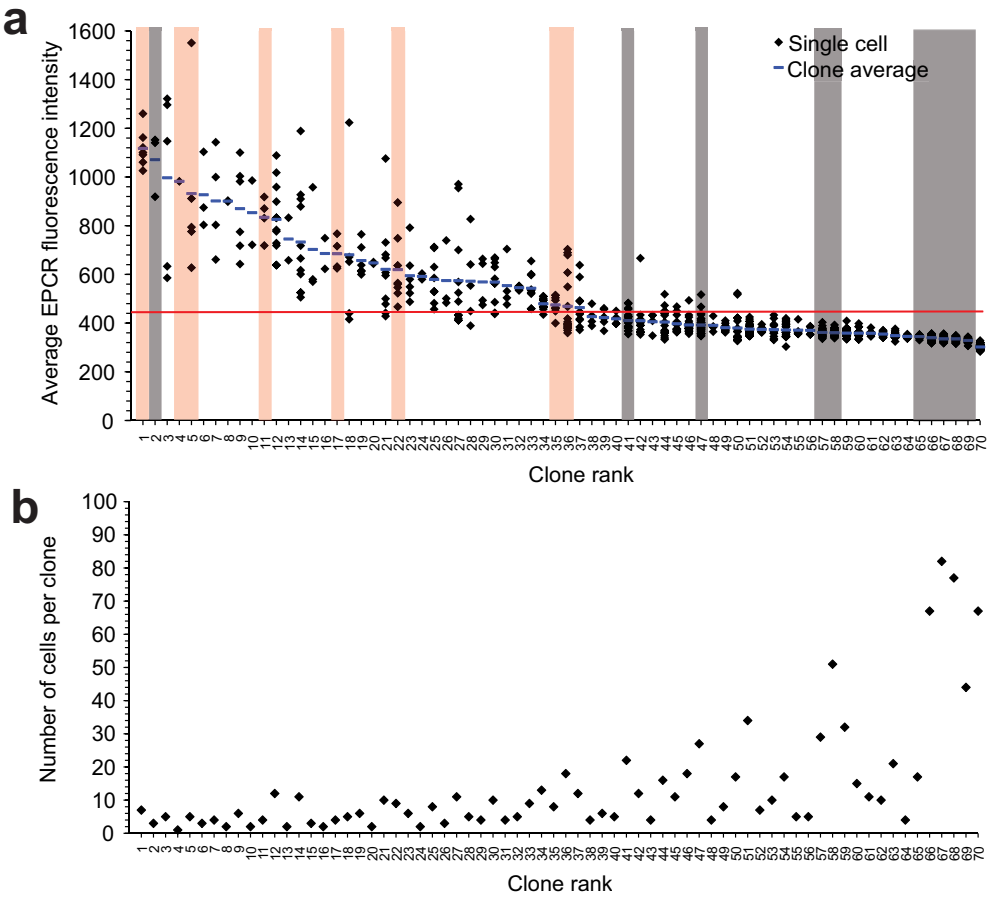


**Figure 3.3 Clones ranked by average EPCR intensity**

(**a**) EPCR expression of cells and clones based on fluorescence intensity after 5 days of culture in the microfluidic cell culture array. One clone out of 71 did not survive the experiment and was excluded from analysis. Each data point (black) represents the average fluorescence intensity of one cell. The average EPCR fluorescent intensity from all cells in a clone is also presented (blue bar). The threshold that distinguished $EPCR^+$ from $EPCR^-$ cells was set to 450 (red line) based on the differences between recovered clones for *in vivo* CRU assays with (shaded red) and without (shaded grey) repopulating activity. (**b**) Distribution of the number of cells at the end of the experiment in each clone.

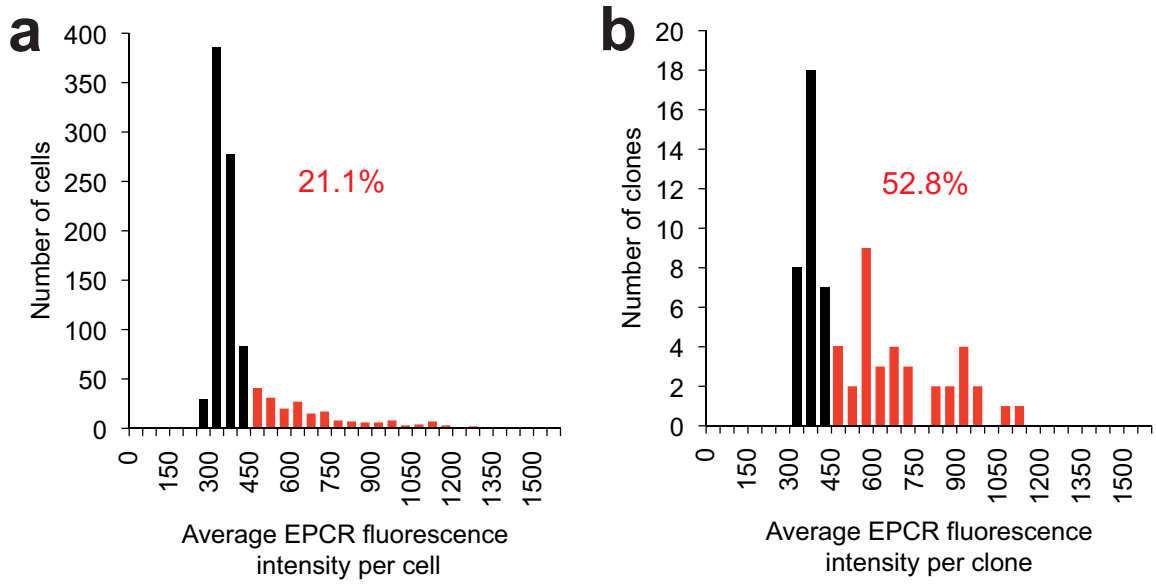


**Figure 3.4 Clonal and cell distributions based on EPCR fluorescence intensity**

(**a**) Distribution of all cells present at the end of the experiment based on their average EPCR fluorescent intensity. Only 21.1% of the entire population was EPCR$^+$. (**b**) Distribution of clones based on their average fluorescence intensity. More than half (52.8%) of the clones had an average EPCR intensity above the threshold (450), demonstrating the importance of *in vitro* clonal analysis to reveal distinct populations of input cells.

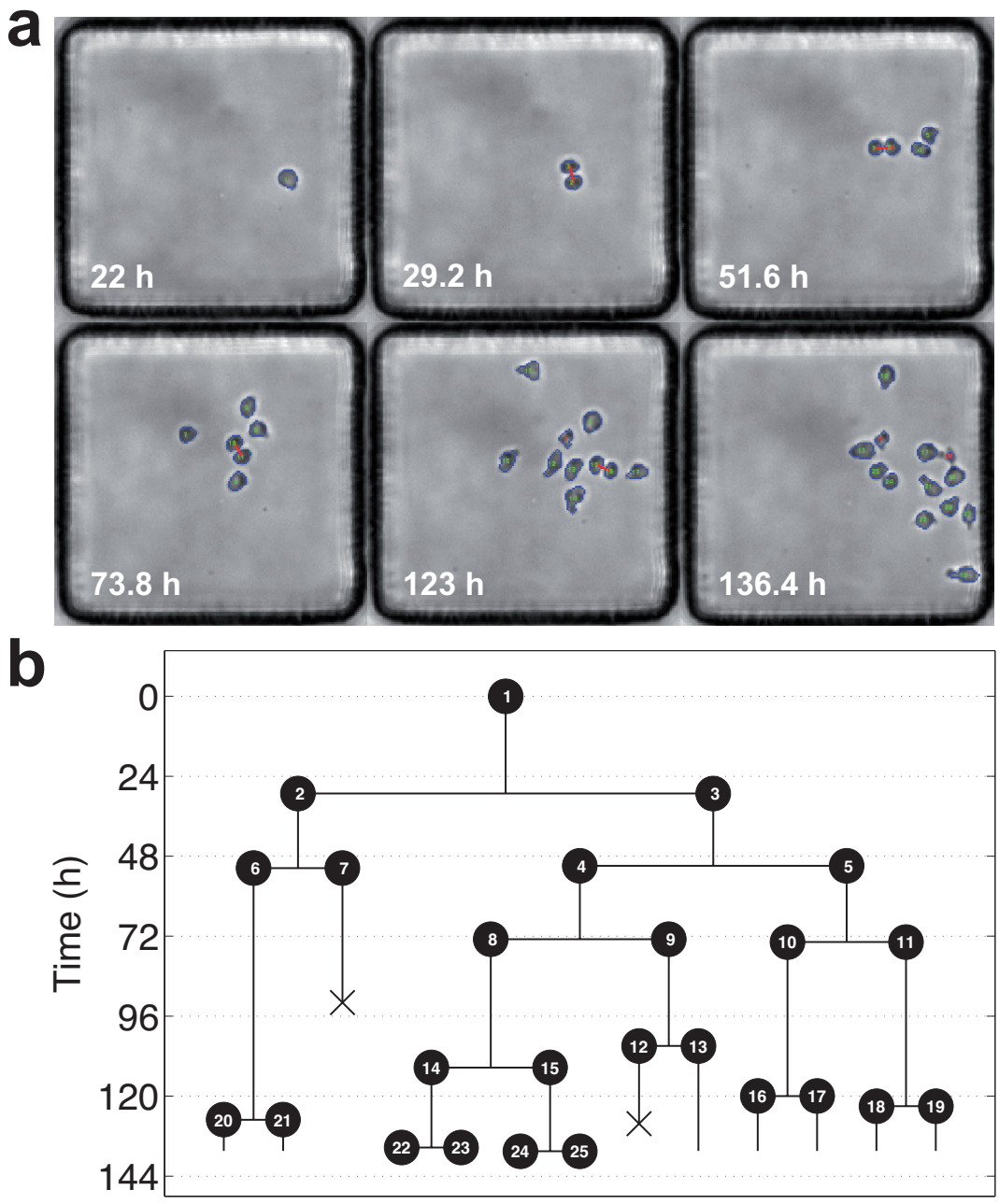


**Figure 3.5 Genealogical tracing of HSCs**

(**a**) Time lapse imaging of a HSC clone. Cells are segmented and assigned a label throughout their lifetime. Division and death events as well as relationships between mother and daughter cells are also tracked as the clone proliferates. Segmented cells are outlined in blue and red lines represent division events. Live cells are labeled in green while dead cells are labeled in red. Segmentation, labeling, division and death errors can be corrected manually using the GUI if necessary. (**b**) Genealogical pedigree generated from the clone in (a). Each T-junction represents a cell division from one mother cell into 2 daughter cells.

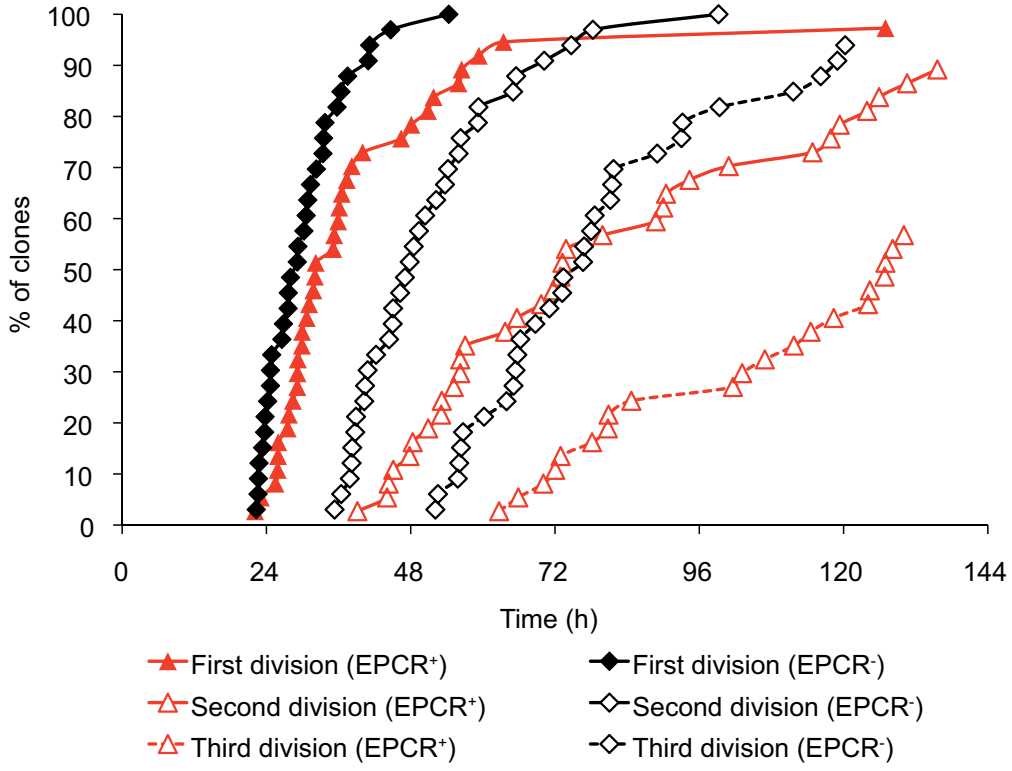


**Figure 3.6 Division kinetics of EPCR$^+$ and EPCR$^-$ clones**

Cumulative division kinetics for the first (30.3 ± 7.3 h, mean ± s.d.), second (51.4 ± 14.2 h, mean ± s.d.) and third divisions (77.4 ± 29.3 h, mean ± s.d.) in EPCR$^-$ clones ($n$ = 33 clones) and for the first (38.6 ± 18.6 h, mean ± s.d.), second (77.4 ± 29.3 h, mean ± s.d.) and third (99.3 ± 23.9 h, mean ± s.d.) divisions for in EPCR$^+$ clones ($n$ = 37 clones). $P$ values between EPCR$^+$ and EPCR$^-$ populations are 0.017, 0.000033 and 0.0013 for the first, second and third divisions respectively.

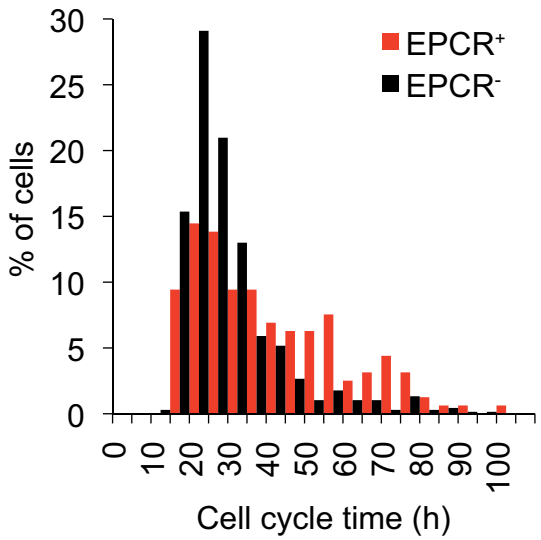


**Figure 3.7 Cell cycle time of individual cells**

Distribution of cell cycle times for all cells in EPCR$^-$ ($n$ = 677 cells; 25.0 ± 13.2 h, mean ± s.d.) and EPCR$^+$ clones ($n$ = 159 cells, 41.0 ± 19.1 h, mean ± s.d.). Cell cycle times were significantly different ($P$ value < $10^{-18}$) between the two populations. Only cells that had divided before the end of the experiment were included in the analysis.

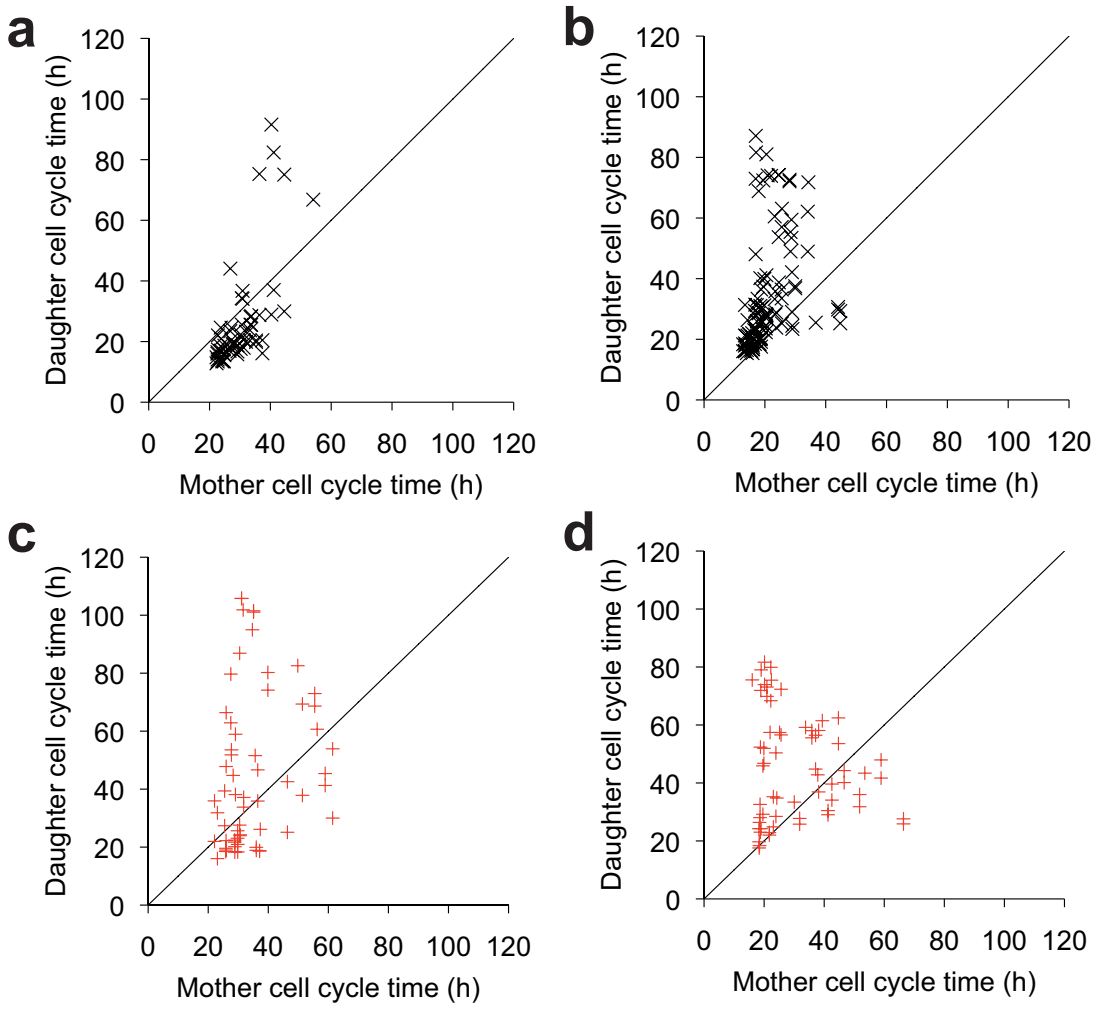
a
b
c
d
Daughter cell cycle time (h)
Mother cell cycle time (h)
0
20
40
60
80
100
120

**Figure 3.8 Relationship between mother and daughter cell cycle time**

(**a**) Relationship between cell cycle times of initial mother single cells (i.e. time to first division) and their daughters (i.e. time between first and second divisions) in $EPCR^-$ clones ($n$ = 65 pairs). The cell cycle time difference between a daughter cell and its mother was on average –4.5 ± 13.3 h. (**b**) Relationship between the cell cycle time of the new daughter cells, now mothers (i.e. time between first and second divisions), and their daughter progeny (i.e. time between second and third divisions) in $EPCR^-$ clones ($n$ = 105 pairs). The cell cycle time difference between a daughter cell and its mother was on average 13.8 ± 17.9 h. (**c**) Relationship between cell cycle times of initial mother single cells (i.e. time to first division) and their daughters (i.e. time between first and second divisions) in $EPCR^+$ ($n$ = 61 pairs) clones. The cell cycle time difference between a daughter cell and its mother was on average 10.7 ± 26.8 h. (**d**) Relationship between the cell cycle time of the new daughter cells, now mothers (i.e. time between first and second divisions), and their daughter progeny (i.e. time between second and third divisions) in $EPCR^+$ clones ($n$ = 62 pairs). The cell cycle time difference between a daughter cell and its mother was on average 9.9 ± 22.6 h. Only cells that had divided before the end of the experiment were included in the analysis. Black lines represent a perfect relationship between mothers and daughters.

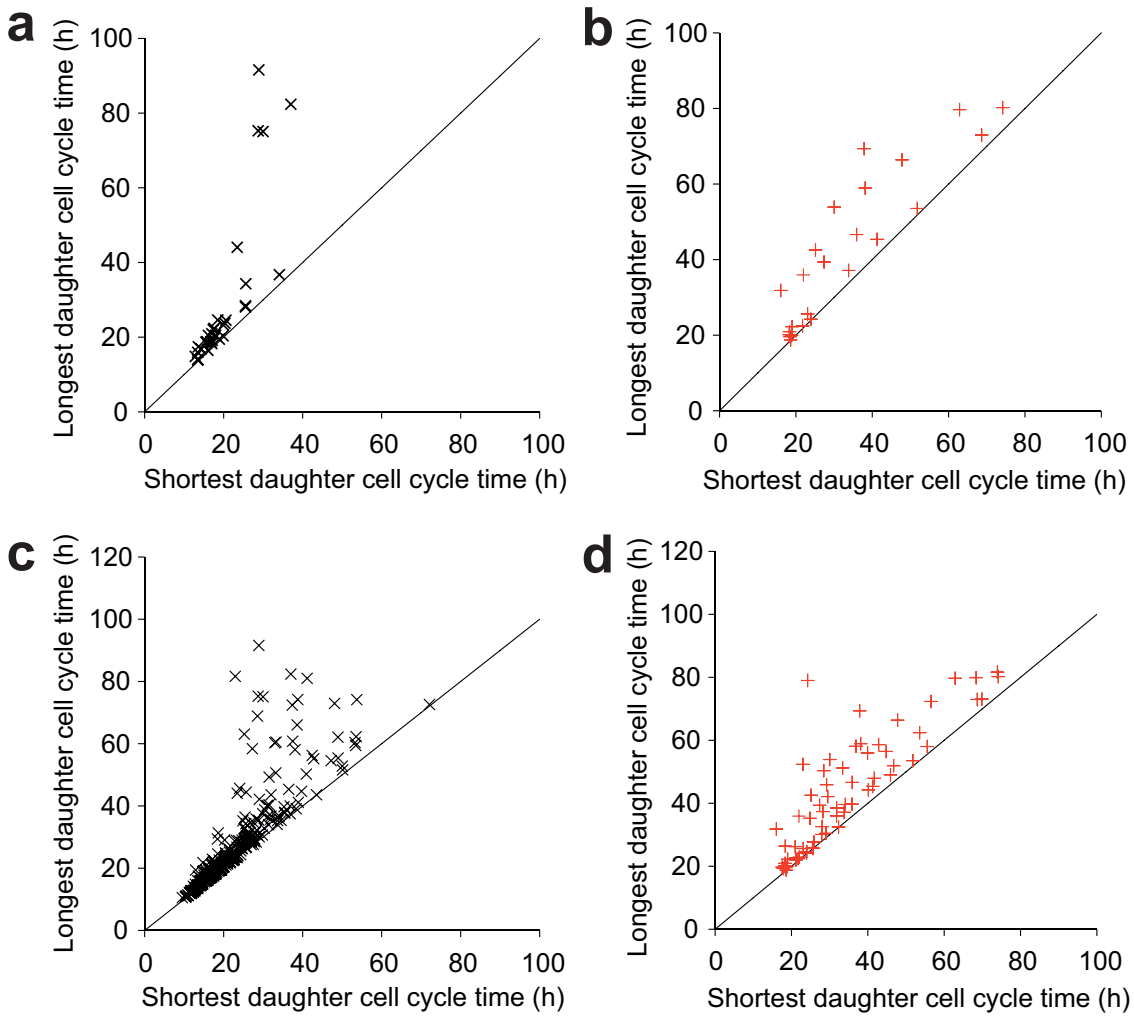


**Figure 3.9 Synchrony of daughter cell pairs**

Cell cycle times for each daughter cell pair following the first division are presented for (**a**) EPCR$^-$ ($n$ = 32 pairs) and (**b**) EPCR$^+$ populations ($n$ = 24 pairs) for EPCR$^+$ clones. (**c**) Cell cycle times for all daughter pairs in EPCR$^-$ (n = 321 pairs) and (**d**) EPCR$^+$ clones ($n$ = 66 pairs). Only cells that had divided before the end of the experiment were included in the analysis. Black lines represent the theoretical limit of perfect synchrony.

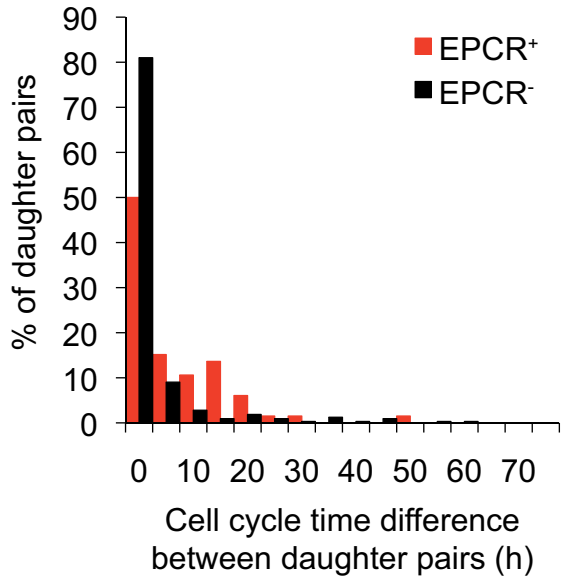


**Figure 3.10 Cell cycle time differences between daughter cell pairs**

Distribution of cell cycle time differences between daughter pairs in EPCR$^-$ ($n$ = 321 daughter pairs; 4.6 ± 8.8 h, mean ± s.d.) and EPCR$^+$ ($n$ = 66 pairs; 8.7 ± 9.6 h, mean ± s.d.) clones. Cell cycle time differences were significantly larger in the EPCR$^+$ population ($P$ value = 0.002). Only cells that had divided before the end of the experiment were included in the analysis.

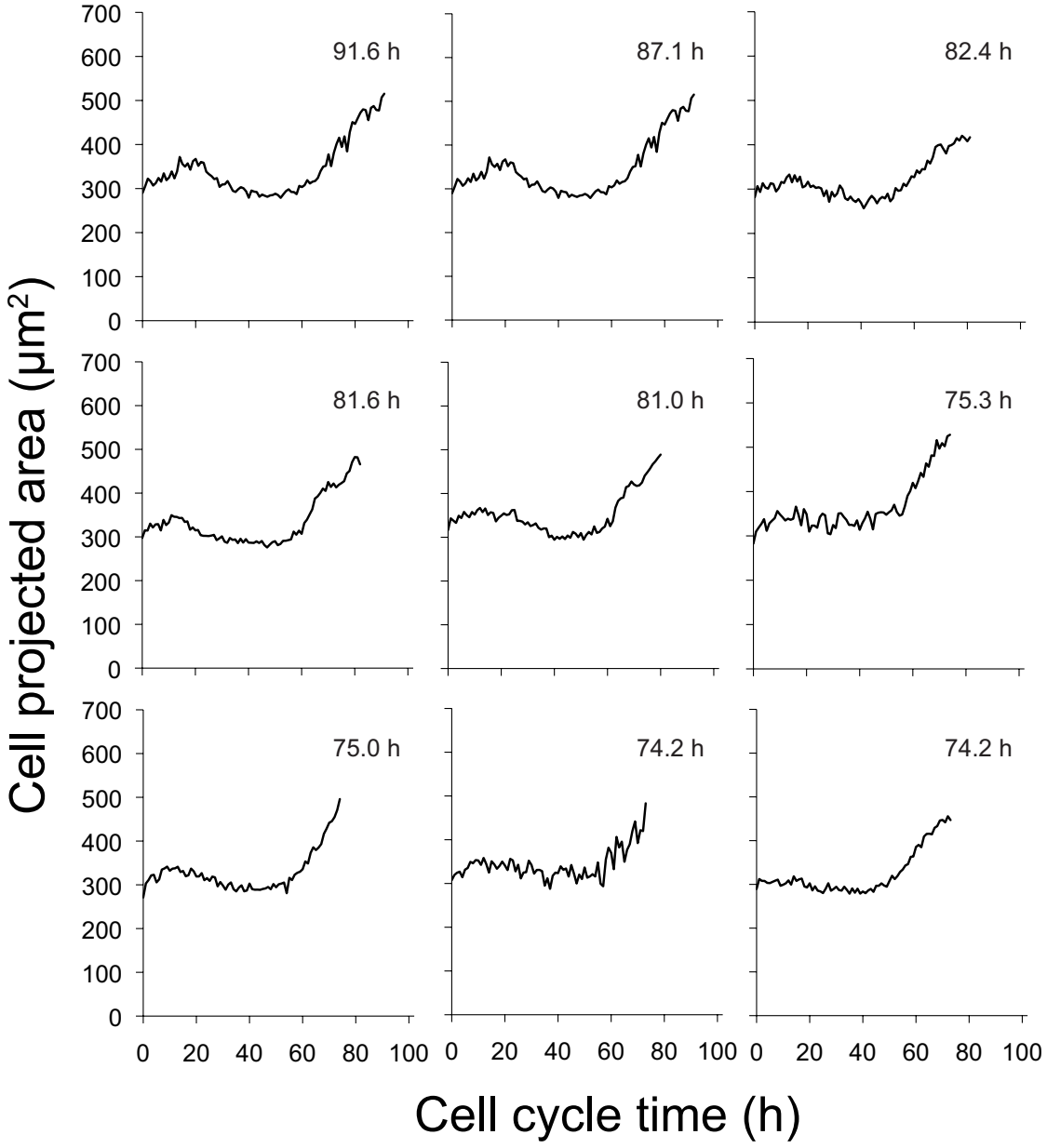


**Figure 3.11 Cell size growth rate of slow cycling cells from EPCR$^-$ clones**

The cell-projected area was averaged for every hour of cell cycle. Nine cells with the longest cell cycle times in the EPCR$^-$ population are shown.

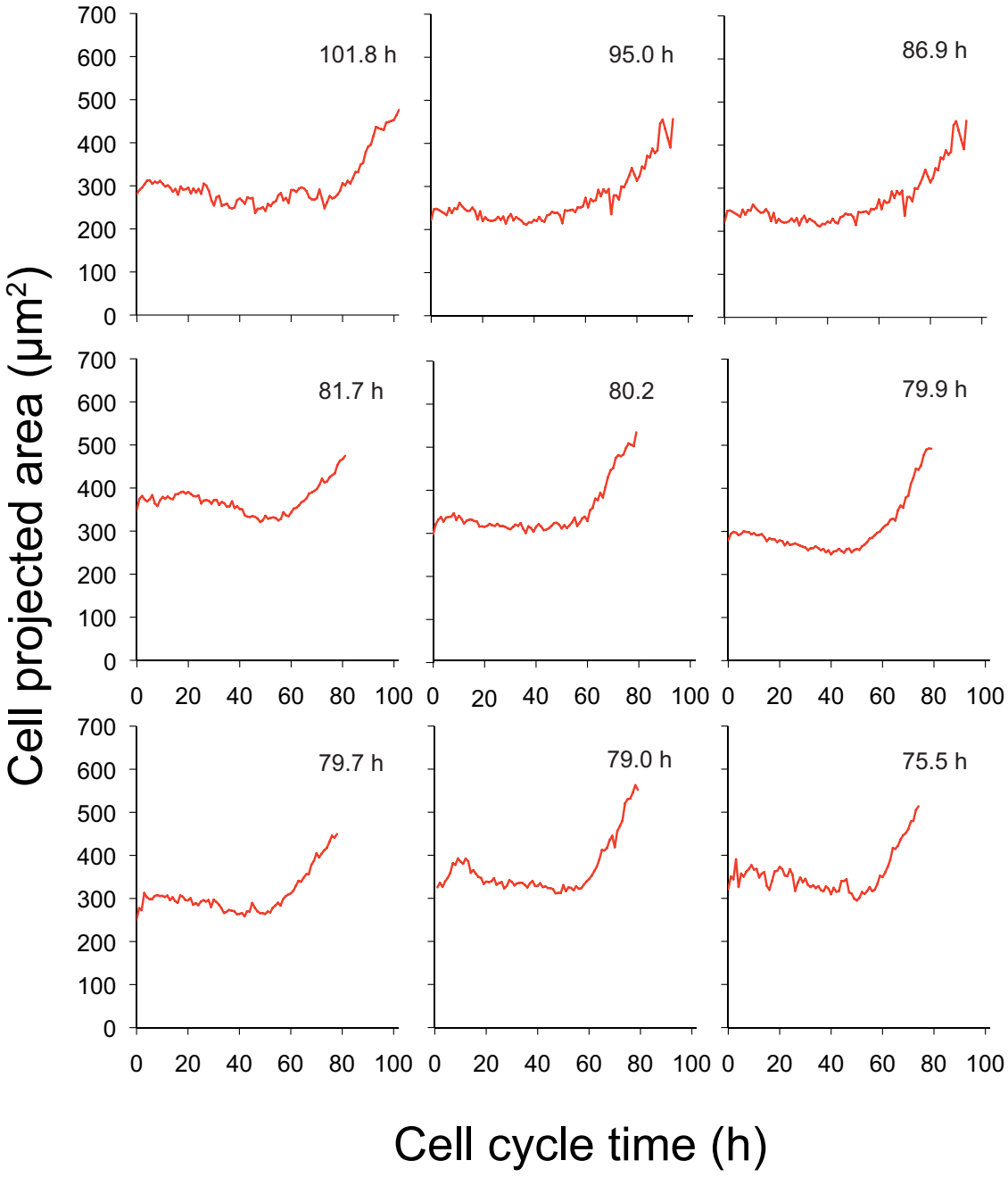


**Figure 3.12 Cell size growth rate of slow cycling cells from EPCR⁺ clones**

The cell-projected area was averaged for every hour of cell cycle. Nine cells with the longest cell cycle times in the EPCR⁺ population are shown.

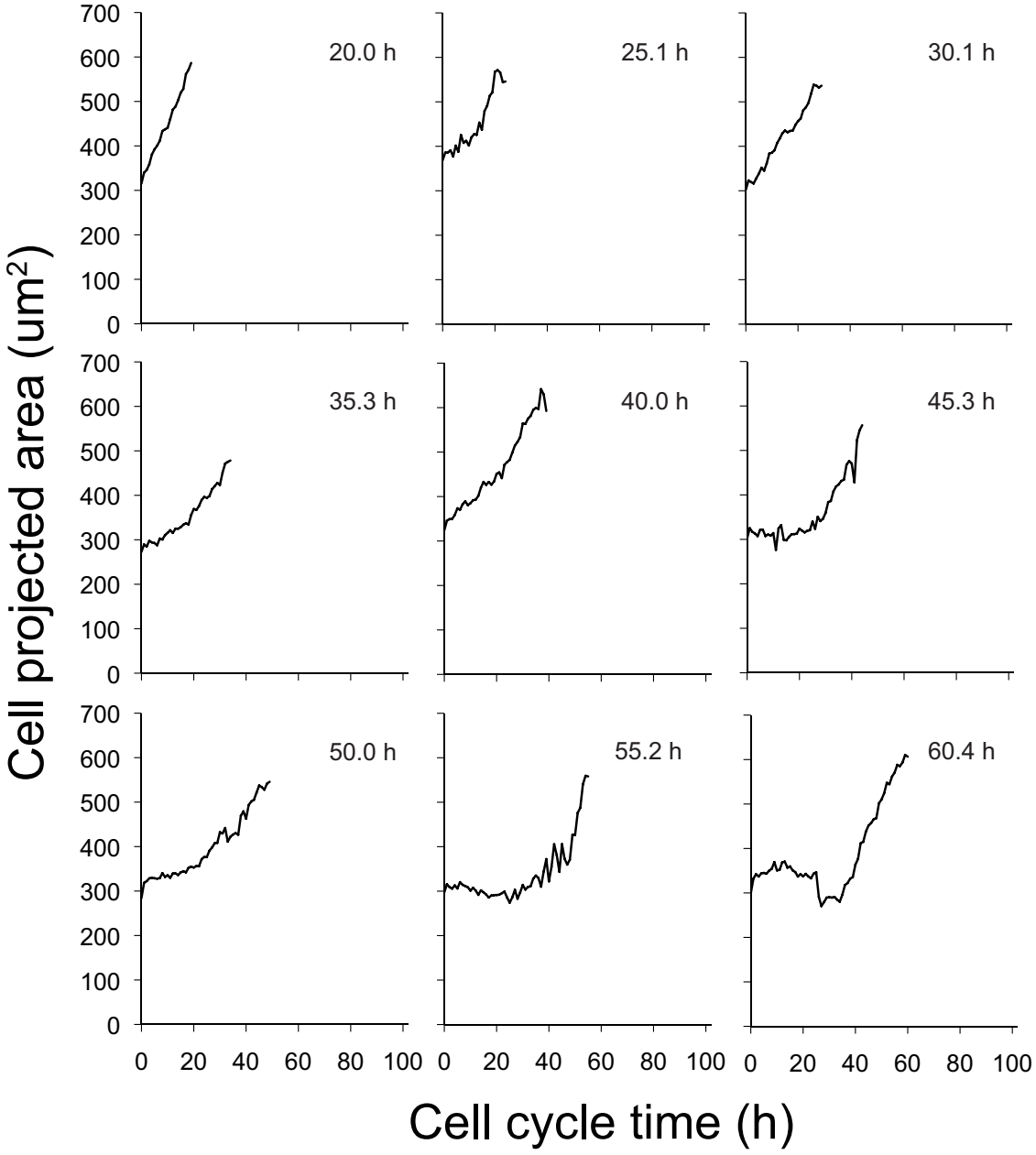


**Figure 3.13 Cell size growth rate of selected cells from EPCR$^-$ clones**

The cell-projected area was averaged for every hour of cell cycle. Nine cells from EPCR$^+$ clones with varying cell cycle times are shown.

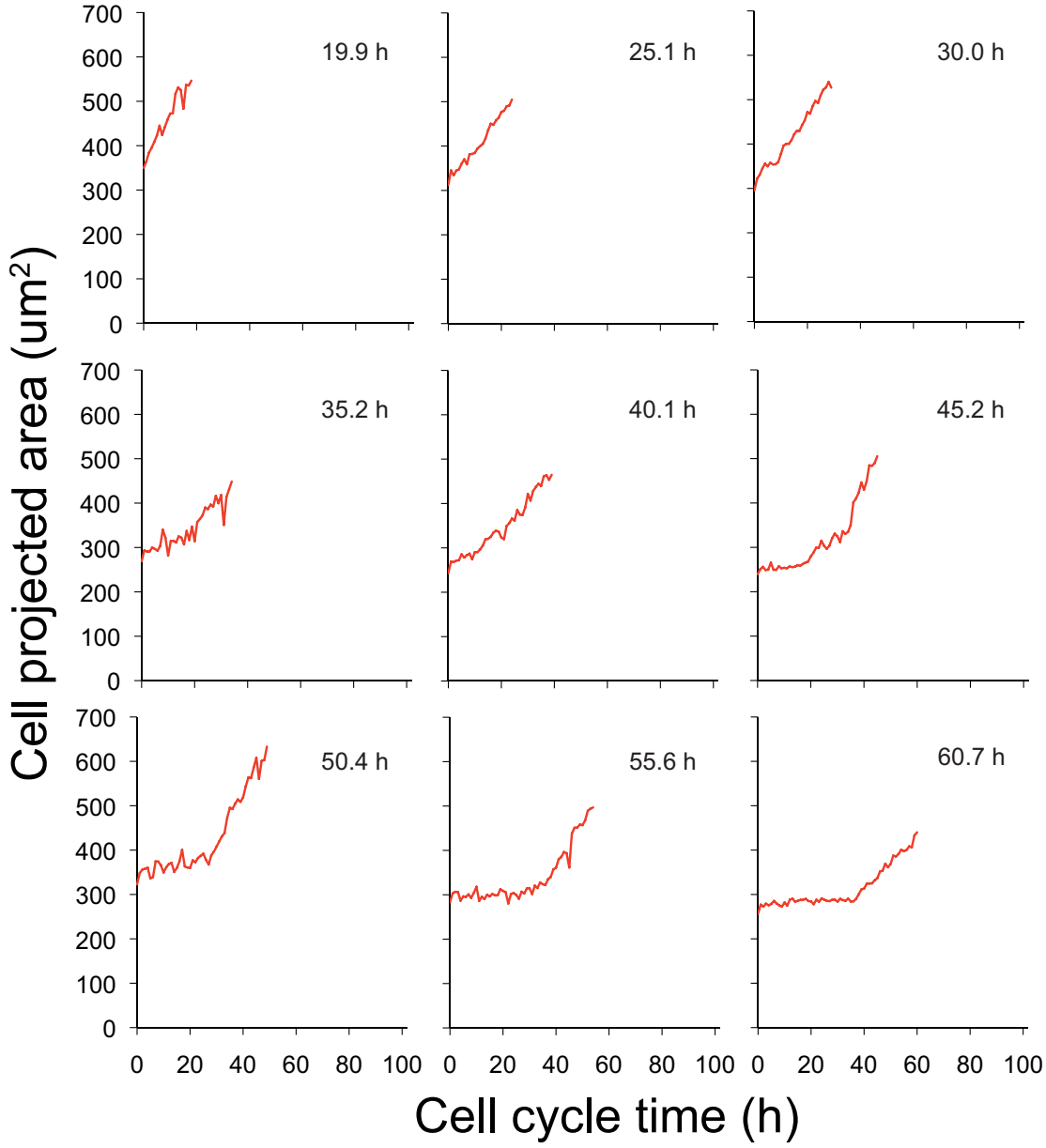


**Figure 3.14 Cell size growth rate of selected cells from EPCR$^+$ clones**

The cell-projected area was averaged for every hour of cell cycle. Nine cells from EPCR$^+$ clones with varying cell cycle times are shown.

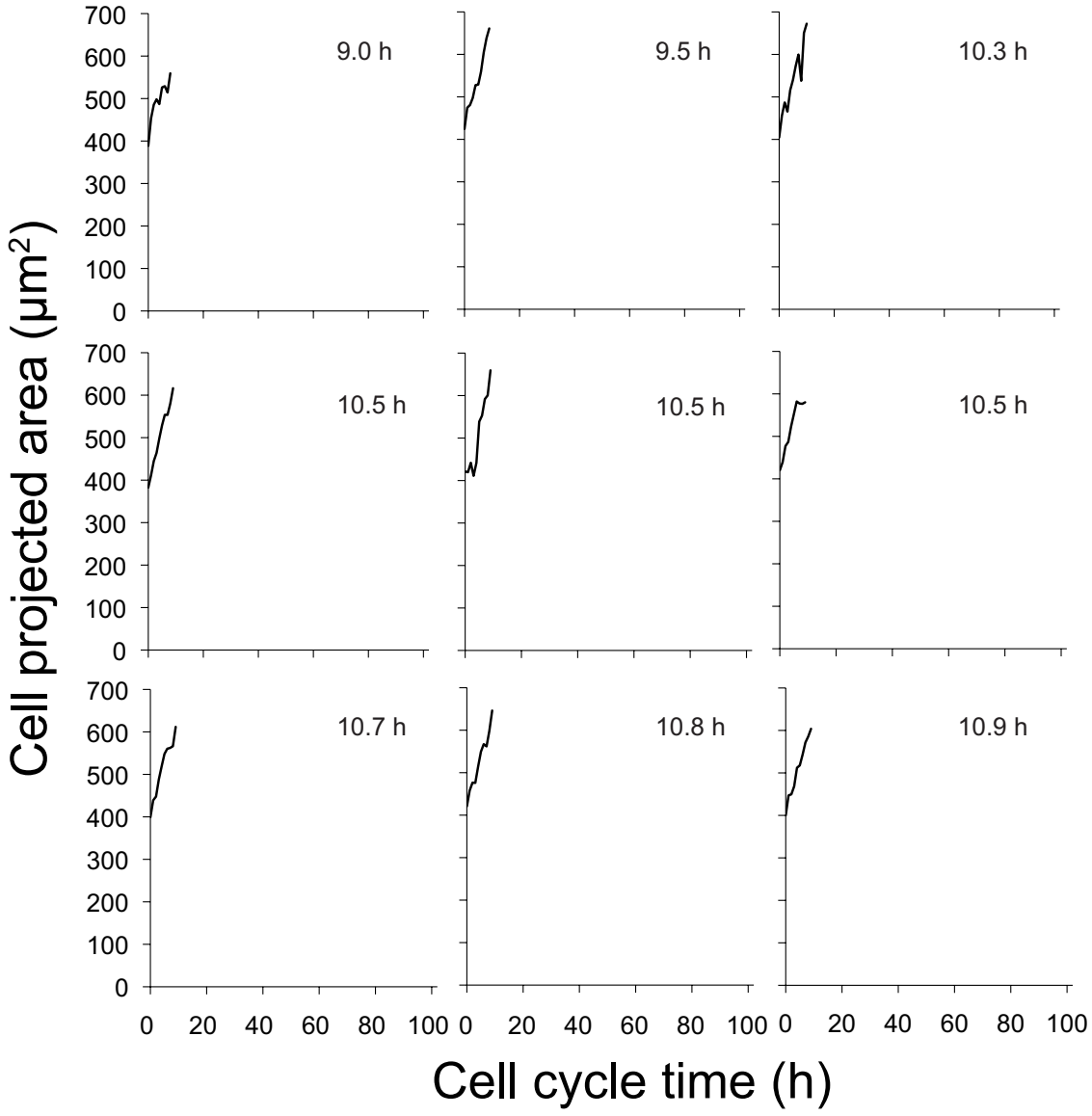


**Figure 3.15 Cell size growth rate of fast cycling cells from EPCR⁻ clones**

The cell-projected area was averaged for every hour of cell cycle. Nine cells with the shortest cell cycle times in the EPCR⁻ population are shown. The average cell size growth rate of these cells was 22.7 ± 3.4 $\mu m^2\ h^{-1}$ (mean ± s.d.).

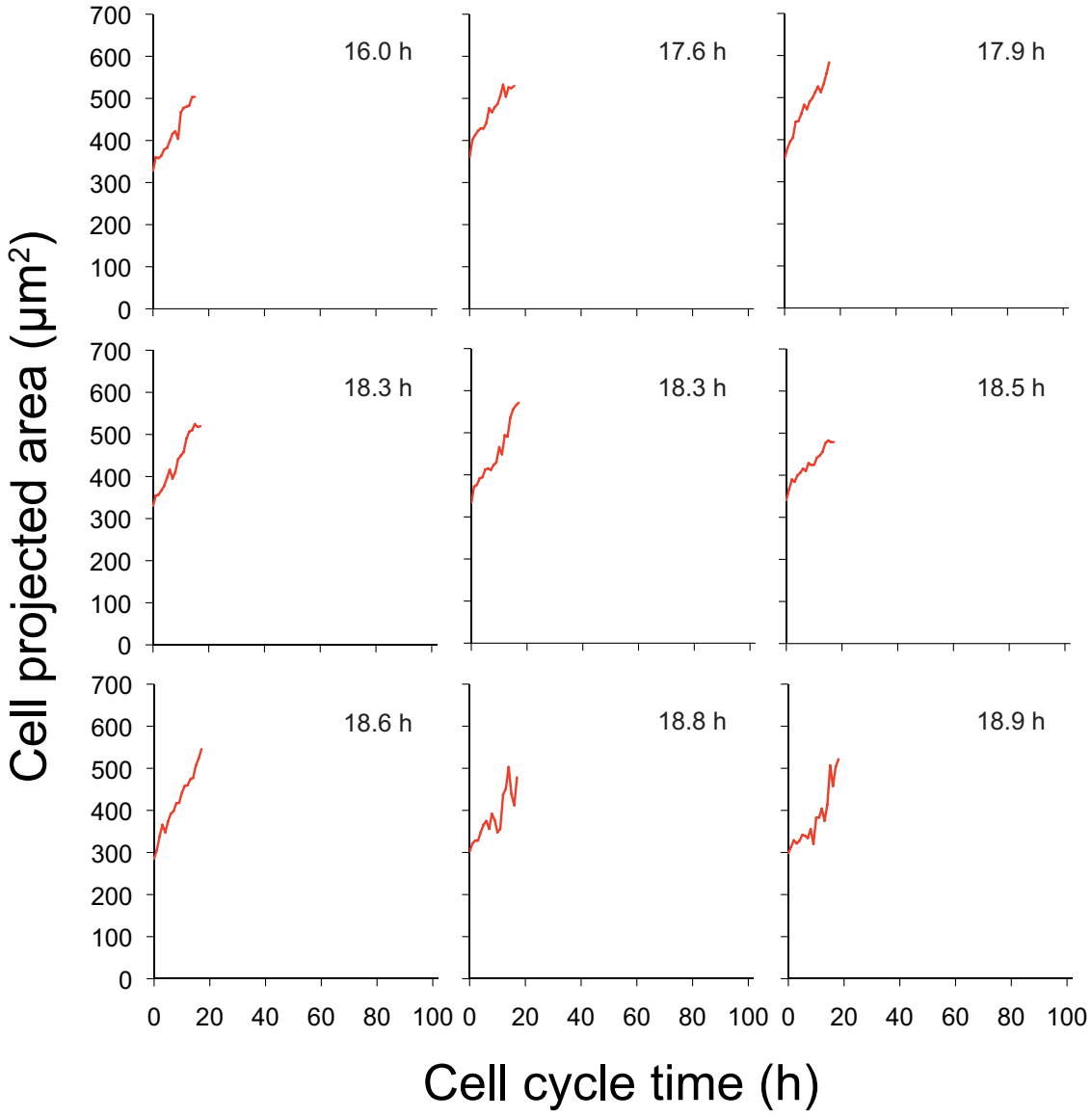


**Figure 3.16 Cell size growth rate of fast cycling cells from EPCR⁺ clones**

The cell-projected area was averaged for every hour of cell cycle. Nine cells with the shortest cell cycle times in the EPCR⁺ population are shown. The average cell size growth rate of these cells was 11.2 ± 3.3 $\mu m^2\ h^{-1}$ (mean ± s.d.).

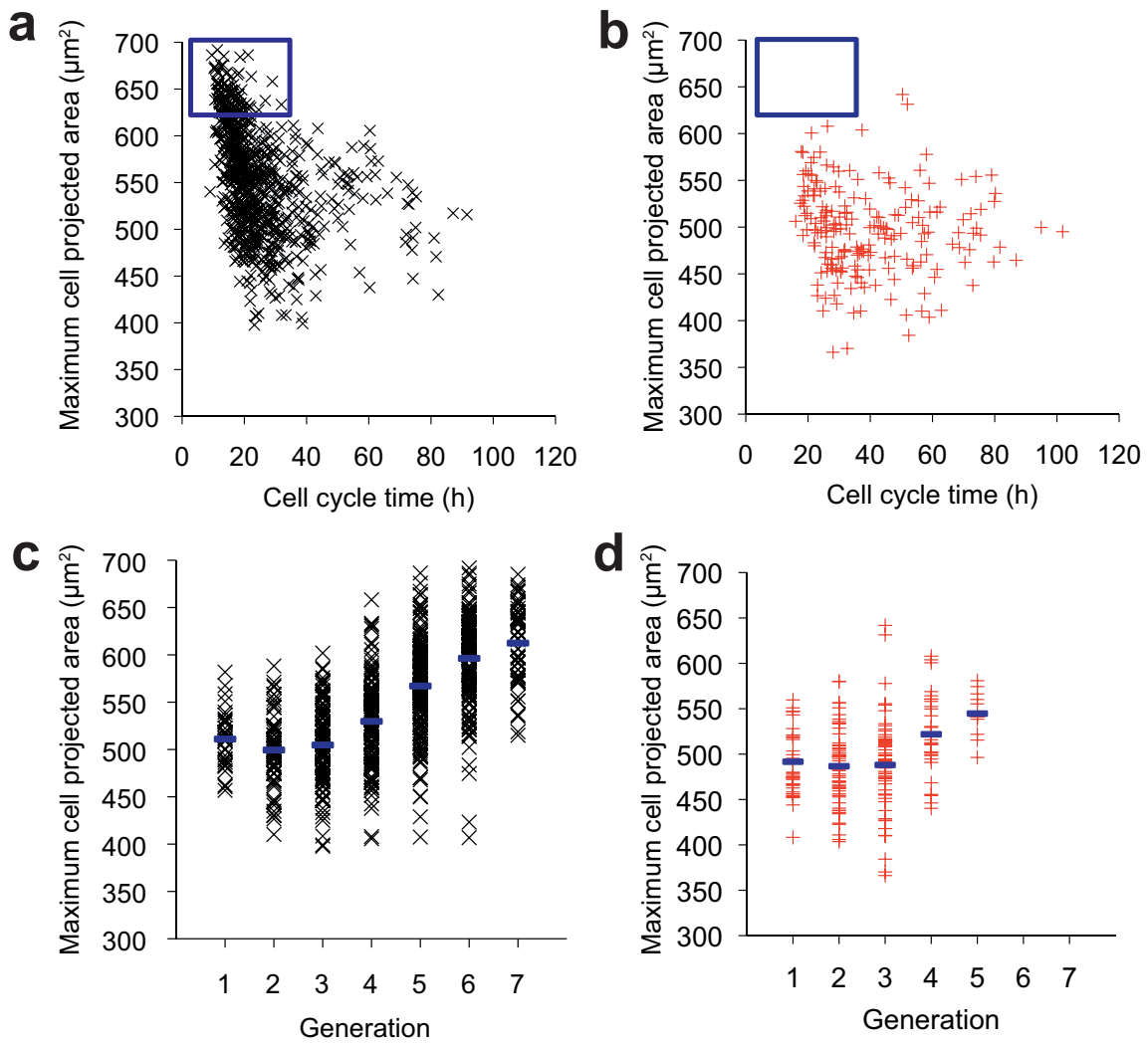


**Figure 3.17 Variations in maximum cell size before division**

The maximum cell-projected area was measured by averaging cell area one hour before division and compared to the cell cycle time of the cells for (**a**) EPCR$^-$ clones ($n$ = 710 cells) and (**b**) EPCR$^+$ clones ($n$ = 195 cells). Blue boxes highlight the population of large and fast cycling cells. Cells that died or did not divide were excluded from this analysis. The maximum cell-projected area before division is shown as a function of the generation of each cell for (**c**) EPCR$^-$ clones ($n$ = 710 cells) and (**d**) EPCR$^+$ clones ($n$ = 195 cells). Blue bars represent the average for each generation.

# CHAPTER 4 High-Throughput Screening and Selection of Clones for Recombinant mAb Production

This work has shown that microfluidic cell culture coupled with high-resolution time-lapse imaging can be a powerful tool to monitor the *in vitro* behavior of mammalian cells. However, experiments in previous chapters have been limited to hematopoietic cells with analysis of intracellular or surface proteins only. In this chapter, the flexibility of the system is demonstrated by the clonal culture of a different suspension cell type, Chinese hamster ovary cells, and the integration of single-cell secreted proteins analysis.

## 4.1 Introduction

Recombinant monoclonal antibodies (mAbs) are essential components of biological assays for applications ranging from cell characterization to diagnostic testing. Over the past 2 decades the use of mAbs for therapeutic purposes has grown to dominate the biotechnology industry with a variety of mAbs coming to market and many more in clinical trials[293], most of them targeting cancer[294,295], autoimmune and inflammatory disorders[195,296]. Chinese Hamster Ovary (CHO) cells are widely used to produce mAbs[189], now favored in large part due to the demonstrated clinical safety and efficacy of their protein products.

An important bottleneck in the development of mAb production processes is the need to generate cell lines that produce large quantities of antibodies. After transfection of the gene of interest, the generation of a stable clone with the desired product quality can take several months. This is normally the longest step in the development of a new protein production

process[216]. Most production cell lines have been generated by performing limiting dilution of a transduced pool of cells in multiwell plates[197,216,220], with often >1,000 wells screened due to the low cell plating efficiency[217,297] and the need to analyze many clones. This method requires at least 2 weeks of culture to allow accumulation of detectable mAbs concentrations before a first measurement can be made. Lowest producing clones are eliminated while highest producers are advanced to the next phase of scale-up, a laborious process that is often repeated in subsequent rounds of sub-cloning to ensure the generation of clonal cell lines[298].

In an effort to increase throughput and to accelerate the identification of high-producing cells, several FACS-based methods have been developed. Cell sorting strategies can be coupled with single-cell deposition, hence eliminating the need for sub-cloning. These strategies involve immunolabeling surface-bound mAbs[227] or integrating a reporter gene into the vector[223-225,299], which can be engineered to minimize the impact of the fluorescent protein on the translation of the desired product[226]. However, in some systems the fluorescence levels of reporter proteins or surface-bound mAbs are poorly correlated to the amounts of secreted mAbs[232]. Therefore, methods have been developed to directly measure the secreted proteins using gels or semi-solid medium that limit diffusion and maintain the secreted mAb molecules in the vicinity of the producing cells. For instance, single cells can be encapsulated in gel microdrops that are subsequently labeled with a fluorescent antibody and sorted to select for high-producing cells[229]. A similar approach is used with matrix-based secretion assays but the product is captured directly onto biotinylated cells using an avidin-bound antibody[230,231] and is then fluorescently labeled before cell sorting. Other secretion assays involve cultivating cells in semi-solid medium over multiple days to allow concentration of the product around the clones, resulting in a visible halo of fluorescently tagged antibody[232,233]. These methods require cells to be seeded

at low densities to ensure clonality in the semi-solid medium such that these conditions may not select cells that will perform well after scale-up in suspension culture medium.

Miniaturization can accelerate secretion assays by rapidly concentrating the products from single cells while providing the throughput needed for large screens. Microwell arrays have been reported to screen for large numbers of antibody-secreting single cells[34,300-302]. For instance, using microengraving cells can be trapped into a microwell array while the secreted antibody is captured onto a functionalized glass cover that is then removed and fluorescently stained prior to being scanned. This method has been multiplexed to assess levels of glycolysation in addition to secretion[301]. However, selected cells must be cultivated in an open array or transferred to multiwell plates for clonal expansion, both dilute conditions. Microfluidic devices capable of identifying single antibody-secreting cells isolated in picoliter-volume aqueous droplets or chambers have also been reported[36,39]. An underexploited feature of these enclosed systems is the use of small volumes to carry out clonal expansion at high seeding densities. Cloning by inoculating one cell into 4 nl yields a concentration of 250,000 cells $ml^{-1}$, thus a comparable seeding density to conventional macroscale passaging. This high concentration can provide a conditioning of the culture environment to potentially enhance the cloning efficiency compared to limiting dilution cultures. Furthermore, the isolation of clones in nanoliter volumes using integrated micro-valves[16] has the advantage of concentrating secreted proteins without the need for a semi-solid matrix, thus allowing for rapid detection of mAb production. Most importantly, the immobilization of suspension cells by sequestering clones in high aspect ratio microfluidic chambers[303] allows the cells to be assayed and cultivated in liquid medium under conditions similar to bioreactor cultures. The operation of these microfluidic devices can easily be automated and combined with time-lapse

imaging to confirm clonality and to track proliferation. We have adapted the microfluidic cell culture platform presented in Chapter 2 to rapidly assay the amount of secreted mAb from single cells and to grow hundreds of clones simultaneously without the need for a semi-solid matrix. Here, we demonstrate the use of this platform to generate clonal cell lines from a pool of suspension-adapted CHO cells producing a recombinant IgG1 mAb.

## 4.2 Materials and Methods

### 4.2.1 CHO Cell Pool Generation

Suspension CHO-S cells (Life Technologies, Invitrogen) were transfected with a CET 1019 HS puromycin vector (EMD Millipore) encoding the light and heavy chains of a human IgG1 monoclonal antibody using an electroporator (Neon Transfection System, Life Technologies). Both the light and heavy chain DNA expression vectors contained the puromycin selection gene marker. A heterogeneous pool of cells was generated after a selection process using puromycin at 15 μg $ml^{-1}$ (Sigma-Aldrich). Cell cultures were scaled up to shake flasks and banked in freezing media containing 95% CD OptiCHO (Life Technologies) and 5% DMSO (Sigma-Aldrich).

### 4.2.2 Maintenance Culture and Medium

Cells were maintained in shake flasks with growth medium consisting of CD OptiCHO (Gibco, Life Technologies) supplemented with 15% CHO CD EfficientFeed A (Gibco, Life Technologies), 15% CHO CD EfficientFeed B (Gibco, Life Technologies), 4.5 mM L-glutamine (EmbryoMax, Millipore), 15 μg $ml^{-1}$ puromycin (Sigma-Aldrich), 0.1 mM hypoxantine and 16 μM thymidine (Gibco, Life Technologies). Shake flasks were maintained at 37 $^{o}$C in a shaking incubator at 125 rpm (Minitron, Infors) with 6 or 10% $CO_2$. Cells

were passaged every 2-3 days and seeded at a concentration ranging from 2-5 × $10^5$ cells $ml^{-1}$.

### 4.2.3 Growth Controls in Cloning Medium

For batch growth controls, cells were seeded at a concentration of 2.5 × $10^5$ cells $ml^{-1}$ and cultivated in 20 ml of cloning medium consisting of RPMI medium (Gibco, Life Technologies) supplemented with 17% CD OptiCHO (Gibco, Life Technologies), 3.75% CHO CD EfficientFeed A (Gibco, Life Technologies), 3.75% CHO CD EfficientFeed B (Gibco, Life Technologies), 1 mM L-glutamine (EmbryoMax, Millipore), 10 μg $ml^{-1}$ insulin (EMD Millipore), 5 μg $ml^{-1}$ transferrin (CellPrime rTransferrin AF, Millipore), 2 g $l^{-1}$ albumin (Cell Prime rAlbumin AF-G, Millipore) and 15 μg $ml^{-1}$ puromycin (Sigma-Aldrich). Samples were taken daily and the viable cell concentration was measured by an automated cell counter (Cedex, Illumina). To measure growth rates from single cells, a U-shaped suspension 96 well-plate (BD Falcon) was rinsed with cloning medium. Cells were diluted to a concentration of 5 cells $ml^{-1}$ and 200 μl was deposited in each well, equivalent to 1 cell per well. Cells were centrifuged for 5 min at 400*g* and left in the incubator for 1-2 h. Wells were manually scored using a microscope to identify the starting number of cells in each well and then the number of cells in colonies originating from single cells was counted every day.

### 4.2.4 Clone Selection Using Limiting Dilution

A parallel study was performed using conventional limiting dilution in 96-well plates. Two flat-bottom plates were seeded at a concentration of 0.5 cells per well in cloning medium. Colonies were evaluated under the microscope on day 7 and based on their shape, only those that appeared to

come from a single cell were transferred to wells of a 24-well plate in growth medium for subsequent titer evaluation. The highest titer clones were scaled up to 125 ml shake flasks and banked as described above. These clones were used for comparison to the clones generated from the microfluidic cell culture array platform.

### 4.2.5 Microfluidic Cell Culture

Microfluidic cell culture arrays containing 1,600 chambers of 4.1 nl (160 μm × 160 μm × 160 μm) were fabricated as described in **Appendix B**. Two days prior to cell loading, the iso-osmotic bath was filled with cloning medium supplemented with penicillin (100 U $ml^{-1}$) and streptomycin (100 μg $ml^{-1}$). The device was connected, primed with cloning medium and maintained in an environmental chamber (Chamlide, LiveCellInstruments) at 37 $^{o}$C and with 5% humidified $CO_2$. Two Petri dishes filled with water were added in the environmental chamber to maintain the humidity. Cells were centrifuged for 5 min at 167*g* and resuspended at a concentration of $2 \times 10^6$ cells $ml^{-1}$ in fresh cloning medium. Cells were then loaded in the microfluidic cell culture array by an approximately 1 μl $min^{-1}$ flow using an integrated micro-pump. Once the array was filled, cells were allowed to settle by gravity to the bottom of the chambers for ~3 min. If needed, this process was repeated until a desired number of single cells was obtained. After the bead immunocapture assay, the cells were cultivated in a batch mode with the isolation valve kept open. Microvalves and image acquisition were controlled by custom scripts (LabVIEW, National Instruments).

### 4.2.6 Bead Immunocapture Assay

Cloning medium supplemented with 100 U $ml^{-1}$ penicillin and 100 μg $ml^{-1}$ streptomycin was used throughout the bead immunocapture assay. Polystyrene protein-A coated beads with an average diameter of 4.9 μm (ProActive® Microspheres, Bangs Laboratories) were washed at least 4 times with cloning medium by successive rounds of centrifugation at 7431*g*. The beads were resuspended at a concentration of 2 mg beads $ml^{-1}$ and immediately loaded into the device at a flow rate of 2 μl $min^{-1}$ from a PTFE tubing maintained in an upright position. Once the array was filled, the flow was stopped and the beads were allowed to settle by gravity to the bottom of the chambers, resulting in an average of 100-150 beads per chambers. Excess beads in the channels were flushed with cloning medium for 5 min at a flow rate of 2 μl $min^{-1}$. The isolation valves were then closed to sequester each chamber and the beads were incubated with cells for 2 h at 37 $^{o}$C. The array was then flushed with cloning medium for 15 min at a flow rate of 2 μl $min^{-1}$. A solution of 20 μg $ml^{-1}$ labeled antibody (Dylight 594-conjugated AffiniPure F(ab')$_2$ fragment of rabbit anti-human IgG (H+L) (Jackson Immunoresearch) diluted in cloning medium was first desalted by centrifugation (Amicon Ultra 0.5-ml 100K, Millipore) and then pumped into the device for 15 min at 2 μl $min^{-1}$. The fluorescent antibody was incubated for 15 min, and then washed with cloning medium for 30 min at 2 μl $min^{-1}$ before imaging.

### 4.2.7 Automated Image Acquisition

Custom scripts (LabVIEW, National Instruments) were developed to allow automated image acquisition of the array divided into 400 frames containing 4 chambers each. The location of every frame was determined by selecting the four array corners, and then extrapolating the coordinates of each frame. The alignment script described in Chapter 2 was used to correct

for the minor distortions in the devices that can be introduced during fabrication so as to position the chambers correctly within each frame. After loading the beads, the focus on each frame was automatically determined by taking a stack of images and identifying the focal point providing the maximum pixel standard deviation within the chambers. Following the bead immunocapture assay, a bright field image and a red fluorescent image (10 ms exposure) were taken for every frame. Frames were subsequently imaged in bright field every 30 min during cell culture.

### 4.2.8 Image Analysis Algorithms

A graphical user interface (GUI) was developed in Matlab (MathWorks) to quantify the CHO cell protein production by measuring the fluorescence intensity emitted from the beads. Since each frame contained 4 chambers, the well boundaries were first identified by blurring the bright field image and subtracting it from the original. This process enhanced areas of high spatial frequency such as the well edges. The wells were then filled and any object smaller than 1,250 pixels were eliminated using a size filter. Artifacts caused by the presence of beads were corrected by dilation and the well edges were adjusted by erosion before creating a mask image of the wells. A bead mask was also created from the bright field image. The beads appeared to be much darker than the background, which allowed their segmentation using an empirically determined brightness threshold. All pixels with intensity below the threshold were set to one, indicating the pixel was part of a bead, while those above the threshold were set to zero. Often, the center of the beads appeared as bright spots in the mask image due to diffraction, causing the beads to look like rings. These rings were closed and filled by a dilation step followed by erosion. Finally, any lone pixels, i.e. a single pixel with a value of one surrounded by pixels with values of zeros,

were removed from the mask. A series of 6 fluorescent images containing empty wells were taken for flat-field correction. The pixel intensity at each location was averaged for the set of images and used to correct for background fluorescence. Next, the bead and well masks were combined and applied to the fluorescent image by multiplying each pixel in the mask image with the corresponding pixel in the fluorescent image. The total fluorescence intensity was calculated by summing the values of all the pixels in the resulting image. The GUI enabled the user to correct for segmentation errors when needed. For the quantification of surface-bound mAb, the GUI allowed the user to make a cell mask by tracing the contours of each cell. This mask was then applied to the fluorescent image to measure the intensity of each cell. The total intensity of the beads and the cells were saved for analysis. The mean intensity of each well was calculated as the total intensity divided by the total bead area. For the selection of antibodies and the generation of the antibody-binding curve, stained beads were deposited on glass slides under a coverslip and imaged. The same algorithm was used to generate the bead mask from bright field images and to measure the fluorescence of the beads (no chamber mask was applicable).

### 4.2.9 Clone Recovery and Expansion

Micropipettes with a tip diameter ranging from 50-100 μm were made from glass capillaries. Prior to cell recovery, the cover layer of the chip was cut inside the area of the bath and removed. Selected clones were recovered with the micropipette using an oil microinjector (IM-9B, Narishige) and deposited in a U-shaped non tissue-culture-treated 96-well plate containing 200 μl of cloning medium supplemented with 100 U $ml^{-1}$ of penicillin and 100 mg $ml^{-1}$ of streptomycin in each well to prevent contamination from the recovery process. Clones were centrifuged for 5 min at 400*g* and incubated for

11 days. Viable clones were then transferred to a 24-well plate containing 1 ml of growth medium. After 5 days of culture, the plate was centrifuged for 5 min at 400*g* and the supernatant was recovered for titer analysis. The clones were then transferred to 6 ml of culture medium in 6-well plates. Once confluent, the selected clones were scaled up to 20-ml shake flask cultures and banked as described above.

### 4.2.10 Batch Shake Flask Cultures

The selected clones were thawed rapidly and resuspended in 20 ml of growth medium in shake flasks. The cells were cultivated and passaged until the viability exceeded 95%. The day before starting shake flask studies, the cells were seeded at a concentration of $5 \times 10^5$ cells $ml^{-1}$. The next day, the cells were seeded at $5 \times 10^5$ cells $ml^{-1}$ in 20 ml of growth medium in duplicate flasks. Cell concentration was measured with an automated cell counter (Cedex, Illumina) on days 5 and 7 for clones generated by limiting dilution and on days 3, 5 and 7 for clones generated from the microfluidic platform. As well, a 1 ml-sample was taken from each flask, centrifuged at 7,341*g* and the mAb concentration in the supernatant titer was measured as described below. The integral viable cell density (IVC) was calculated as follows:

$$IVC_{i+1} = 0.5 \times \left(C_{i+1} + C_i\right) \times (t_{i+1} - t_i) + IVC_i \qquad (4.1)$$

where $C$ is viable cell concentration (cell $ml^{-1}$) and $t$ is the time in culture (days). The titer was plotted against the IVC and the slope up to day 5 was used to calculate the cell specific productivity (SPR).

### 4.2.11 Measurement of mAb Titers

Secreted mAb titers were measured by biolayer interferometry using the Octet RED96 Analysis System (Forté Bio, Pall Life Sciences) with Protein A Biosensors (Forté Bio, Pall Life Sciences). A standard curve from a purified mAb standard of known concentration was generated with each run, ranging from 0-50 μg $ml^{-1}$ for low concentration samples and 0-500 μg $ml^{-1}$ for high concentration samples. Supernatants exceeding the dynamic range were diluted appropriately and reanalyzed.

### 4.2.12 Statistical Analysis

The error bars were calculated using the standard deviation of the mean. A two-tailed unpaired *t*-test with unequal variance calculated the cloning efficiency *P* values. The coefficients of determination ($R^2$) were based on least-square linear regressions. The coefficient of variation (CV) was calculated as the standard deviation over the mean. The theoretical Poisson distribution was calculated as follows:

$$P(x) = \frac{e^{-\mu_c}\mu_c^{\,x}}{x!} \qquad (4.2)$$

where $P(x)$ = probability of having a chamber containing $x$ cells

$x$ = number of cells per chamber

$\mu_c$ = average number of cells per chamber

The antibody binding curve to the bead was calculated using the following Langmuir equation:

$$I = I_{\max}\left(\frac{K \cdot c_{Ab}}{1 + K \cdot c_{Ab}}\right) \qquad (4.3)$$

The constants $I_{max}$ and $K$ were determined by a Langmuir regression using the following equation:

$$\frac{c_{Ab}}{I} = \frac{c_{Ab}}{I_{\max}} + \frac{1}{K \cdot I_{\max}} \qquad (4.4)$$

where $I$ = bead fluorescence intensity

$I_{max}$ = maximum bead fluorescence intensity

$K$ = equilibrium constant (ml $\mu g^{-1}$)

$c_{Ab}$ = IgG1 antibody concentration ($\mu g$ $ml^{-1}$)

## 4.3 Results

### 4.3.1 Microfluidic Secretion Assay and Clonal Expansion

In clonal cultures the accumulation of secreted antibody sufficient for detection normally requires many days (e.g. 2 weeks), considerably extending the duration of initial cell specific productivity screens. This analysis is confounded by varied clonal growth rates at low seeding density and influenced by evaporation from small volume cultures. To address these challenges we developed a system to analyze within a few hours the productivity of single cells by taking advantage of the far more rapid product accumulation and the high cell seeding density provided by nanoliter-volume chambers. Our microfluidic platform was fabricated using multilayer soft lithography as described in Chapter 2. Each of the 1,600 chambers in the array was 4.1 nl in volume, thus providing single-cell seeding concentrations comparable to conventional macroscale passages. The microfluidic device included micro-pumps downstream of the array to control loading rates and isolation valves to sequester all of the chambers when needed. In a first step, a pool of transfected CHO cells producing varied levels of a recombinant monoclonal human IgG1 antibody was loaded into the array. Different seeding concentrations were tested and samples at $2 \times 10^6$ cells $ml^{-1}$ yielded a high proportion of chambers filled with single cells (typically 300-400 out of 1,600), close to the theoretical maximum of a Poisson distribution for this stochastic loading process (**Fig 4.1**). The high aspect ratio of the chambers sequestered suspension cells by gravity (**Fig 4.2a**). Cells were then washed thoroughly to remove antibodies in the medium. Cloning medium containing polystyrene beads coated with protein A (diameter: 4.9 μm) was then introduced into the device and these beads were allowed to settle (**Fig. 4.2b**). A medium wash was performed to clear beads that had not been captured (e.g. in the channels between chambers) and the isolation valve was then

closed for 2 h (**Fig. 4.2c**). Following the incubation period, the array was washed with medium (**Fig. 4.2d**) and a solution of labeled detection antibody was loaded into the device. The chambers were isolated for an additional 15 min (**Fig. 4.2e**). We tested multiple antibodies and observed that $F(ab')_2$ fragments generally showed lower non-specific binding, consistent with their lack of constant region with affinity for Protein A (**Fig. 4.3**). The Dylight 594-conjugated $F(ab')_2$ fragment of rabbit anti-human IgG (H+L) gave the highest signal-to-noise ratio and was selected for the assay. The array was washed extensively to remove any unbound fluorescent antibody (**Fig. 4.2f**). A custom algorithm was then used to automatically focus on the beads and sets of bright field and fluorescent images were acquired from the entire array. After the assay, the isolation valve was left open and the cells were cultivated in batch mode for 4.5 days (**Fig. 4.2g**). High-producing clones with good proliferative capacity were then recovered from the device for further expansion.

### 4.3.2 Assessment of Productivity from Single Cells

Custom scripts were developed to automatically segment the beads from bright field images and to measure the fluorescence intensity in bead-covered areas (**Fig. 4.4**). The mean bead intensity was calculated by dividing the total bead intensity in a chamber by the total projected area of the beads. Since beads often merged during segmentation, we estimated the numbers of beads by dividing the total bead area by the theoretical projected area of one bead. Using a concentration of 2 mg beads $ml^{-1}$ typically resulted in on average 100-150 beads per chamber. An example of the bead distribution is provided in **Fig. 4.5**. We have developed a custom software to assess the accuracy of our image analysis algorithm and to manually correct bead segmentation errors. Aside from a few outliers, our bead immunocapture algorithm identified the top producer cells from a population (**Fig. 4.6**),

thereby demonstrating the possible rapid automation of the assay. We generated a curve of the mean bead intensity by making serial dilutions from a known concentration sample of the secreted IgG1 antibody. The bead saturation occurred at 8 μg of antibody (mg beads)$^{-1}$ (**Fig. 4.7**), consistent with the manufacturer specifications. Typical mean intensity values obtained in the bead immunocapture assay for the top 5% producing cells fell below the saturation level of the beads, thus providing sufficient dynamic range to distinguish the highest producers from the rest of the population. Assuming infinite association and no dissociation, we calculated that the maximum time constant for mAbs to be captured onto a single bead in one chamber with a homogeneous starting concentration is ~50 min (**Appendix E**). This suggests that a 2-hour assay with an average of 130 beads should be sufficiently long to enable efficient antibody capture.

We asked whether the bead immunocapture assay had enough sensitivity to distinguish producing cells from a pool of CHO cells transfected to secrete a human IgG1 monoclonal antibody. Since the stochastic loading process introduced few cells into the array, it was possible to compare the mean bead intensities of chambers containing single cells to the intensities of cell-free chambers. Highest producers had mean bead intensities that were 2 orders of magnitude larger than non-producing cells and the detectable producing cell population (32.7% of the cells) was easily distinguished from the low or non-producing population whose chamber intensity distribution matched that of the cell-free chambers (**Fig. 4.8a**). We performed a traditional limiting dilution assay in parallel on the same pool of cells and found similar fractions of producing clones (34.4%) (**Fig. 4.8b**).

### 4.3.3 Enhanced Cloning Efficiency

To test whether the microfluidic array could sustain maximal growth rates in clonal cultures, we compared the average growth rates of single cells in the microfluidic array to the average growth rates of single cells in multiwell plates (culture volume: 200 μl) and shake flask cultures seeded at $2.5 \times 10^5$ cells $ml^{-1}$. The cells had reduced growth rates when seeded as single cells in multiwell plates compared to shake flask cultures. In contrast, clonal cultures in the microfluidic device had growth rates comparable to the shake flask cultures (**Fig. 4.9a**). A single cell in a 4-nl microfluidic chamber is at an effective concentration of ~$2.5 \times 10^5$ cells $ml^{-1}$, and thus quickly provides a conditioned medium environment as these concentrations do in shake flask cultures. We then asked whether the microfluidic array could increase the cloning efficiency due to this higher seeding concentration. We used the percentage of clones with more than 8 cells after 72 h of culture to calculate the cloning efficiency. Clones in multiwell plates on average doubled every 23.2 h, and therefore clones with normal growth were expected to have gone through at least 3 divisions after 3 days. Single cells cultivated in the microfluidic array had a significantly higher cloning efficiency than those seeded in multiwell plates ($P$ value = 0.06), most likely due to medium conditioning effects amplified by the 4-nl volumes (**Fig. 4.9b**). This enhanced cloning efficiency could allow the recovery of high-producing clones that would not survive limiting dilution in multiwell plates.

### 4.3.4 Relationship Between Surface-Bound and Secreted mAb

Membrane-bound antibody staining has been used as a tool to enrich for high-producing cells[227,304]. However, there have been contradicting reports as to whether membrane-bound antibody is a reliable indicator of the amount of secreted proteins[227,228,232]. Our technology can conveniently measure

membrane-bound and secreted mAbs produced by single cells simultaneously. We observed many instances where secreting cells did not stain for antibodies on their surface (e.g. **Fig. 4.10a**) and, inversely, where non-secreting cells exhibited surface antibodies (e.g. **Fig 4.10b**). We did not see a strong correlation ($R^2 = 0.22$) between the specific cell productivity and cell intensity (**Fig. 4.10c**). While the population with high levels of surface-bound antibody appeared to contain a greater fraction of high-producing cells, our results showed that surface mAb staining often excludes cells with high productivity and includes cells with low productivity.

### 4.3.5 Recovery and Expansion of High-Producing Clones

Clones from the same pool of CHO cells were isolated and analyzed for their antibody productivity in the microfluidic array, cultivated for 4.5 days and then transferred into 96-well plates. Out of the 308 clones, 60 were recovered including the 10% top producers as well as medium, low and non-producing clones that had met the proliferation criteria (>8 cells at 72 h). Of the 60 clones, 95 % continued to proliferate in the 96-well plates (e.g. **Fig. 4.11**). They were cultured for 9 additional days, then transferred into 1 ml of medium in 24-well plates and after 5 days of culture, the supernatant was recovered for titer analysis. As shown in **Fig. 4.12a,** all single cells without productivity in the microfluidic screening were also negative after recovery, suggesting that there was no cross-contamination during the recovery process. The microfluidic and multiwell measurements followed similar trends. We further scaled up to batch shake flask cultures 10 of the top 12 clones identified by the single-cell microfluidic assay. Four of these clones had already decreased their productivity at the 24-well plate stage (**Fig. 4.12b**) and likewise did not perform well in the shake flasks (**Fig. 4.13a,b**). The six high-ranked clones that had maintained their productivity at the 24-well plate stage (within the top 3.9% of the initial population) gave titers between

200-500 mg $ml^{-1}$ (**Fig. 4.12c**) with maximum specific productivities averaging 7.2 ± 1.5 pg $cell^{-1}$ $day^{-1}$ (**Fig. 4.12d**). The highest single-cell productivity identified with the microfluidic assay also gave the highest cell specific productivity in shake flask cultures, demonstrating the ability of the microfluidic single-cell secretion assay to identify and generate highly productive cell lines. The 2 highest ranked clones generated by limiting dilution, corresponding to the top 3.1% of 64 clones, had a comparable average SPR of 7.6 ± 1.4 pg $cell^{-1}$ $ml^{-1}$ (*P* value = 0.74) (**Fig. 4.14**). The recovery, analysis and expansion of 10 high-ranked clones from the device led to 6 clones with SPR above 6 pg $cell^{-1}$ $day^{-1}$. In contrast, by limiting dilution the analysis of 64 wells led to only 3 clones with such productivities. The initial screening using the microfluidic cell culture array led to a 13-fold enrichment of high-producing cells, thereby greatly reducing the burden of expanding and sampling large numbers of clones. In addition, 24-well plate titers of clones recovered from the microfluidic array were much more predictive of shake flask titers ($R^2$ = 0.93) than clones generated by limiting dilution ($R^2$ = 0.01) (**Figs. 3.15a,b**). The productivity of several clones generated by the later method was underestimated at the 24-well plate stage, likely due to the impaired growth associated with limiting dilution cloning.

## 4.4 Discussion

Our microfluidic platform provides many advantages for the selection of high-producing clones. Single-cell analysis allows hundreds of cells to be screened in a few hours, thereby eliminating the need to expand large numbers of clones in multiwell plates. This results in considerable economies in culture medium, culture vessels, time and labor. The prototype used in this study contained 1,600 chambers, enabling the analysis of 300-400 single cells per experiment. The design is easily scalable and the number of chambers could be increased several fold for populations where more clones need to be

analyzed. With the current dimensions, up to 20,000 chambers could fit on a single glass slide. Screening for a larger number of cells could identify clones with higher productivities without increasing the number of clones to be scaled up. This microfluidic approach differs from other single-cell secretion assays by allowing the analysis and culture of cells directly in medium without the need for a semi-solid matrix to contain the colonies and their secreted product. As described in Chapter 2, this cell culture system was initially optimized and tested on hematopoietic stem cells to obtain robust growth rates and cellular functions comparable to large-scale cultures. The sensitivity of CHO cells to media conditioning has revealed that another benefit of miniaturization is the rapid establishment of an adequate culture environment for small numbers of cells. Nanoliter-volume chambers allowed cells to be assayed and cultivated at seeding concentrations comparable to shake flask cultures. The higher cloning efficiency obtained from sequestering cells in small volumes can select additional clones that only thrive at high cell concentrations. Extending the culture for 4-5 days allowed clones to expand to cells numbers that made them more likely to survive when they were transferred to a multiwell plate, in turn increasing the number of high-producing clones recovered. Since cells were analyzed within 2 hours of being retrieved from a shake flask culture, they were more likely to be in a similar state to suspension cultures than if they were assayed after multiple days of static culture (e.g. 96-well plate). Together these features bring the right environment to obtain good prediction of the cell specific productivity in batch shake flasks cultures from single-cell measurements. As opposed to multiwell limiting dilution screens that are the result of both productivity and growth performance, our microfluidic system independently measures cell productivity. While growth is an important factor in obtaining high titers, growth rates in static cultures starting from low seeding density often differ from suspension cultures that can be optimized by subsequent medium improvement. Indeed, the high seeding concentrations provided by

the microfluidic array allowed better prediction of shake flask titers at the 24-well plate stage by minimizing the confounding effects of lower clonal growth rates observed in limiting dilution experiments. It could be possible to further exploit the flexibility of the system by retrieving cells from a fed-batch culture for analysis and assaying them in conditioned media, leading to an even closer match to the conditions typically used for large-scale mAb production.

Microengraving methods provide great flexibility to make secretion measurements at different time points[34,35]. However, the bead immunocapture assay in an enclosed microfluidic device has distinct advantages for applications where clonal expansion and recovery are needed. With its integrated iso-osmotic bath the microfluidic cell culture array provides an adequate cell culture environment for long-term *in situ* clonal expansion at non-diluted concentrations. In contrast, microengraving methods cannot sustain long-term proliferation in enclosed chambers and require either single-cell recovery followed by expansion in multiwell plates or immersion of the open microwell array in a large volume of medium. In addition, fibronectin coating and attachment periods of up to 6-12 h are needed to ensure that single cells are not lost when the glass slide is removed, after which cells are trypsinized for recovery[300]. Our high-aspect ratio chambers gently capture the cells by gravity, enabling suspension-adapted cell lines to be rapidly assayed on a non-adhesive surface and to be gently recovered without enzymatic dissociation.

The easy coupling of microfluidic devices with time-lapse imaging allowed clonal tracking over time, including the initial verification of clonality. That colonies arose from single cells was confirmed by visual observation. Alternatively, the process could be automated with high accuracy using a live stain on the cells. The use of programmable microfluidic systems makes this platform well suited for industrial applications and

easier to automate than microengraving methods. For the production of therapeutic mAbs, the detection antibody could be replaced by a labeled recombinant Protein A and hence provide a process devoid of animal components. It could be possible also to capture the secreted antibody directly onto Protein A- or Protein G-coated PDMS chambers instead of using bead immunocapture. However, the hydrophobic nature of PDMS provides a low-binding surface, which can be a desirable feature to maintain cells that have been adapted for suspension culture. Moreover, the use of beads in proximity of the cells concentrates the signal and possibly leads to better sensitivity.

Predicting the performance of an entire clone from a single cell within 2 hours could be influenced by significant temporal variations in mAb secretion. Reports have shown that variations in secretion levels throughout cell cycle are mainly attributed to changes in cell size[299,305] but since those were made on population measurement it is not clear whether the productivity of a single cell changes as it grows. Single-cell protein secretion in yeast has been measured by microengraving and no relation was found between productivity and cell cycle stage but stochastic variations were observed[35]. Single-molecule analysis of mRNA transcripts have shown bursts of transcription by CHO and other cell types[306,307], leading to large fluctuations in transcript expression. However, simultaneous measurements of transcript and protein levels have shown that transcriptional fluctuations are not entirely propagated to secretion levels[299] with the secretion machinery being the limiting factor at high transcriptional levels[308,309]. This suggests that even though secretion rates can be influenced by stochastic variations[35], screening results based on single-cell secretion are less prone to be confounded by temporal variations than would be measurements obtained from transcriptional analysis at the single-cell level (e.g. fluorescent expression vectors)[299]. Our platform can measure both surface and secreted mAb levels simultaneously. The assay could further be combined with

fluorescent reporters to gain a better understanding of the factors regulating mAb production at the transcription, translation and secretion levels.

The generation of stable clones is an important aspect of cell line selection. Generally, the assessment of stability is performed over multiple passages. A decline in productivity will propagate to a detectable fraction of the population much faster if the initial assay is done on a single cell rather than a bigger colony. Indeed, a fraction of the highly ranked clones exhibited lower productivities in multiwell plates than in the microfluidic assay. These discrepancies can be due to production instability or stochastic variations at the time of the assay. These clones can readily be identified and eliminated at the 24-well plate stage to avoid investing resources and efforts on the scale up of either poor producers or unstable clones. Single-cell analysis is a powerful tool to assess the heterogeneity in cell populations. Analysis of intracellular mAb using FACS is used by some as a tool to identify unstable clones[215]. Our platform could enable secretion analysis on single cells from clonal population to obtain an early assessment of clone homogeneity and detect signs of instability.

The throughput, sensitivity, flexibility and ease of automation of microfluidic single-cell analysis systems bring new tools to accelerate the development of mAbs. Cell line selection is only one example from a plethora of immunological applications that could benefit from the combination of clonal cell culture and high-throughput secretion screens. These include hybridoma generation, isolation of rare activated T cells, selection of new antibodies from primary cells or directed evolution in B cells. With the ability to obtain robust and, as shown in this work, more efficient culture conditions in small volumes, microfluidic devices have the potential to become platforms of choice for identifying rare cells in heterogeneous populations.

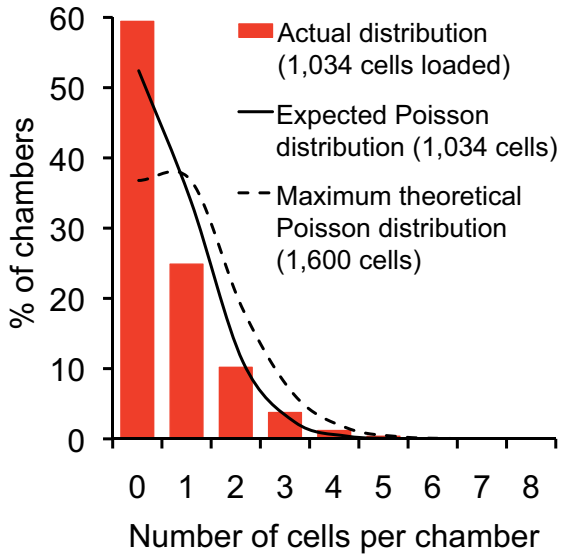


**Figure 4.1 Typical seeding density**

Around 25% of the 1,600 chambers contained single cells at a loading concentration of $2 \times 10^6$ cells $ml^{-1}$ (total: 1,034 cells), close to the expected Poisson distribution and the theoretical maximum of a Poisson distribution for an average of 1 cell per well (total: 1,600 cells). The discrete theoretical distributions are shown as lines for clearer representation.

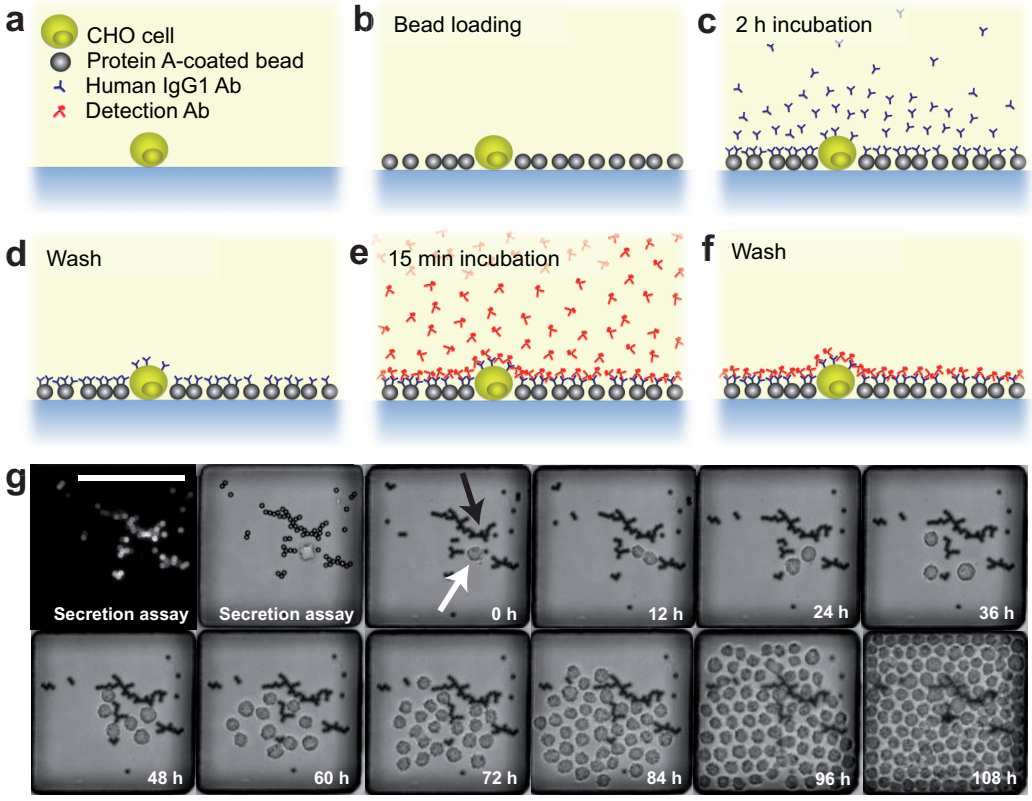


**Figure 4.2 Bead immunocapture assay to measure antibody secretion from single cells**

(**a**) Cells were loaded stochastically into an array of 1,600 chambers (4.1 nl). (**b**) Protein A-coated beads (diameter: 4.9 μm) were introduced and (**c**) the chambers were isolated for 2 h using microvalves. (**d**) The array was then washed and (**e**) Dylight 594-conjugated F(ab')$_2$ fragment of rabbit anti-human IgG (H+L) was introduced for 15 min. (**f**) The array was washed again and fluorescent images were taken to identify producing cells. (**g**) Example of fluorescent and bright field images from the bead immunocapture assay (top left) followed by time-lapse imaging of the clone for 4.5 days. The polystyrene beads are the darker objects (black arrow) while the cells are more transparent (white arrow). Cloning medium was used throughout this assay. Scale bar, 100 μm.

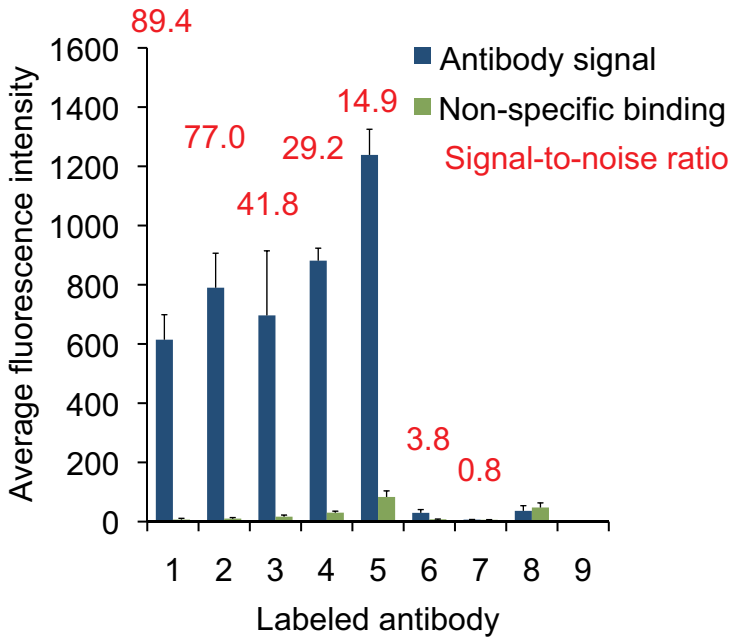


**Figure 4.3 Antibody selection for the bead immunocapture assay**

Fluorescence intensity was compared for beads exposed to cloning medium only (non-specific binding) and supernatant from a 3-day batch culture of CHO cells (antibody signal). The following polyclonal labeled antibodies were tested at a concentration of 20 μg $ml^{-1}$: (1) Dylight 594-conjugated $F(ab')_2$ fragment of rabbit anti-human IgG (H+L), (2) Dylight 594-conjugated $F(ab')_2$ fragment of goat anti-human IgG (H+L), (3) Dylight 594-conjugated $F(ab')_2$ fragment of donkey anti-human IgG (H+L), (4) Dylight 594-conjugated $F(ab')_2$ fragment of goat anti-human IgG, $F(ab')_2$ fragment-specific (5) Alexa 594-conjugated goat anti-human IgG (H+L) (6) Biotin-conjugated $F(ab')_2$ fragment of chicken (H+L) labeled with Dylight 594-neutravidin and (7) FITC-conjugated $F(ab')_2$ fragment of chicken (H+L). Lines 8 and 9 show bead autofluorescence in the red and green channels respectively. The Dylight 594-conjugated $F(ab')_2$ fragment of rabbit anti-human IgG (H+L) had the highest signal-to-noise ratio and was chosen for the assay.

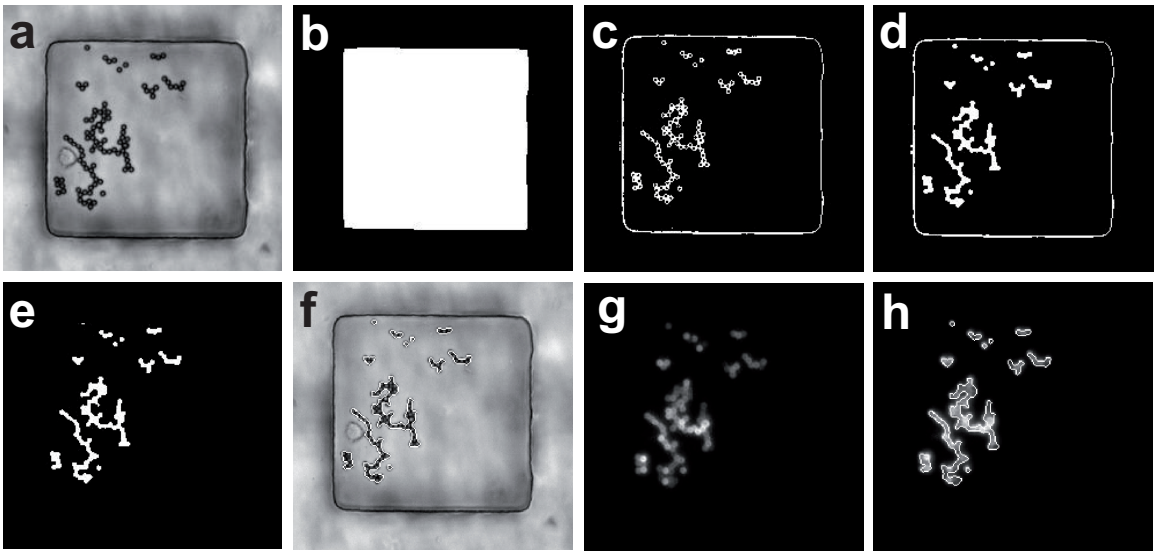


**Figure 4.4 Automated bead segmentation and measurement of mean bead intensity**

(**a**) The bright field image was first used to locate the well contours using blurring and subtraction of the original image. (**b**) The well contour was filled to create a mask of the well. (**c**) The bright field image was segmented using a set threshold and (**d**) beads were filled by a combination of dilation and erosion. (**e**) Both images (b) and (d) were multiplied to obtain a bead mask. (**f**) The bead mask in (e) was used to segment the beads and to obtain the total bead area. (**g**) The fluorescent image was multiplied by the bead mask in (e), resulting in (**h**) the measurement of the total fluorescence intensity. The mean bead intensity was measured by dividing the total intensity by the total bead area.

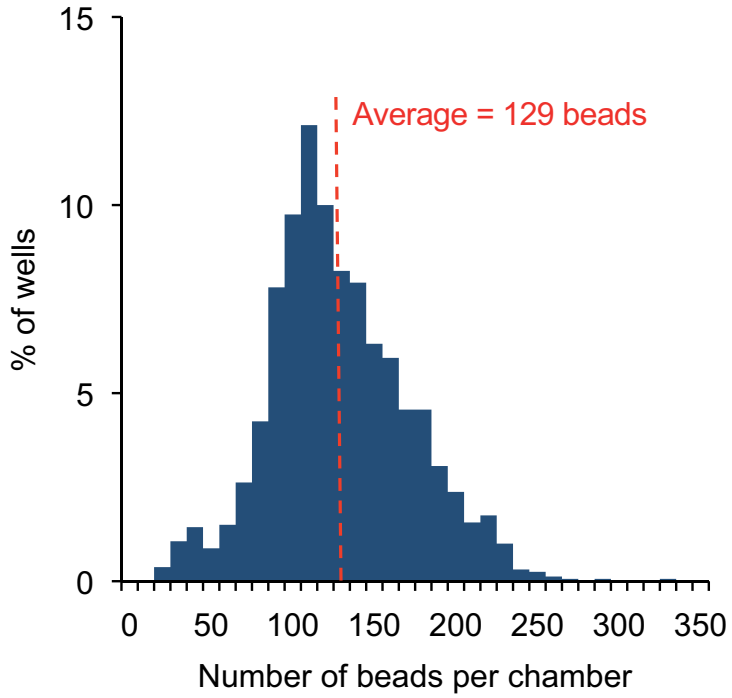


**Figure 4.5 Typical bead distribution**

(**a**) Typical bead distribution in the microfluidic cell culture array. On average, 129 beads per chamber were loaded using a solution containing 2 mg beads $ml^{-1}$.

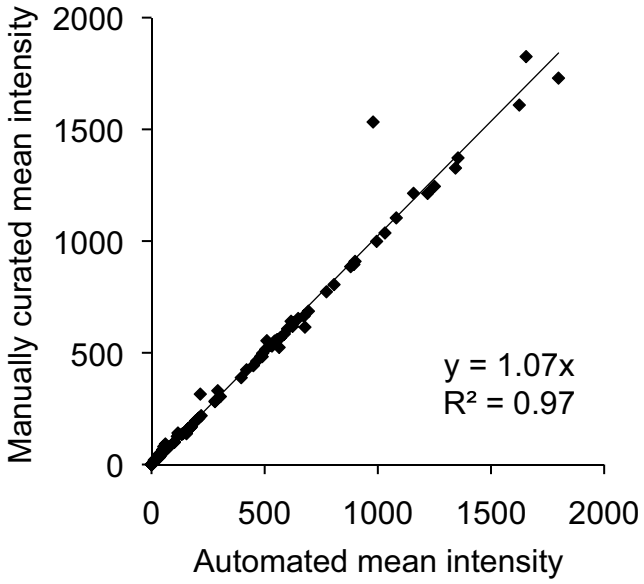


**Figure 4.6 Accuracy of the bead intensity measurement algorithm**

Images were manually curated to correct for segmentation errors and compared to the automated measurement. The automated image analysis algorithm accurately measured the bead mean fluorescence intensity. The outlier is due to poor segmentation caused by shadow from the iso-osmotic bath.

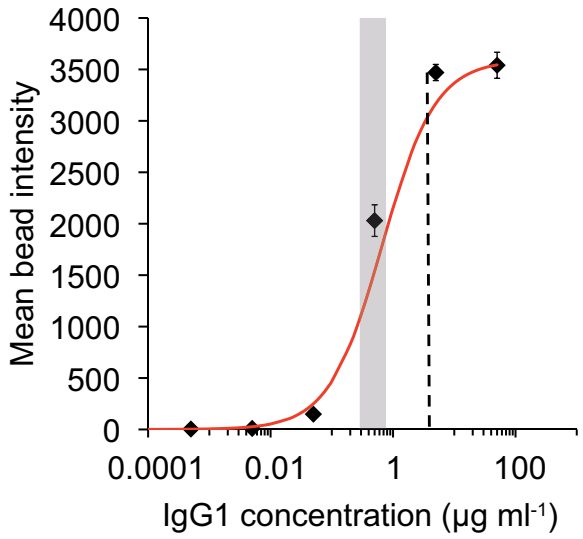


**Figure 4.7 Mean bead intensity as a function of the antibody concentration**

The antibody solutions were mixed to constant amounts of beads in tubes (0.5 mg $ml^{-1}$), incubated for 2 h, washed, and incubated for 15 min with the labeled antibody. After multiple washes, the beads were mounted on glass slides. Bright field and fluorescent picture sets were taken to measure the mean bead intensity for each concentration. The red line represents the data fit to a Langmuir equation ($I_{max}$ = 3,592; $K$ = 1.50 ml $\mu g^{-1}$). Typical mean intensities for chambers containing the top 5% producer cells (shaded area) fell below saturation levels, corresponding to local concentrations of ~0.3-0.8 µg $ml^{-1}$. Saturation occurred at around 4 µg $ml^{-1}$, corresponding to 8 µg antibody (mg bead)$^{-1}$ (dashed line), consistent with the manufacturer specifications.

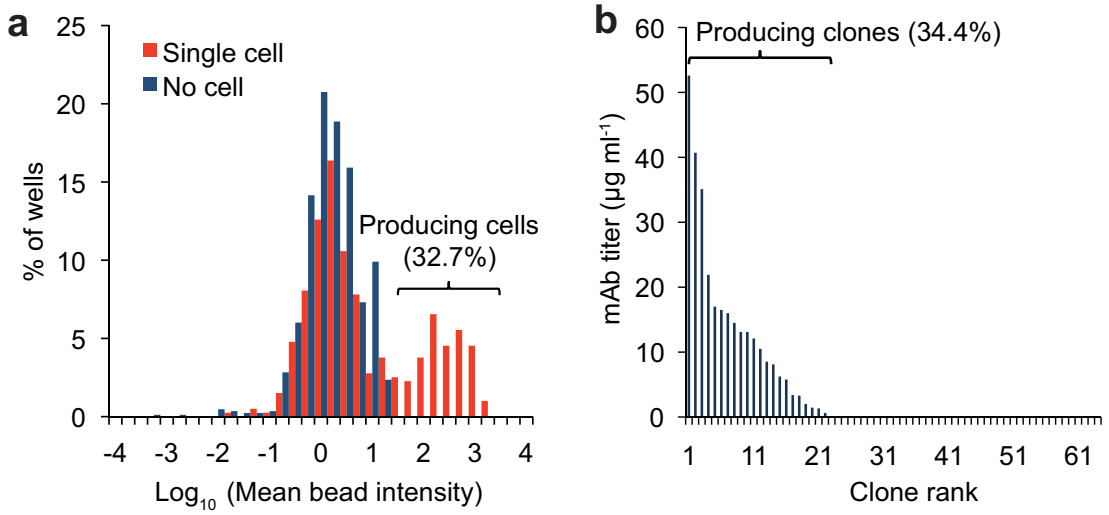


**Figure 4.8 Quantification of antibody secretion using microfluidic and limiting dilution methods**

(**a**) The mean bead intensity distinguishes high-producing cells from non-producing cells by several orders of magnitude. Analysis of wells that did not contain cells ($n$ = 848 chambers) compared to chambers that contained single cells ($n$ = 397 chambers) showed minimal cross-contamination between chambers. Empty wells had a distribution of mean bead intensities ($\mu$ = 2.96; $CV$ = 3.58) comparable to the distribution of non-producing cells ($\mu$ = 2.70; CV = 3.17). 32.7% of single cells had levels of mAb above the intensity of empty wells. (**b**) Distribution of clones generated by standard limiting dilution method. Cells were seeded at 0.5 cells $ml^{-1}$ in 96 well plates and cultured for 14 days before being transferred to 24-well plates. Antibody titers in the supernatants from 24-well plates were measured after 5 additional days of culture. Of the 64 clones, 22 (34.4%) had detectable levels of mAb.

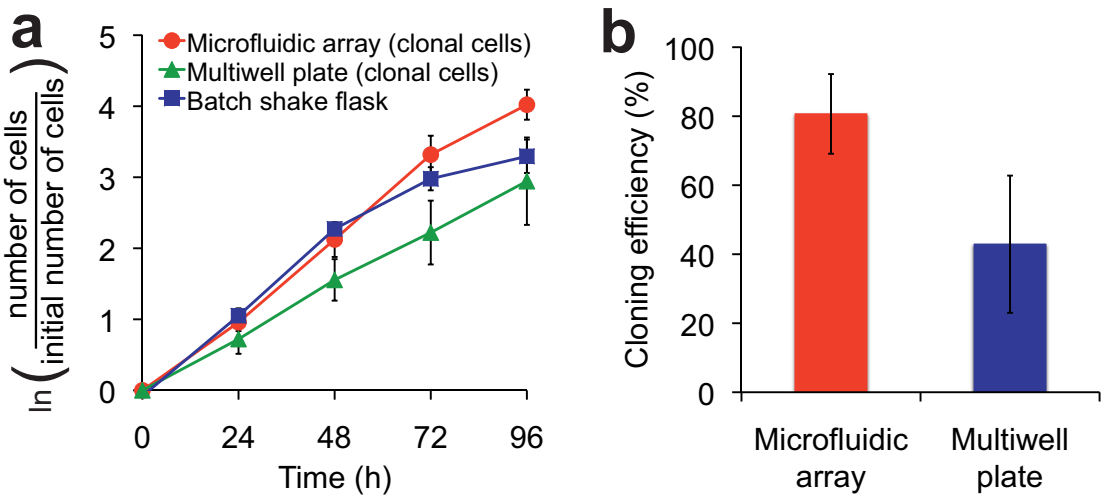


**Figure 4.9 Improved cell growth and cloning efficiency in the microfluidic cell culture array**

(**a**) Growth curves (error bars, s.d.) of CHO cells cultivated in shake flasks ($n$ = 3 experiments in triplicate seeded at $2.5 \times 10^5$ cells $ml^{-1}$), as single cells in 96 well plates ($n$ = 3 experiments; 27-36 clones per plate) or in the microfluidic array ($n$ = 3 experiments; 50 clones tracked per experiment) (**b**) Improved cloning efficiency in the microfluidic cell culture array ($n$ = 3 experiments; error bars, s.d.; $P$ value = 0.06). The cloning efficiency was measured as the percentage of clones that had more than 8 cells at 72 h. This criterion was selected based on the doubling rate of clones growing in multiwell plates (23.2 h) from (a) as clones growing at a normal rate should have undergone at least 3 divisions by 72 h.

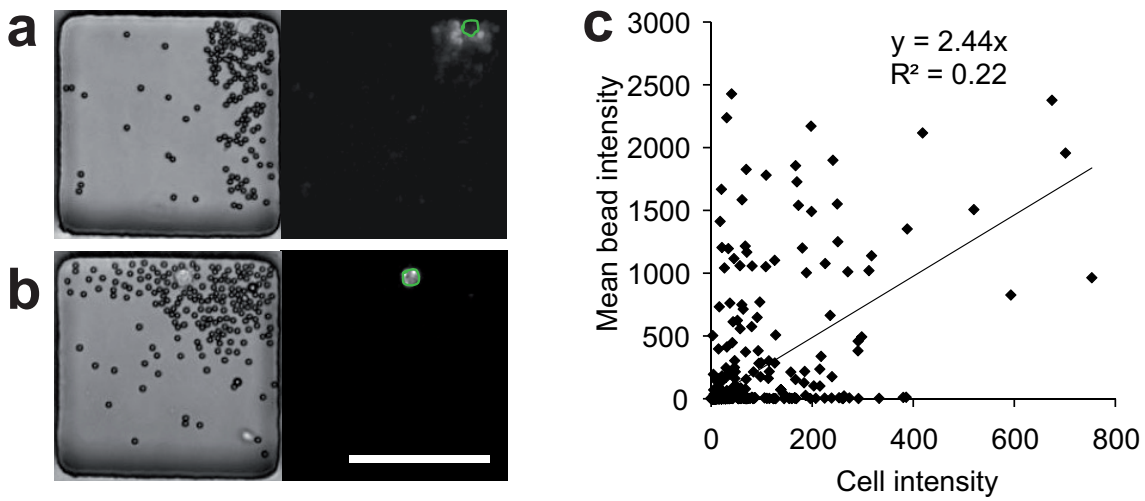


**Figure 4.10 Simultaneous measurement of membrane-bound and secreted mAbs**

(**a**) Example of a secreting cell with no antibody bound on its membrane. (**b**) Example of a non-secreting cell with membrane-bound antibody. Cell outlines are highlighted in green. Scale bar, 100 μm. (**c**) Membrane-bound antibody shows poor correlation with secretion levels.

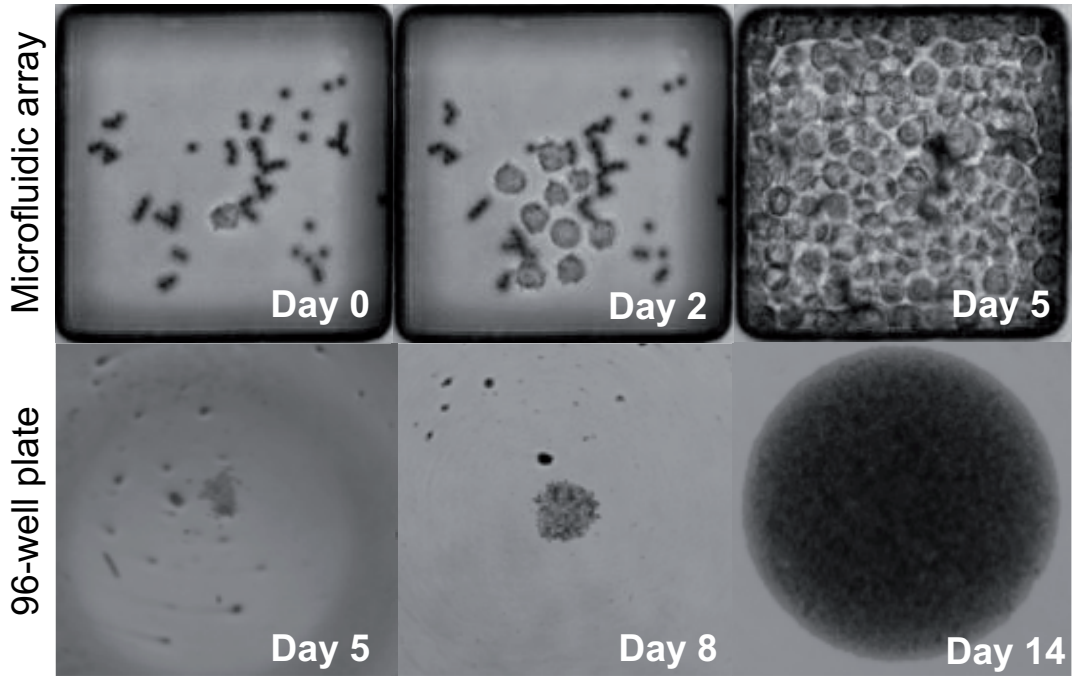


**Figure 4.11 Recovery of selected clones**

Example of a CHO cell cultivated in the microfluidic array for 5 days and recovered in a 96-well plate for further expansion.

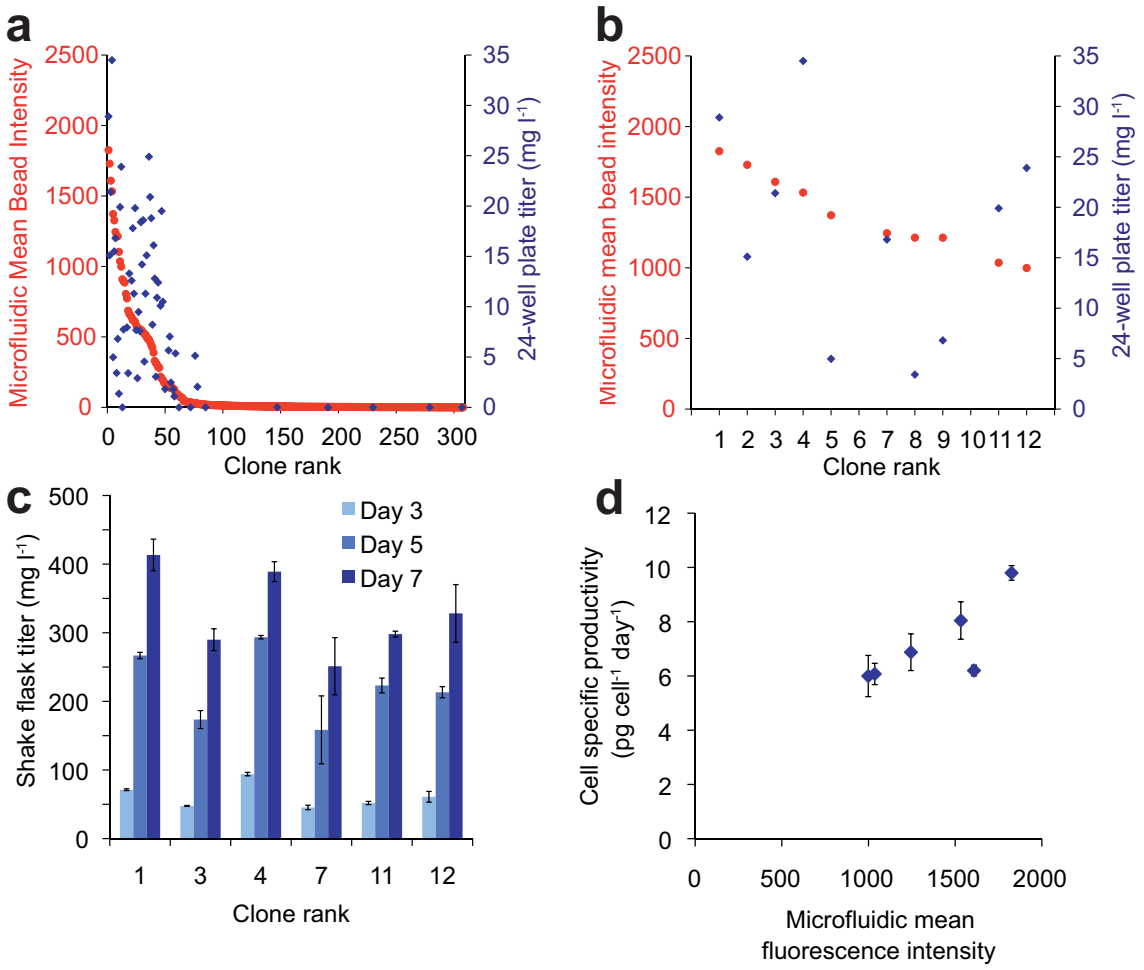


**Figure 4.12 Selection of high-producing clones**

(**a**) Comparison of microfluidic secretion assay (red) with titers at the 24-well plate stage (blue). Single cells from one experiment ($n$ = 308 cells) were ranked based on the mean fluorescence bead intensity in each microfluidic chambers (red). Out of these, 60 clones were recovered and scaled up to the 24-well plate stage (blue). (**b**) Out of the 10 clones that were scaled up, 4 clones were already showing signs of decreased productivity at the 24-well plate stage (shaded area) and were excluded from the screen. (**c**) Batch shake flask titers of the remaining 6 clones are shown after 3, 5 and 7 days in culture ($n$ = 2 flasks; error bars, s.d.). (**d**) Maximum cell specific productivity measured after 5 days in batch shake flask culture shown as a function of the microfluidic mean fluorescence intensity measured from the single cell that gave rise to the clone ($n$ = 2 flasks; error bars, s.d.).

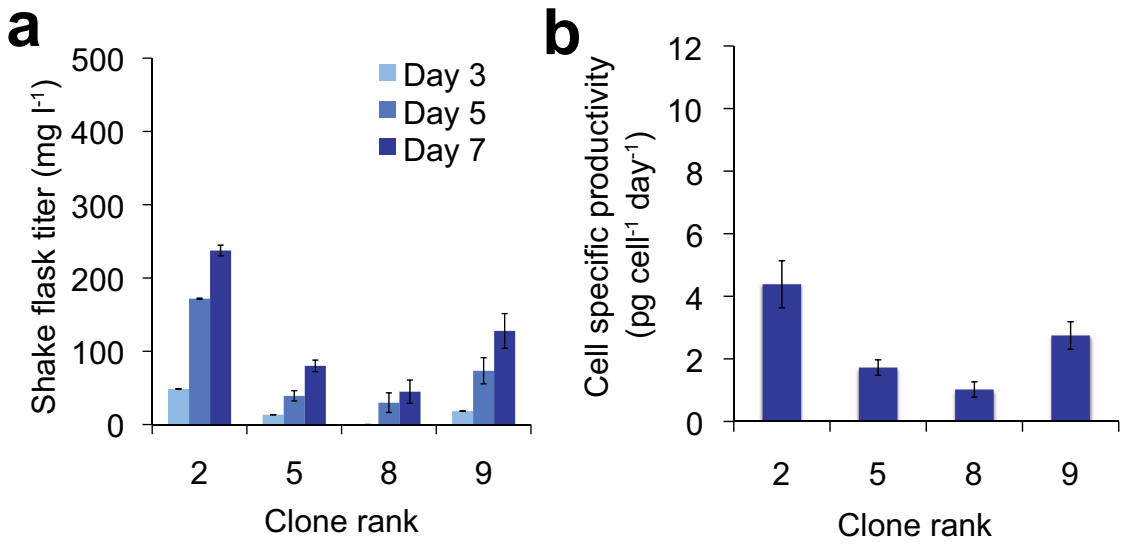


**Figure 4.13 Batch shake flask titers of eliminated clones**

Clones that scored high in the microfluidic assay but showed drops in productivity at the 24-well plate stage are presented. (**a**) Titers after 3, 5 and 7 days in culture ($n$ = 2 flasks; error bar, s.d.) and (**b**) cell specific productivities ($n$ = 2 flasks; error bar, s.d.) at day 5 are shown.

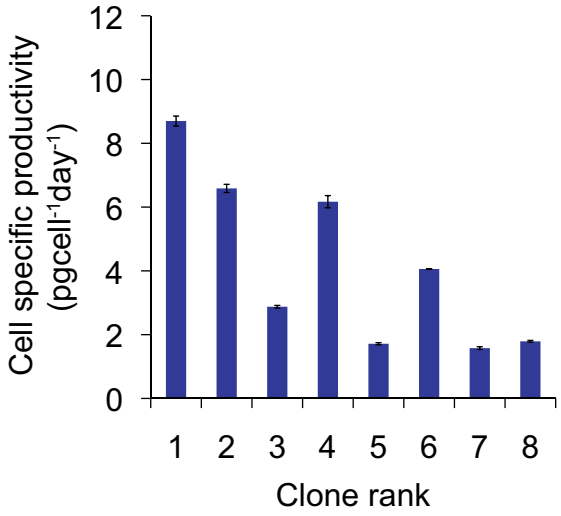


**Figure 4.14 Performance of clones selected by limiting dilution**

Two 96-well plates were screened using standard limiting dilution, resulting in 64 clones. Cell specific productivities after 5 days of batch shake flask culture are presented for the top 8 clones identified by limiting dilution ($n$ = 2 flasks; error bar, s.d.).

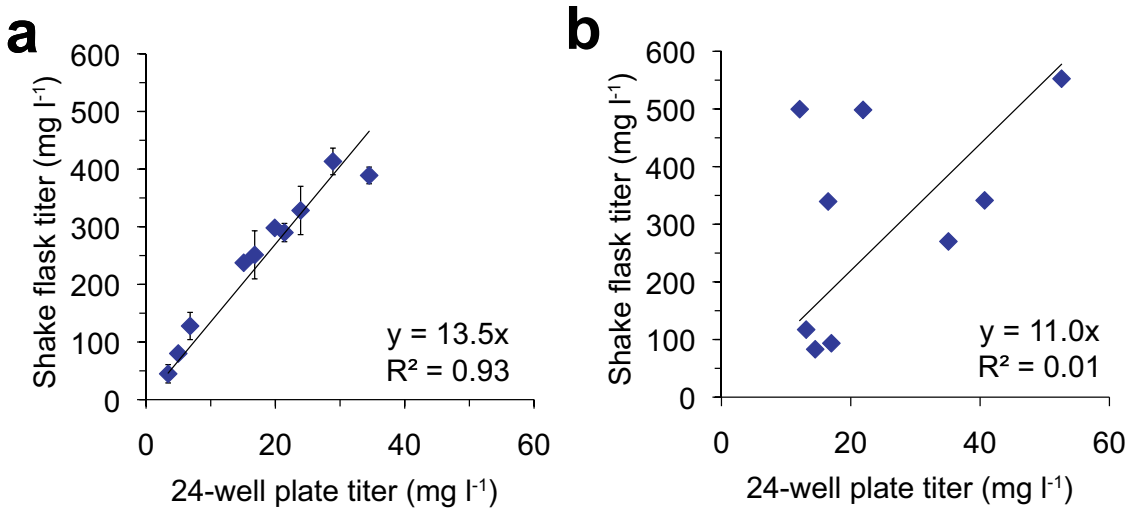


**Figure 4.15 Relationship between 24-well plate assay and batch shake flask titers using microfluidic and limiting dilution methods**

(**a**) Correlation between titers in 24-well plates and batch shake flask cultures from clones recovered from the microfluidic cell culture array ($n$ = 2 flasks; error bar, s.d.). (**b**) Correlation between titers in 24-well plates and batch shake flask cultures from clones generated by limiting dilution ($n$ = 2 flasks; error bar, s.d.).

# CHAPTER 5 Conclusions and Recommendations

Microfluidic technologies based on multilayer soft lithography have advanced at an impressive pace since the fabrication of the first micro-valve[17]. In the past decade, the field has grown from several proof-of-concept reports to a variety of practical applications allowing new biological insights to be revealed. Microfluidic gene expression analysis has progressed the most rapidly and has already been adopted by several laboratories[7,310] while cell culture applications have been much slower to develop into useful technologies. This is due in part to the limited accessibility of microfluidic cell culture systems outside of engineering laboratories but also to the reluctance of biologists to risk sacrificing rare and precious samples with an unproven technology. Living systems and mammalian cells in particular can be very sensitive to fluctuations in environmental conditions that are a more likely to occur in small volumes, hence making it difficult to obtain robust and reproducible data. This work has tackled this problem by providing solutions to the major hurdles limiting long-term microfluidic cell culture. In addition, the chamber design has allowed live suspension cells to be studied and characterized using features such as reagent exchange, live immunostaining, secretion assays, time-lapse imaging, genealogical tracing and cell recovery. The technology has enabled interesting discoveries in HSC biology to be made and has led to the establishment of a new method that facilitates the generation of clonal cell lines.

## 5.1 Significance of the Work

Creating an environment that can sustain normal cellular behavior is a critical step before attempting to address biological questions. Otherwise, cellular responses may be hard to distinguish under sub-optimal conditions

or worse, lead to erroneous conclusions. There are abundant reports on adherent cells cultivated in microfluidic devices but very limited progress had been made with suspension cells prior to this work. This research effort is the first demonstration of long-term clonal culture of mammalian suspension cells in microfluidic devices. We used HSC-enriched populations containing cytokine-dependent and sensitive cells as the most rigorous test to demonstrate our ability to perform mammalian cell culture, and showed that the microfluidic system can sustain normal cell viability and growth rates as well as stem cell function using *in vivo* CRU assays. These assays are the gold standard for assessing stem cell activity and among the most stringent methods for the analysis of mammalian cell properties. Most of the considerations presented to obtain robust microfluidic cell culture are also relevant to other cell types, including adherent cells, therefore increasing the impact of this work to a wide range of applications.

The establishment of a robust microfluidic system has allowed us to perform with confidence experiments involving small numbers of rare cells. The microfluidic cell culture platform has yielded new insights on factors regulating HSC cell cycle and survival *in vitro*. The ability to perform automated temporal stimulation and monitoring of clones has enabled experiments that would have been very hard to execute otherwise. This has led to the discovery that a high SF concentration is required for cell survival at the time of exit from quiescence, after which cells can no longer be rescued from low SF concentrations. Furthermore, tracking clonal cultures immediately after transduction with NA10hd has enabled the measurement of growth kinetics without interference from non-transduced cells, demonstrating that the increased stem cell expansion mediated by NA10hd overexpression is not due to reduced cell cycle times. We also found that *in vitro* persistence of EPCR in progeny derived from single cells could be an indicator of repopulating activity in a clone. By developing the right

analytical tools, we have shown that clonal studies with increased time-resolution can reveal interesting patterns in the genealogical pedigrees of these cells, for instance that cells from clones with persistent EPCR expression have longer cell cycle times and a more asynchroneous behavior that clones that have lost EPCR after *in vitro* culture.

For some cell types, the high cell concentrations reached in nanoliter-volume chambers is a problem that can generally be addressed by perfusion. We have shown that this limitation can be turned into an asset for other cell types (e.g. CHO cells) that do not thrive at low seeding concentrations and for which high levels of perfusion may be detrimental. In addition to the growth advantage conferred by small volumes, the rapid concentration of secreted proteins was exploited to reduce from weeks to hours the time required to reach detectable concentrations. These two features were combined to target the longest step in the race to large-scale production from a candidate mAb sequence, decreasing the workload of the otherwise tedious and cumbersome cell line selection process. We have demonstrated that the microfluidic cell culture array is not only a relevant tool for research but also a technology with great potential for industrial applications. This work has shown that robust microfluidic mammalian cell culture could be achieved and exploited to characterize clones in ways that would often not be possible using macroscale techniques.

## 5.2 Practical Considerations for Microfluidic Cell Culture

The integration of an iso-osmotic bath inside the device has been a key element to enable long-term culture of mammalian cells. Before the bath was introduced, cell viability and growth were both impaired and experiments were impossible to reproduce. The bath solved these issues, providing consistent results and growth performance that matched or exceeded

macroscale cultures. One hypothesis to explain the bath efficacy is that it serves as a reservoir that equilibrates with the medium to greatly reduce the amount of water vapor that would otherwise escape from the culture through highly gas-permeable PDMS. Priming the device for 1-2 days prior to cell loading in the microincubator with humidified air seemed to leave enough time for the vapor permeation equilibrium to be reached, and therefore prevent osmolarity shifts from occurring during cell culture. Mathematical modeling could be used to further characterize the system, for instance by identifying the minimum time required to reach this equilibrium and reduce the preparation time before each experiment. Since PDMS is also permeable to small hydrophobic molecules[98], the media-filled bath may also bring faster equilibrium of any small hydrophobic components in the cell culture medium. Replacing the bath with PBS could determine whether the loss of medium components in PDMS should really be a concern for mammalian cell culture.

Another benefit of the bath may be that it replaces a considerable amount of PDMS with culture medium, thereby reducing the flux of uncured molecules that could leach into the medium where they could be toxic for the cells[80]. In some cases PDMS has to be used at off-stochiometric ratios for multilayer bonding. However, the integration of 10:1 PDMS layers whenever possible using alternative bonding strategies such as stamping and plasma bonding can help minimize the levels of uncured molecules. The use of PDMS that has a short curing time (Sylgard 184, Dow Corning) combined with curing over multiple days, autoclaving and exchange of the priming culture medium prior to cell loading can together reduce the likelihood of generating a toxic culture environment. However, more methodical testing could be done to determine whether each of these steps is necessary. When setting up the system around the microfluidic device, special care should be taken to avoid using plastics, sealants or adhesives that could release toxic solvents. PTFE tubing is preferred to Tygon tubing for its low reactivity and low gas

permeability. Another key element to enable robust cell culture is to minimize perturbations from the surrounding environment as these can quickly propagate to small culture volumes. This can be achieved by enclosing the microscope and incubator in an opaque heated box, thereby shielding the microfluidic system from often-considerable laboratory temperature and humidity fluctuations.

Stress should also be minimized as much as possible during the cell loading process. Although other approaches may work as well, in our system controlling the pumping speed instead of using dead-end filling or pressure-driven flow and maintaining the right incubator temperature ensured that cells were intact when they entered the device. Likewise, inlet and outlets were both pressurized to avoid the formation of air bubbles. When working with small numbers of cells, these should be concentrated in the smallest volume possible for loading (<10 μl). Many cells will enter the device at the beginning of cell loading but those remaining will tend to concentrate at the end meniscus of the fluid line. Therefore, it is important to load the entire volume into the device to obtain a maximum number of cells. This can be done by replacing the empty tubing with new tubing filled with medium as soon as the fluid interface enters the stainless steel pin connected to the device, thereby pushing the cell contents with medium without introducing air into the device.

In many microfluidic cell culture reports, high perfusion rates have been used to mitigate evaporation and toxicity problems on adherent cells[74,258]. By following the techniques described above, batch cultures on CHO cells can be performed for at least 5 days with normal growth rates and without perfusion. However, there is a need to perform medium exchange for other cell types and applications. Perfusion of suspension cells can be difficult since it requires a trapping mechanism to immobilize the cells. The positioning of a small flow channel at the top of larger chambers with high

aspect ratio is a gentle and efficient way to retain clones by gravity while allowing medium exchange. This configuration also brings great flexibility to flow the reagents needed for assays such as live immunostaining or secretion bead immunocapture. In addition, the use of deep chambers enables the selective recovery of clones, an important feature for applications that require clonal expansion or subsequent *in vivo* analysis.

## 5.3 Future Directions

The microfluidic cell culture arrays presented in this work had sufficient flexibility to study and characterize different cellular systems. However, several technical improvements could be made to increase the reproducibility of the devices and facilitate full automation. For instance, the bottom layer containing the cell culture chambers is currently made of 5:1 PDMS. Uneven PDMS height and alignment of this layer during fabrication can cause distortions and lead to shifts in frames or focal planes. In addition, the presence of the PDMS layer underneath the cells limits the focal depth and generates background fluorescence at lower wavelengths, making it difficult to multiplex several fluorescent antibodies. In a recent review, Berthier *et al.* explains how PDMS causes challenges for mammalian cell culture in a field where polystyrene has been the standard for years[311]. Alternatives combining hot-embossed plastics with the flexibility of PDMS-based MSL could provide significant advantages. Chambers could instead be fabricated using a biocompatible, highly transparent thermoplastic (e.g. cyclin olefin polymer or copolymer) that could also replace the glass slide[312,313]. The use of plastic would enable greater reproducibility from device to device and facilitate its translation to a commercial product. The device mounted on plastic could be made entirely out of 10:1 PDMS using plasma bonding, thereby reducing the need for long curing periods required for cell culture on PDMS at off-stochiometric ratios.

We have shown that manual cell recovery is an efficient method to retrieve clones from the device. However, it requires highly trained personal with good technical skills and the speed of clone recovery (~30 clones $h^{-1}$) limits the number of clones that can be retrieved after each experiment. Increased standardization of device fabrication would facilitate the development of a cell recovery robot to automate clone retrieval. A robot would eliminate the potential for human errors and allow the microfluidic system to be operated by researchers with minimal training.

Abundant cell numbers are available when working with cells lines whereas purified primary cell populations are often much smaller, especially for rare cells sorted from precious clinical samples. Loading small numbers of cells (<1,000 cells) into the device with high efficiency can be difficult as they can be left in the multiwell or original tube, or lost in the inlet tubing, the channels and the inlet port. The design could be improved to enable better loading efficiency by either fabricating the inlet port at the same depth as the inlet channel, building inlet ports with a conical shape or integrating a pre-loading chamber where cells could be directly loaded into the device with a micropipette.

In this work, we have presented two devices, containing 1,600 and 6,144 chambers respectively. A number of applications such as cell line selection could benefit from higher throughput. The scalability of microfluidics could easily allow devices with up to 20,000 chambers to be designed and making smaller chambers than those presented in this work could further increase the throughput. However, the duration of experiments may be limited if cell counting is required since the cells would no longer be distinguishable in a monolayer past confluence. The current serial design allows a maximum number of chambers to be placed in a given area. However, it also means that content from upstream chambers goes through all downstream chambers. Since medium exchange occurred relatively

quickly, this configuration did not affect cellular behaviour and assays in this work. However, for applications where cross-contamination needs to be entirely avoided, a parallel configuration may be optimal. The device could also be modified to address each chamber individually, albeit these improvements would require a reduction of throughput.

Most immunostaining experiments were performed in small devices with only one inlet and one outlet. Multiple inlets could be added to fully automate the process and avoid manual exchange of reagent lines. The need for these modifications is specific to the cellular system being studied and the questions being asked by each experiment. The improvements suggested above would greatly facilitate the operation of the microfluidic platform. The development of user-friendly, automated and easy-to-operate systems is important to encourage the adoption of microfluidic cell culture platforms by more biologists[314].

Some of the experiments presented here could also have been done in microwell arrays. However, unique advantages of programmable microfluidic cell culture systems reside in the ability to perform automated reagent exchanges, temporal stimulation of cells and to increase effective concentrations by confining cells in small volumes. For instance, it was shown in Chapter 2 that HSCs could be rescued from low SF concentration before 16 h of culture. An interesting follow up experiment would be to expose cells to a pulse of high SF concentration between 16 and 24 h and see whether exposure to high SF concentration when most of the cells exit quiescence is sufficient to maintain survival. Lutolf and colleagues have shown that functionalizing microwells with ligands could lead to stem cell expansion[59,60]. Combining both temporal stimulation and surface-bound molecules could lead to a closer simulation of the stem cell niche.

Surface markers can provide information about the state of HSCs but only a fraction of proteins are expressed at the membrane surface. Some genes that are associated with stem cell activity are expressed internally, and fluorescent reporters, either transiently expressed or integrated into mice genome, would be powerful tools to combine with our microfluidic system. Reliable reporters could give new insights on the mechanisms of cytokine responses during self-renewal and differentiation. For instance, Schroeder and his group have demonstrated the instructive mechanism of cytokines in lineage choice by combining genealogical tracing of cells with fluorescent reporters[179]. An interesting experiment would be to perform genealogical tracing on normal and NA10hd-transduced cells, and then to evaluate if the HSC expansion characteristic of NA10hd cells results in more $EPCR^+$ clones with longer cell cycle times.

Microfluidic devices also are great tools to study autocrine and paracrine signaling[66,71]. The current designs could be adapted for such studies, for instance by placing multiple cells types in isolated chambers or eliminating cell-cell contact interactions by physically isolating cells in chambers while enabling diffusion of secreted factors through a connecting top flow channel. With proper surface coating, the microfluidic cell culture array could also be used to grow adherent cells, enabling the co-culture of different cell types. This approach could be employed for sensitive cellular systems requiring feeder cells or stimulation from other cell types.

The cell line selection platform presented in Chapter 4 has already received great interest from the biotechnology sector. As many patents are approaching their expiry date, a number of biosimilars are expected to enter the market[196,315]. The downward pressure on the price will force biotechnology companies to find innovative ways to produce these products at a lower cost. Tools to enable faster progression to market at lower expenses will be part of the solution. The cell line selection platform is one example on

how this cumbersome step can be simplified by screening large numbers of cells in conditions comparable to bioreactor cultures. Potentially, one could also look at the clonal distribution of secreted antibodies on a few hundreds cells to detect early signs of instability. There is a general trend in the industry to analyze clones in small fed-batch cultures as early as possible to accurately predict titers in fed-batch processes. Deep-well 96 well plates (e.g. BioLector, m2pLabs) and miniature bioreactors (e.g. ambr, TAPBiosystems) are examples of increasing popularity. Thanks to the high cell seeding concentration in nanovolume chambers, microfluidic devices could be used to start fed-batch cultures even at the single-cell level. Devices could be fabricated with feed chambers that could mimic fed-batch protocols. Clones would condition their own culture early in the process, potentially leading to better prediction of their performance in fed-batch cultures. The use of intracellular reporters of mAb expression would greatly ease the monitoring of cellular behavior in real-time using microfluidic systems[299].

The recent publication of the CHO genome will open new avenues for cell line engineering to generate mAb-producing clones with desired properties[316]. New technologies enabling site-specific integration are poised to be adopted by industry[202,204,317-319]. Zinc-finger endonucleases and targeted genome editing can lead to a high fraction of producing cells, therefore limiting the number of clones screened for cell line generation. These methods could also be designed to generate more stable cell lines. Some of the biotechnology industry leaders are already incorporating these strategies in their process development. However, current platforms are limited to one site of integration and therefore tend to yield lower productivities than clones generated by random integration[320]. Even with these technologies, variations in titers and stability are observed within populations and the need for clonal selection remains. The integration of multiple hot spots could lead to

increased titers in the future but the heterogeneity of CHO cells should remain a positive attribute to exploit.

Obtaining higher titers has long been a major goal in the industry. For most mAbs, current titers are sufficient and in some old facilities designed for much lower titers they do not even have the capacity to benefit from higher titers. Another priority is to obtain sufficient product quality. For biosimilars in particular, the clone selection criteria also require product quality attributes such as antibody binding affinity and glycosylation patterns. The bead immunocapture assay could be improved to assess mAb quality, for instance by using labeled antibodies against specific glycans and assessing binding characteristics using different labeled antigen concentrations[36]. Glycosylation patterns can be influenced by optimizing medium and culture conditions but it should be beneficial to start assessing product quality earlier in a high-throughput fashion under small-scale conditions similar to bioreactors.

The potential applications of this technology in immunology go beyond cell line selection. The platform could be used, for instance, to find rare activated T cells in co-culture with antigen-presenting dendritic cells by modifying the assay to screen for clones that are both proliferating and secreting IL-2. The microfluidic cell culture array could also be amenable to other antibody-producing cell types such as B cells and hybridomas. A modified platform with higher throughput could for instance be used to screen for rare antibody-secreting cells with the goal of finding new mAbs specific to relevant antigens. The platform could also be useful for directed evolution studies in B cells[321] by allowing rapid protein characterization and sub-cloning.

When designing microfluidic devices for new biological systems, it is strongly advisable to involve biologists early in the design process to make

devices capable of answering the right questions. Too often, engineers tend to develop technologies first and then try to find the right application for it. This work arose from a close collaboration with a strong team of stem cell biologists, whose input throughout the technology development phase has been an invaluable element for the success of this research effort. This project is a clear demonstration that interdisciplinary research is essential to bridge the gap between engineering and biology and to transform proof-of-concept ideas into technologies that can provide new biological findings.

# Bibliography


1 Dykstra, B., Kent, D., Bowie, M., McCaffrey, L., Hamilton, M., Lyons, K., Lee, S.J., Brinkman, R., & Eaves, C. Long-term propagation of distinct hematopoietic differentiation programs in vivo. *Cell Stem Cell*, 1(2), 218-229 (2007).

2 Graf, T. & Stadtfeld, M. Heterogeneity of embryonic and adult stem cells. *Cell Stem Cell*, 3(5), 480-483 (2008).

3 Narsinh, K.H., Sun, N., Sanchez-Freire, V., Lee, A.S., Almeida, P., Hu, S., Jan, T., Wilson, K.D., Leong, D., Rosenberg, J., Yao, M., Robbins, R.C., & Wu, J.C. Single cell transcriptional profiling reveals heterogeneity of human induced pluripotent stem cells. *Journal of Clinical Investigation*, 121(3), 1217-1221 (2011).

4 Fidler, I.J. Tumor heterogeneity and biology of cancer invasion and metastasis *Cancer Research*, 38(9), 2651-2660 (1978).

5 Anderson, K., Lutz, C., van Delft, F.W., Bateman, C.M., Guo, Y., Colman, S.M., Kempski, H., Moorman, A.V., Titley, I., Swansbury, J., Kearney, L., Enver, T., & Greaves, M. Genetic variegation of clonal architecture and propagating cells in leukaemia. *Nature*, 469(7330), 356-361 (2011).

6 Stockholm, D., Benchaouir, R., Picot, J., Rameau, P., Neildez, T.M.A., Landini, G., Laplace-Builhé, C., & Paldi, A. The origin of phenotypic heterogeneity in a clonal cell population in vitro. *PLoS One*, 2(4), e394 (2007).

7 Yin, H. & Marshall, D. Microfluidics for single cell analysis. *Current Opinion in Biotechnology*, 23(1), 110-119 (2012).

8 El-Ali, J., Sorger, P.K., & Jensen, K.F. Cells on chips. *Nature*, 442(7101), 403-411 (2006).

9 Stewart, M.D., Patterson, K., Somervell, M.H., & Willson, C.G. Organic imaging materials: a view of the future. *Journal of Physical Organic Chemistry*, 13(12), 767-774 (2000).

10 Xia, Y.N. & Whitesides, G.M. Soft lithography. *Annual Review of Materials Science*, 28, 153-184 (1998).

11 Duffy, D.C., McDonald, J.C., Schueller, O.J.A., & Whitesides, G.M. Rapid prototyping of microfluidic systems in poly(dimethylsiloxane). *Analytical Chemistry*, 70(23), 4974-4984 (1998).

12 Whitesides, G.M., Ostuni, E., Takayama, S., Jiang, X.Y., & Ingber, D.E. Soft lithography in biology and biochemistry. *Annual Review of Biomedical Engineering*, 3, 335-373 (2001).

13 Lee, J.N., Jiang, X., Ryan, D., & Whitesides, G.M. Compatibility of mammalian cells on surfaces of poly(dimethylsiloxane). *Langmuir*, 20(26), 11684-11691 (2004).

14 Ng, J.M.K., Gitlin, I., Stroock, A.D., & Whitesides, G.M. Components for integrated poly(dimethylsiloxane) microfluidic systems. *Electrophoresis*, 23(20), 3461-3473 (2002).

15 Sia, S.K. & Whitesides, G.M. Microfluidic devices fabricated in poly(dimethylsiloxane) for biological studies. *Electrophoresis*, 24(21), 3563-3576 (2003).

16 Thorsen, T., Maerkl, S.J., & Quake, S.R. Microfluidic large-scale integration. *Science*, 298(5593), 580-584 (2002).

17 Unger, M.A., Chou, H.P., Thorsen, T., Scherer, A., & Quake, S.R. Monolithic microfabricated valves and pumps by multilayer soft lithography. *Science*, 288(5463), 113-116 (2000).

18 Hansen, C. & Quake, S.R. Microfluidics in structural biology: smaller, faster... better. *Current Opinion in Structural Biology*, 13(5), 538-544 (2003).

19 Wu, M. & Singh, A.K. Single-cell protein analysis. *Current Opinion in Biotechnology*, 23(1), 83-88 (2012).

20 Zare, R.N. & Kim, S. Microfluidic platforms for single-cell analysis. *Annual Review of Biomedical Engineering*, 12, 187-201 (2010).

21 Guo, G., Huss, M., Tong, G.Q., Wang, C., Sun, L.L., Clarke, N.D., & Robson, P. Resolution of cell fate decisions revealed by single-cell gene expression analysis from zygote to blastocyst. *Developmental Cell*, 18(4), 675-685 (2010).

22 Yoo, A.S., Sun, A.X., Li, L., Shcheglovitov, A., Portmann, T., Li, Y., Lee-Messer, C., Dolmetsch, R.E., Tsien, R.W., & Crabtree, G.R. MicroRNA-mediated conversion of human fibroblasts to neurons. *Nature*, 476(7359), 228-231 (2011).

23 Dalerba, P., Kalisky, T., Sahoo, D. *et al.* Single-cell dissection of transcriptional heterogeneity in human colon tumors. *Nature Biotechnology*, 29(12), 1120-1127 (2011).

24 Diehn, M., Cho, R.W., Lobo, N.A. *et al.* Association of reactive oxygen species levels and radioresistance in cancer stem cells. *Nature*, 458(7239), 780-783 (2009).

25 Petriv, O., Kuchenbauer, F., Delaney, A. *et al.* Comprehensive microRNA expression profiling of the hematopoietic hierarchy. *Proceedings of the National Academy of Sciences of the United States of America*, 107(35), 15443-15448 (2010).

26 White, A.K., VanInsberghe, M., Petriv, O.I., Hamidi, M., Sikorski, D., Marra, M.A., Piret, J., Aparicio, S., & Hansen, C.L. High-throughput microfluidic single-cell RT-qPCR. *Proceedings of the National Academy of Sciences of the United States of America*, 108(34), 13999-14004 (2011).

27 Spike, B.T., Engle, D.D., Lin, J.C., Cheung, S.K., La, J., & Wahl, G.M. A mammary stem cell population identified and characterized in late embryogenesis reveals similarities to human breast cancer. *Cell Stem Cell*, 10(2), 183-197 (2012).

28 Glotzbach, J.P., Januszyk, M., Vial, I.N., Wong, V.W., Gelbard, A., Kalisky, T., Thangarajah, H., Longaker, M.T., Quake, S.R., Chu, G., & Gurtner, G.C. An information theoretic, microfluidic-based single cell analysis permits identification of subpopulations among putatively homogeneous stem cells. *PLoS One*, 6(6), 10 (2011).

29 Navin, N., Kendall, J., Troge, J., Andrews, P., Rodgers, L., McIndoo, J., Cook, K., Stepansky, A., Levy, D., Esposito, D., Muthuswamy, L., Krasnitz, A., McCombie, W.R., Hicks, J., & Wigler, M. Tumour evolution inferred by single-cell sequencing. *Nature*, 472(7341), 90-94 (2011).

30 Fan, H.C., Wang, J., Potanina, A., & Quake, S.R. Whole-genome molecular haplotyping of single cells. *Nature Biotechnology*, 29(1), 51-57 (2011).

31 Blainey, P.C., Mosier, A.C., Potanina, A., Francis, C.A., & Quake, S.R. Genome of a low-salinity ammonia-oxidizing archaeon determined by single-cell and metagenomic analysis. *PLoS One*, 6(2), e16626 (2011).

32 Leung, K., Zahn, H., Leaver, T., Konwar, K.M., Hanson, N.W., Pagé, A.P., Lo, C.-C., Chain, P.S., Hallam, S.J., & Hansen, C.L. A

programmable droplet-based microfluidic device applied to multiparameter analysis of single microbes and microbial communities. *Proceedings of the National Academy of Sciences*, 109(20), 7665-7670 (2012).

33 Taniguchi, Y., Choi, P., Li, G., Chen, H., Babu, M., Hearn, J., Emili, A., & Xie, X. Quantifying E-coli proteome and transcriptome with single-molecule sensitivity in single cells. *Science*, 329(5991), 533-538 (2010).

34 Love, J.C., Ronan, J.L., Grotenbreg, G.M., van der Veen, A.G., & Ploegh, H.L. A microengraving method for rapid selection of single cells producing antigen-specific antibodies. *Nature Biotechnology*, 24(6), 703-707 (2006).

35 Love, K.R., Panagiotou, V., Jiang, B., Stadheim, T.A., & Love, J.C. Integrated single-cell analysis shows Pichia pastoris secretes protein stochastically. *Biotechnology and Bioengineering*, 106(2), 319-325 (2010).

36 Singhal, A., Haynes, C.A., & Hansen, C.L. Microfluidic measurement of antibody-antigen binding kinetics from low-abundance samples and single cells. *Analytical Chemistry*, 82(20), 8671-8679 (2010).

37 Ma, C., Fan, R., Ahmad, H., Shi, Q., Comin-Anduix, B., Chodon, T., Koya, R.C., Liu, C.-C., Kwong, G.A., Radu, C.G., Ribas, A., & Heath, J.R. A clinical microchip for evaluation of single immune cells reveals high functional heterogeneity in phenotypically similar T cells. *Nature Medicine*, 17(6), 738-743 (2011).

38 Shi, Q., Qin, L., Wei, W., Geng, F., Fan, R., Shin, Y.S., Guo, D., Hood, L., Mischel, P.S., & Heath, J.R. Single-cell proteomic chip for profiling intracellular signaling pathways in single tumor cells. *Proceedings of the National Academy of Sciences of the United States of America*, 109(2), 419-424 (2011).

39 Koester, S., Angile, F.E., Duan, H., Agresti, J.J., Wintner, A., Schmitz, C., Rowat, A.C., Merten, C.A., Pisignano, D., Griffiths, A.D., & Weitz, D.A. Drop-based microfluidic devices for encapsulation of single cells. *Lab on a Chip*, 8(7), 1110-1115 (2008).

40 Konry, T., Dominguez-Villar, M., Baecher-Allan, C., Hafler, D.A., & Yarmush, M.L. Droplet-based microfluidic platforms for single T cell secretion analysis of IL-10 cytokine. *Biosensors & Bioelectronics*, 26(5), 2707-2710 (2011).

41 Brouzes, E., Medkova, M., Savenelli, N., Marran, D., Twardowski, M., Hutchison, J.B., Rothberg, J.M., Link, D.R., Perrimon, N., & Samuels, M.L. Droplet microfluidic technology for single-cell high-throughput screening. *Proceedings of the National Academy of Sciences of the United States of America*, 106(34), 14195-14200 (2009).

42 Paliwal, S., Iglesias, P.A., Campbell, K., Hilioti, Z., Groisman, A., & Levchenko, A. MAPK-mediated bimodal gene expression and adaptive gradient sensing in yeast. *Nature*, 446(7131), 46-51 (2007).

43 Bennett, M.R., Pang, W.L., Ostroff, N.A., Baumgartner, B.L., Nayak, S., Tsimring, L.S., & Hasty, J. Metabolic gene regulation in a dynamically changing environment. *Nature*, 454(7208), 1119-1122 (2008).

44 Hersen, P., McClean, M.N., Mahadevan, L., & Ramanathan, S. Signal processing by the HOG MAP kinase pathway. *Proceedings of the National Academy of Sciences of the United States of America*, 105(20), 7165-7170 (2008).

45 Taylor, R.J., Falconnet, D., Niemisto, A., Ramsey, S.A., Prinz, S., Shmulevich, I., Galitski, T., & Hansen, C.L. Dynamic analysis of MAPK signaling using a high-throughput microfluidic single-cell imaging platform. *Proceedings of the National Academy of Sciences of the United States of America*, 106(10), 3758-3763 (2009).

46 Falconnet, D., Niemisto, A., Taylor, R.J., Ricicova, M., Galitski, T., Shmulevich, I., & Hansen, C.L. High-throughput tracking of single yeast cells in a microfluidic imaging matrix. *Lab on a Chip*, 11(3), 466-473 (2011).

47 Rowat, A.C., Bird, J.C., Agresti, J.J., Rando, O.J., & Weitz, D.A. Tracking lineages of single cells in lines using a microfluidic device. *Proceedings of the National Academy of Sciences of the United States of America*, 106(43), 18149-18154 (2009).

48 Godin, M., Delgado, F.F., Son, S.M., Grover, W.H., Bryan, A.K., Tzur, A., Jorgensen, P., Payer, K., Grossman, A.D., Kirschner, M.W., & Manalis, S.R. Using buoyant mass to measure the growth of single cells. *Nature Methods*, 7(5), 387-390 (2010).

49 Son, S., Tzur, A., Weng, Y., Jorgensen, P., Kim, J., Kirschner, M.W., & Manalis, S.R. Direct observation of mammalian cell growth and size regulation. *Nature Methods*, 9(9), 910-912 (2012).

50 Grover, W.H., Bryan, A.K., Diez-Silva, M., Suresh, S., Higgins, J.M., & Manalis, S.R. Measuring single-cell density. *Proceedings of the National Academy of Sciences of the United States of America*, 108(27), 10992-10996 (2011).

51 Tokimitsu, Y., Kishi, H., Kondo, S., Honda, R., Tajiri, K., Motoki, K., Ozawa, T., Kadowaki, S., Obata, T., Fujiki, S., Tateno, C., Takaishi, H., Chayama, K., Yoshizato, K., Tamiya, E., Sugiyama, T., & Muraguchi, A. Single lymphocyte analysis with a microwell array chip. *Cytometry Part A*, 71A(12), 1003-1010 (2007).

52 Rettig, J.R. & Folch, A. Large-scale single-cell trapping and imaging using microwell arrays. *Analytical Chemistry*, 77(17), 5628-5634 (2005).

53 Deutsch, M., Deutsch, A., Shirihai, O., Hurevich, I., Afrimzon, E., Shafran, Y., & Zurgil, N. A novel miniature cell retainer for correlative high-content analysis of individual untethered non-adherent cells. *Lab on a Chip*, 6(8), 995-1000 (2006).

54 Revzin, A., Sekine, K., Sin, A., Tompkins, R.G., & Toner, M. Development of a microfabricated cytometry platform for characterization and sorting of individual leukocytes. *Lab on a Chip*, 5(1), 30-37 (2005).

55 Dykstra, B., Ramunas, J., Kent, D., McCaffrey, L., Szumsky, E., Kelly, L., Farn, K., Blaylock, A., Eaves, C., & Jervis, E. High-resolution video monitoring of hematopoietic stem cells cultured in single-cell arrays identifies new features of self-renewal. *Proceedings of the National Academy of Sciences of the United States of America*, 103(21), 8185-8190 (2006).

56 Chen, H., Li, J., Zhang, H., Li, M., Rosengarten, G., & Nordon, R.E. Microwell perfusion array for high-throughput, long-term imaging of clonal growth. *Biomicrofluidics*, 5(4) (2011).

57 Chin, V.I., Taupin, P., Sanga, S., Scheel, J., Gage, F.H., & Bhatia, S.N. Microfabricated platform for studying stem cell fates. *Biotechnology and Bioengineering*, 88(3), 399-415 (2004).

58 Guldevall, K., Vanherberghen, B., Frisk, T., Hurtig, J., Christakou, A.E., Manneberg, O., Lindstrom, S., Andersson-Svahn, H., Wiklund, M., & Onfelt, B. Imaging immune surveillance of individual natural killer cells confined in microwell arrays. *PLoS One*, 5(11) (2012).

59 Lutolf, M.P., Doyonnas, R., Havenstrite, K., Koleckar, K., & Blau, H.M. Perturbation of single hematopoietic stem cell fates in artificial niches. *Integrative Biology*, 1(1), 59-69 (2009).

60 Gobaa, S., Hoehnel, S., Roccio, M., Negro, A., Kobel, S., & Lutolf, M.P. Artificial niche microarrays for probing single stem cell fate in high throughput. *Nature Methods*, 8(11), 949-955 (2011).

61 Tay, S., Hughey, J.J., Lee, T.K., Lipniacki, T., Quake, S.R., & Covert, M.W. Single-cell NF-kappa B dynamics reveal digital activation and analogue information processing. *Nature*, 466(7303), 267-271 (2010).

62 Cheong, R., Wang, C.J., & Levchenko, A. High content cell screening in a microfluidic device. *Molecular & Cellular Proteomics*, 8(3), 433-442 (2009).

63 Fosbrink, M., Aye-Han, N.N., Cheong, R., Levchenko, A., & Zhang, J. Visualization of JNK activity dynamics with a genetically encoded fluorescent biosensor. *Proceedings of the National Academy of Sciences of the United States of America*, 107(12), 5459-5464 (2010).

64 Gomez-Sjoberg, R., Leyrat, A.A., Pirone, D.M., Chen, C.S., & Quake, S.R. Versatile, fully automated, microfluidic cell culture system. *Analytical Chemistry*, 79(22), 8557-8563 (2007).

65 Toh, Y.C., Zhang, C., Zhang, J., Khong, Y.M., Chang, S., Samper, V.D., van Noort, D., Hutmacher, D.W., & Yu, H.R. A novel 3D mammalian cell perfusion-culture system in microfluidic channels. *Lab on a Chip*, 7(3), 302-309 (2007).

66 Moledina, F., Clarke, G., Oskooei, A., Onishi, K., Gunther, A., & Zandstra, P.W. Predictive microfluidic control of regulatory ligand trajectories in individual pluripotent cells. *Proceedings of the National Academy of Sciences of the United States of America*, 109(9), 3264-3269 (2012).

67 Albrecht, D.R., Underhill, G.H., Resnikoff, J., Mendelson, A., Bhatia, S.N., & Shah, J.V. Microfluidics-integrated time-lapse imaging for analysis of cellular dynamics. *Integrative Biology*, 2(5-6), 278-287 (2010).

68 Kamei, K.I., Guo, S.L., Yu, Z.T.F., Takahashi, H., Gschweng, E., Suh, C., Wang, X.P., Tang, J.G., McLaughlin, J., Witte, O.N., Lee, K.B., & Tseng, H.R. An integrated microfluidic culture device for quantitative analysis of human embryonic stem cells. *Lab on a Chip*, 9(4), 555-563 (2009).

69 Blagovic, K., Kim, L.L.Y., & Voldman, J. Microfluidic perfusion for regulating diffusible signaling in stem cells. *PLoS One*, 6(8), 11 (2011).

70 Przybyla, L.M. & Voldman, J. Attenuation of extrinsic signaling reveals the importance of matrix remodeling on maintenance of embryonic stem cell self-renewal. *Proceedings of the National Academy of Sciences of the United States of America*, 109(3), 835-840 (2012).

71 Tumarkin, E., Tzadu, L., Csaszar, E., Seo, M., Zhang, H., Lee, A., Peerani, R., Purpura, K., Zandstra, P.W., & Kumacheva, E. High-throughput combinatorial cell co-culture using microfluidics. *Integrative Biology*, 3(6), 653-662 (2011).

72 Balagadde, F.K., You, L.C., Hansen, C.L., Arnold, F.H., & Quake, S.R. Long-term monitoring of bacteria undergoing programmed population control in a microchemostat. *Science*, 309(5731), 137-140 (2005).

73 Mirzaei, M., Pla-Roca, M., Safavieh, R., Nazarova, E., Safavieh, M., Li, H., Vogel, J., & Juncker, D. Microfluidic perfusion system for culturing and imaging yeast cell microarrays and rapidly exchanging media. *Lab on a Chip*, 10(18), 2449-2457 (2010).

74 Gomez-Sjoberg, R., Leyrat, A.A., Pirone, D.M., Chen, C.S., & Quake, S.R. Versatile, fully automated, microfluidic cell culture system. *Analytical Chemistry*, 79, 8557-8563 (2007).

75 Lee, P.J., Hung, P.J., Rao, V.M., & Lee, L.P. Nanoliter scale microbioreactor array for quantitative cell biology. *Biotechnology and Bioengineering*, 94(1), 5-14 (2006).

76 Wang, Z.H., Kim, M.C., Marquez, M., & Thorsen, T. High-density microfluidic arrays for cell cytotoxicity analysis. *Lab on a Chip*, 7(6), 740-745 (2007).

77 Mehta, G., Kiel, M.J., Lee, J.W., Kotov, N., Linderman, J.J., & Takayama, S. Polyelectrolyte-clay-protein layer films on microfluidic PDMS bioreactor surfaces for primary murine bone marrow culture. *Advanced Functional Materials*, 17(15), 2701-2709 (2007).

78 Korin, N., Bransky, A., Dinnar, U., & Levenberg, S. Periodic "flow-stop" perfusion microchannel bioreactors for mammalian and human embryonic stem cell long-term culture. *Biomedical Microdevices*, 11(1), 87-94 (2009).

79 Lin, Z., Cherng-Wen, T., Roy, P., & Trau, D. In-situ measurement of cellular microenvironments in a microfluidic device. *Lab on a Chip*, 9(2), 257-262 (2009).

80 Millet, L.J., Stewart, M.E., Sweedler, J.V., Nuzzo, R.G., & Gillette, M.U. Microfluidic devices for culturing primary mammalian neurons at low densities. *Lab on a Chip*, 7(8), 987-994 (2007).

81 Wang, L., Ni, X.F., Luo, C.X., Zhang, Z.L., Pang, D.W., & Chen, Y. Self-loading and cell culture in one layer microfluidic devices. *Biomedical Microdevices*, 11(3), 679-684 (2009).

82 Ziolkowska, K., Jedrych, E., Kwapiszewski, R., Lopacinska, J., Skolimowski, M., & Chudy, M. PDMS/glass microfluidic cell culture system for cytotoxicity tests and cells passage. *Sensors and Actuators B-Chemical*, 145(1), 533-542 (2010).

83 Paguirigan, A.L. & Beebe, D.J. From the cellular perspective: exploring differences in the cellular baseline in macroscale and microfluidic cultures. *Integrative Biology*, 1(2), 182-195 (2009).

84 Mehta, G., Mehta, K., Sud, D., Song, J.W., Bersano-Begey, T., Futai, N., Heo, Y.S., Mycek, M.A., Linderman, J.J., & Takayama, S. Quantitative measurement and control of oxygen levels in microfluidic poly(dimethylsiloxane) bioreactors during cell culture. *Biomedical Microdevices*, 9(2), 123-134 (2007).

85 Shiku, H., Saito, T., Wu, C.C., Yasukawa, T., Yokoo, M., Abe, H., Matsue, T., & Yamada, H. Oxygen permeability of surface-modified poly(dimethylsiloxane) characterized by scanning electrochemical microscopy. *Chemistry Letters*, 35(2), 234-235 (2006).

86 Favre, E., Schaetzel, P., Nguygen, Q.T., Clement, R., & Neel, J. Sorption, diffusion and vapor permeation of various penetrants through dense poly(dimethylsiloxane) membranes - A transport analysis. *Journal of Membrane Science*, 92(2), 169-184 (1994).

87 Randall, G.C. & Doyle, P.S. Permeation-driven flow in poly(dimethylsiloxane) microfluidic devices. *Proceedings of the National Academy of Sciences of the United States of America*, 102(31), 10813-10818 (2005).

88 Watson, J.M. & Baron, M.G. The behaviour of water in poly(dimethylsiloxane). *Journal of Membrane Science*, 110(1), 47-57 (1996).

89 Takagi, M., Hayashi, H., & Yoshida, T. The effect of osmolarity on metabolism and morphology in adhesion and suspension chinese hamster ovary cells producing tissue plasminogen activator. *Cytotechnology*, 32(3), 171-179 (2000).

90 Ozturk, S.S. & Palsson, B.O. Effect of medium osmolarity on hybridoma growth, metabolism and antibody production. *Biotechnology and Bioengineering*, 37(10), 989-993 (1991).

91 Heo, Y.S., Cabrera, L.M., Song, J.W., Futai, N., Tung, Y.C., Smith, G.D., & Takayama, S. Characterization and resolution of evaporation-mediated osmolality shifts that constrain microfluidic cell culture in poly(dimethylsiloxane) devices. *Analytical Chemistry*, 79(3), 1126-1134 (2007).

92 Swain, J.E., Cabrera, L., Xu, X., & Smith, G.D. Microdrop preparation factors influence culture-media osmolality, which can impair mouse embryo preimplantation development. *Reproductive Biomedicine Online*, 24(2), 142-147 (2011).

93 Miyoshi, K., Abeydeera, L.R., Okuda, K., & Niwa, K. Effects of osmolarity and amino acids in a chemically-defined medium on devleopment of rat one-cell embryos. *Journal of Reproduction and Fertility*, 103(1), 27-32 (1995).

94 Mata, A., Fleischman, A.J., & Roy, S. Characterization of polydimethylsiloxane (PDMS) properties for biomedical micro/nanosystems. *Biomedical Microdevices*, 7(4), 281-293 (2005).

95 Walker, G.M., Zeringue, H.C., & Beebe, D.J. Microenvironment design considerations for cellular scale studies. *Lab on a Chip*, 4(2), 91-97 (2004).

96 Regehr, K.J., Domenech, M., Koepsel, J.T., Carver, K.C., Ellison-Zelski, S.J., Murphy, W.L., Schuler, L.A., Alarid, E.T., & Beebe, D.J. Biological implications of polydimethylsiloxane-based microfluidic cell culture. *Lab on a Chip*, 9(15), 2132-2139 (2009).

97 Zheng, C.H., Chen, G.E., Pang, Y.H., & Huang, Y.Y. An integrated microfluidic device for long-term culture of isolated single mammalian cells. *Science China-Chemistry*, 55(4), 502-507 (2012).

98 Toepke, M.W. & Beebe, D.J. PDMS absorption of small molecules and consequences in microfluidic applications. *Lab on a Chip*, 6(12), 1484-1486 (2006).

99 Wang, J.D., Douville, N.J., Takayama, S., & Elsayed, M. Quantitative analysis of molecular absorption into PDMS microfluidic channels. *Annals of biomedical engineering*, 40(9), 1862-1873 (2012).

100 Lee, J.N., Park, C., & Whitesides, G.M. Solvent compatibility of poly(dimethylsiloxane)-based microfluidic devices. *Analytical Chemistry*, 75(23), 6544-6554 (2003).

101 Kraghhansen, U. Molecular aspects of ligand-binding to serum-albumin. *Pharmacological Reviews*, 33(1), 17-53 (1981).

102 Chumbimuni-Torres, K.Y., Coronado, R.E., Mfuh, A.M., Castro-Guerrero, C., Silva, M.F., Negrete, G.R., Bizios, R., & Garcia, C.D. Adsorption of proteins to thin-films of PDMS and its effect on the adhesion of human endothelial cells. *RSC Advances*, 1(4), 706-714 (2011).

103 Barbulovic-Nad, I., Au, S.H., & Wheeler, A.R. A microfluidic platform for complete mammalian cell culture. *Lab on a Chip*, 10(12), 1536-1542 (2010).

104 Hufnagel, H., Huebner, A., Gulch, C., Guse, K., Abell, C., & Hollfelder, F. An integrated cell culture lab on a chip: modular microdevices for cultivation of mammalian cells and delivery into microfluidic microdroplets. *Lab on a Chip*, 9(11), 1576-1582 (2009).

105 Wang, H.Y., Bao, N., & Lu, C. A microfluidic cell array with individually addressable culture chambers. *Biosensors & Bioelectronics*, 24(4), 613-617 (2008).

106 Orkin, S.H. & Zon, L.I. Hematopoiesis: An evolving paradigm for stem cell biology. *Cell*, 132(4), 631-644 (2008).

107 Ogawa, M., Porter, P.N., & Nakahata, T. Renewal and commitment to differentiation of hamatopoietic stem cells (an interpretive review). *Blood*, 61(5), 823-829 (1983).

108 Kondo, M., Wagers, A.J., Manz, M.G., Prohaska, S.S., Scherer, D.C., Beilhack, G.E., Shizuru, J.A., & Weissman, I.L. Biology of hematopoietic stem cells and progenitors: Implications for clinical application. *Annual Review of Immunology*, 21, 759-806 (2003).

109 Doulatov, S., Notta, F., Eppert, K., Nguyen, L.T., Ohashi, P.S., & Dick, J.E. Revised map of the human progenitor hierarchy shows the origin of macrophages and dendritic cells in early lymphoid development. *Nature Immunology*, 11(7), 585-593 (2010).

110 Kawamoto, H. & Katsura, Y. A new paradigm for hematopoietic cell lineages: revision of the classical concept of the myeloid-lymphoid dichotomy. *Trends in Immunology*, 30(5), 193-200 (2009).

111 Brown, G., Hughes, P.J., Michell, R.H., Rolink, A.G., & Ceredig, R. The sequential determination model of hematopoiesis. *Trends in Immunology*, 28, 442-448 (2007).

112 Ceredig, R., Rolink, A.G., & Brown, G. Models of haematopoiesis: seeing the wood for the trees. *Nature Reviews Immunology*, 9(4), 293-300 (2009).

113 Glauche, I., Cross, M., Loeffler, M., & Roeder, I. Lineage specification of hematopoietic stem cells: Mathematical modeling and biological implications. *Stem Cells*, 25(7), 1791-1799 (2007).

114 Palani, S. & Sarkar, C.A. Integrating extrinsic and intrinsic cues into a minimal model of lineage commitment for hematopoietic progenitors. *PLoS Computational Biology*, 5(9), e1000518 (2009).

115 Shapiro, M.J. & Shapiro, V.S. Transcriptional repressors, corepressors and chromatin modifying enzymes in T cell development. *Cytokine*, 53(3), 271-281 (2011).

116 Laslo, P., Spooner, C.J., Warmflash, A., Lancki, D.W., Lee, H.-J., Sciammas, R., Gantner, B.N., Dinner, A.R., & Singh, H. Multilineage transcriptional priming and determination of alternate hematopoietic cell fates. *Cell*, 126(4), 755-766 (2006).

117 Trompouki, E., Bowman, T.V., Lawton, L.N., Fan, Z.P., Wu, D.-C., DiBiase, A., Martin, C.S., Cech, J.N., Sessa, A.K., Leblanc, J.L., Li, P., Durand, E.M., Mosimann, C., Heffner, G.C., Daley, G.Q., Paulson, R.F., Young, R.A., & Zon, L.I. Lineage regulators direct BMP and Wnt pathways to cell-specific programs during differentiation and regeneration. *Cell*, 147(3), 577-589 (2011).

118 El Gazzar, M. & McCall, C.E. MicroRNAs regulatory networks in myeloid lineage development and differentiation: regulators of the regulators. *Immunology and Cell Biology*, 90(6), 587-593 (2012).

119 Reavie, L., Della Gatta, G., Crusio, K., Aranda-Orgilles, B., Buckley, S.M., Thompson, B., Lee, E., Gao, J., Bredemeyer, A.L., Helmink, B.A., Zavadil, J., Sleckman, B.P., Palomero, T., Ferrando, A., & Aifantis, I. Regulation of hematopoietic stem cell differentiation by a single ubiquitin ligase-substrate complex. *Nature Immunology*, 11(3), 207-U203 (2010).

120 Bruno, B., Rotta, M., Patriarca, F. *et al.* A comparison of allografting with autografting for newly diagnosed myeloma. *New England Journal of Medicine*, 356(11), 1110-1120 (2007).

121 Borgmann, A., Schmid, H., Hartmann, R., Baumgarten, E., Hermann, K., Klingebiel, T., Ebell, W., Zintl, F., Gadner, H., & Henze, G. Autologous bone-marrow transplants compared with chemotherapy for children with acute lymphoblastic-leukemia in a 2nd remission - a matched-pair analysis. *Lancet*, 346(8979), 873-876 (1995).

122 Cavazzana-Calvo, M., Hacein-Bey, S., Basile, C.D., Gross, F., Yvon, E., Nusbaum, P., Selz, F., Hue, C., Certain, S., Casanova, J.L., Bousso, P., Le Deist, F., & Fischer, A. Gene therapy of human severe combined immunodeficiency (SCID)-X1 disease. *Science*, 288(5466), 669-672 (2000).

123 Hacein-Bey-Abina, S., Von Kalle, C., Schmidt, M. *et al.* LMO2-associated clonal T cell proliferation in two patients after gene therapy for SCID-X1. *Science*, 302(5644), 415-419 (2003).

124 Morrison, S.J., Hemmati, H.D., Wandycz, A.M., & Weissman, I.L. The purification and characterization of fetal liver hematopoietic stem cells. *Proceedings of the National Academy of Sciences of the United States of America*, 92(22), 10302-10306 (1995).

125 Richman, C.M., Weiner, R.S., & Yankee, R.A. Increase in circulating stem-cells following chemotherapy in man. *Blood*, 47(6), 1031-1039 (1976).

126 Morrison, S.J., Wright, D.E., & Weissman, I.L. Cyclophosphamide/granulocyte colony-stimulating factor induces hematopoietic stem cells to proliferate prior to mobilization. *Proceedings of the National Academy of Sciences of the United States of America*, 94(5), 1908-1913 (1997).

127 Wilson, A. & Trumpp, A. Bone-marrow haematopoietic-stem-cell niches. *Nature Reviews Immunology*, 6(2), 93-106 (2006).

128 Garrett, R.W. & Emerson, S.G. Bone and blood vessels: The hard and the soft of hematopoietic stem cell niches. *Cell Stem Cell*, 4(6), 503-506 (2009).

129 Adams, G.B. & Scadden, D.T. The hematopoietic stem cell in its place. *Nature Immunology*, 7(4), 333-337 (2006).

130 Petzer, A.L., Zandstra, P.W., Piret, J.M., & Eaves, C.J. Differential cytokine effects on primitive (CD34+CD38(-)) human hematopoietic cells: Novel responses to Flt3-ligand and thrombopoietin. *Journal of Experimental Medicine*, 183(6), 2551-2558 (1996).

131 Bhatia, M., Bonnet, D., Kapp, U., Wang, J.C.Y., Murdoch, B., & Dick, J.E. Quantitative analysis reveals expansion of human hematopoietic repopulating cells after short-term ex vivo culture. *Journal of Experimental Medicine*, 186(4), 619-624 (1997).

132 Zandstra, P.W., Conneally, E., Petzer, A.L., Piret, J.M., & Eaves, C.J. Cytokine manipulation of primitive human hematopoietic cell self-renewal. *Proceedings of the National Academy of Sciences of the United States of America*, 94(9), 4698-4703 (1997).

133 Audet, J., Zandstra, P.W., Eaves, C.J., & Piret, J.M. Advances in hematopoietic stem cell culture. *Current Opinion in Biotechnology*, 9(2), 146-151 (1998).

134 Audet, J., Miller, C.L., Eaves, C.J., & Piret, J.M. Common and distinct features of cytokine effects on hematopoietic stem and progenitor cells revealed by dose-response surface analysis. *Biotechnology and Bioengineering*, 80(4), 393-404 (2002).

135 Delaney, C., Heimfeld, S., Brashem-Stein, C., Voorhies, H., Manger, R.L., & Bernstein, I.D. Notch-mediated expansion of human cord blood progenitor cells capable of rapid myeloid reconstitution. *Nature Medicine*, 16(2), 232-236 (2010).

136 Zon, L.I. Intrinsic and extrinsic control of haematopoietic stem-cell self-renewal. *Nature*, 453(7193), 306-313 (2008).

137 Deneault, E., Cellot, S., Faubert, A., Laverdure, J.P., Frechette, M., Chagraoui, J., Mayotte, N., Sauvageau, M., Ting, S.B., & Sauvageau, G. A functional screen to identify novel effectors of hematopoietic stem cell activity. *Cell*, 137(2), 369-379 (2009).

138 Argiropoulos, B. & Humphries, R.K. Hox genes in hematopoiesis and leukemogenesis. *Oncogene*, 26(47), 6766-6776 (2007).

139 Pineault, N., Abramovich, C., Ohta, H., & Humphries, R.K. Differential and common leukemogenic potentials of multiple NUP98-Hox fusion proteins alone or with Meis1. *Molecular and Cellular Biology*, 24(5), 1907-1917 (2004).

140 Pineault, N., Abramovich, C., & Humphries, R.K. Transplantable cell lines generated with NUP98-Hox fusion genes undergo leukemic progression by Meis1 independent of its binding to DNA. *Leukemia*, 19(4), 636-643 (2005).

141 Ohta, H., Sekulovic, S., Bakovic, S., Eaves, C.J., Pineault, N., Gasparetto, M., Smith, C., Sauvageau, G., & Humphries, R.K. Near-maximal expansions of hematopoietic stem cells in culture using NUP98-HOX fusions. *Experimental Hematology*, 35(5), 817-830 (2007).

142 Sekulovic, S., Gasparetto, M., Lecault, V., Hoesli, C.A., Kent, D.G., Rosten, P., Wan, A., Brookes, C., Hansen, C.L., Piret, J.M., Smith, C., Eaves, C.J., & Humphries, R.K. Ontogeny stage-independent and high-level clonal expansion in vitro of mouse hematopoietic stem cells stimulated by an engineered NUP98-HOX fusion transcription factor. *Blood*, 118(16), 4366-4376 (2011).

143 Osawa, M., Hanada, K., Hamada, H., & Nakauchi, H. Long-term lymphohematopoietic reconstitution by a single CD34-low/negative hematopoietic stem cell. *Science*, 273(5272), 242-245 (1996).

144 Christensen, J.L. & Weissman, I.L. Flk-2 is a marker in hematopoietic stem cell differentiation: A simple method to isolate long-term stem cells. *Proceedings of the National Academy of Sciences of the United States of America*, 98(25), 14541-14546 (2001).

145 Civin, C.I., Strauss, L.C., Brovall, C., Fackler, M.J., Schwartz, J.F., & Shaper, J.H. Hematopoietic progenitor-cell surface-antigen defined by a monoclonal-antibody raised against Kg-1a cells. *Journal of Immunology*, 133(1), 157-165 (1984).

146 Uchida, N. & Weissman, I.L. Searching for hematopoietic stem-cells - evidence that Thy-1.1(Lo) Lin- Sca-1+ cells are the only stem-cells in C57bl/Ka-Thy-1.1 bone-marrow. *Journal of Experimental Medicine*, 175(1), 175-184 (1992).

147 Goodell, M.A., Brose, K., Paradis, G., Conner, A.S., & Mulligan, R.C. Isolation and functional properties of murine hematopoietic stem cells that are replicating in vivo. *Journal of Experimental Medicine*, 183(4), 1797-1806 (1996).

148 Wognum, A.W., Eaves, A.C., & Thomas, T.E. Identification and isolation of hematopoietic stem cells. *Archives of Medical Research*, 34(6), 461-475 (2003).

149 Yilmaz, O.H., Kiel, M.J., & Morrison, S.J. SLAM family markers are conserved among hematopoietic stem cells from old and reconstituted mice and markedly increase their purity. *Blood*, 107(3), 924-930 (2006).

150 Kiel, M.J., Yilmaz, O.H., Iwashita, T., Yilmaz, O.H., Terhorst, C., & Morrison, S.J. SLAM family receptors distinguish hematopoietic stem and progenitor cells and reveal endothelial niches for stem cells. *Cell*, 121(7), 1109-1121 (2005).

151 Kent, D.G., Copley, M.R., Benz, C., Wohrer, S., Dykstra, B.J., Ma, E., Cheyne, J., Zhao, Y.J., Bowie, M.B., Zhao, Y., Gasparetto, M., Delaney, A., Smith, C., Marra, M., & Eaves, C.J. Prospective isolation and molecular characterization of hematopoietic stem cells with durable self-renewal potential. *Blood*, 113(25), 6342-6350 (2009).

152 Ramos, C.A., Bowman, T.A., Boles, N.C., Merchant, A.A., Zheng, Y.Y., Parra, I., Fuqua, S.A.W., Shaw, C.A., & Goodell, M.A. Evidence for diversity in transcriptional profiles of single hematopoietic stem cells. *PLoS Genetics*, 2(9), 1487-1499 (2006).

153 Dykstra, B., Kent, D., Bowie, M., McCaffrey, L., Hamilton, M., Lyons, K., Lee, S.-J., Brinkman, R., & Eaves, C. Long-term propagation of distinct hematopoietic differentiation programs in vivo. *Cell Stem Cell*, 1(2), 218-229 (2007).

154 Challen, G.A., Boles, N.C., Chambers, S.M., & Goodell, M.A. Distinct hematopoietic stem cell subtypes are differentially regulated by TGF-beta 1. *Cell Stem Cell*, 6(3), 265-278 (2010).

155 Benveniste, P., Frelin, C., Janmohamed, S., Barbara, M., Herrington, R., Hyam, D., & Iscove, N.N. Intermediate-term hematopoietic stem cells with extended but time-limited reconstitution potential. *Cell Stem Cell*, 6(1), 48-58 (2010).

156 van Os, R., Kamminga, L.M., & de Haan, G. Stem cell assays: Something old, something new, something borrowed. *Stem Cells*, 22(7), 1181-1190 (2004).

157 Eaves, C., Miller, C., Conneally, E., Audet, J., Oostendorp, R., Cashman, J., Zandstra, P., Rose-John, S., Piret, J., & Eaves, A. Introduction to stem cell biology in vitro - Threshold to the future. *Annals of the New York Academy of Sciences*, 872(1), 1-8 (1999).

158 Coulombel, L. Identification of hematopoietic stem/progenitor cells: strength and drawbacks of functional assays. *Oncogene*, 23(43), 7210-7222 (2004).

159 Ploemacher, R.E., Vandersluijs, J.P., Voerman, J.S.A., & Brons, N.H.C. An in vitro limiting-dilution assay of long-term repopulating hematopoietic stem-cells in the mouse. *Blood*, 74(8), 2755-2763 (1989).

160 Sutherland, H.J., Eaves, C.J., Eaves, A.C., Dragowska, W., & Lansdorp, P.M. Characterization and partial-purification of human marrow-cells capable of initiating long-term hematopoiesis in vitro. *Blood*, 74(5), 1563-1570 (1989).

161 Harrison, D.E. Competitive repopulation - New assay for long-term stem-cell functional-capacity. *Blood*, 55(1), 77-81 (1980).

162 Szilvassy, S.J., Humphries, R.K., Lansdorp, P.M., Eaves, A.C., & Eaves, C.J. Quantitative assay for totipotent reconstituting hematopoietic stem-cells by a competitive repopulation strategy. *Proceedings of the National Academy of Sciences of the United States of America*, 87(22), 8736-8740 (1990).

163 Lu, R., Neff, N.F., Quake, S.R., & Weissman, I.L. Tracking single hematopoietic stem cells in vivo using high-throughput sequencing in conjunction with viral genetic barcoding. *Nature Biotechnology*, 29(10), 928-933 (2011).

164 Brummendorf, T.H., Dragowska, W., Zijlmans, J., Thornbury, G., & Lansdorp, P.M. Asymmetric cell divisions sustain long-term hematopoiesis from single-sorted human fetal liver cells. *Journal of Experimental Medicine*, 188(6), 1117-1124 (1998).

165 Huang, S., Law, P., Francis, K., Palsson, B.O., & Ho, A.D. Symmetry of initial cell divisions among primitive hematopoietic progenitors is independent of ontogenic age and regulatory molecules. *Blood*, 94(8), 2595-2604 (1999).

166 Young, J.C., Varma, A., DiGiusto, D., & Backer, M.P. Retention of quiescent hematopoietic cells with high proliferative potential during ex vivo stem cell culture. *Blood*, 87(2), 545-556 (1996).

167 Punzel, M., Zhang, T., Liu, D.H., Eckstein, V., & Ho, A.D. Functional analysis of initial cell divisions defines the subsequent fate of individual human CD34(+)CD38(-) cells. *Experimental Hematology*, 30(5), 464-472 (2002).

168 Punzel, M., Liu, D.H., Zhang, T., Eckstein, V., Miesala, K., & Ho, A.D. The symmetry of initial divisions of human hematopoietic progenitors is altered only by the cellular microenvironment. *Experimental Hematology*, 31(4), 339-347 (2003).

169 Song, Y., Bahnson, A., Hall, N., Yu, H., Shen, H., Koebler, D., Houck, R., Xie, Y., & Cheng, T. Stem cell traits in long-term co-culture revealed by time-lapse imaging. *Leukemia*, 24(1), 153-161 (2010).

170 Giebel, B., Zhang, T., Beckmann, J., Spanholtz, J., Wernet, P., Ho, A.D., & Punzel, M. Primitive human hematopoietic cells give rise to differentially specified daughter cells upon their initial cell division. *Blood*, 107(5), 2146-2152 (2006).

171 Kent, D.G., Dykstra, B.J., Cheyne, J., Ma, E., & Eaves, C.J. Steel factor coordinately regulates the molecular signature and biologic function of hematopoietic stem cells. *Blood*, 112(3), 560-567 (2008).

172 Audet, J., Miller, C.L., Rose-John, S., Piret, J.M., & Eaves, C.J. Distinct role of gp130 activation in promoting self-renewal divisions by mitogenically stimulated murine hematopoietic stem cells. *Proceedings of the National Academy of Sciences of the United States of America*, 98(4), 1757-1762 (2001).

173 Lang, P., Yeow, K., Nichols, A., & Scheer, A. Cellular imaging in drug discovery. *Nature Reviews Drug Discovery*, 5(4), 343-356 (2006).

174 Scherf, N., Franke, K., Glauche, I., Kurth, I., Bornhauser, M., Werner, C., Pompe, T., & Roeder, I. On the symmetry of siblings: automated single-cell tracking to quantify the behavior of hematopoietic stem cells in a biomimetic setup. *Experimental Hematology*, 40(2), 119-130 (2012).

175 Eilken, H.M., Nishikawa, S.I., & Schroeder, T. Continuous single-cell imaging of blood generation from haemogenic endothelium. *Nature*, 457(7231), 896-900 (2009).

176 Wang, Q.L., Niemi, J., Tan, C.M., You, L.C., & West, M. Image segmentation and dynamic lineage analysis in single-cell fluorescence microscopy. *Cytometry Part A*, 77A(1), 101-110 (2010).

177 Schroeder, T. Asymmetric cell division in normal and malignant hematopoietic precursor cells. *Cell Stem Cell*, 1, 479-481 (2007).

178 Schroeder, T. Imaging stem-cell-driven regeneration in mammals. *Nature*, 453(7193), 345-351 (2008).

179 Rieger, M.A., Hoppe, P.S., Smejkal, B.M., Eitelhuber, A.C., & Schroeder, T. Hematopoietic cytokines can instruct lineage choice. *Science*, 325(5937), 217-218 (2009).

180 Wu, M.F., Kwon, H.Y., Rattis, F., Blum, J., Zhao, C., Ashkenazi, R., Jackson, T.L., Gaiano, N., Oliver, T., & Reya, T. Imaging hematopoietic precursor division in real time. *Cell Stem Cell*, 1(5), 541-554 (2007).

181 Wu, M.F., Kwon, H.Y., Rattis, F., Blum, J., Zhao, C., Ashkenazi, R., Jackson, T.L., Gaiano, N., Oliver, T., & Reya, T. Imaging hematopoietic precursor division in real time. *Cell Stem Cell*, 1, 541-554 (2007).

182 Beckmann, J., Scheitza, S., Wernet, P., Fischer, J.C., & Giebel, B. Asymmetric cell division within the human hematopoietic stem and progenitor cell compartment: identification of asymmetrically segregating proteins. *Blood*, 109(12), 5494-5501 (2007).

183 Ting, S.B., Deneault, E., Hope, K., Cellot, S., Chagraoui, J., Mayotte, N., Dorn, J.F., Laverdure, J.-P., Harvey, M., Hawkins, E.D., Russell, S.M., Maddox, P.S., Iscove, N.N., & Sauvageau, G. Asymmetric segregation and self-renewal of hematopoietic stem and progenitor cells with endocytic Ap2a2. *Blood*, 119(11), 2510-2522 (2012).

184 Wlodkowic, D., Faley, S., Zagnoni, M., Wikswo, J.P., & Cooper, J.M. Microfluidic single-cell array cytometry for the analysis of tumor apoptosis. *Analytical Chemistry*, 81(13), 5517-5523 (2009).

185 Faley, S., Seale, K., Hughey, J., Schaffer, D.K., VanCornpernolle, S., McKinney, B., Baudenbacher, F., Unutmaz, D., & Wikswo, J.P. Microfluidic platform for real-time signaling analysis of multiple single T cells in parallel. *Lab on a Chip*, 8(10), 1700-1712 (2008).

186 Faley, S.L., Copland, M., Wlodkowic, D., Kolch, W., Seale, K.T., Wikswo, J.P., & Cooper, J.M. Microfluidic single cell arrays to interrogate signalling dynamics of individual, patient-derived hematopoietic stem cells. *Lab on a Chip*, 9(18), 2659-2664 (2009).

187 Tjio, J.H. & Puck, T.T. Genetics of somatic mammalian cells. *The Journal of Experimental Medicine*, 108(2), 259-268 (1958).

188 Urlaub, G. & Chasin, L.A. Isolation of Chinese hamster cell mutants deficient in dihydrofolate-reductase activity. *Proceedings of the National Academy of Sciences of the United States of America*, 77(7), 4216-4220 (1980).

189 Jayapal, K.P., Wlaschin, K.F., Hu, W., & Yap, M.G.S. Recombinant protein therapeutics from CHO cells - 20 years and counting. *Chemical Engineering Progress*, 103, 40-47 (2007).

190 Borer, J.S. T-PA and the principles of drug approval. *New England Journal of Medicine*, 317(26), 1659-1661 (1987).

191 Collen, D. & Lijnen, H.R. The tissue-type plasminogen activator story. *Arteriosclerosis Thrombosis and Vascular Biology*, 29(8), 1151-1155 (2009).

192 Hacker, D.L., De Jesus, M., & Wurm, F.M. 25 years of recombinant proteins from reactor-grown cells - Where do we go from here? *Biotechnology Advances*, 27(6), 1023-1027 (2009).

193 Kim, J.Y., Kim, Y.G., & Lee, G.M. CHO cells in biotechnology for production of recombinant proteins: current state and further potential. *Applied Microbiology and Biotechnology*, 93(3), 917-930 (2012).

194 Aggarwal, S. What's fueling the biotech engine-2010 to 2011. *Nature Biotechnology*, 29(12), 1083-1089 (2011).

195 Chan, A.C. & Carter, P.J. Therapeutic antibodies for autoimmunity and inflammation. *Nature Reviews Immunology*, 10(5), 301-316 (2010).

196 Moran, N. Biotech innovators jump on biosimilars bandwagon. *Nature Biotechnology*, 30(4), 297-299 (2012).

197 Rita Costa, A., Elisa Rodrigues, M., Henriques, M., Azeredo, J., & Oliveira, R. Guidelines to cell engineering for monoclonal antibody production. *European Journal of Pharmaceutics and Biopharmaceutics*, 74(2), 127-138 (2010).

198 Bebbington, C.R., Renner, G., Thomson, S., King, D., Abrams, D., & Yarranton, G.T. High-level expression of a recombinant antibody from myeloma cells using a glutamine-synthetase gene as an amplifiable selectable marker. *Bio/Technology*, 10(2), 169-175 (1992).

199 Girod, P.A., Zahn-Zabal, M., & Mermod, N. Use of the chicken lysozyme 5 ' matrix attachment region to generate high producer CHO cell lines. *Biotechnology and Bioengineering*, 91(1), 1-11 (2005).

200 Kwaks, T.H.J., Barnett, P., Hemrika, W., Siersma, T., Sewalt, R., Satijn, D.P.E., Brons, J.F., van Blokland, R., Kwakman, P., Kruckeberg, A.L., Kelder, A., & Otte, A.P. Identification of anti-repressor elements that confer high and stable protein production in mammalian cells. *Nature Biotechnology*, 21(5), 553-558 (2003).

201 Huang, Y., Li, Y., Wang, Y.G., Gu, X., Wang, Y., & Shen, B.F. An efficient and targeted gene integration system for high-level antibody expression. *Journal of Immunological Methods*, 322(1-2), 28-39 (2007).

202 Santiago, Y., Chan, E., Liu, P.-Q., Orlando, S., Zhang, L., Urnov, F.D., Holmes, M.C., Guschin, D., Waite, A., Miller, J.C., Rebar, E.J., Gregory, P.D., Klug, A., & Collingwood, T.N. Targeted gene knockout in mammalian cells by using engineered zinc-finger nucleases. *Proceedings of the National Academy of Sciences*, 105(15), 5809-5814 (2008).

203 Cost, G.J., Freyvert, Y., Vafiadis, A., Santiago, Y., Miller, J.C., Rebar, E., Collingwood, T.N., Snowden, A., & Gregory, P.D. BAK and BAX deletion using zinc-finger nucleases yields apoptosis-resistant CHO cells. *Biotechnology and Bioengineering*, 105(2), 330-340 (2010).

204 Malphettes, L., Freyvert, Y., Chang, J., Liu, P.-Q., Chan, E., Miller, J.C., Zhou, Z., Nguyen, T., Tsai, C., Snowden, A.W., Collingwood, T.N., Gregory, P.D., & Cost, G.J. Highly efficient deletion of FUT8 in CHO cell lines using zinc-finger nucleases yields cells that produce completely nonfucosylated antibodies. *Biotechnology and Bioengineering*, 106(5), 774-783 (2010).

205 Guarna, M.M., Fann, C.H., Busby, S.J., Walker, K.M., Kilburn, D.G., & Piret, J.M. Effect of cDNA copy number on secretion rate of activated protein. *Biotechnology and Bioengineering*, 46(1), 22-27 (1995).

206 Barnes, L.M., Bentley, C.M., & Dickson, A.J. Stability of protein production from recombinant mammalian cells. *Biotechnology and Bioengineering*, 81(6), 631-639 (2003).

207 Pallavicini, M.G., Deteresa, P.S., Rosette, C., Gray, J.W., & Wurm, F.M. Effects of methotrexate on transfected DNA stability in mammalian cells. *Molecular and Cellular Biology*, 10(1), 401-404 (1990).

208 Fann, C.H., Guirgis, F., Chen, G., Lao, M.S., & Piret, J.M. Limitations to the amplification and stability of human tissue-type plasminogen activator expression by Chinese hamster ovary cells. *Biotechnology and Bioengineering*, 69(2), 204-212 (2000).

209 Kaufman, R.J. & Schimke, R.T. Amplification and loss of dihydrofolate-reductase genes in a Chinese hamster ovary cell line. *Molecular and Cellular Biology*, 1(12), 1069-1076 (1981).

210 Yang, Y.S., Mariati, Chusainow, J., & Yap, M.G.S. DNA methylation contributes to loss in productivity of monoclonal antibody-producing CHO cell lines. *Journal of Biotechnology*, 147(3-4), 180-185 (2010).

211 Kim, M., O'Callaghan, P.M., Droms, K.A., & James, D.C. A mechanistic understanding of production instability in CHO cell lines expressing recombinant monoclonal antibodies. *Biotechnology and Bioengineering*, 108(10), 2434-2446 (2011).

212 Yoshikawa, Y., Nakanishi, F., Ogura, Y., Oi, D., Omasa, T., Katakura, Y., Kishimoto, M., & Suga, K. Amplified gene location in chromosomal DNA affected recombinant protein production and stability of amplified genes. *Biotechnology Progress*, 16(5), 710-715 (2000).

213 Morrison, C.J., McMaster, W.R., & Piret, J.M. Differential stability of proteolytically active and inactive recombinant metalloproteinase in Chinese hamster ovary cells. *Biotechnology and Bioengineering*, 53(6), 594-600 (1997).

214 He, L., Winterrowd, C., Kadura, I., & Frye, C. Transgene copy number distribution profiles in recombinant CHO cell lines revealed by single cell analyses. *Biotechnology and Bioengineering*, 109(7), 1713-1722 (2012).

215 Dorai, H., Corisdeo, S., Ellis, D., Kinney, C., Chomo, M., Hawley-Nelson, P., Moore, G., Betenbaugh, M.J., & Ganguly, S. Early prediction of instability of chinese hamster ovary cell lines expressing recombinant antibodies and antibody-fusion proteins. *Biotechnology and Bioengineering*, 109(4), 1016-1030 (2011).

216 Chartrain, M. & Chu, L. Development and production of commercial therapeutic monoclonal antibodies in mammalian cell expression aystems: An overview of the current upstream technologies. *Current Pharmaceutical Biotechnology*, 9(6), 447-467 (2008).

217 Porter, A.J., Racher, A.J., Preziosi, R., & Dickson, A.J. Strategies for selecting recombinant CHO cell lines for cGMP manufacturing: Improving the efficiency of cell line generation. *Biotechnology Progress*, 26(5), 1455-1464 (2010).

218 Porter, A.J., Dickson, A.J., & Racher, A.J. Strategies for selecting recombinant CHO cell lines for cGMP manufacturing: Realizing the potential in bioreactors. *Biotechnology Progress*, 26(5), 1446-1454 (2012).

219 Lindgren, K., Salmen, A., Lundgren, M., Bylund, L., Ebler, A., Faldt, E., Sorvik, L., Fenge, C., & Skoging-Nyberg, U. Automation of cell line development. *Cytotechnology*, 59(1), 1-10 (2009).

220 Browne, S.M. & Al-Rubeai, M. Selection methods for high-producing mammalian cell lines. *Trends in Biotechnology*, 25(9), 425-432 (2007).

221 Kumar, N. & Borth, N. Flow-cytometry and cell sorting: An efficient approach to investigate productivity and cell physiology in mammalian cell factories. *Methods*, 56(3), 366-374 (2012).

222 Carroll, S. & Al-Rubeai, M. The selection of high-producing cell lines using flow cytometry and cell sorting. *Expert Opinion on Biological Therapy*, 4(11), 1821-1829 (2004).

223 Mancia, F., Patel, S.D., Rajala, M.W., Scherer, P.E., Nemes, A., Schieren, I., Hendrickson, W.A., & Shapiro, L. Optimization of protein production in mammalian cells with a coexpressed fluorescent marker. *Structure*, 12(8), 1355-1360 (2004).

224 Meng, Y.G., Liang, J., Wong, W.L., & Chisholm, V. Green fluorescent protein as a second selectable marker for selection of high producing clones from transfected CHO cells. *Gene*, 242(1-2), 201-207 (2000).

225 Bailey, C.G., Tait, A.S., & Sunstrom, N.A. High-throughput clonal selection of recombinant CHO cells using a dominant selectable and amplifiable metallothionein-GFP fusion protein. *Biotechnology and Bioengineering*, 80(6), 670-676 (2002).

226 Cairns, V.R., DeMaria, C.T., Poulin, F., Sancho, J., Liu, P., Zhang, J., Campos-Rivera, J., Karey, K.P., & Estes, S. Utilization of non-AUG initiation codons in a flow cytometric method for efficient selection of recombinant cell lines. *Biotechnology and Bioengineering*, 108(11), 2611-2622 (2011).

227 Brezinsky, S.C.G., Chiang, G.G., Szilvasi, A., Mohan, S., Shapiro, R.I., MacLean, A., Sisk, W., & Thill, G. A simple method for enriching populations of transfected CHO cells for cells of higher specific productivity. *Journal of Immunological Methods*, 277(1-2), 141-155 (2003).

228 Meilhoc, E., Wittrup, K.D., & Bailey, J.E. Application of flow cytometric measurement of surface IgG in kinetic-analysis of monoclonal antibody systhesis and secretion by murine hybridoma cells. *Journal of Immunological Methods*, 121(2), 167-174 (1989).

229 Powell, K.T. & Weaver, J.C. Gel microdroplets and flow-cytometry - Rapid determination of antibody secretion by individual cells within a cell population. *Bio/Technology*, 8(4), 333-337 (1990).

230 Manz, R., Assenmacher, M., Pfluger, E., Miltenyi, S., & Radbruch, A. Analysis and sorting of live cells according to secreted molecules, relocated to a cell-surface affinity matrix. *Proceedings of the National Academy of Sciences of the United States of America*, 92(6), 1921-1925 (1995).

231 Borth, N., Zeyda, M., & Katinger, H. Efficient selection of high-producing subclones during gene amplification of recombinant Chinese hamster ovary cells by flow cytometry and cell sorting. *Biotechnology and Bioengineering*, 71(4), 266-273 (2000).

232 Hanania, E.G., Fieck, A., Stevens, J., Bodzin, L.J., Palsson, B.O., & Koller, M.R. Automated in situ measurement of cell-specific antibody secretion and laser-mediated purification for rapid cloning of highly-secreting producers. *Biotechnology and Bioengineering*, 91(7), 872-876 (2005).

233 Dharshanan, S., Chong, H., Hung, C.S., Zamrod, Z., & Kamal, N. Rapid automated selection of mammalian cell line secreting high level of humanized monoclonal antibody using Clone Pix FL system and the correlation between exterior median intensity and antibody productivity. *Electronic Journal of Biotechnology*, 14(2) (2011).

234 Ong, S.M., Zhang, C., Toh, Y.C., Kim, S.H., Foo, H.L., Tan, C.H., van Noort, D., Park, S., & Yu, H. A gel-free 3D microfluidic cell culture system. *Biomaterials*, 29(22), 3237-3244 (2008).

235 Sivagnanam, V., Song, B., Vandevyver, C., Bunzli, J.C.G., & Gijs, M.A.M. Selective breast cancer cell capture, culture, and immunocytochemical analysis using self-assembled magnetic bead patterns in a microfluidic chip. *Langmuir*, 26(9), 6091-6096 (2010).

236 Villa, M., Pope, S., Conover, J., & Fan, T.H. Growth of primary embryo cells in a microculture system. *Biomedical Microdevices*, 12(2), 253-261 (2010).

237 Walsh, C.L., Babin, B.M., Kasinskas, R.W., Foster, J.A., McGarry, M.J., & Forbes, N.S. A multipurpose microfluidic device designed to mimic microenvironment gradients and develop targeted cancer therapeutics. *Lab on a Chip*, 9(4), 545-554 (2009).

238 Torisawa, Y.S., Chueh, B.H., Huh, D., Ramamurthy, P., Roth, T.M., Barald, K.F., & Takayama, S. Efficient formation of uniform-sized embryoid bodies using a compartmentalized microchannel device. *Lab on a Chip*, 7(6), 770-776 (2007).

239 Prokop, A., Prokop, Z., Schaffer, D., Kozlov, E., Wikswo, J., Cliffel, D., & Baudenbacher, F. NanoLiterBioReactor: Long-term mammalian cell culture at nanofabricated scale. *Biomedical Microdevices*, 6(4), 325-339 (2004).

240 Masand, S.N., Mignone, L., Zahn, J.D., & Shreiber, D.I. Nanoporous membrane-sealed microfluidic devices for improved cell viability. *Biomedical Microdevices*, 13(6), 955-961 (2011).

241 Wei, H.B., Li, H.F., Mao, S.F., & Lin, J.M. Cell signaling analysis by mass spectrometry under coculture conditions on an integrated microfluidic device. *Analytical Chemistry*, 83(24), 9306-9313 (2011).

242 O'Neill, A.T., Monteiro-Riviere, N.A., & Walker, G.M. Characterization of microfluidic human epidermal keratinocyte culture. *Cytotechnology*, 56(3), 197-207 (2008).

243 Yu, Z.T.F., Kamei, K.I., Takahashi, H., Shu, C.J., Wang, X.P., He, G.W., Silverman, R., Radu, C.G., Witte, O.N., Lee, K.B., & Tseng, H.R. Integrated microfluidic devices for combinatorial cell-based assays. *Biomedical Microdevices*, 11(3), 547-555 (2009).

244 Lam, R.H.W., Kim, M.C., & Thorsen, T. Culturing aerobic and anaerobic bacteria and mammalian cells with a microfluidic differential oxygenator. *Analytical Chemistry*, 81(14), 5918-5924 (2009).

245 Lii, J., Hsu, W.J., Parsa, H., Das, A., Rouse, R., & Sia, S.K. Real-time microfluidic system for studying mammalian cells in 3D microenvironments. *Analytical Chemistry*, 80(10), 3640-3647 (2008).

246 Tian, X.L., Wang, S.Y., Zhang, Z., & Lv, D.C. Rat bone marrow-derived schwann-like cells differentiated by the optimal inducers combination on microfluidic chip and their functional performance. *PLoS One*, 7(8), 11 (2012).

247 Kane, B.J., Zinner, M.J., Yarmush, M.L., & Toner, M. Liver-specific functional studies in a microfluidic array of primary mammalian hepatocytes. *Analytical Chemistry*, 78(13), 4291-4298 (2006).

248 Hung, P.J., Lee, P.J., Sabounchi, P., Aghdam, N., Lin, R., & Lee, L.P. A novel high aspect ratio microfluidic design to provide a stable and uniform microenvironment for cell growth in a high throughput mammalian cell culture array. *Lab on a Chip*, 5(1), 44-48 (2005).

249 Lindstrom, S., Mori, K., Ohashi, T., & Andersson-Svahn, H. A microwell array device with integrated microfluidic components for enhanced single-cell analysis. *Electrophoresis*, 30(24), 4166-4171 (2009).

250 Bowie, M.B., McKnight, K.D., Kent, D.G., McCaffrey, L., Hoodless, P.A., & Eaves, C.J. Hematopoietic stem cells proliferate until after birth and show a reversible phase-specific engraftment defect. *Journal of Clinical Investigation*, 116(10), 2808-2816 (2006).

251 Dykstra, B., Kent, D., Bowie, M., McCaffrey, L., Hamilton, M., Lyons, K., Lee, S.J., Brinkman, R., & Eaves, C. Long-term propagation of distinct hematopoietic differentiation programs in vivo. *Cell Stem Cell*, 1, 218-229 (2007).

252 Yamazaki, S. & Nakauchi, H. Insights into signaling and function of hematopoietic stem cells at the single-cell level. *Current Opinion in Hematology*, 16(4), 255-258 (2009).

253 Uchida, N., Dykstra, B., Lyons, K.J., Leung, F.Y., & Eaves, C.J. Different in vivo repopulating activities of purified hematopoietic stem cells before and after being stimulated to divide in vitro with the same kinetics. *Experimental Hematology*, 31(12), 1338-1347 (2003).

254 Wheeler, A.R., Throndset, W.R., Whelan, R.J., Leach, A.M., Zare, R.N., Liao, Y.H., Farrell, K., Manger, I.D., & Daridon, A. Microfluidic device for single-cell analysis. *Analytical Chemistry*, 75(14), 3581-3586 (2003).

255 Hsieh, C.C., Huang, S.B., Wu, P.C., Shieh, D.B., & Lee, G.B. A microfluidic cell culture platform for real-time cellular imaging. *Biomedical Microdevices*, 11(4), 903-913 (2009).

256 Figallo, E., Cannizzaro, C., Gerecht, S., Burdick, J.A., Langer, R., Elvassore, N., & Vunjak-Novakovic, G. Micro-bioreactor array for controlling cellular microenvironments. *Lab on a Chip*, 7(6), 710-719 (2007).

257 Kim, L., Vahey, M.D., Lee, H.Y., & Voldman, J. Microfluidic arrays for logarithmically perfused embryonic stem cell culture. *Lab on a Chip*, 6(3), 394-406 (2006).

258 Kim, L., Toh, Y.C., Voldman, J., & Yu, H. A practical guide to microfluidic perfusion culture of adherent mammalian cells. *Lab on a Chip*, 7(6), 681-694 (2007).

259 Tourovskaia, A., Figueroa-Masot, X., & Folch, A. Differentiation-on-a-chip: A microfluidic platform for long-term cell culture studies. *Lab on a Chip*, 5(1), 14-19 (2005).

260 Satyanarayana, S., Karnik, R.N., & Majumdar, A. Stamp-and-stick room-temperature bonding technique for microdevices. *Journal of Microelectromechanical Systems*, 14(2), 392-399 (2005).

261 Belanger, M.C. & Marois, Y. Hemocompatibility, biocompatibility, inflammatory and in vivo studies of primary reference materials low-density polyethylene and polydimethylsiloxane: A review. *Journal of Biomedical Materials Research*, 58(5), 467-477 (2001).

262 Heo, Y.S., Cabrera, L.M., Song, J.W., Futai, N., Tung, Y.C., Smith, G.D., & Takayama, S. Characterization and resolution of evaporation-mediated osmolality shifts that constrain microfluidic cell culture in poly(dimethylsiloxane) devices. *Analytical Chemistry*, 79(3), 1126-1134 (2007).

263 Berthier, E., Warrick, J., Yu, H., & Beebe, D.J. Managing evaporation for more robust microscale assays - Part 1. Volume loss in high throughput assays. *Lab on a Chip*, 8(6), 852-859 (2008).

264 Paguirigan, A.L. & Beebe, D.J. Microfluidics meet cell biology: bridging the gap by validation and application of microscale techniques for cell biological assays. *Bioessays*, 30(9), 811-821 (2008).

265 Hansen, C.L., Classen, S., Berger, J.M., & Quake, S.R. A microfluidic device for kinetic optimization of protein crystallization and in situ structure determination. *Journal of the American Chemical Society*, 128(10), 3142-3143 (2006).

266 Shim, J.U., Cristobal, G., Link, D.R., Thorsen, T., Jia, Y.W., Piattelli, K., & Fraden, S. Control and measurement of the phase behavior of aqueous solutions using microfluidics. *Journal of the American Chemical Society*, 129(28), 8825-8835 (2007).

267 Hosokawa, M., Arakaki, A., Takahashi, M., Mori, T., Takeyama, H., & Matsunaga, T. High-density microcavity array for cell detection: single-cell analysis of hematopoietic stem cells in peripheral blood mononuclear cells. *Analytical Chemistry*, 81(13), 5308-5313 (2009).

268 Kurth, I., Franke, K., Pompe, T., Bornhauser, M., & Werner, C. Hematopoietic stem and progenitor cells in adhesive microcavities. *Integrative Biology*, 1(5-6), 427-434 (2009).

269 Moeller, H.C., Mian, M.K., Shrivastava, S., Chung, B.G., & Khademhosseini, A. A microwell array system for stem cell culture. *Biomaterials*, 29(6), 752-763 (2008).

270 Wei, X., Sims, C.E., & Allbritton, N.L. Microcup arrays for the efficient isolation and cloning of cells. *Analytical Chemistry*, 82(8), 3161-3167 (2010).

271 Ma, N.N., Koelling, K.W., & Chalmers, J.J. Fabrication and use of a transient contractional flow device to quantify the sensitivity of mammalian and insect cells to hydrodynamic forces. *Biotechnology and Bioengineering*, 80(4), 428-437 (2002).

272 Moghe, P.V., Nelson, R.D., & Tranquillo, R.T. Cytokine-stimulated chemotaxis of human neutrophils in a 3-D conjoined fibrin gel assay. *Journal of Immunological Methods*, 180(2), 193-211 (1995).

273 Broxmeyer, H.E., Maze, R., Miyazawa, K., Carow, C., Hendrie, P.C., Cooper, S., Hangoc, G., Vadhanraj, S., & Lu, L. The kit receptor and its ligand, Steel factor, as regulators of hematopoiesis. *Cancer Cells - A Monthly Review*, 3(12), 480-487 (1991).

274 Bowie, M.B., Kent, D.G., Copley, M.R., & Eaves, C.J. Steel factor responsiveness regulates the high self-renewal phenotype of fetal hematopoietic stem cells. *Blood*, 109(11), 5043-5048 (2007).

275 Cohen, A.R., Gomes, F.L.A.F., Roysam, B., & Cayouette, M. Computational prediction of neural progenitor cell fates. *Nature Methods*, 7(3), 213-218 (2010).

276 Kokkaliaris, K.D., Loeffler, D., & Schroeder, T. Advances in tracking hematopoiesis at the single-cell level. *Current Opinion in Hematology*, 19(4), 243-249 (2012).

277 Schroeder, T. Long-term single-cell imaging of mammalian stem cells. *Nature Methods*, 8(4), S30-S35 (2011).

278 Ho, A.D. & Wagner, W. The beauty of asymmetry: asymmetric divisions and self-renewal in the haematopoietic system. *Current Opinion in Hematology*, 14(4), 330-336 (2007).

279 Kent, D., Copley, M., Benz, C., Dykstra, B., Bowie, M., & Eaves, C. Regulation of hematopoietic stem cells by the steel factor/KIT signaling pathway. *Clinical Cancer Research*, 14(7), 1926-1930 (2008).

280 Balazs, A.B., Fabian, A.J., Esmon, C.T., & Mulligan, R.C. Endothelial protein C receptor (CD201) explicitly identifies hematopoietic stem cells in murine bone marrow. *Blood*, 107(6), 2317-2321 (2006).

281 Schroeder, T. Hematopoietic stem cell heterogeneity: Subtypes, not unpredictable behavior. *Cell Stem Cell*, 6(3), 203-207 (2010).

282 Petzer, A.L., Hogge, D.E., Lansdorp, P.M., Reid, D.S., & Eaves, C.J. Self-renewal of primitive human hematopoietic cells (long-term-culture-initiating cells) in vitro and their expansion in defined medium. *Proceedings of the National Academy of Sciences of the United States of America*, 93(4), 1470-1474 (1996).

283 Abe, T., Masuya, M., & Ogawa, M. An efficient method for single hematopoietic stem cell engraftment in mice based on cell-cycle dormancy of hematopoietic stem cells. *Experimental Hematology*, 38(7), 603-608 (2010).

284 Rapoport, D.H., Becker, T., Mamlouk, A.M., Schicktanz, S., & Kruse, C. A novel validation algorithm allows for automated cell tracking and the extraction of biologically meaningful parameters. *PLoS One*, 6(11), 16 (2011).

285 Habibian, H.K., Peters, S.O., Hsieh, C.C., Wuu, J., Vergilis, K., Grimaldi, C.I., Reilly, J., Carlson, J.E., Frimberger, A.E., Stewart, F.M., & Quesenberry, P.J. The fluctuating phenotype of the lymphohematopoietic stem cell with cell cycle transit. *Journal of Experimental Medicine*, 188(2), 393-398 (1998).

286 Orschell-Traycoff, C.M., Hiatt, K., Dagher, R.N., Rice, S., Yoder, M.C., & Srour, E.F. Homing and engraftment potential of Sca-1(+)lin(-) cells fractionated on the basis of adhesion molecule expression and position in cell cycle. *Blood*, 96(4), 1380-1387 (2000).

287 Beckmann, J., Scheitza, S., Wernet, P., Fischer, J.C., & Giebel, B. Asymmetric cell division within the human hematopoietic stem and progenitor cell compartment: identification of asymmetrically segregating proteins. *Blood*, 109(12), 5494-5501 (2007).

288 Glauche, I., Moore, K., Thielecke, L., Horn, K., Loeffler, M., & Roeder, I. Stem cell proliferation and quiescence-Two sides of the same coin. *PLoS Computational Biology*, 5(7) (2009).

289 Scholzen, T. & Gerdes, J. The Ki-67 protein: From the known and the unknown. *Journal of Cellular Physiology*, 182(3), 311-322 (2000).

290 Sakaue-Sawano, A., Kurokawa, H., Morimura, T., Hanyu, A., Hama, H., Osawa, H., Kashiwagi, S., Fukami, K., Miyata, T., Miyoshi, H., Imamura, T., Ogawa, M., Masai, H., & Miyawaki, A. Visualizing spatiotemporal dynamics of multicellular cell-cycle progression. *Cell*, 132(3), 487-498 (2008).

291 Cohen, A.R., Gomes, F., Roysam, B., & Cayouette, M. Computational prediction of neural progenitor cell fates. *Nature Methods*, 7(3), 213-218 (2010).

292 Son, S., Tzur, A., Weng, Y., Jorgensen, P., Kim, J., Kirschner, M.W., & Manalis, S. Direct observation of mammalian cell growth and size regulation. *Nature Methods* (2012).

293 Nelson, A.L., Dhimolea, E., & Reichert, J.M. Development trends for human monoclonal antibody therapeutics. *Nature Reviews Drug Discovery*, 9(10), 767-774 (2010).

294 Weiner, L.M., Surana, R., & Wang, S.Z. Monoclonal antibodies: versatile platforms for cancer immunotherapy. *Nature Reviews Immunology*, 10(5), 317-327 (2010).

295 Scott, A.M., Wolchok, J.D., & Old, L.J. Antibody therapy of cancer. *Nature Reviews Cancer*, 12(4), 278-287 (2012).

296 Taylor, P.C. & Feldmann, M. Anti-TNF biologic agents: still the therapy of choice for rheumatoid arthritis. *Nature Reviews Rheumatology*, 5(10), 578-582 (2009).

297 McCullough, K.C., Butcher, R.N., & Parkinson, D. Hybridoma cell lines secreting monoclonal antibodies against foot and mouth disease virus (FMDV). II. Cloning conditions *Journal of Biological Standardization*, 11(3), 183-194 (1983).

298 Underwood, P.A. & Bean, P.A. Hazards of the limiting-dilution method of cloning hybridomas. *Journal of Immunological Methods*, 107(1), 119-128 (1988).

299 Pilbrough, W., Munro, T.P., & Gray, P. Intraclonal protein expression heterogeneity in recombinant CHO cells. *PLoS One*, 4(12), 11 (2009).

300 Park, S., Han, J., Kim, W., Lee, G.M., & Kim, H.-S. Rapid selection of single cells with high antibody production rates by microwell array. *Journal of Biotechnology*, 156(3), 197-202 (2011).

301 Park, S., Kim, W., Kim, Y., Son, Y.D., Lee, S.C., Kim, E., Kim, S.H., Kim, J.H., & Kim, H.S. Array-based analysis of secreted glycoproteins for rapid selection of a single cell producing a glycoprotein with desired glycosylation. *Analytical Chemistry*, 82(13), 5830-5837 (2010).

302 Jin, A., Ozawa, T., Tajiri, K., Obata, T., Kondo, S., Kinoshita, K., Kadowaki, S., Takahashi, K., Sugiyama, T., Kishi, H., & Muraguchi, A. A rapid and efficient single-cell manipulation method for screening antigen-specific antibody-secreting cells from human peripheral blood. *Nature Medicine*, 15(9), 1088-1092 (2009).

303 Lecault, V., VanInsberghe, M., Sekulovic, S., Knapp, D.J.H.F., Wohrer, S., Bowden, W., Viel, F., McLaughlin, T., Jarandehei, A., Miller, M., Falconnet, D., White, A.K., Kent, D.G., Copley, M.R., Taghipour, F., Eaves, C.J., Humphries, R.K., Piret, J.M., & Hansen, C.L. High-throughput analysis of single hematopoietic stem cell proliferation in microfluidic cell culture arrays. *Nature Methods*, 8(7), 581-586 (2011).

304 Pichler, J., Hesse, F., Wieser, M., Kunert, R., Galosy, S.S., Mott, J.E., & Borth, N. A study on the temperature dependency and time course of the cold capture antibody secretion assay. *Journal of Biotechnology*, 141(1-2), 80-83 (2009).

305 Lloyd, D.R., Holmes, P., Jackson, L.P., Emery, A.N., & Al-Rubeai, M. Relationship between cell size, cell cycle and specific recombinant protein productivity. *Cytotechnology*, 34(1-2), 59-70 (2000).

306 Raj, A., Peskin, C.S., Tranchina, D., Vargas, D.Y., & Tyagi, S. Stochastic mRNA synthesis in mammalian cells. *PLoS Biology*, 4(10), 1707-1719 (2006).

307 Raj, A., van den Bogaard, P., Rifkin, S.A., van Oudenaarden, A., & Tyagi, S. Imaging individual mRNA molecules using multiple singly labeled probes. *Nature Methods*, 5(10), 877-879 (2008).

308 Fann, C.H., Guarna, M.M., Kilburn, D.G., & Piret, J.M. Relationship between recombinant activated protein C secretion rates and mRNA levels in baby hamster kidney cells. *Biotechnology and Bioengineering*, 63(4), 464-472 (1999).

309 Schroder, M. & Friedl, P. Overexpression of recombinant human antithrombin III in Chinese hamster ovary cells results in

malformation and decreased secretion of recombinant protein. *Biotechnology and Bioengineering*, 53(6), 547-559 (1997).

310 Liu, P. & Mathies, R.A. Integrated microfluidic systems for high-performance genetic analysis. *Trends in Biotechnology*, 27(10), 572-581 (2009).

311 Berthier, E., Young, E.W.K., & Beebe, D. Engineers are from PDMS-land, Biologists are from Polystyrenia. *Lab on a Chip*, 12(7), 1224-1237 (2012).

312 van Midwoud, P.M., Janse, A., Merema, M.T., Groothuis, G.M.M., & Verpoorte, E. Comparison of biocompatibility and adsorption properties of different plastics for advanced microfluidic cell and tissue culture models. *Analytical Chemistry*, 84(9), 3938-3944 (2012).

313 Leech, P.W. Hot embossing of cyclic olefin copolymers. *Journal of Micromechanics and Microengineering*, 19(5), 5 (2009).

314 Young, E.W.K., Pak, C., Kahl, B.S., Yang, D.T., Callander, N.S., Miyamoto, S., & Beebe, D.J. e-Blood Microscale functional cytomics for studying hematologic cancers. *Blood*, 119(10), E76-E85 (2012).

315 Kling, J. Fresh from the pipeline 2011. *Nature Biotechnology*, 30(2), 128-131 (2012).

316 Xu, X., Nagarajan, H., Lewis, N.E. *et al.* The genomic sequence of the Chinese hamster ovary (CHO)-K1 cell line. *Nature Biotechnology*, 29(8), 735-741 (2011).

317 Urnov, F.D., Rebar, E.J., Holmes, M.C., Zhang, H.S., & Gregory, P.D. Genome editing with engineered zinc finger nucleases. *Nature Reviews Genetics*, 11(9), 636-646 (2010).

318 Kim, J.Y., Kim, Y.-G., & Lee, G.M. CHO cells in biotechnology for production of recombinant proteins: current state and further potential. *Applied Microbiology and Biotechnology*, 93(3), 917-930 (2012).

319 Kennard, M.L., Goosney, D.L., Monteith, D., Roe, S., Fischer, D., & Mott, J. Auditioning of CHO host cell lines using the artificial chromosome expression (ACE) technology. *Biotechnology and Bioengineering*, 104(3), 526-539 (2009).

320 Agrawal, V. & Bal, M. Strategies for rapid production of therapeutic proteins in mammalian cells. *BioProcess International*, 10(4), 32-48 (2012).

321 Majors, B.S., Chiang, G.G., Pederson, N.E., & Betenbaugh, M.J. Directed evolution of mammalian anti-apoptosis proteins by somatic hypermutation. *Protein Engineering Design & Selection*, 25(1), 27-38 (2012).

322 Pokric, B. & Pucar, Z. 2-cross immunodiffusion technique - Diffusion coefficients and precipitating titers of IgG in human serum and rabbit serum antibodies *Analytical Biochemistry*, 93(1), 103-114 (1979).

# Appendix A Mold Fabrication Protocol

Each new microfluidic design was created with a drawing software (AutoCAD, Autodesk). A micro-pump was located downstream of the array to avoid crushing the cells and control the speed during the loading process. Depending on the application, microfluidic cell culture arrays contained from 1,600 to 6,144 chambers in the order of ~4 nl each. Multiplexers, isolation valves and hydration lines were added when necessary to offer a better control of the microenvironment. Designs were printed at 20,000 dots per inch (d.p.i) on transparent masks. The fabrication of molds on a silicone substrate was performed using common photolithography techniques as described below.

## Flow Wafer

The flow wafer contained higher inlet channels (40 μm) to minimize clogging, flow channels with reflow to allow valving (12 μm) and cell culture chambers (160 μm). Each layer was built onto the flow wafer as described below.

### Flow channels

1. Dehydrate a wafer for 10-15 min at 150 °C.
2. Treat the wafer with vapor phase hexamethyldisilazane (HMDS) for at least 2 min.
3. Pour SPR220-7.0 resist on half the diameter of the wafer.
4. Ramp at 500 rpm for 10 seconds, then spin at 1,500 rpm for 90 s.
5. Pre-bake the wafer at 115 °C for 120 s.
6. Expose for 30 s.
7. Wait 30 min to rehydrate the resist.
8. Develop in MF319 primary bath for around 5-10 min, then rinse in an MF319 secondary bath.
9. Rinse with DI water and dry the wafer with compressed nitrogen.
10. Ramp from room temperature to 190 °C and leave overnight for hard bake.

*Aim: 11-13 μm after reflow*

**Inlet channels**

1. Pour SU8-50 resist on half the diameter of the wafer.
2. Ramp at 500 rpm for 30 s, then spin at 2,500 rpm for 30 s.
3. Soft bake the wafer for 2 min at 65 °C, 10 min at 95 °C, and 2 min at 65 °C.
4. Expose for 7 s.
5. Perform a post-exposure bake for 2 min at 65 °C, 10 min at 95 °C, and 2 min at 65 °C.
6. Develop in an SU8 developer primary bath for around 4 min, then rinse in a SU8 developer secondary bath.
7. Rinse with IPA and dry the wafer with compressed nitrogen.

*Aim: 40 μm*

**Chambers**

1. Pour SU8-100 resist on half the diameter of the wafer.
2. Ramp at 500 rpm for 10 s, then spin at 1,300 rpm for 50 s.
3. Soft bake the wafer for 5 min at 65 °C, 70 min at 95 °C, and 5 min at 65 °C.
4. Expose for 25 s.
5. Perform a post-exposure bake for 5 min at 65 °C, 18 min at 95 °C, and 5 min at 65 °C.
6. Develop in an SU8 developer primary bath for around 20 min, then rinse in a SU8 developer secondary bath.
7. Rinse with isopropyl alcohol (IPA) and dry the wafer with compressed nitrogen.
8. Ramp up and down from room temperature to 135 °C for 20 min.

*Aim: 160 μm*

## Control Wafer

The control wafer consisted of only one layer containing all lines for valves and pumps lines and was fabricated as follows.

1. Dehydrate a wafer for 10-15 min at 150 $^{o}$C.
2. Pour SU8-50 resist on half the diameter of the wafer.
3. Ramp at 500 rpm for 10 s, then spin at 4,200 rpm for 40 s.
4. Soft bake the wafer for 2 min at 65 $^{o}$C, 4 min at 95 $^{o}$C, and 2 min at 65 $^{o}$C.
5. Expose for 2 min.
6. Perform a post-exposure bake for 2 min at 65 $^{o}$C, 6 min at 95 $^{o}$C, and 2 min at 65 $^{o}$C.
7. Develop in an SU8 developer primary bath for around 2 min, then rinse in a SU8 developer second bath.
8. Rinse with IPA and dry the wafer with compressed nitrogen.
9. Ramp up and down from room temperature to 135 $^{o}$C for 20 min.

*Aim: 25 μm*

# Appendix B Device Fabrication Protocol

Wafers were reused to make devices as long as the structures remained intact. The procedure below was followed to fabricate devices with an integrated iso-osmotic bath using Sylgard 184 (Dow Corning) PDMS.

## Cleaning

1. If the wafers are not coated with parylene, place them in a plastic box with trimethylchlorosilane (TMCS) for at least 2 min.
2. Pour 15.0 g RTV-A and 1.5 g RTV-B (10:1 ratio) per wafer into a cup, then place the cup in the mixer and mix together.
3. While mixing, wrap one Petri dish per wafer with aluminum foil.
4. Pour PDMS onto each wafer and tilt the dish so that wafer is covered with PDMS and that PDMS overflows on the foil.
5. If the flow layer requires cleaning, place the wafer in the degasser until no air bubble remains.
6. Place at 80 $^{o}$C in oven for at least 20 min.

*Wafers can be left overnight after performing this step.*

## Flow Layer

1. If the flow wafers are not coated with parylene, place them in a plastic box with TMCS for at least 2 min.
2. Pour 12.5 g RTV-A and 2.5 g RTV-B (5:1 ratio) per wafer in a cup, then place cup in the mixer and mix together.
3. While mixing, prepare aluminum wrap using a metal dish with a 3-inch diameter.
4. Place wafers in aluminum holders and press wafer down on the bottom of the holder by folding the aluminum foil on top of wafer edges.
5. Pour PDMS onto each wafer, and level the aluminum holder with 2 micropipette tips.
6. Place into degasser, start vacuum, and degas until no visible bubbles are left. Prepare control layer during that time.
7. Remove from degasser and level again with 2 micropipette tips. Let sit for at least 15 min.
8. Place in 80 $^{o}$C oven for 18 min with the control layer.

## Control Layer

1. Cut around the cleaned wafer with a surgical knife and peel off the PDMS to release the cleaned wafer.
2. Place cleaned control wafer in plastic box with TMCS for at least 2 min.
3. Pour 15.0 g RTV-A and 0.75 g RTV-B (20:1 ratio) into a cup, then place the cup in the mixer and mix.
4. Turn on gas and vacuum for spinner.
5. Set spinner recipe to ramp in 5 s to 500 rpm, dwell at 500 rpm for 10 s, ramp to 1630 rpm in 10 s, dwell at 1630 rpm for 60 s, and ramp down to 0 rpm in 5 s. The PDMS height should be 10 μm higher than the control features. Adjust accordingly using a spin curve.
6. Place wafer carefully on the centre of spinner chuck, then close lid and secure with copper slab and execute the spinner recipe.
7. After spinning, remove the wafer from the spinner and place in a clean, new Petri dish. Let sit for at least 15 min.
8. Place in 80 $^{o}$C oven for 18 min. The control and flow layers should both go into the oven at the same time.

## Membrane

1. Cut around cleaned wafer with surgical knife and peel off PDMS.
2. Pour 15.0 g RTV-A and 0.75 g RTV-B (20:1 ratio) in a cup, then place cup in the mixer and mix.
3. Turn on gas and vacuum for spinner.
4. Set spinner recipe to ramp in 5 s to 500 rpm, dwell at 500 rpm for 10 seconds, ramp to 500 rpm in 10 s, dwell at 500 rpm for 60 s, and ramp down to 0 rpm in 5 s. A thinner membrane will result in leaky valves while a membrane too thick does not spread evenly on the wafer.
5. Place wafer carefully on the centre of the spinner chuck, then close lid and secure with copper slab and execute the spinner recipe.
6. After spinning, remove wafer from the spinner and place in clean, new Petri dish.
7. Let sit for at least 15 min and align the flow and control layers during that time.
8. Place in 80 $^{o}$C oven for 12 min (13 min after the flow/control duo has been placed in the oven).

## Flow/Control Alignment

1. Remove both flow and control wafers from the oven.
2. Cut inside the edge of the flow wafer with a surgical knife, then peel off the PDMS layer from the wafer.
3. Place control wafer under the microscope.
4. Align flow layer to control layer, trying to work quickly and not peeling off and on too much.
5. Push down any bubbles that remain between the two layers and place in 80 $^{o}$C oven for 25 min. The blank should come out of the oven at the same time as the flow/control combo. Time out accordingly.

## Membrane/Duo Alignment

1. Remove both flow/control duo and blank wafers from the oven.
2. Cut around the edge of the control/flow wafer with a surgical knife, then peel off PDMS layer from silicon wafer
3. Place flow/control duo onto blank layer.
4. Push down any bubbles that remain between the two layers, and place in 80 $^{o}$C oven for at least 1 h.

*Wafers can be left in the oven overnight after this step.*

## Bath Layer

1. Pour 40.0 g RTV-A and 4.0 g RTV-B (10:1 ratio) in a cup, then place the cup in the mixer and mix. This amount of PDMS gives a sufficient height to provide good support structure for inlet and outlet ports.
2. While mixing, prepare aluminum wrap using a metal dish with a 3-inch diameter.
3. Press down wafer to the bottom by folding the aluminum foil on top of wafer edges.
4. Pour PDMS onto blank wafer, and level the aluminum holder with 2 micropipette tips.
5. Place into degasser, start vacuum and degas until no visible bubbles are left.
6. Remove from the degasser and level again with 2 micropipette tips.
7. Place in 80 $^{o}$C oven for 20 min.

## Cover Layer

1. Pour 14.0 g RTV-A and 1.4 g RTV-B (10:1 ratio) in a cup, then place cup in the mixer and mix.
2. While mixing, prepare aluminum wrap using a metal dish with a 3-inch diameter.
3. Press down wafer to the bottom by folding the aluminum foil on top of wafer edges.
4. Pour PDMS onto each wafer, and level the aluminum holder with 2 micropipette tips.
5. Place into degasser, start vacuum and degas until no visible bubbles are left.
6. Remove from degasser and level again with 2 micropipette tips.
7. Place in 80 $^{o}$C oven for 20 min.

## Chip Assembly

1. Remove flow/control/membrane wafer, and blank wafers from the oven and let cool for about 5 min.
2. Dice layers into individual chips and place the chips on a ball bearing bed, flow layer down.
3. Dice the bath layer and cut inside to create a bath having the area of the array. Leave enough space for the ports and the edges.
4. Punch holes that go in the corner of each side of the bath.
5. Dice the cover layers into pieces bigger that each chip.
6. Clean all surfaces with scotch-tape.
7. Mix together about 10.0 g RTV-A and 1.0 g RTV-B (10:1 ratio) in a cup, then place in mixer and mix.
8. Set spinner to spin at 6,000 rpm for 6 min.
9. Remove blank wafer from the oven, place on spinner, pour PDMS and spin.
10. Remove from spinner and place in Petri dish.
11. Stamp the bath portion onto the liquid blank wafer and leave for 30 s. Make sure to stamp the right side of the bath.
12. Remove from wafer, and stick together with the flow/control portion.
13. Remove bubbles between layers.
14. Mix together about 10.0 g RTV-A and 1.0 g RTV-B (10:1 ratio) in a cup, then place in mixer and mix.
15. Set spinner to spin at 6,000 rpm for 6 min.
16. Remove blank wafer and place on spinner, pour on PDMS, and spin.
17. Remove from spinner and place in Petri dish.
18. Stamp the cover layer portion onto the liquid blank wafer and leave for 30 s.
19. Remove from wafer, and stick on top of the bath portion.

20. Remove bubbles between layers.
21. Leave chips to cure at room temperature overnight on ball bearings and place them in the oven the next day.

*After this step, the chips can be left in the oven.*

## Hole Punch and Bonding to Glass

22. Remove chips from the oven and punch appropriate holes with a clean bit.
23. Clean glass slides with IPA and PDMS chips with Scotch tape.
24. Use plasma bonder to bond together chips and glass slides (25 s).
25. Cure at 80 $^{o}$C in oven overnight.

*The total curing time at 80 $^{o}$C should equal at least 5 days before testing of chips, and chips should be 12 days old and autoclaved before use for cell culture.*

# Appendix C Rate of Water Loss from the Iso-Osmotic Bath

Water vapor loss from the osmotic bath may be modeled as a near-Fickian diffusion and has a flux given by:

$$J = -D\nabla C \tag{C.1}$$

where $D$ is the diffusion constant of water vapor in PDMS (~$8.5 \times 10^{-10}$ $m^2$ $s^{-1}$)[87] and $C$ is the concentration of water vapor in the bulk PDMS.

The iso-osmotic bath covers the area of the array (20 mm × 11 mm) and has a height of ~5 mm. The majority of vapor loss occurs through the top surface of the chamber that is sealed with a 1 mm thick layer of PDMS and through the long and short sides of the bath that are sealed with 5 mm and 3 mm thick edges of PDMS respectively. This is well approximated as a one-dimensional diffusion for problem given by:

$$J = -D\Delta C / L \tag{C.2}$$

where $L$ is the thickness of the PDMS sealing the top and 4 sides of the osmotic bath.

We assume a saturated water vapor concentration on the inside surface of the PDMS membrane (~40 mol $m^{-3}$)[87]. Assuming a 90% relative humidity in the incubator, the approximated water vapor concentration at the outside surface of the chip is 0.9 × 40 mol $m^{-3}$ = 36 mol $m^{-3}$, giving a total vapor flux of ~2 × $10^{-8}$ g $s^{-1}$. This corresponds to a loss of 9 μl over a 5-day experiment. Given a total osmotic bath volume of 1.1 ml this results in approximately 0.8 % change in osmotic strength during an experiment.

# Appendix D Genealogical Pedigrees of E-SLAM Cells

| Frame | Well | Clone rank | Population | EPCR intensity | Repopulating activity |
|---|---|---|---|---|---|
| 7 | 4 | 1 | EPCR$^+$ | 1117.5 | Yes |

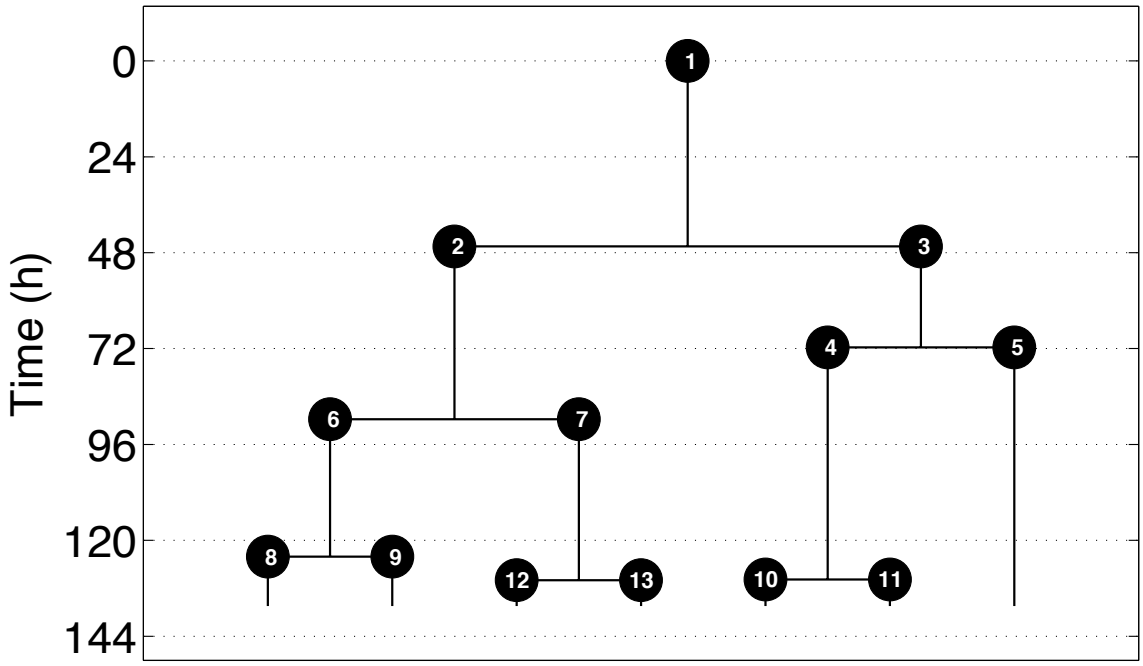

| Frame | Well | Clone rank | Population | EPCR intensity | Repopulating activity |
|---|---|---|---|---|---|
| 25 | 4 | 2 | EPCR$^+$ | 1070.8 | No |

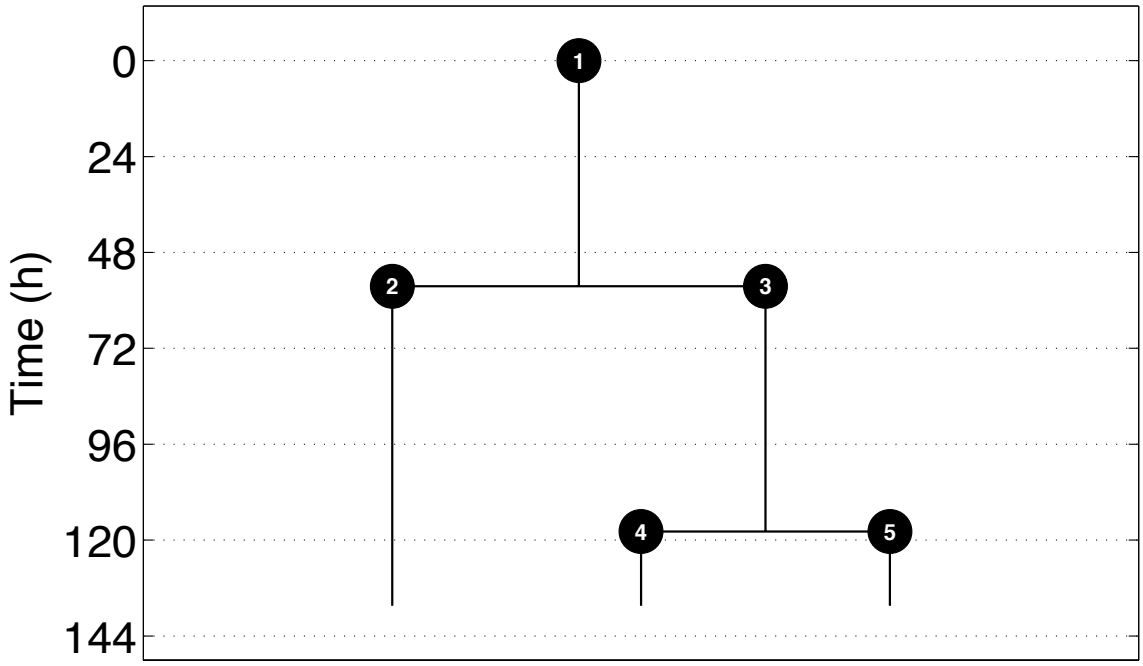


| Frame | Well | Clone rank | Population | EPCR intensity | Repopulating activity |
|---|---|---|---|---|---|
| 35 | 4 | 3 | EPCR$^+$ | 996.8 | N/A |

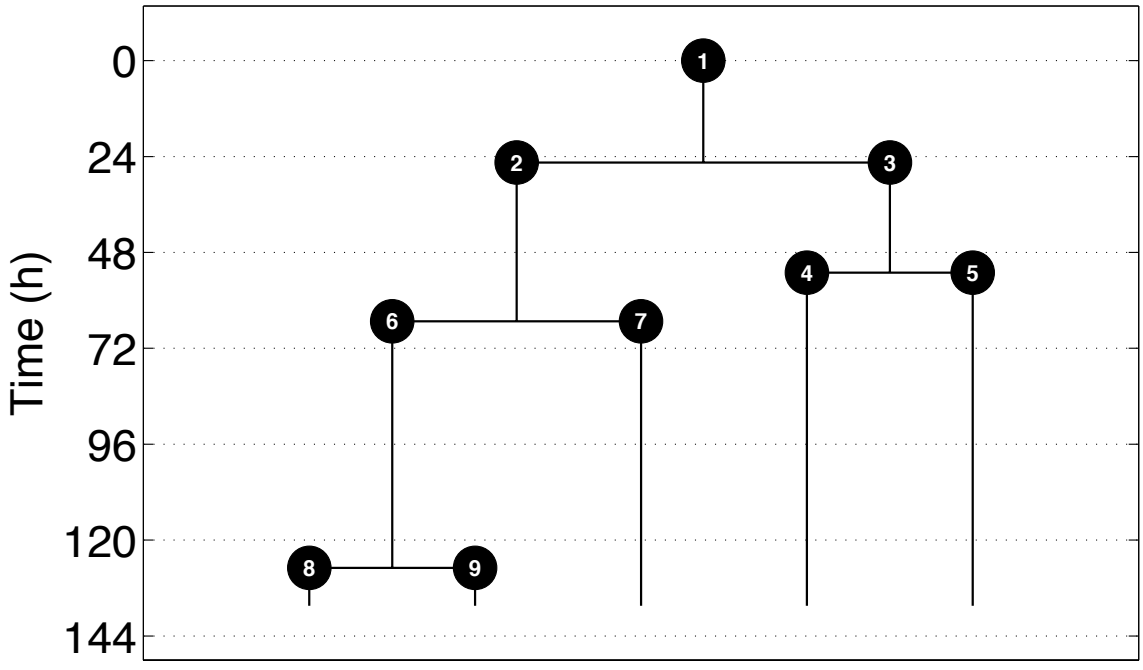

| Frame | Well | Clone rank | Population | EPCR intensity | Repopulating activity |
|---|---|---|---|---|---|
| 40 | 3 | 4 | EPCR$^+$ | 982.3 | Yes |

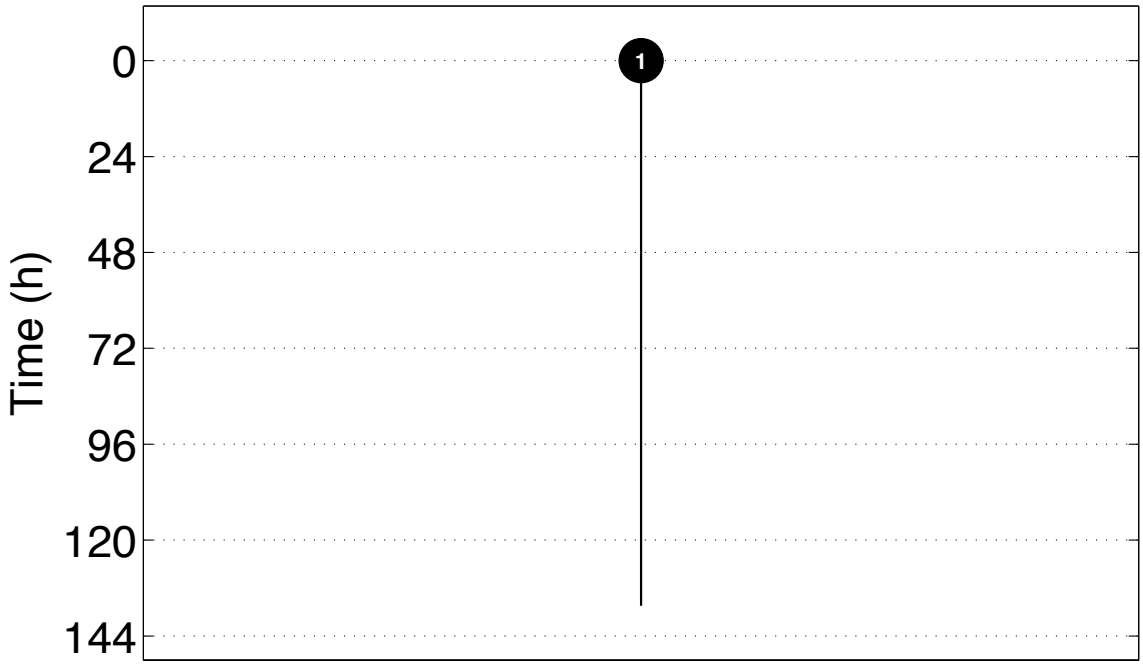


| Frame | Well | Clone rank | Population | EPCR intensity | Repopulating activity |
|---|---|---|---|---|---|
| 45 | 2 | 5 | EPCR$^+$ | 932.0 | Yes |

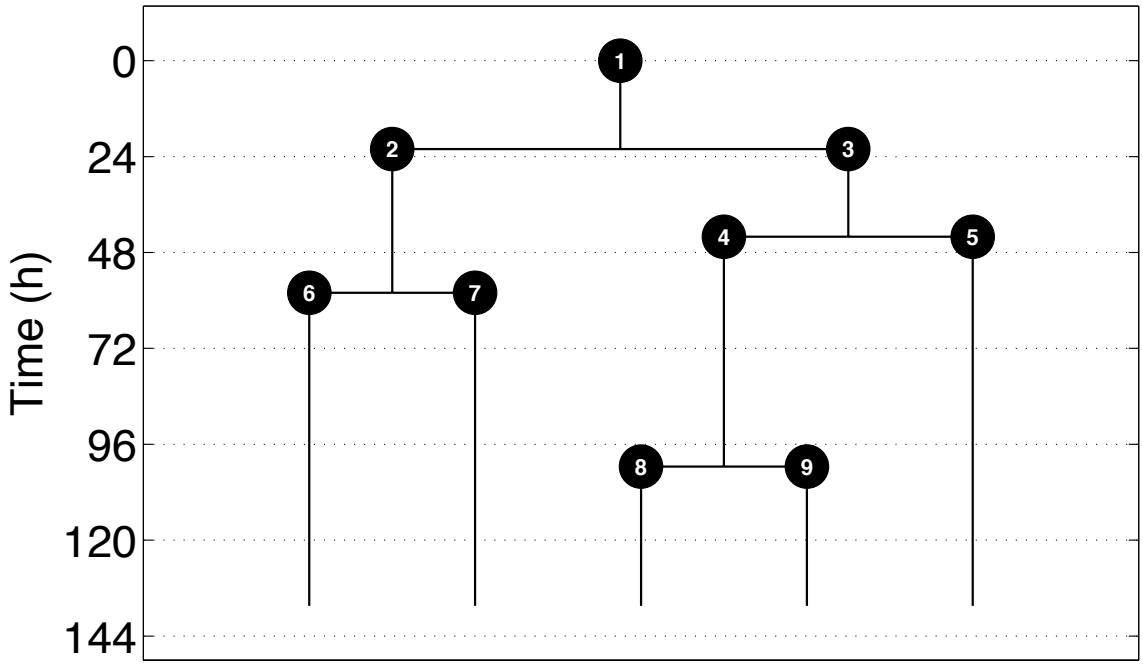

| Frame | Well | Clone rank | Population | EPCR intensity | Repopulating activity |
|---|---|---|---|---|---|
| 41 | 1 | 6 | EPCR+ | 927.1 | N/A |

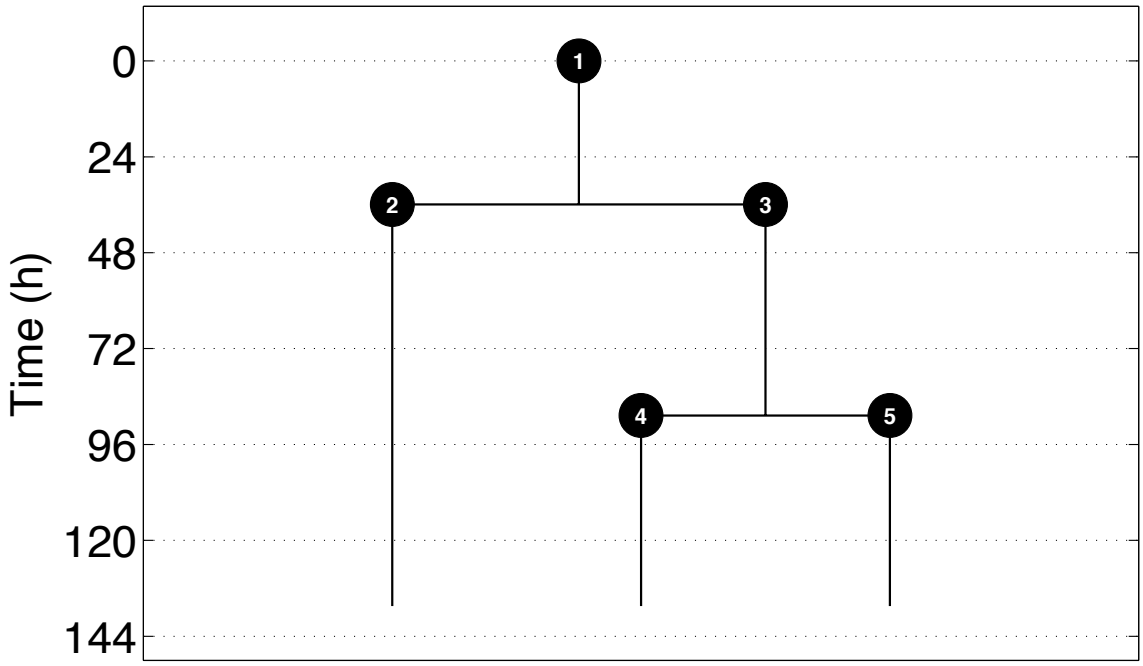


| Frame | Well | Clone rank | Population | EPCR intensity | Repopulating activity |
|---|---|---|---|---|---|
| 23 | 2 | 7 | EPCR+ | 901.7 | N/A |

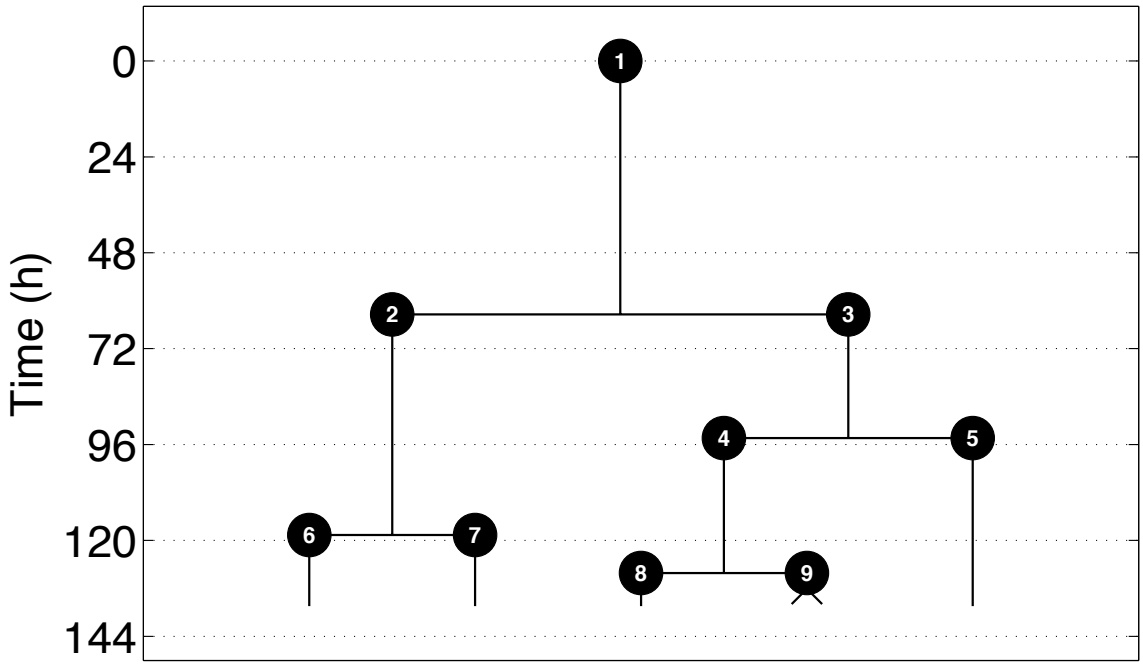

| Frame | Well | Clone rank | Population | EPCR intensity | Repopulating activity |
|---|---|---|---|---|---|
| 44 | 3 | 8 | EPCR$^+$ | 901.0 | N/A |

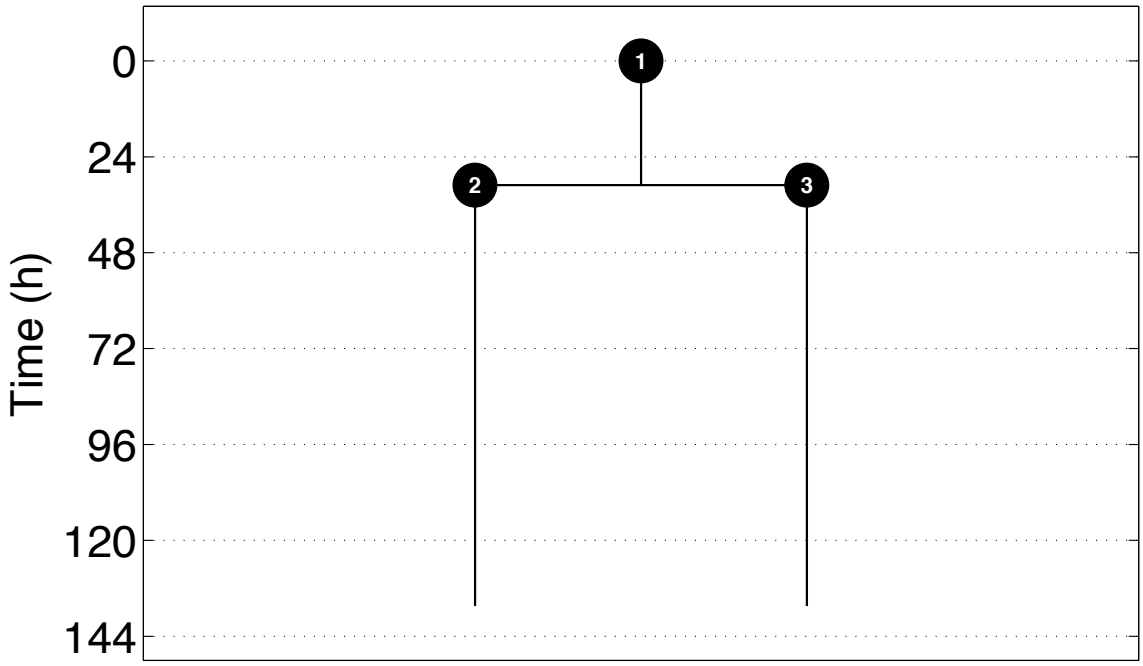


| Frame | Well | Clone rank | Population | EPCR intensity | Repopulating activity |
|---|---|---|---|---|---|
| 38 | 1 | 9 | EPCR$^+$ | 870.1 | N/A |

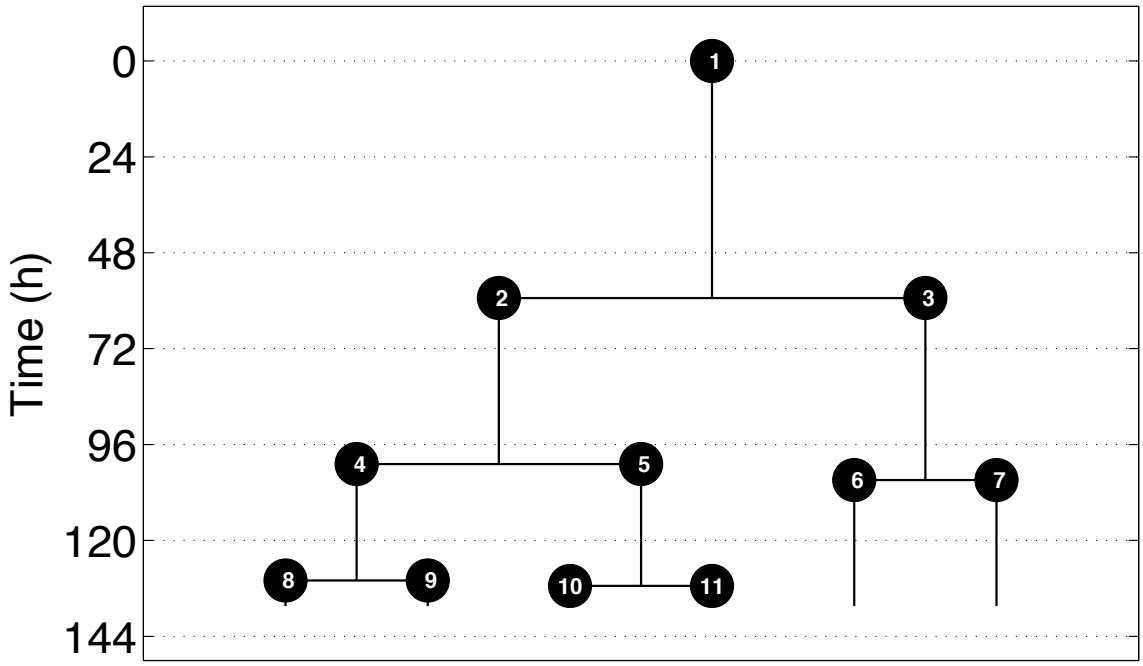

| Frame | Well | Clone rank | Population | EPCR intensity | Repopulating activity |
|---|---|---|---|---|---|
| 31 | 2 | 10 | EPCR$^+$ | 853.5 | N/A |

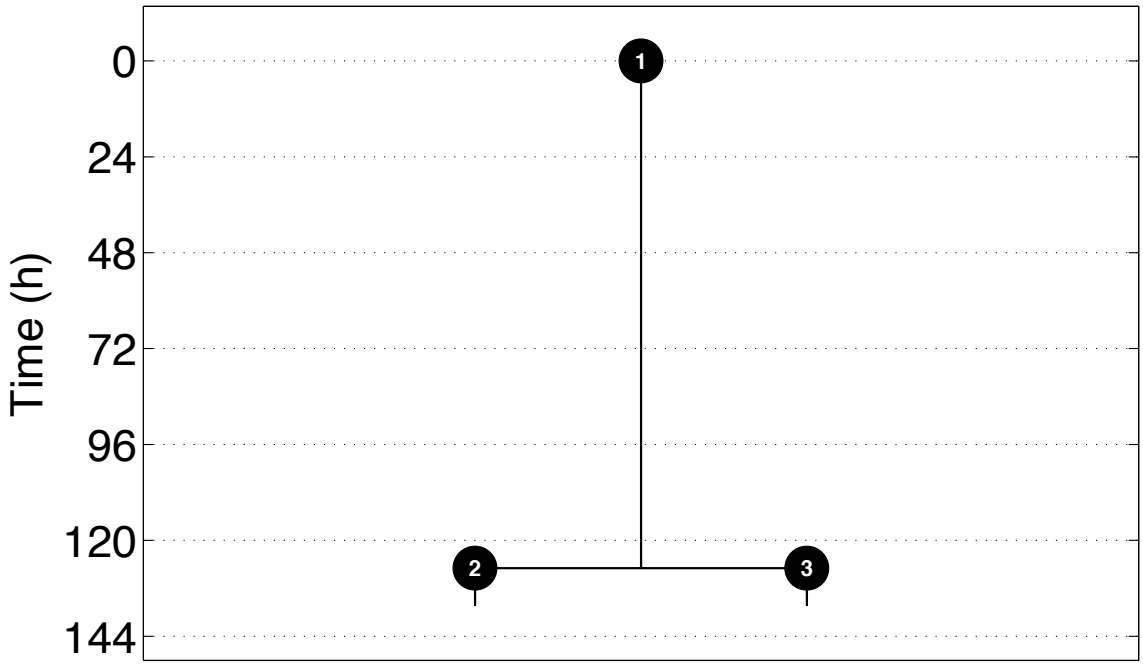


| Frame | Well | Clone rank | Population | EPCR intensity | Repopulating activity |
|---|---|---|---|---|---|
| 10 | 2 | 11 | EPCR$^+$ | 834.5 | Yes |

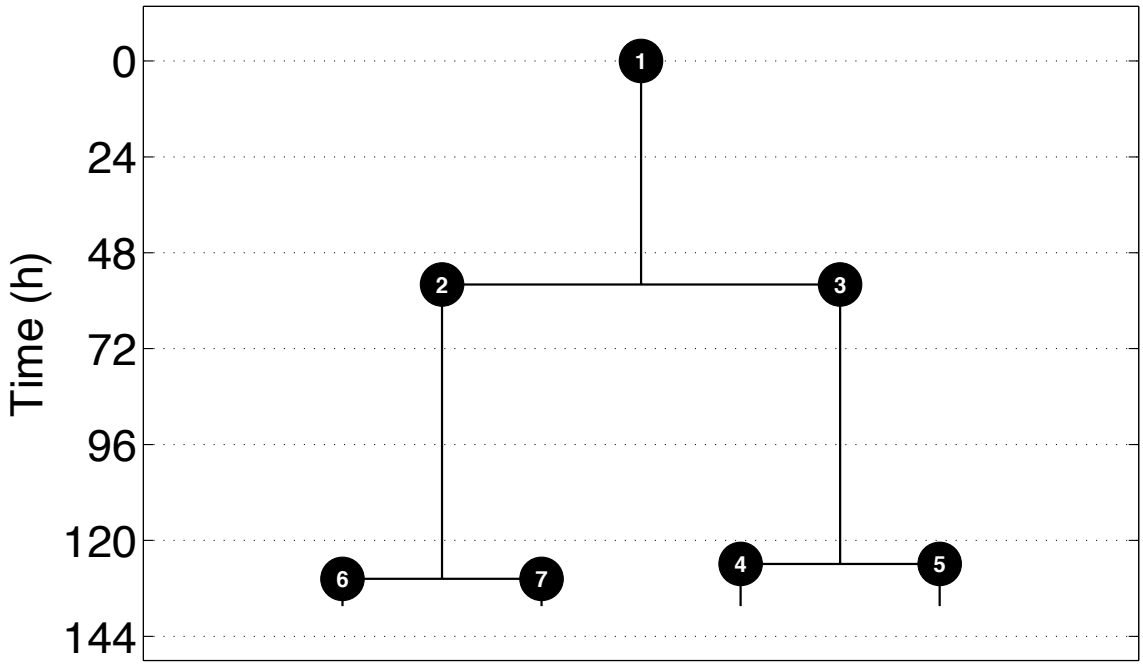

| Frame | Well | Clone rank | Population | EPCR intensity | Repopulating activity |
|---|---|---|---|---|---|
| 46 | 3 | 12 | EPCR+ | 826.0 | N/A |

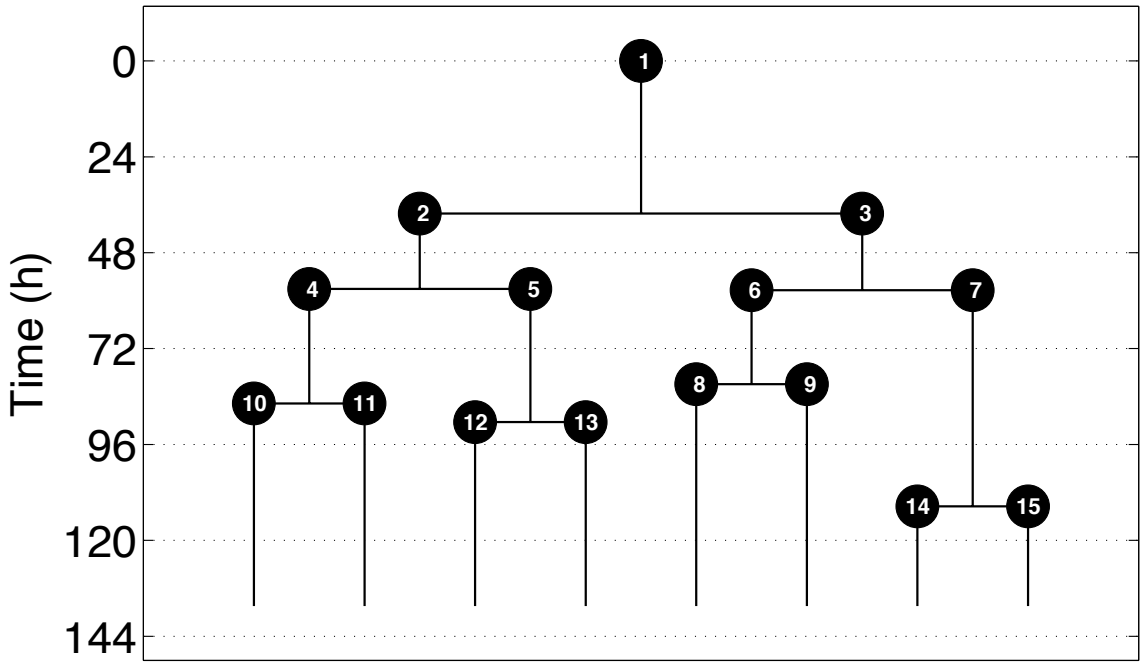


| Frame | Well | Clone rank | Population | EPCR intensity | Repopulating activity |
|---|---|---|---|---|---|
| 16 | 2 | 13 | EPCR+ | 745.4 | N/A |

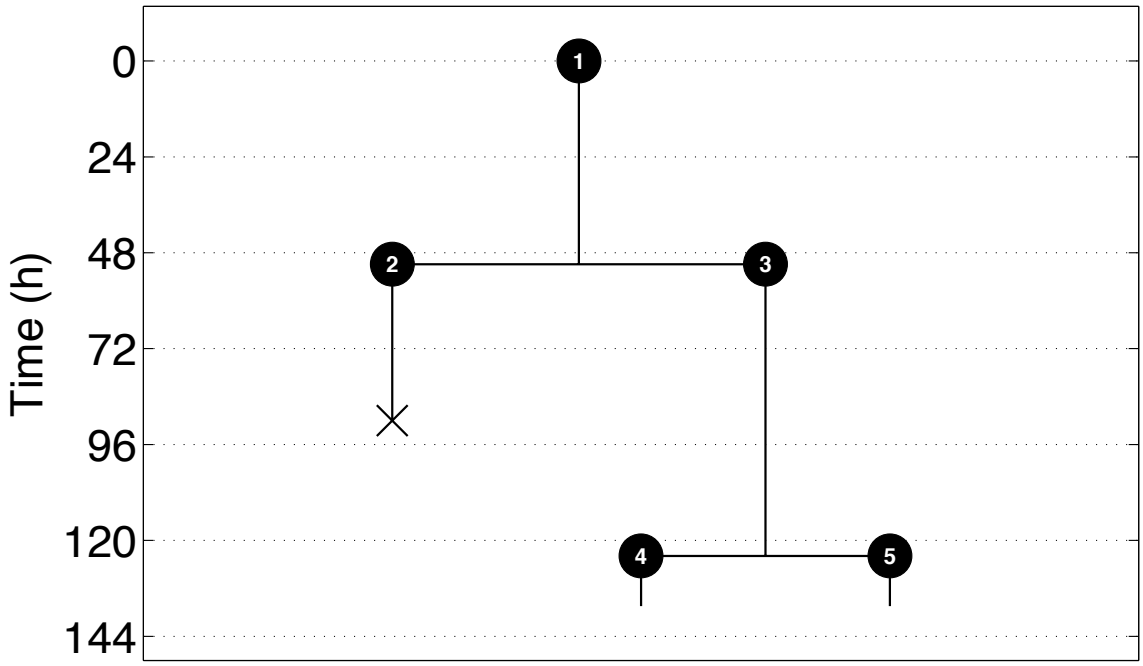

| Frame | Well | Clone rank | Population | EPCR intensity | Repopulating activity |
|---|---|---|---|---|---|
| 46 | 4 | 14 | EPCR$^+$ | 733.0 | N/A |

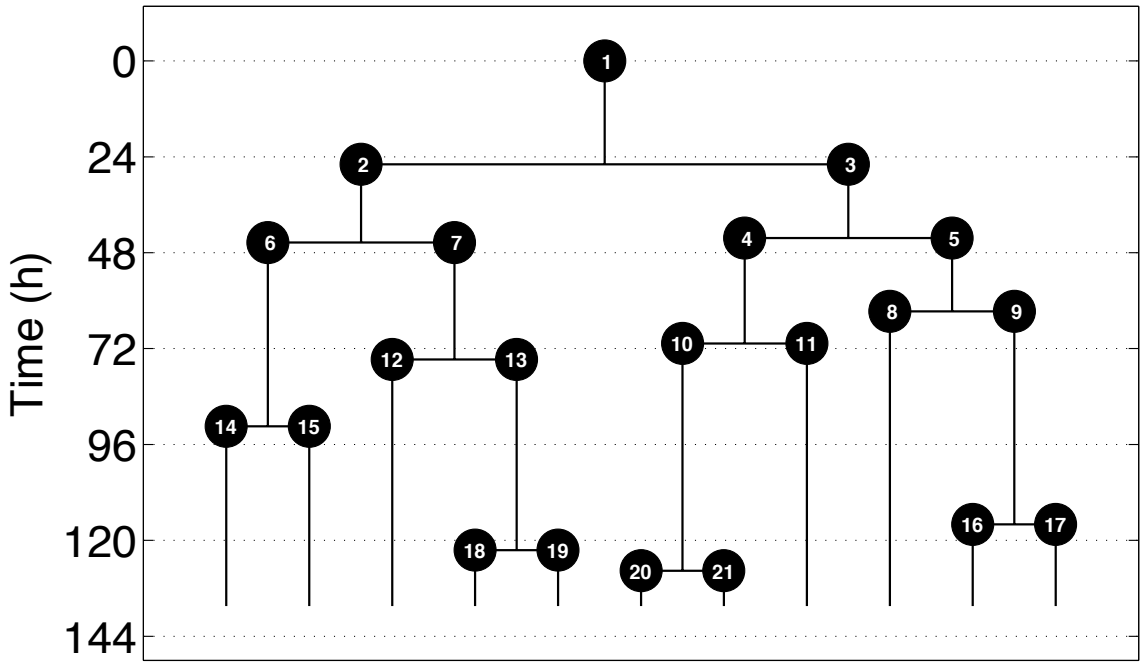


| Frame | Well | Clone rank | Population | EPCR intensity | Repopulating activity |
|---|---|---|---|---|---|
| 42 | 3 | 15 | EPCR$^+$ | 702.6 | N/A |

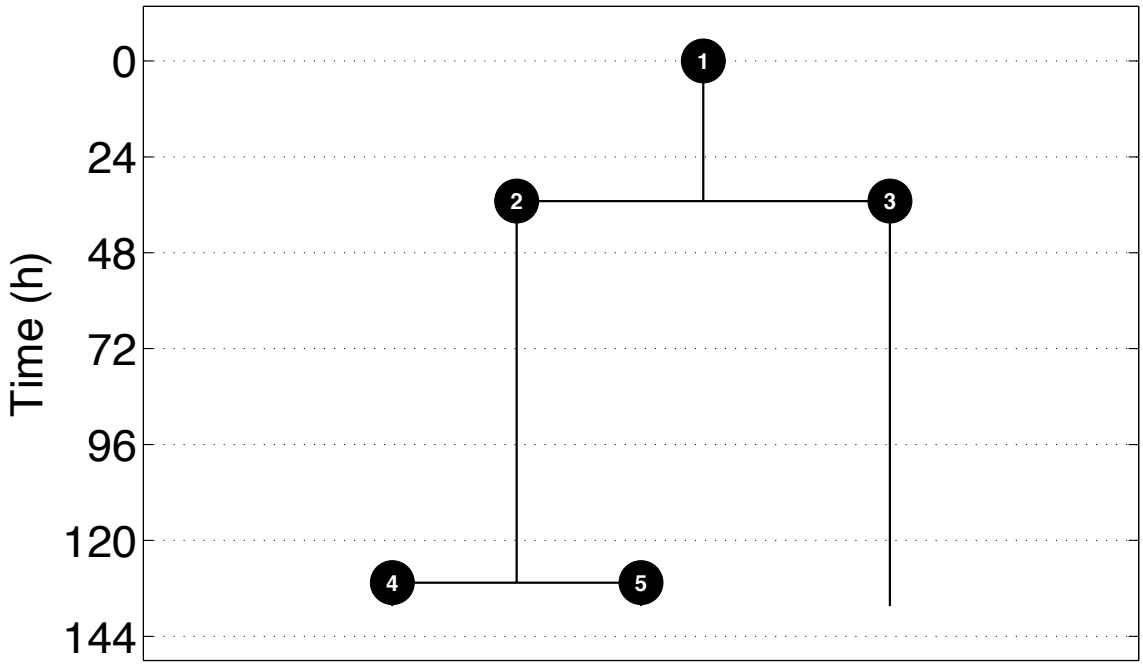

| Frame | Well | Clone rank | Population | EPCR intensity | Repopulating activity |
|---|---|---|---|---|---|
| 46 | 2 | 16 | EPCR$^+$ | 685.8 | N/A |

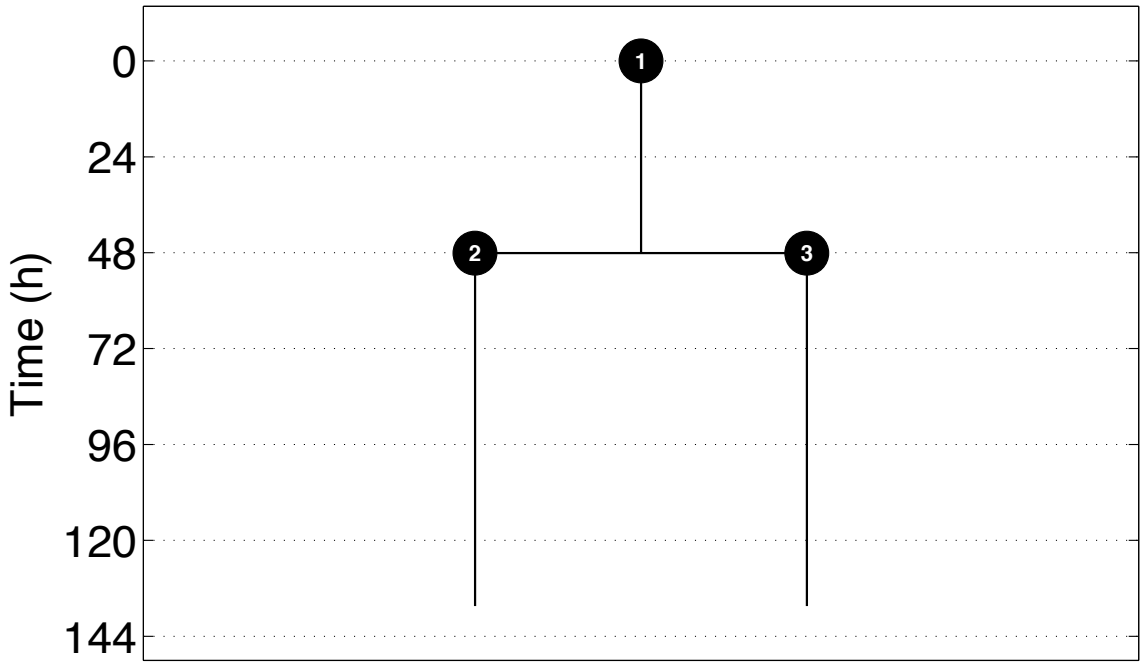


| Frame | Well | Clone rank | Population | EPCR intensity | Repopulating activity |
|---|---|---|---|---|---|
| 14 | 1 | 17 | EPCR$^+$ | 685.0 | Yes |

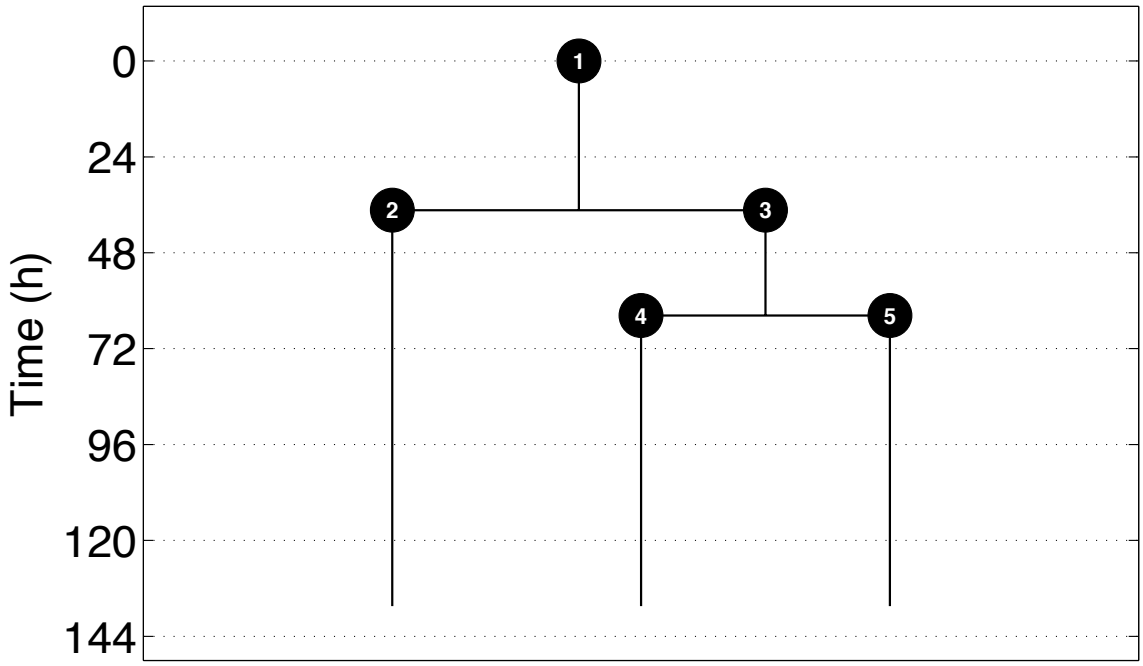

| Frame | Well | Clone rank | Population | EPCR intensity | Repopulating activity |
|---|---|---|---|---|---|
| 12 | 1 | 18 | EPCR+ | 680.6 | N/A |

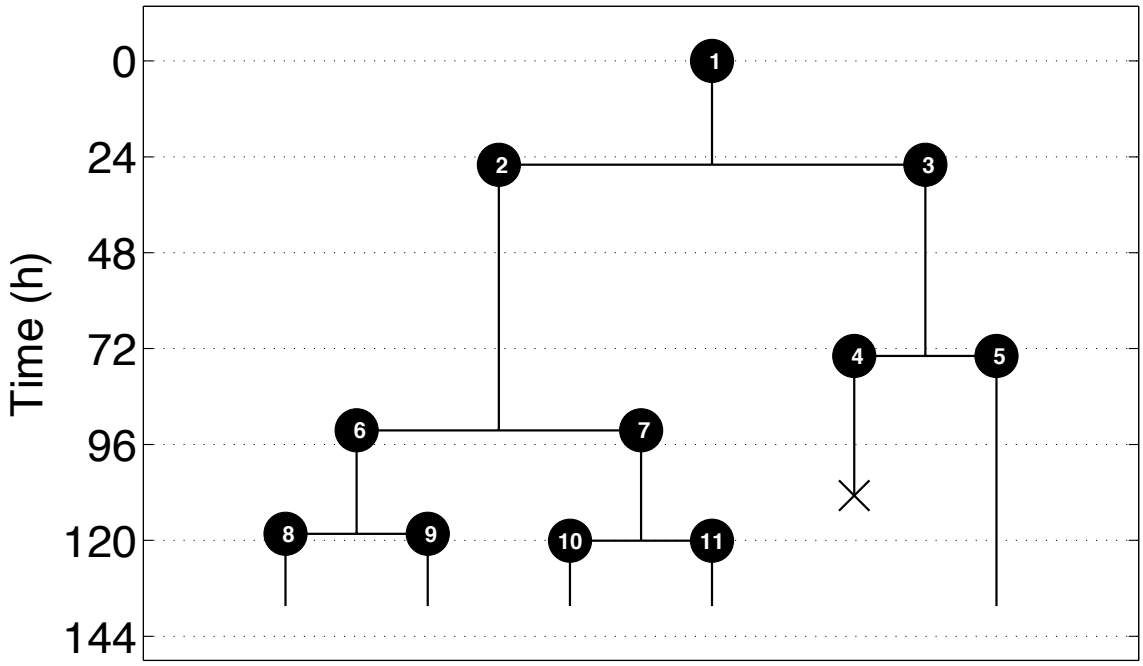


| Frame | Well | Clone rank | Population | EPCR intensity | Repopulating activity |
|---|---|---|---|---|---|
| 8 | 3 | 19 | EPCR+ | 656.9 | N/A |

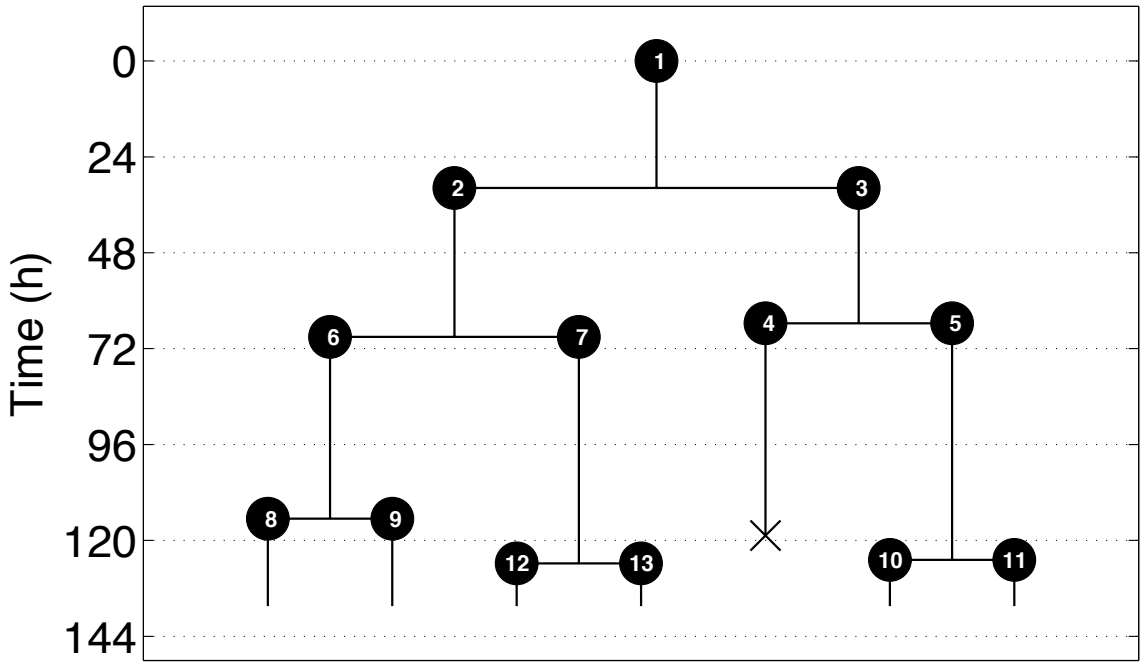

| Frame | Well | Clone rank | Population | EPCR intensity | Repopulating activity |
|---|---|---|---|---|---|
| 39 | 1 | 20 | EPCR+ | 647.2 | N/A |

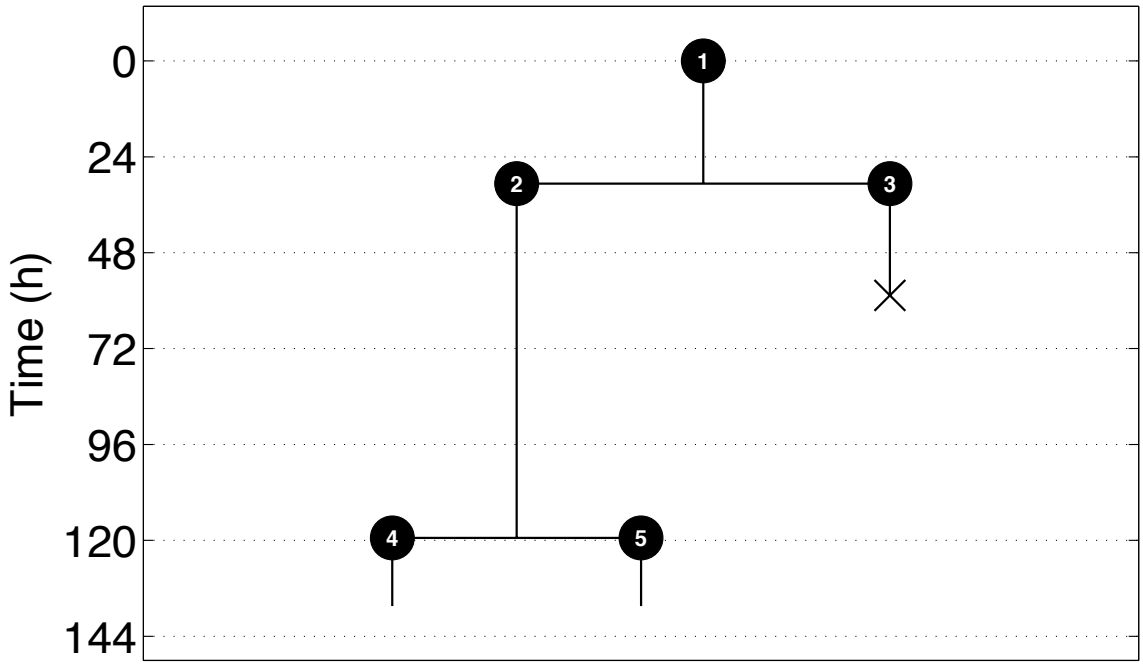


| Frame | Well | Clone rank | Population | EPCR intensity | Repopulating activity |
|---|---|---|---|---|---|
| 31 | 3 | 21 | EPCR+ | 620.8 | N/A |

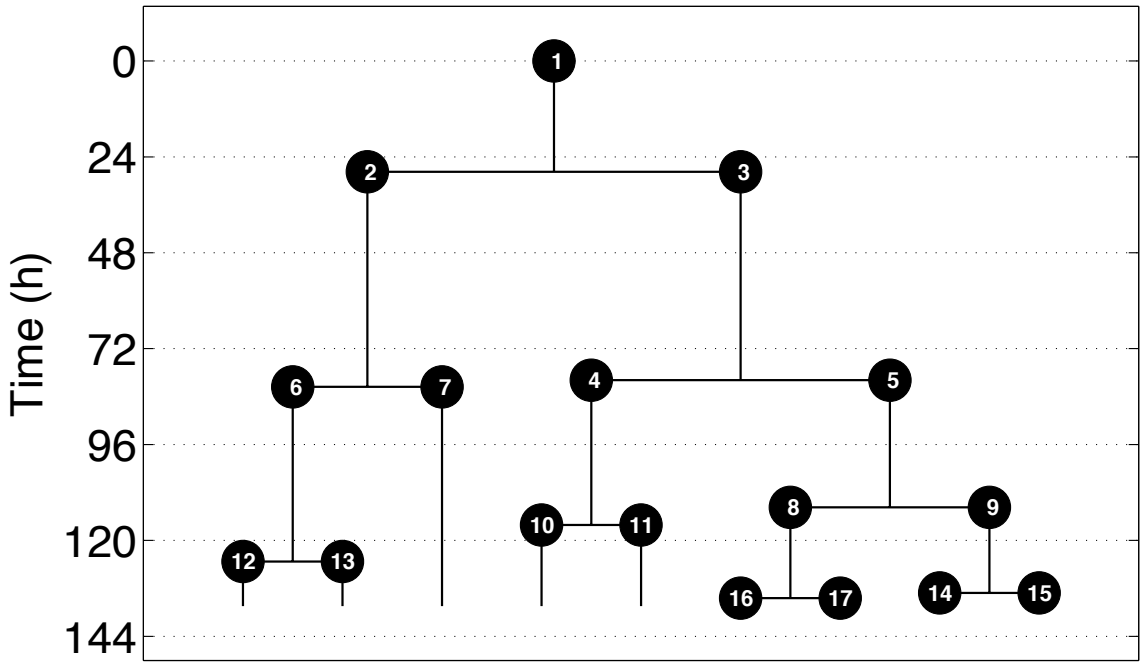

| Frame | Well | Clone rank | Population | EPCR intensity | Repopulating activity |
|---|---|---|---|---|---|
| 15 | 2 | 22 | EPCR+ | 619.6 | Yes |

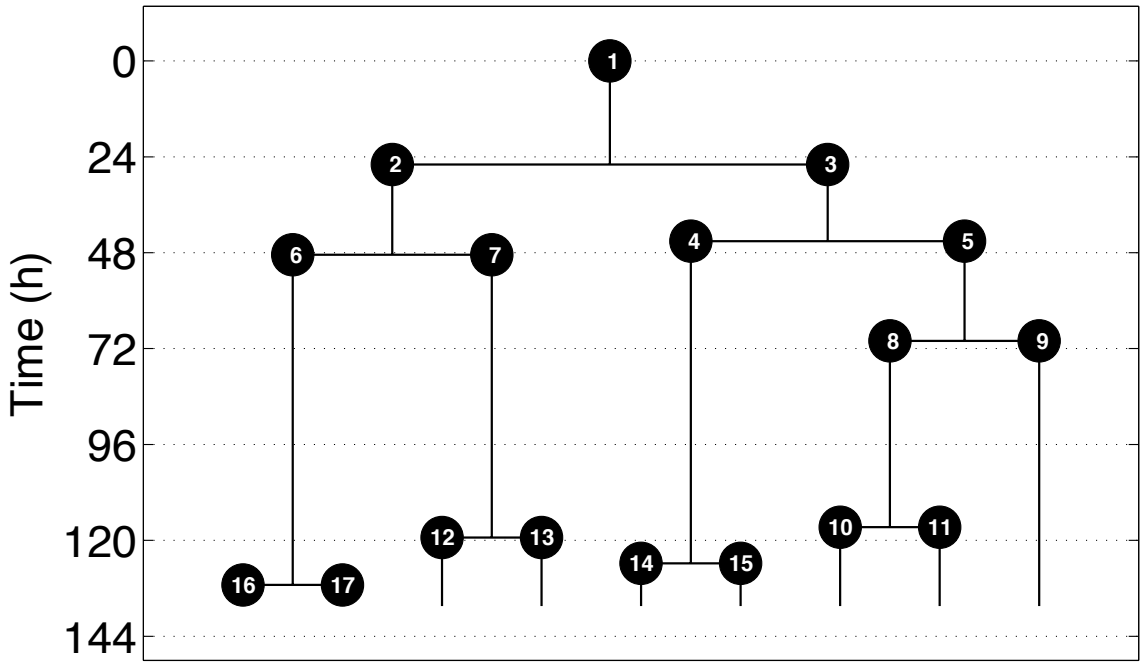


| Frame | Well | Clone rank | Population | EPCR intensity | Repopulating activity |
|---|---|---|---|---|---|
| 27 | 3 | 23 | EPCR+ | 594.6 | N/A |

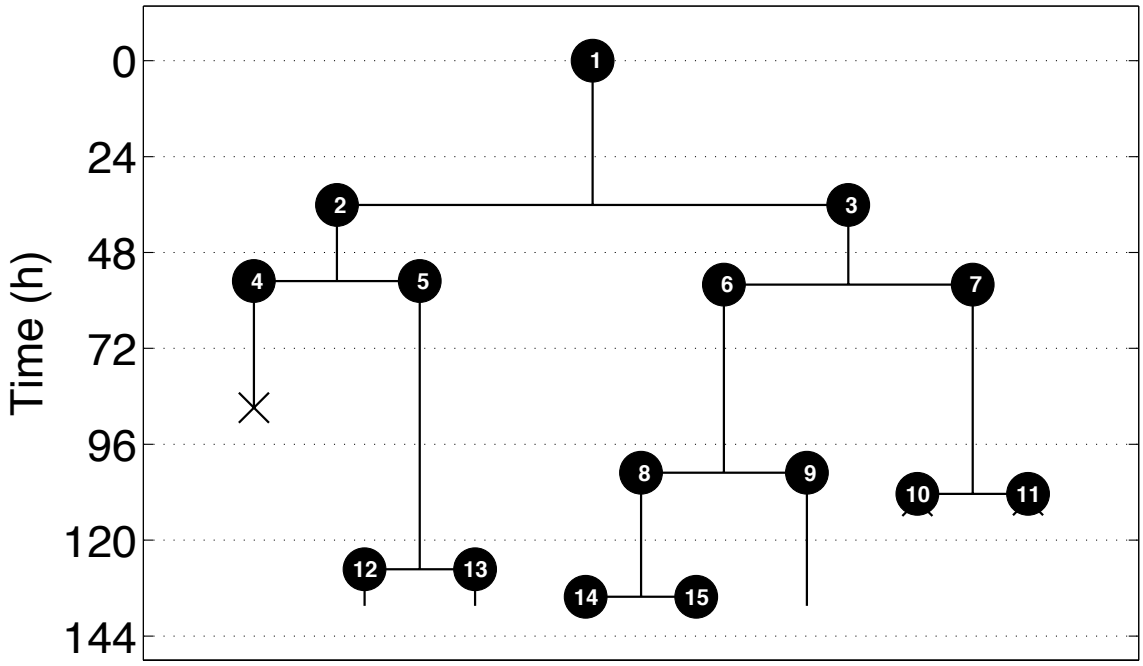

| Frame | Well | Clone rank | Population | EPCR intensity | Repopulating activity |
|---|---|---|---|---|---|
| 44 | 1 | 24 | EPCR+ | 591.8 | N/A |

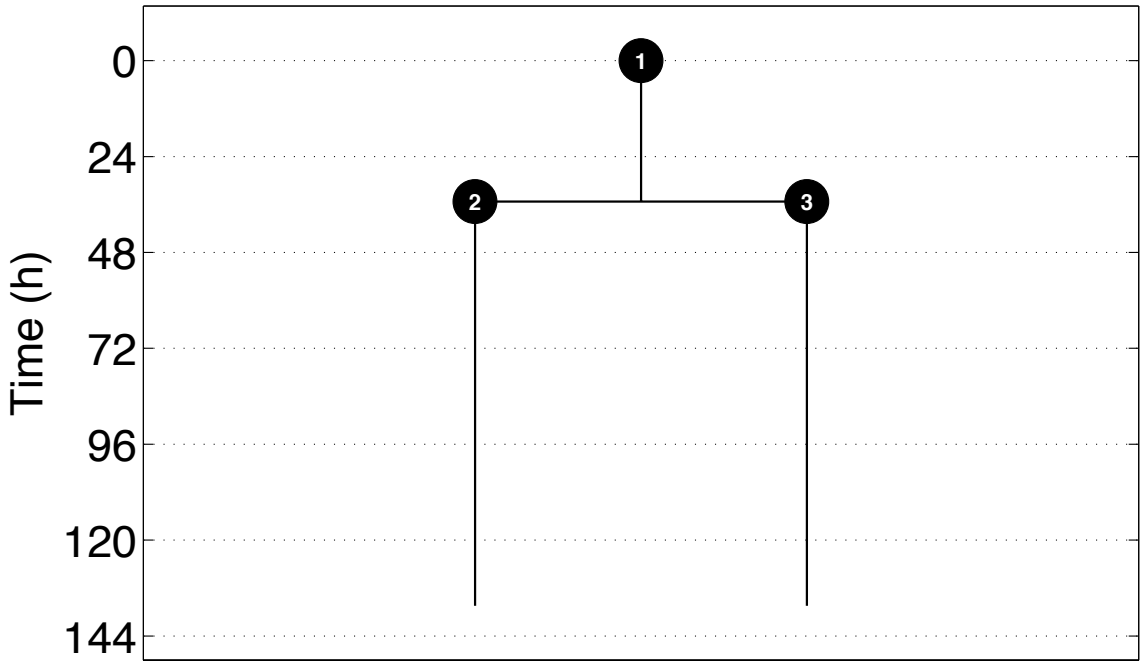


| Frame | Well | Clone rank | Population | EPCR intensity | Repopulating activity |
|---|---|---|---|---|---|
| 45 | 1 | 25 | EPCR+ | 579.4 | N/A |

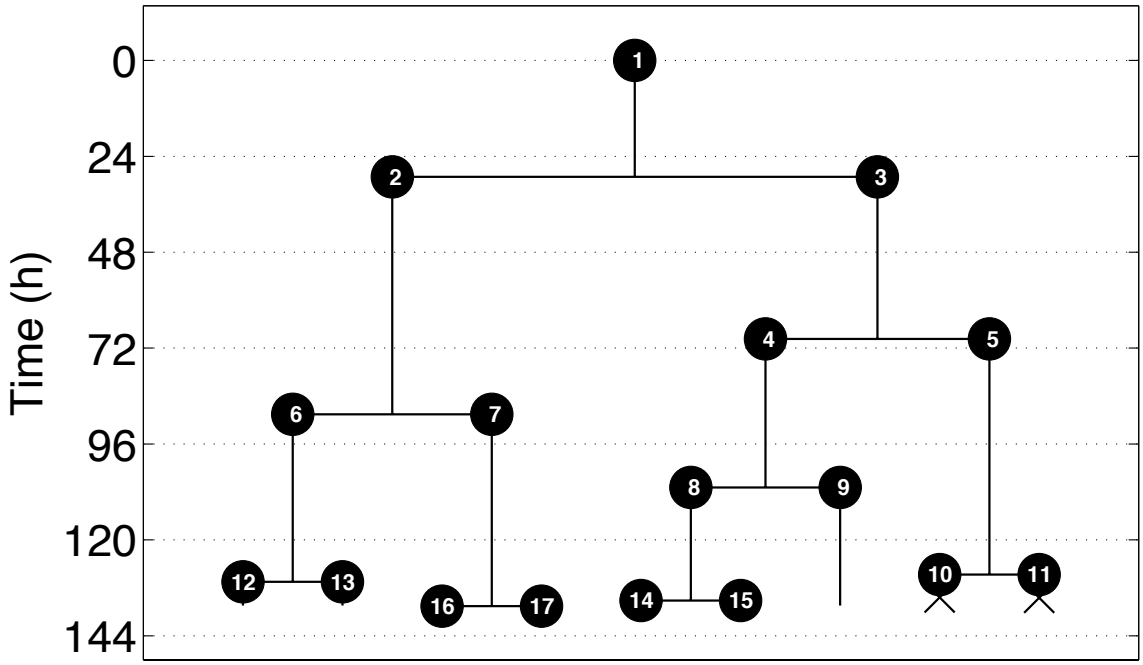

| Frame | Well | Clone rank | Population | EPCR intensity | Repopulating activity |
|---|---|---|---|---|---|
| 13 | 1 | 26 | EPCR+ | 574.7 | N/A |

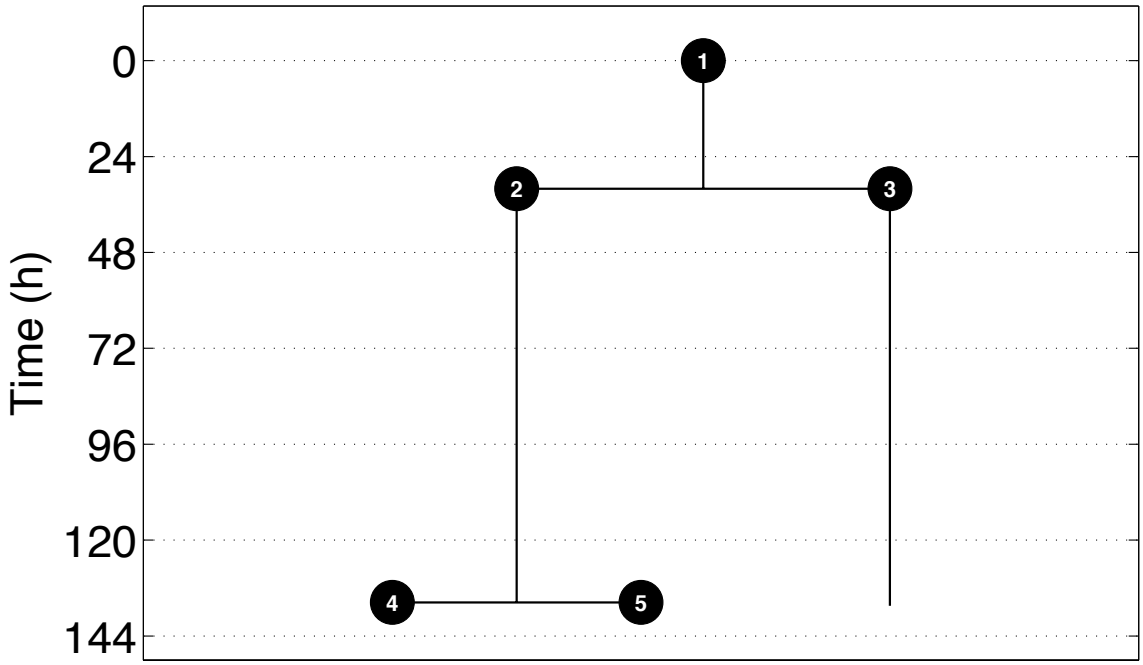


| Frame | Well | Clone rank | Population | EPCR intensity | Repopulating activity |
|---|---|---|---|---|---|
| 39 | 2 | 27 | EPCR+ | 574.2 | N/A |

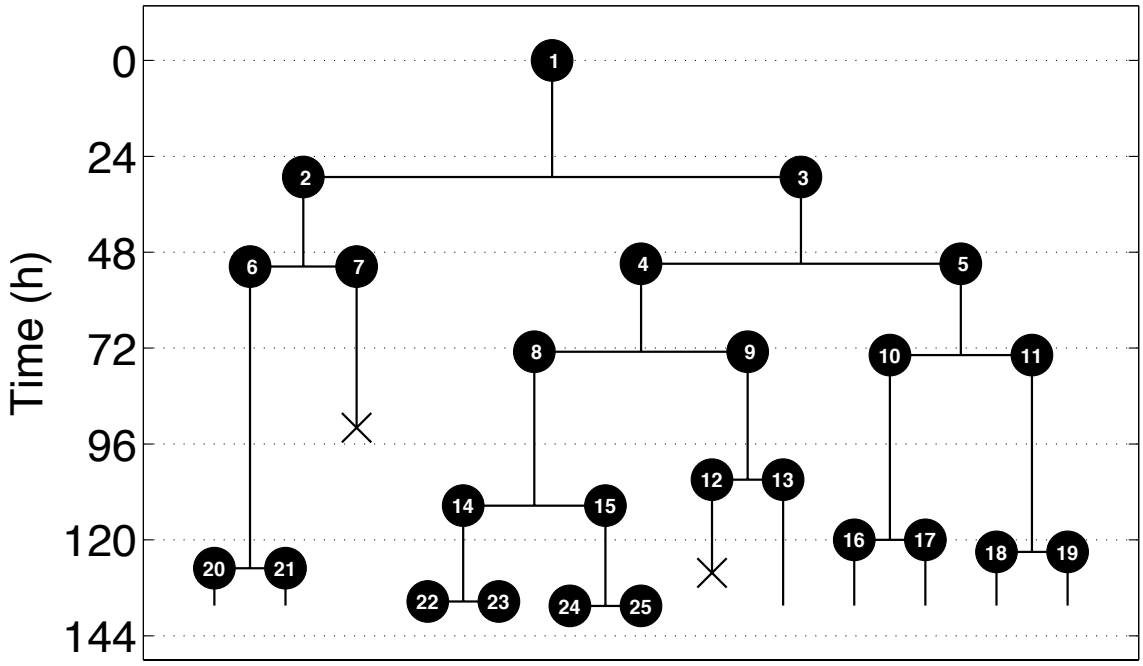

| Frame | Well | Clone rank | Population | EPCR intensity | Repopulating activity |
|---|---|---|---|---|---|
| 7 | 1 | 28 | EPCR+ | 572.1 | N/A |

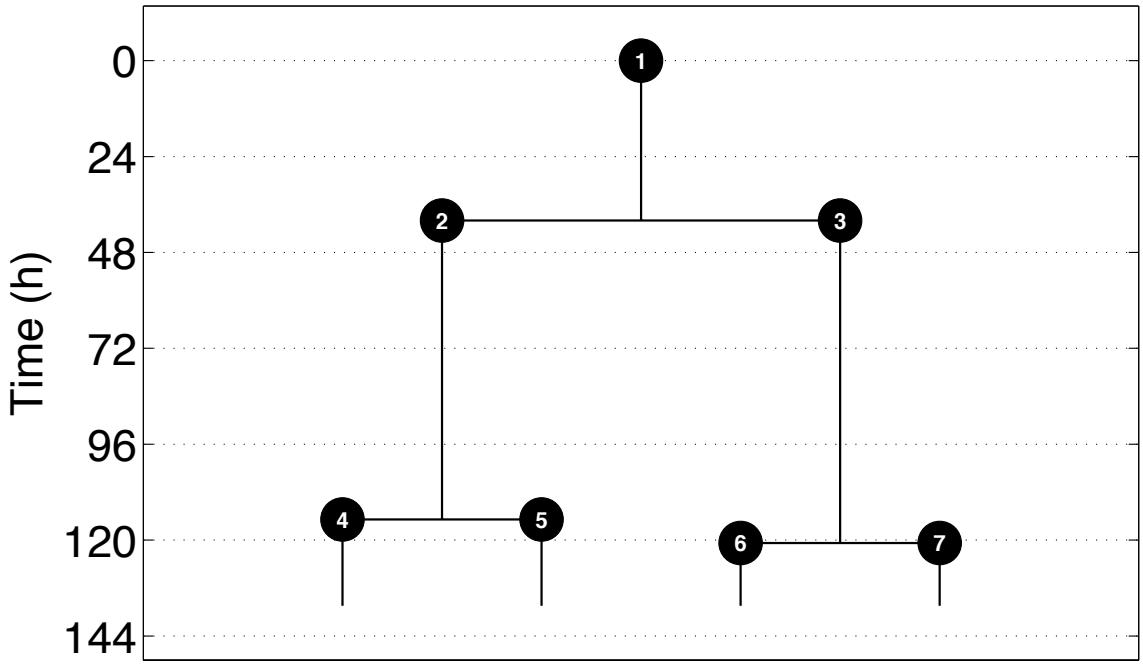


| Frame | Well | Clone rank | Population | EPCR intensity | Repopulating activity |
|---|---|---|---|---|---|
| 1 | 4 | 29 | EPCR+ | 569.0 | N/A |

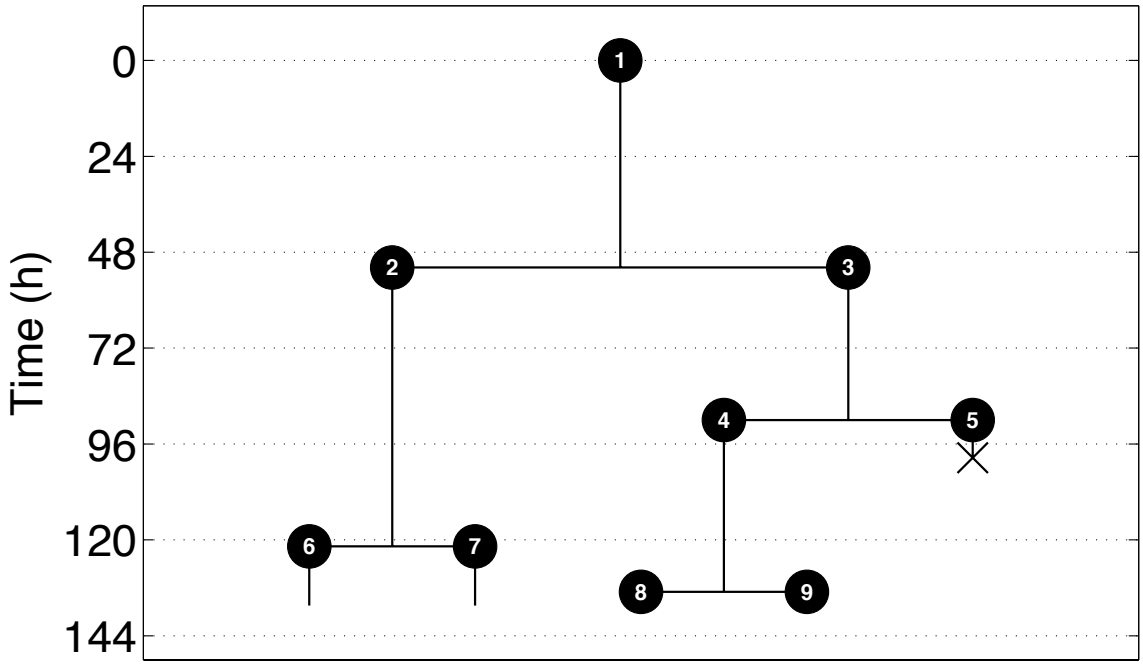

| Frame | Well | Clone rank | Population | EPCR intensity | Repopulating activity |
|---|---|---|---|---|---|
| 43 | 3 | 30 | EPCR+ | 568.6 | N/A |

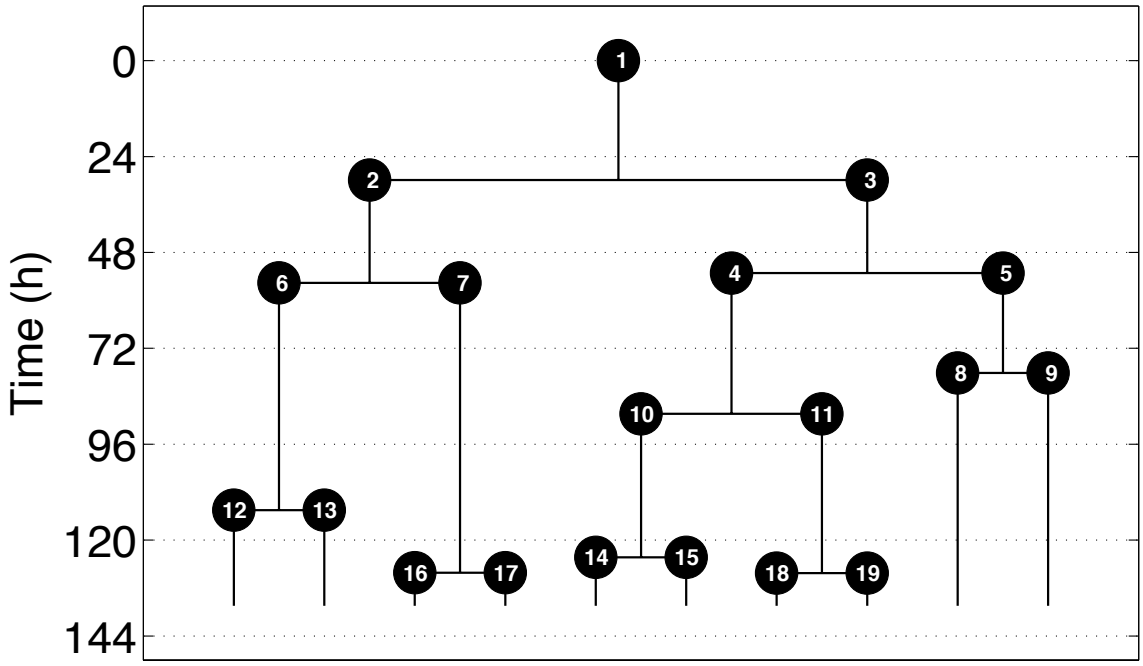


| Frame | Well | Clone rank | Population | EPCR intensity | Repopulating activity |
|---|---|---|---|---|---|
| 10 | 1 | 31 | EPCR+ | 553.9 | N/A |

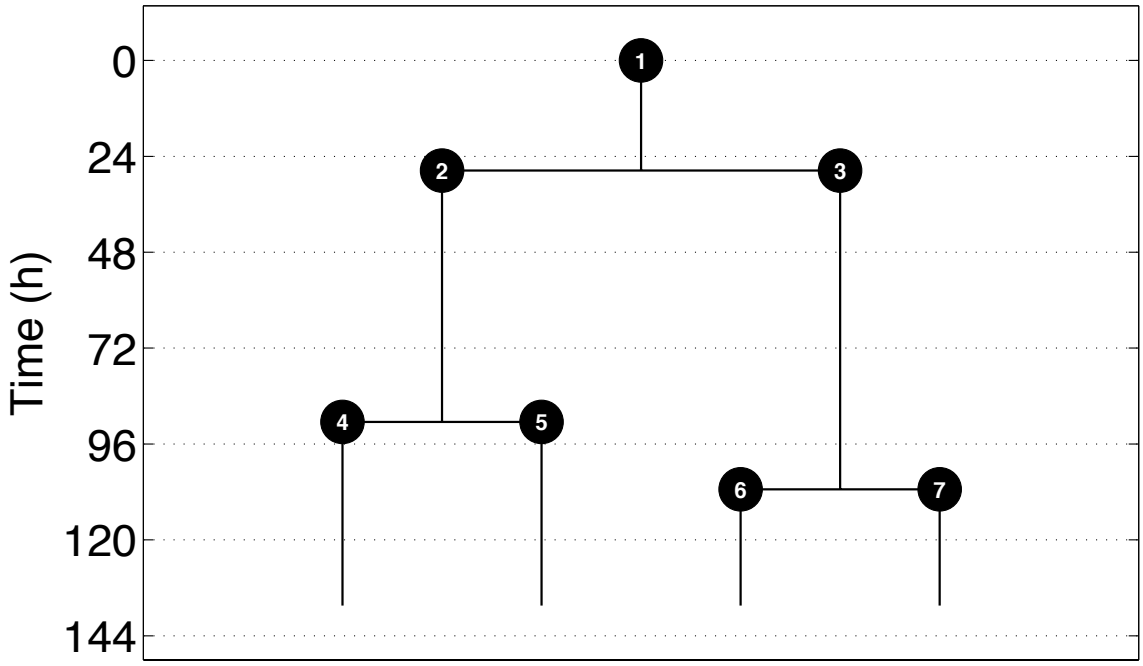

| Frame | Well | Clone rank | Population | EPCR intensity | Repopulating activity |
|---|---|---|---|---|---|
| 47 | 2 | 32 | EPCR+ | 545.5 | N/A |

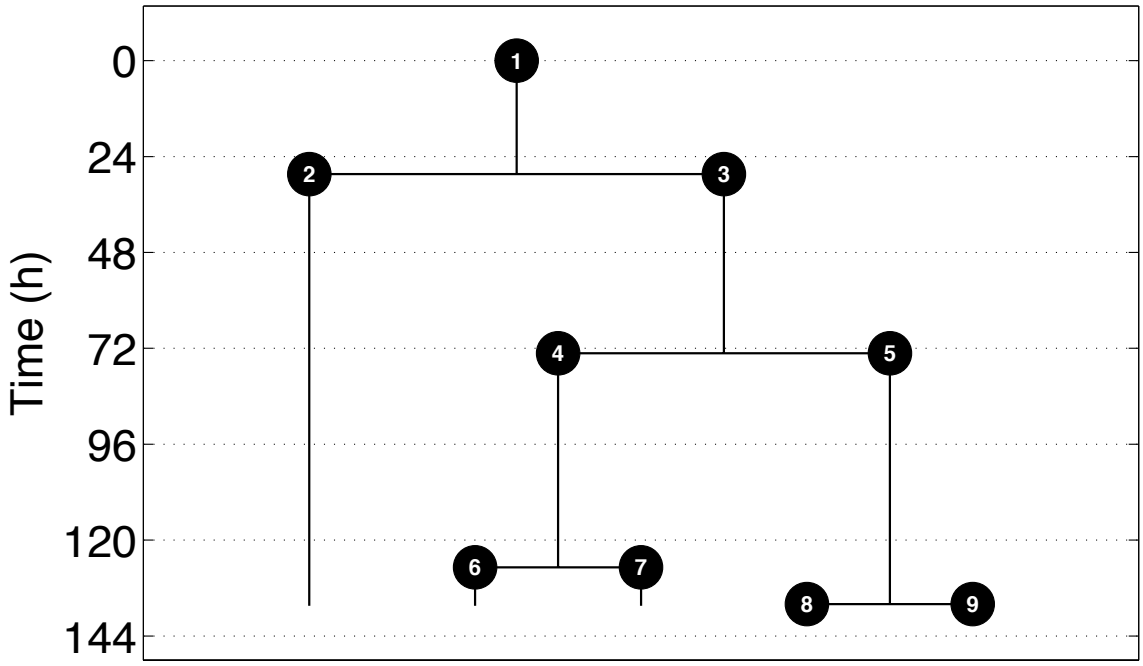


| Frame | Well | Clone rank | Population | EPCR intensity | Repopulating activity |
|---|---|---|---|---|---|
| 3 | 4 | 33 | EPCR+ | 543.2 | N/A |

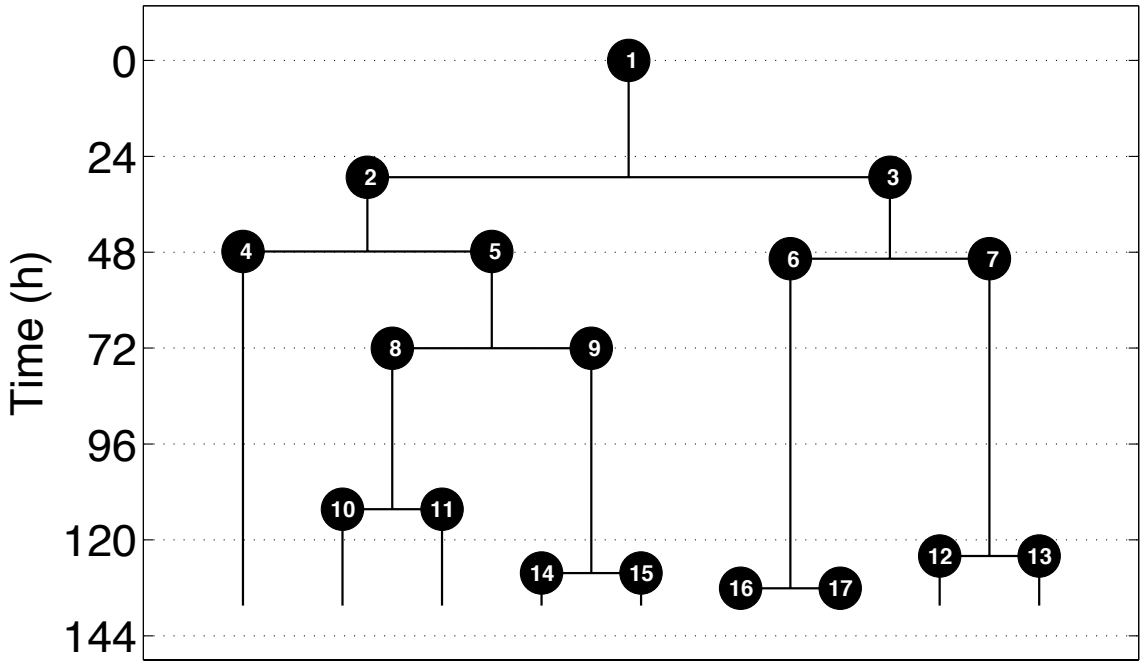

| Frame | Well | Clone rank | Population | EPCR intensity | Repopulating activity |
|---|---|---|---|---|---|
| 42 | 4 | 34 | EPCR+ | 479.3 | N/A |

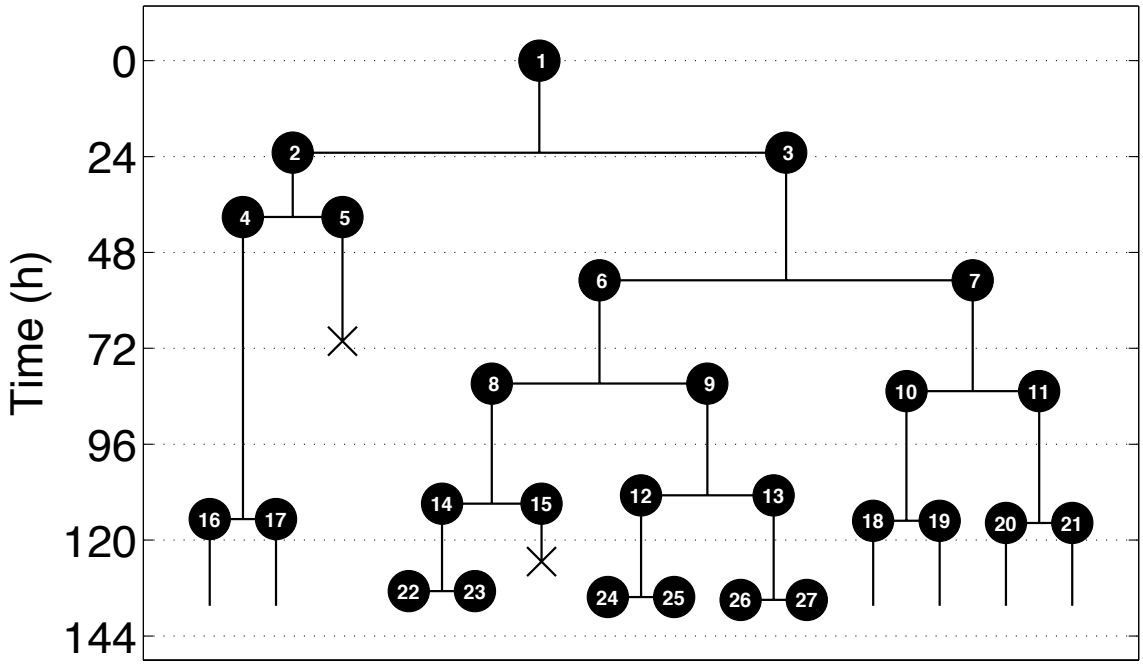


| Frame | Well | Clone rank | Population | EPCR intensity | Repopulating activity |
|---|---|---|---|---|---|
| 22 | 2 | 35 | EPCR+ | 474.7 | Yes |

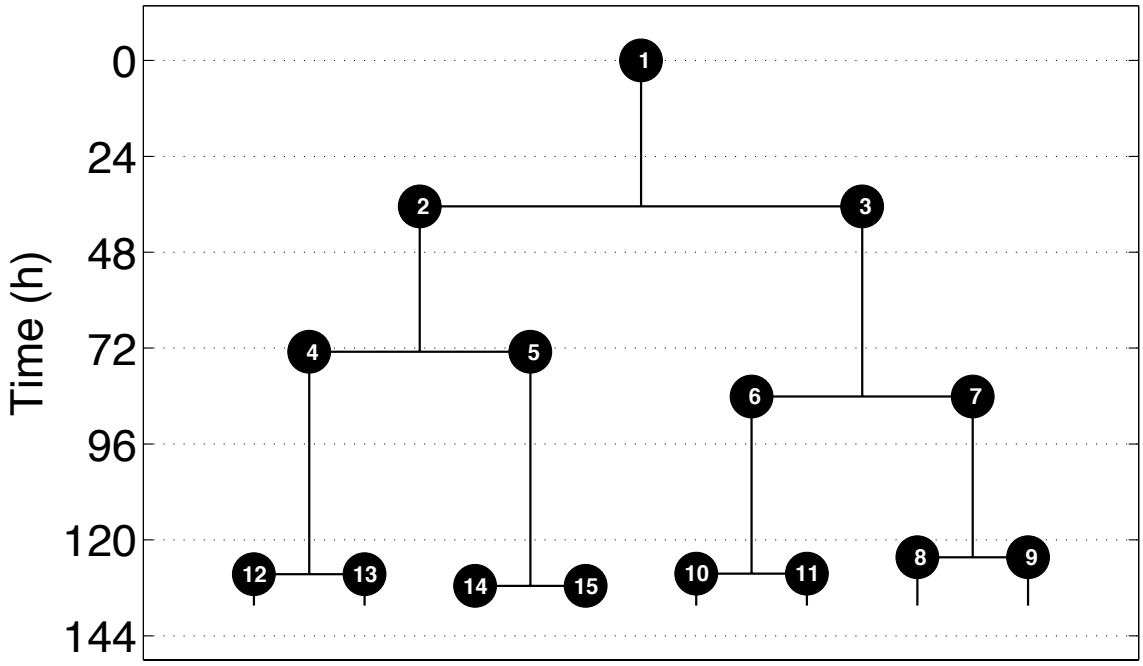

| Frame | Well | Clone rank | Population | EPCR intensity | Repopulating activity |
|---|---|---|---|---|---|
| 20 | 1 | 36 | EPCR+ | 469.0 | Yes |

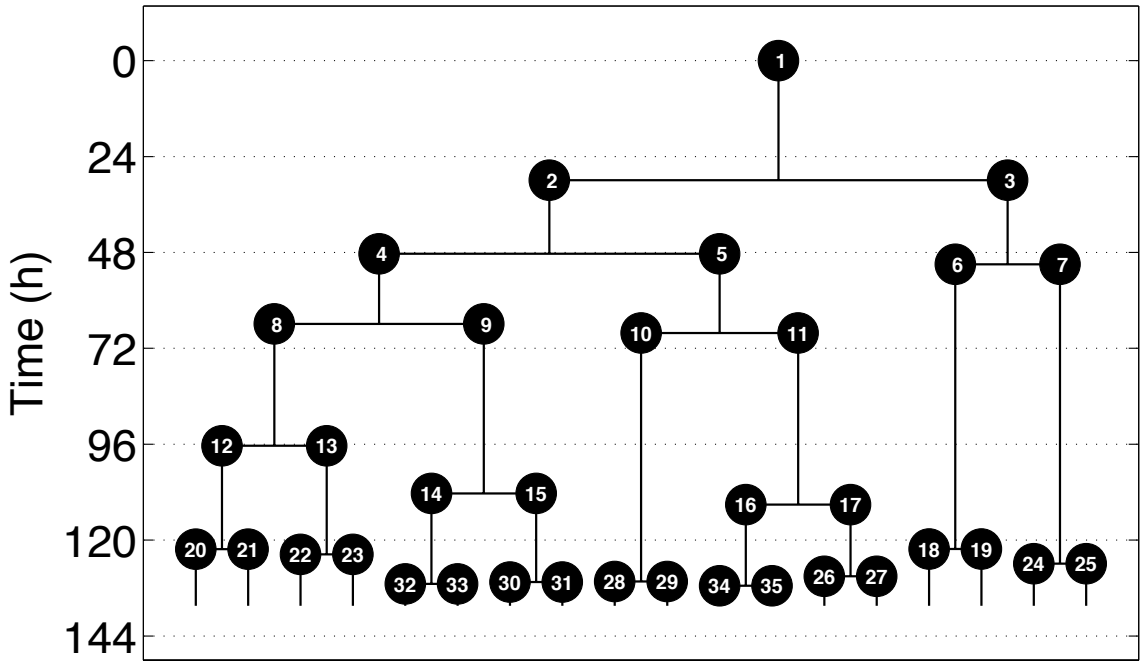


| Frame | Well | Clone rank | Population | EPCR intensity | Repopulating activity |
|---|---|---|---|---|---|
| 10 | 4 | 37 | EPCR+ | 463.7 | N/A |

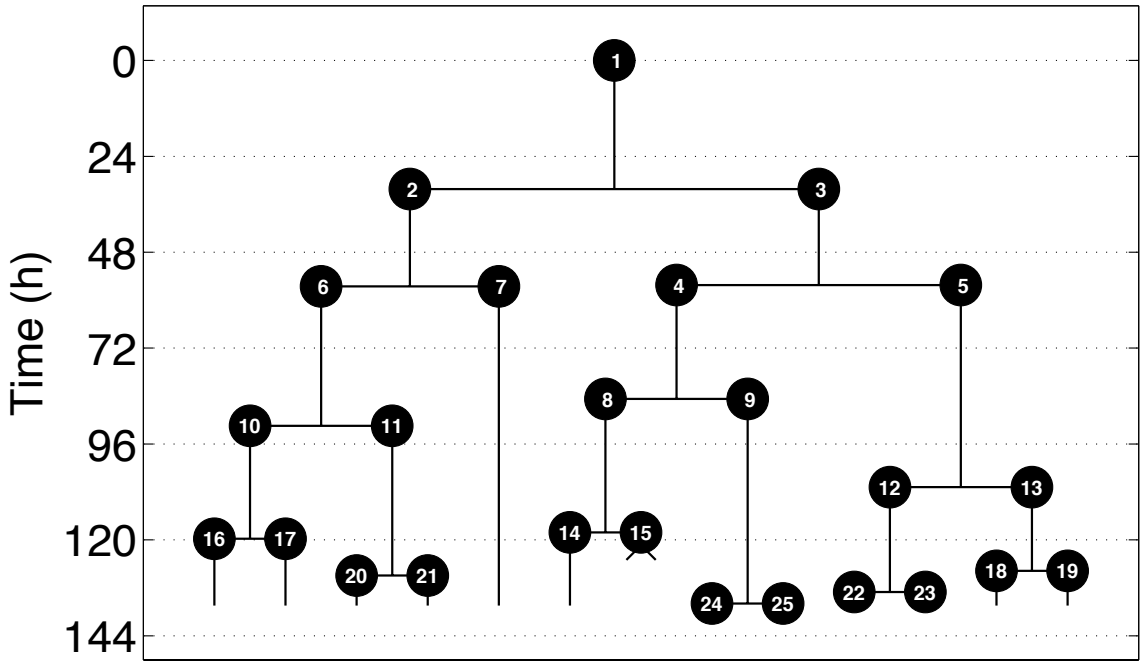

| Frame | Well | Clone rank | Population | EPCR intensity | Repopulating activity |
|---|---|---|---|---|---|
| 37 | 3 | 38 | EPCR$^-$ | 426.5 | N/A |

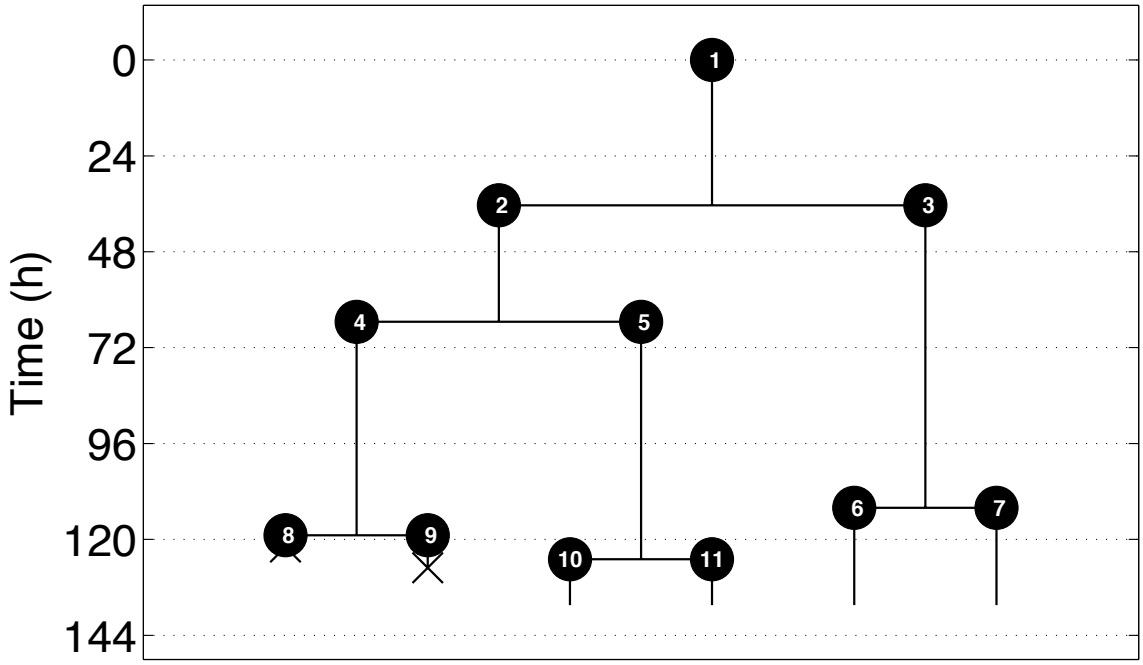


| Frame | Well | Clone rank | Population | EPCR intensity | Repopulating activity |
|---|---|---|---|---|---|
| 38 | 3 | 39 | EPCR$^-$ | 422.6 | N/A |

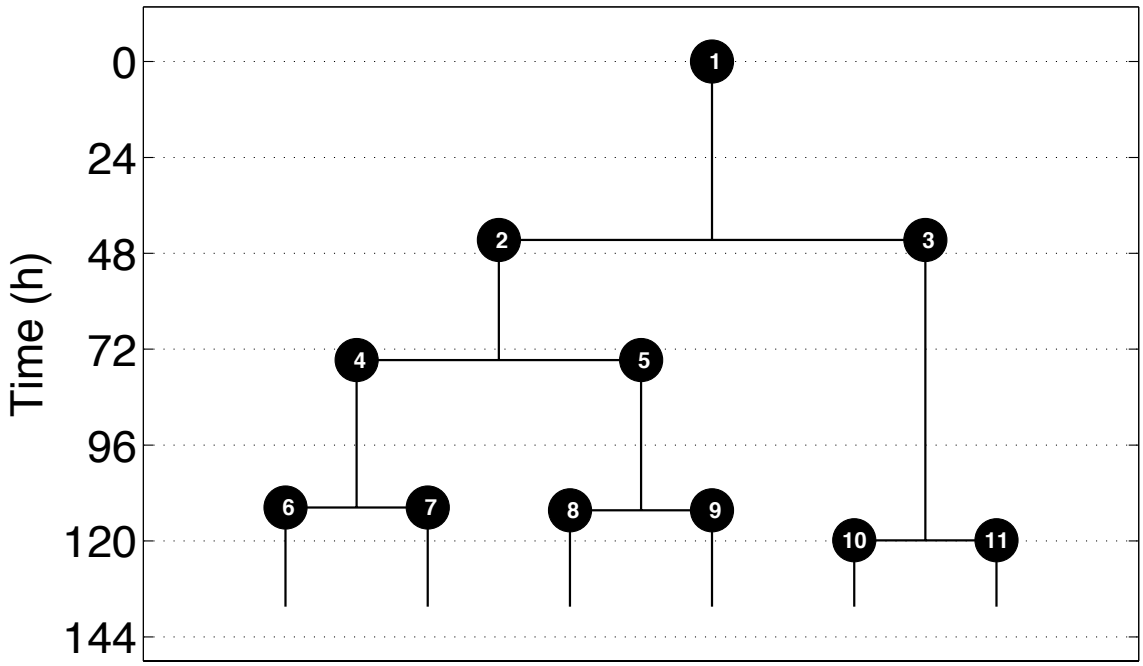

| Frame | Well | Clone rank | Population | EPCR intensity | Repopulating activity |
|---|---|---|---|---|---|
| 26 | 1 | 40 | EPCR$^-$ | 417.6 | N/A |

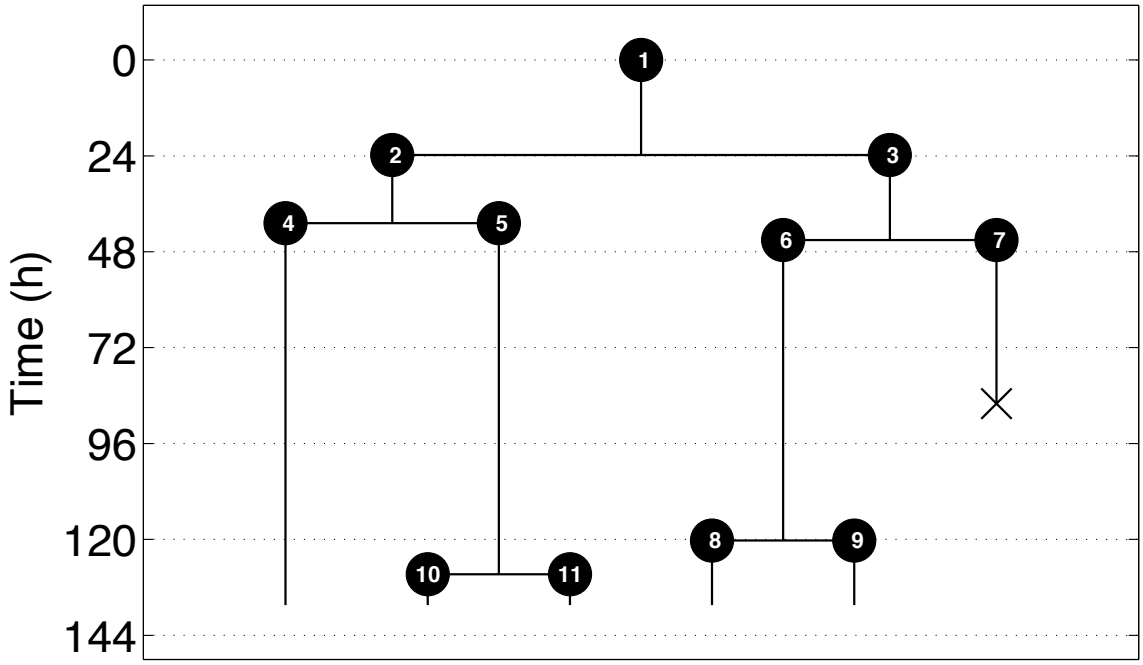


| Frame | Well | Clone rank | Population | EPCR intensity | Repopulating activity |
|---|---|---|---|---|---|
| 13 | 2 | 41 | EPCR$^-$ | 410.4 | No |

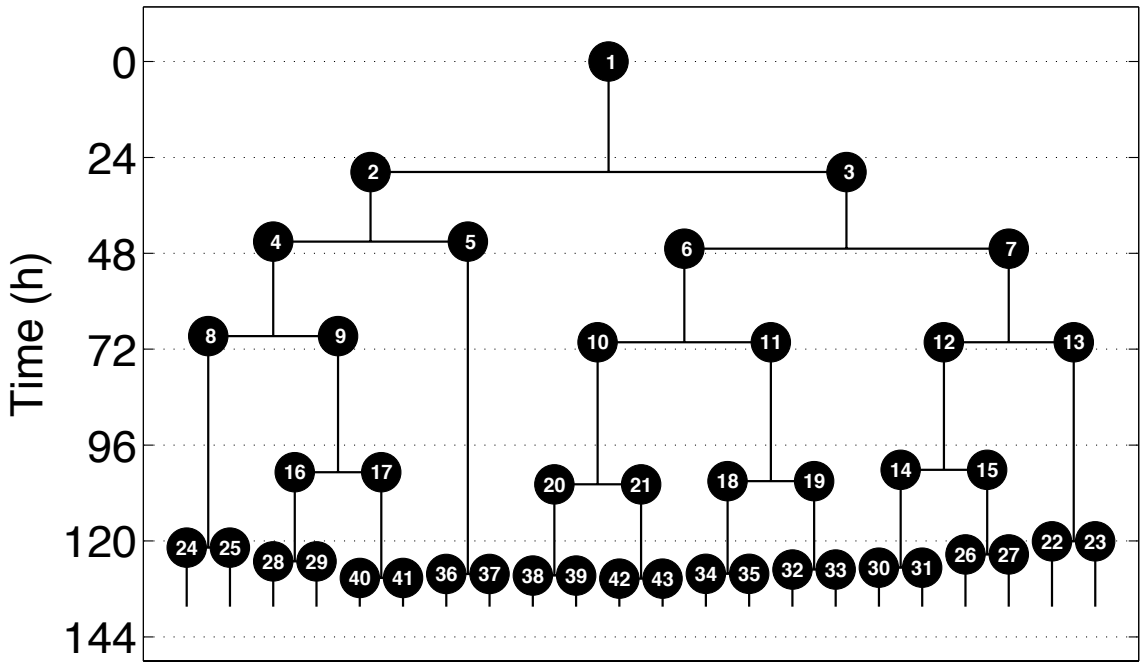

| Frame | Well | Clone rank | Population | EPCR intensity | Repopulating activity |
|---|---|---|---|---|---|
| 19 | 1 | 42 | EPCR$^-$ | 409.8 | N/A |

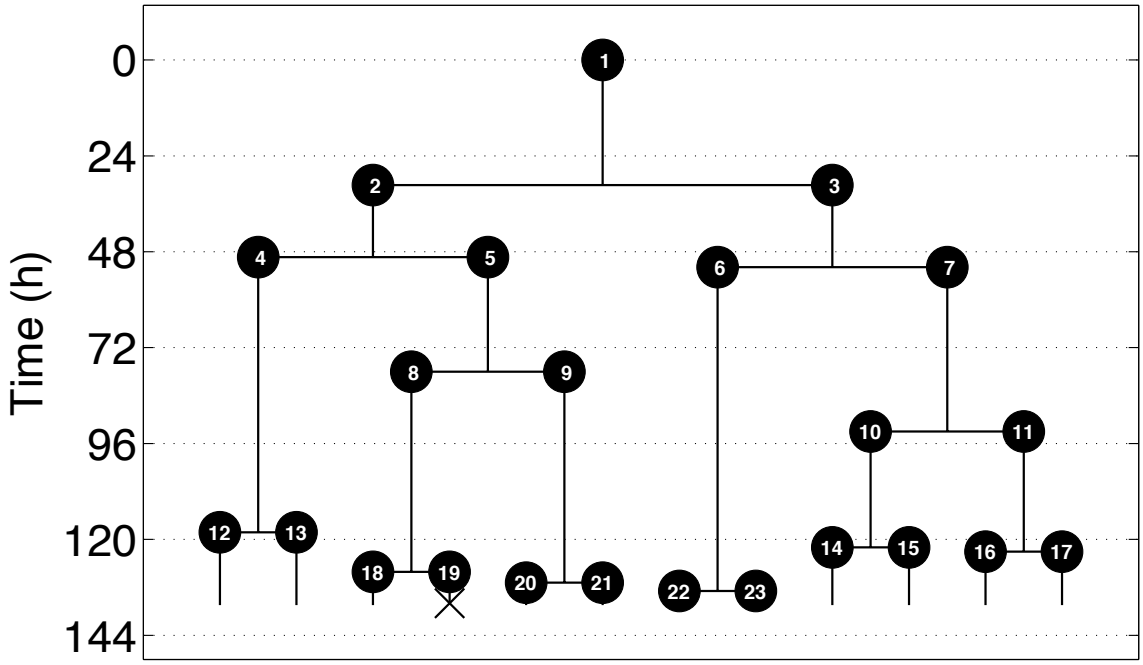


| Frame | Well | Clone rank | Population | EPCR intensity | Repopulating activity |
|---|---|---|---|---|---|
| 9 | 1 | 43 | EPCR$^-$ | 405.5 | N/A |

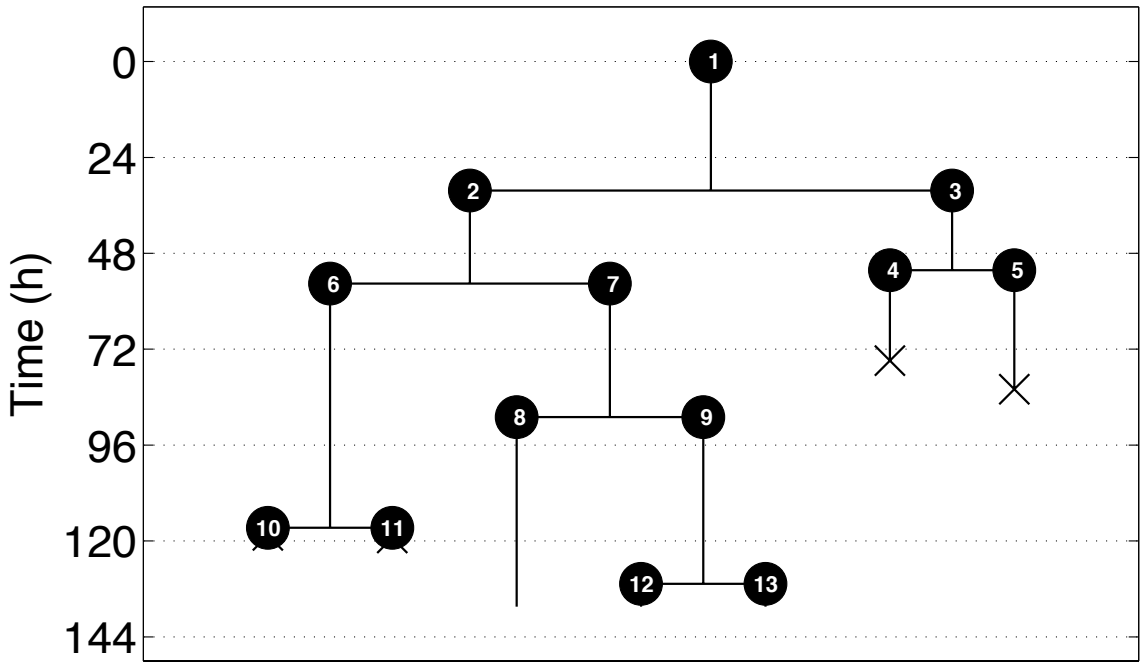

| Frame | Well | Clone rank | Population | EPCR intensity | Repopulating activity |
|---|---|---|---|---|---|
| 28 | 4 | 44 | EPCR$^-$ | 404.4 | N/A |

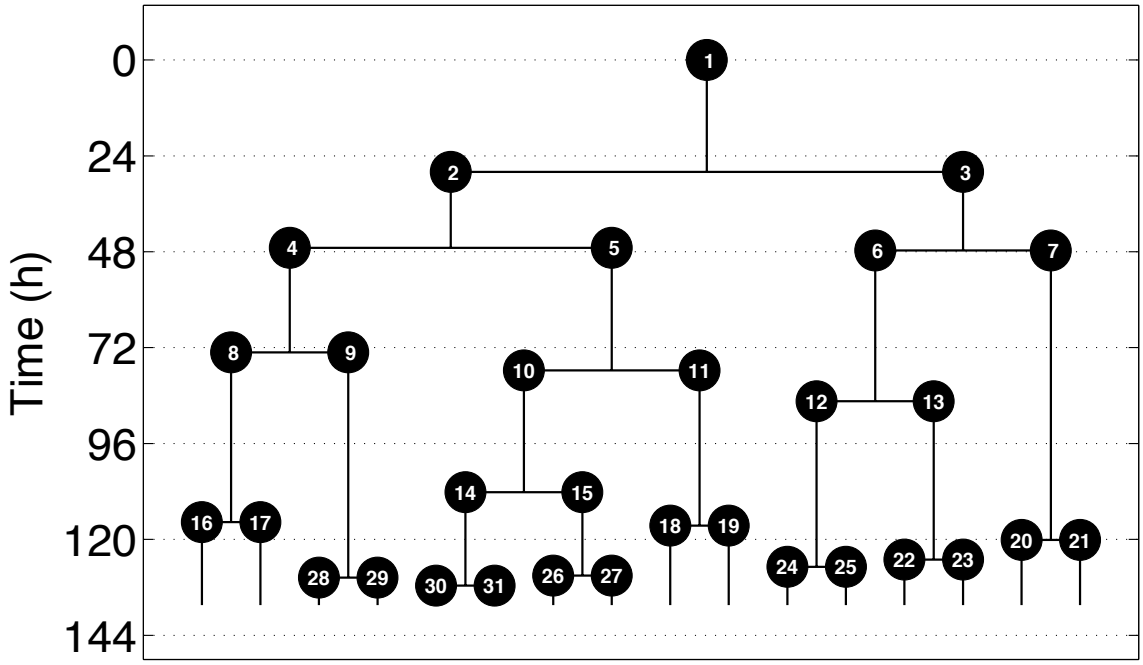


| Frame | Well | Clone rank | Population | EPCR intensity | Repopulating activity |
|---|---|---|---|---|---|
| 35 | 2 | 45 | EPCR$^-$ | 397.3 | N/A |

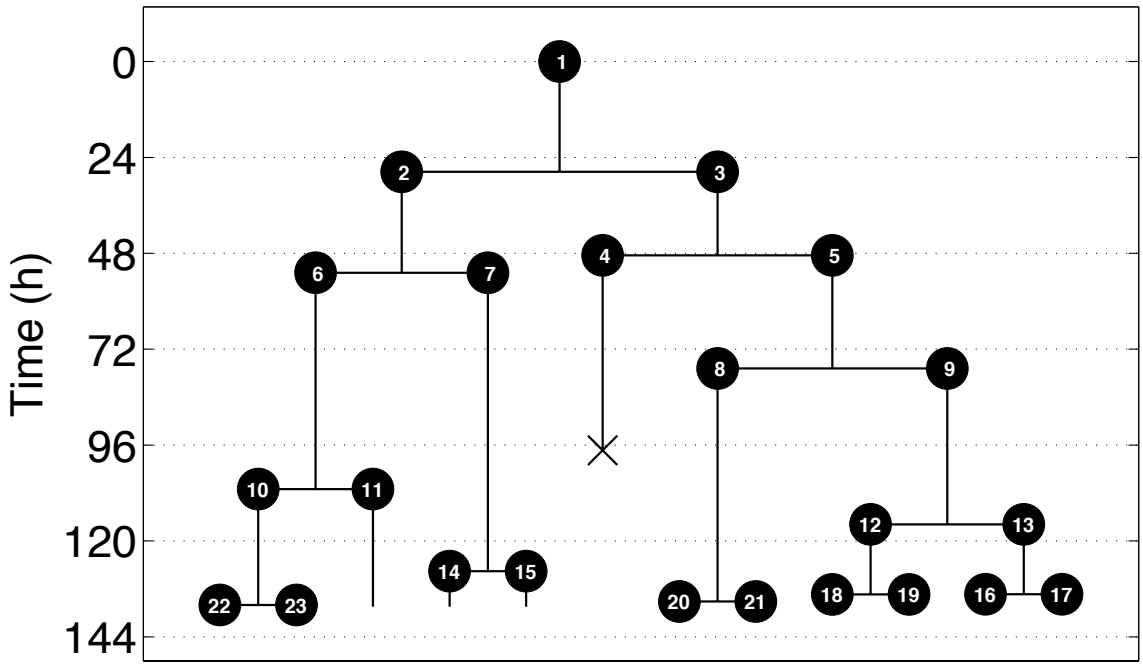

| Frame | Well | Clone rank | Population | EPCR intensity | Repopulating activity |
|---|---|---|---|---|---|
| 47 | 3 | 46 | EPCR$^-$ | 392.4 | N/A |

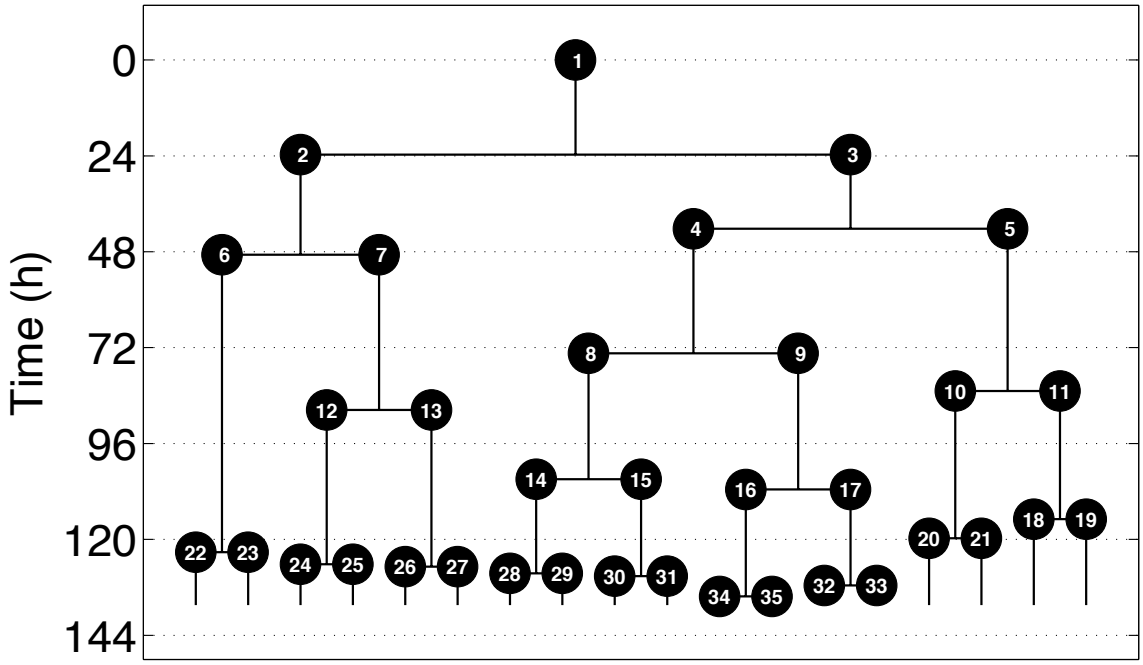


| Frame | Well | Clone rank | Population | EPCR intensity | Repopulating activity |
|---|---|---|---|---|---|
| 11 | 1 | 47 | EPCR$^-$ | 391.9 | No |

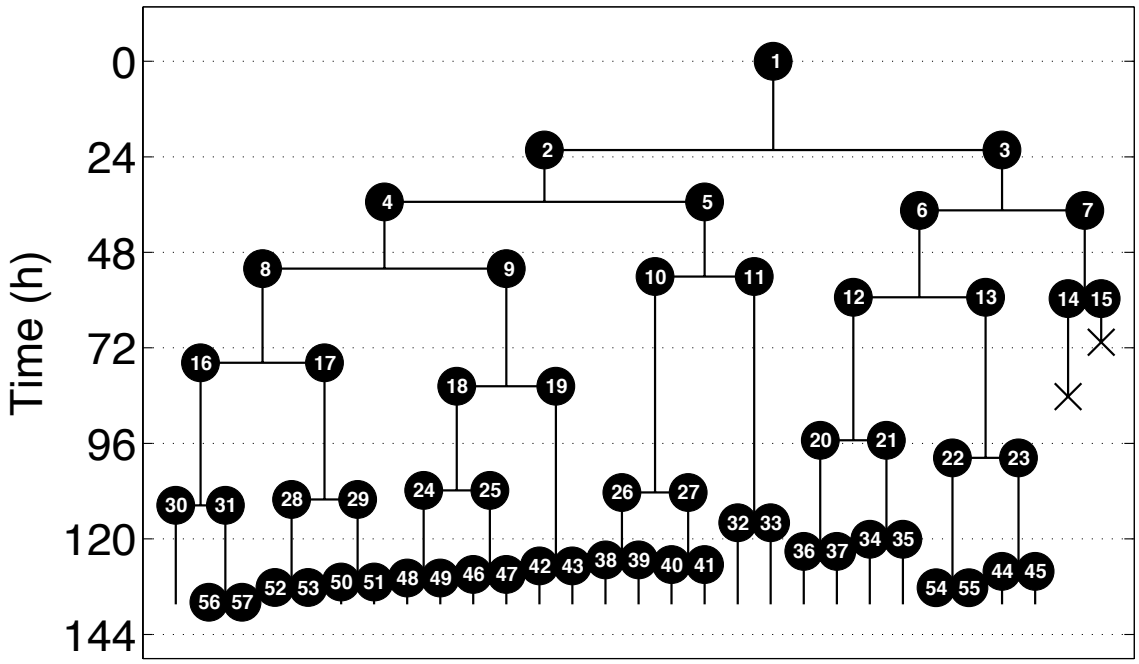

| Frame | Well | Clone rank | Population | EPCR intensity | Repopulating activity |
|---|---|---|---|---|---|
| 28 | 1 | 48 | EPCR$^-$ | 390.9 | N/A |

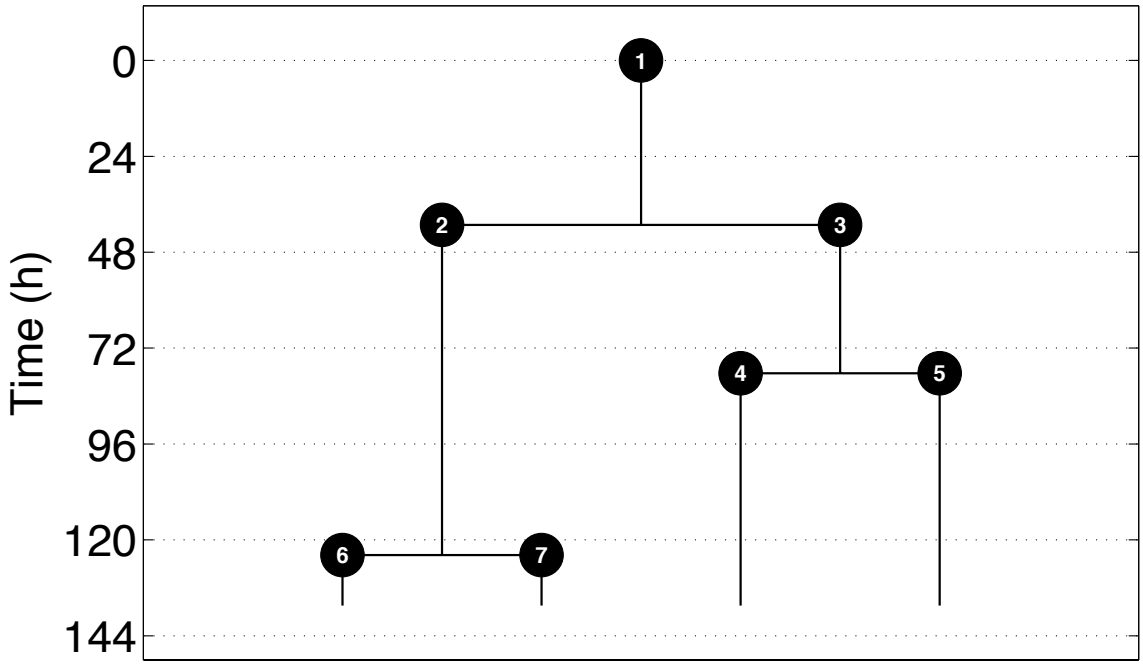


| Frame | Well | Clone rank | Population | EPCR intensity | Repopulating activity |
|---|---|---|---|---|---|
| 18 | 2 | 49 | EPCR$^-$ | 381.2 | N/A |

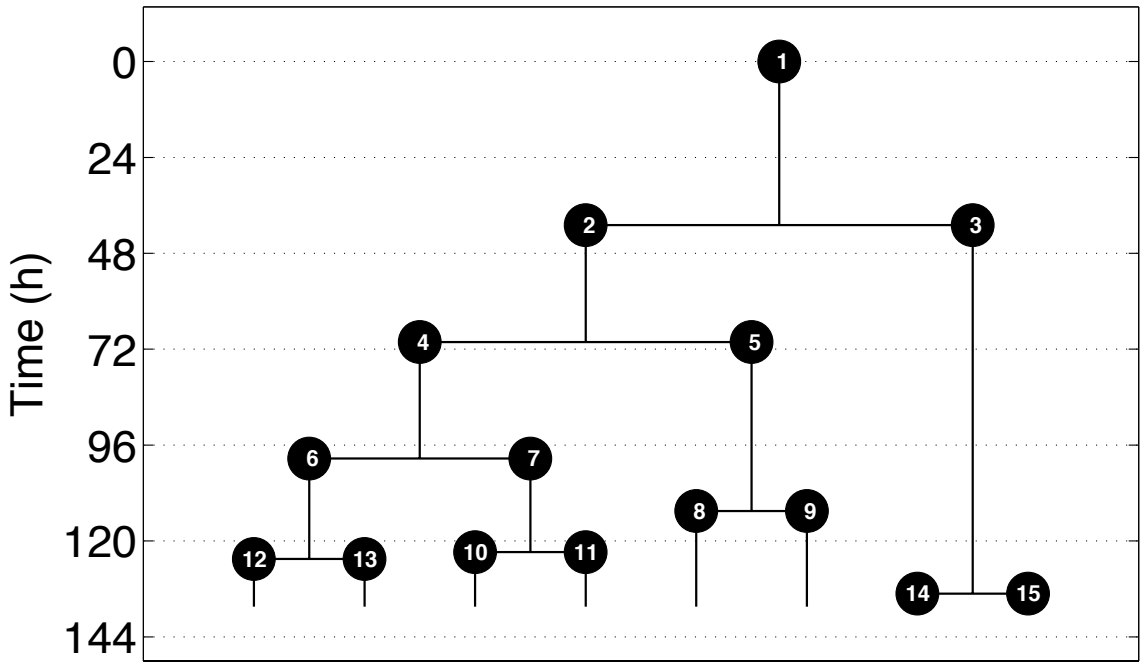

| Frame | Well | Clone rank | Population | EPCR intensity | Repopulating activity |
|---|---|---|---|---|---|
| 4 | 3 | 50 | EPCR$^-$ | 380.0 | N/A |

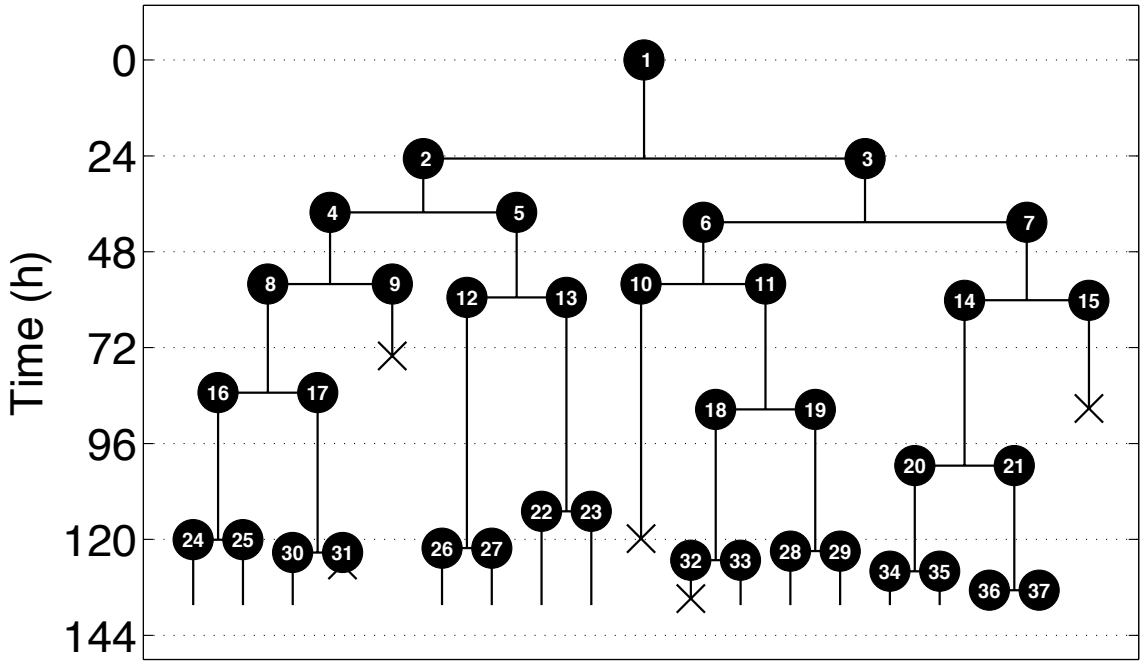


| Frame | Well | Clone rank | Population | EPCR intensity | Repopulating activity |
|---|---|---|---|---|---|
| 5 | 4 | 51 | EPCR$^-$ | 375.3 | N/A |

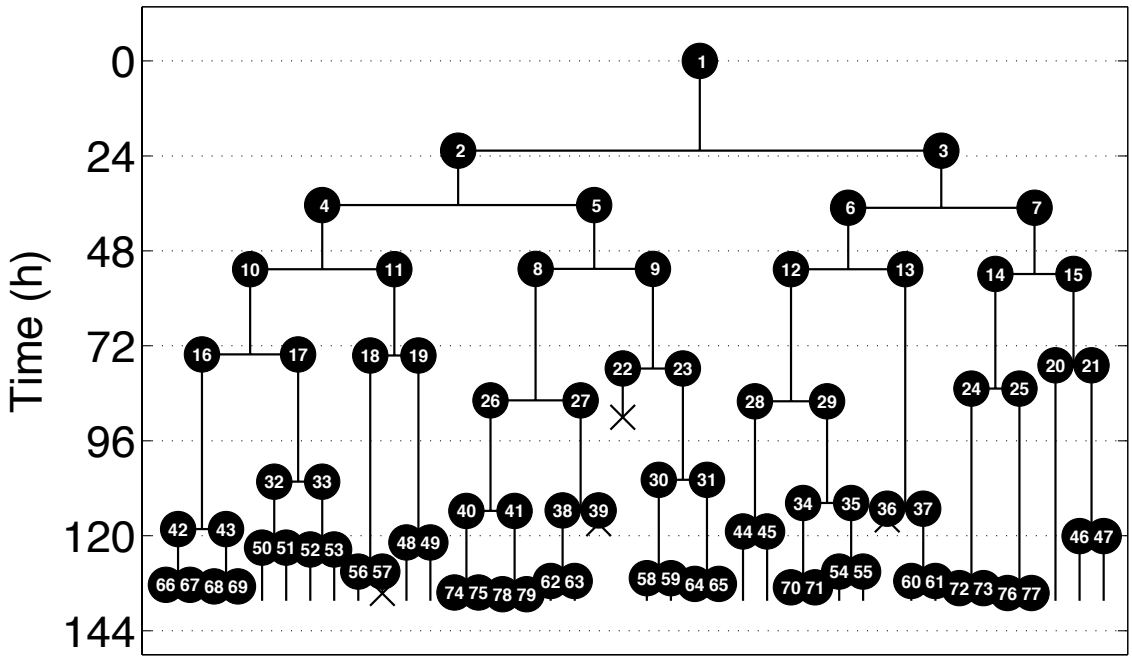

| Frame | Well | Clone rank | Population | EPCR intensity | Repopulating activity |
|---|---|---|---|---|---|
| 34 | 2 | 52 | EPCR$^-$ | 374.3 | N/A |

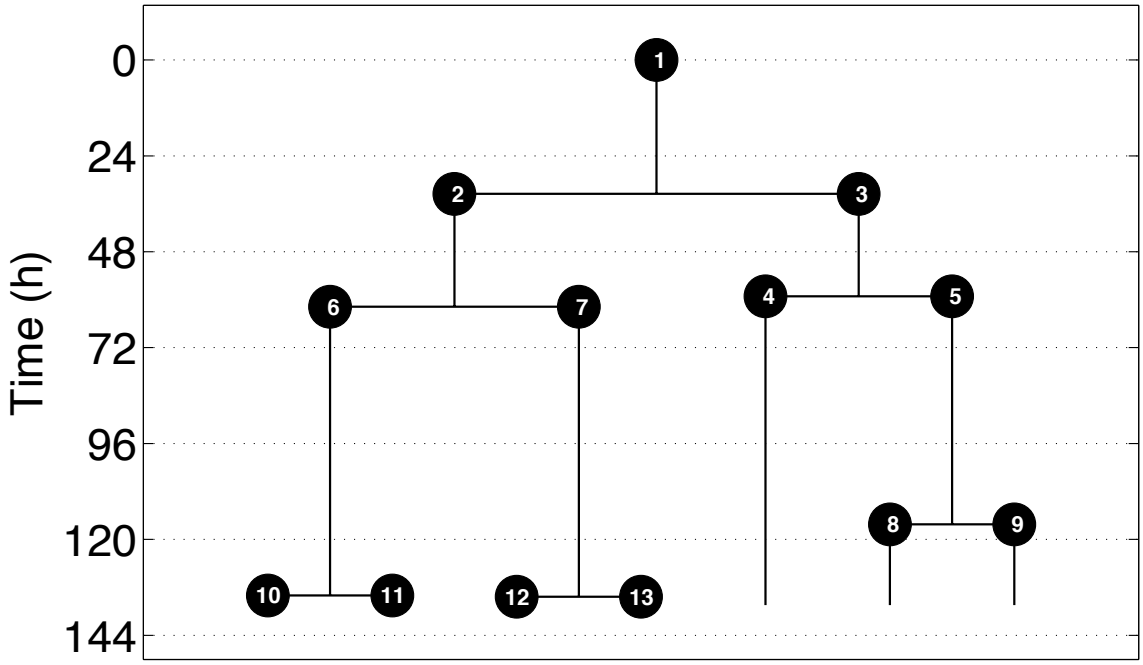


| Frame | Well | Clone rank | Population | EPCR intensity | Repopulating activity |
|---|---|---|---|---|---|
| 30 | 3 | 53 | EPCR$^-$ | 373.2 | N/A |

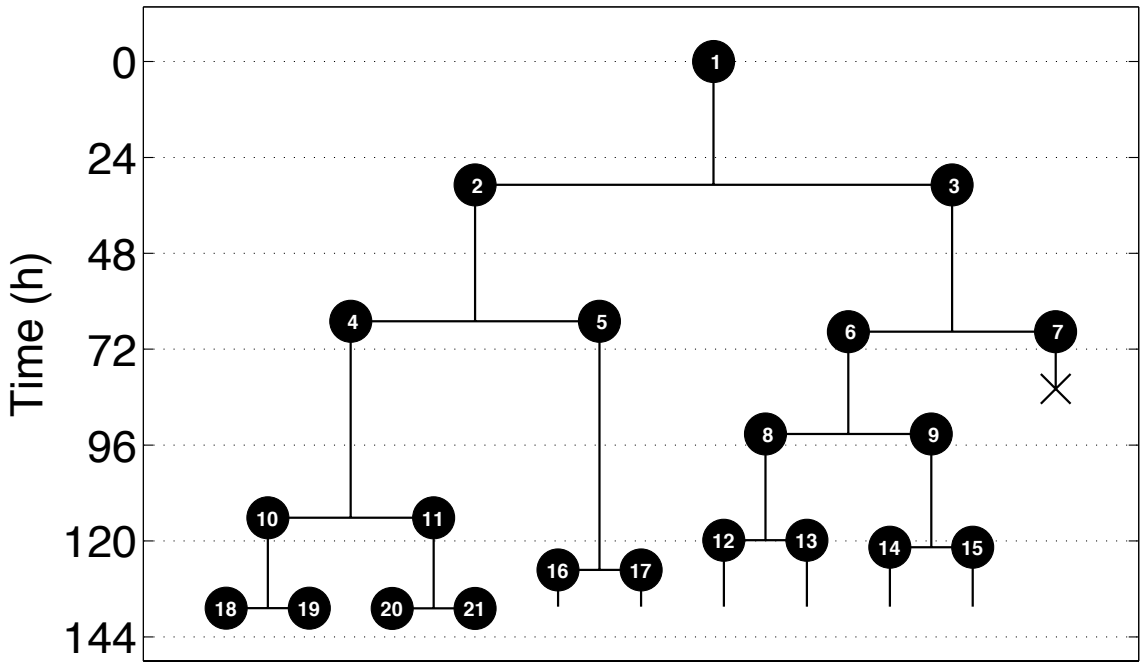

| Frame | Well | Clone rank | Population | EPCR intensity | Repopulating activity |
|---|---|---|---|---|---|
| 24 | 3 | 54 | EPCR$^-$ | 371.9 | N/A |

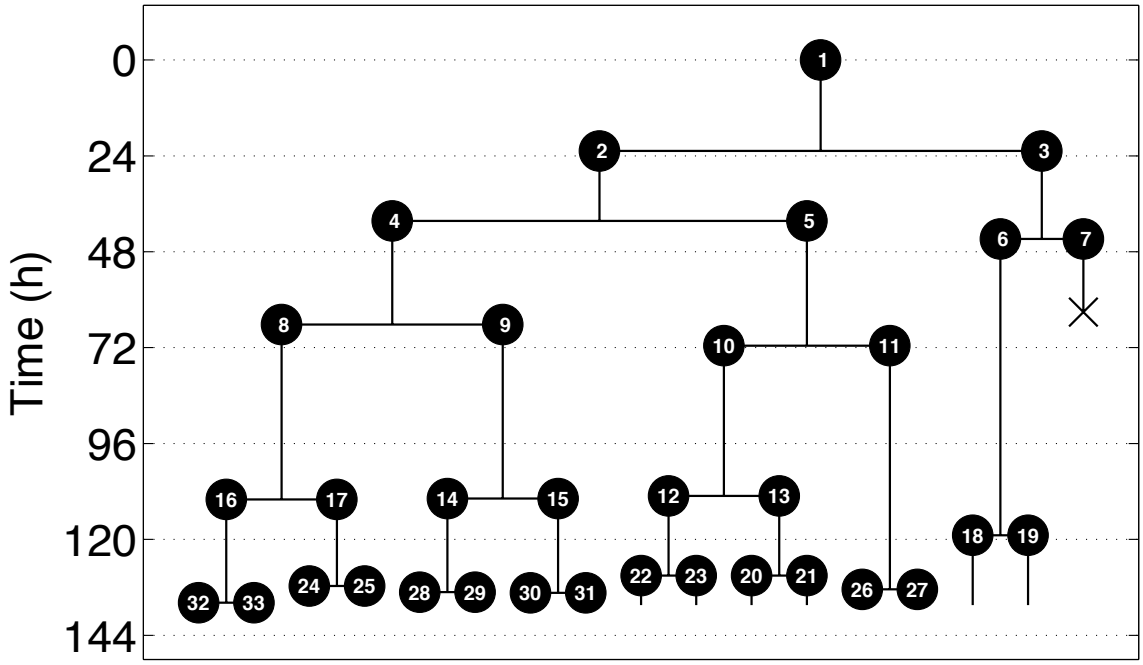


| Frame | Well | Clone rank | Population | EPCR intensity | Repopulating activity |
|---|---|---|---|---|---|
| 2 | 4 | 55 | EPCR$^-$ | 371.1 | N/A |

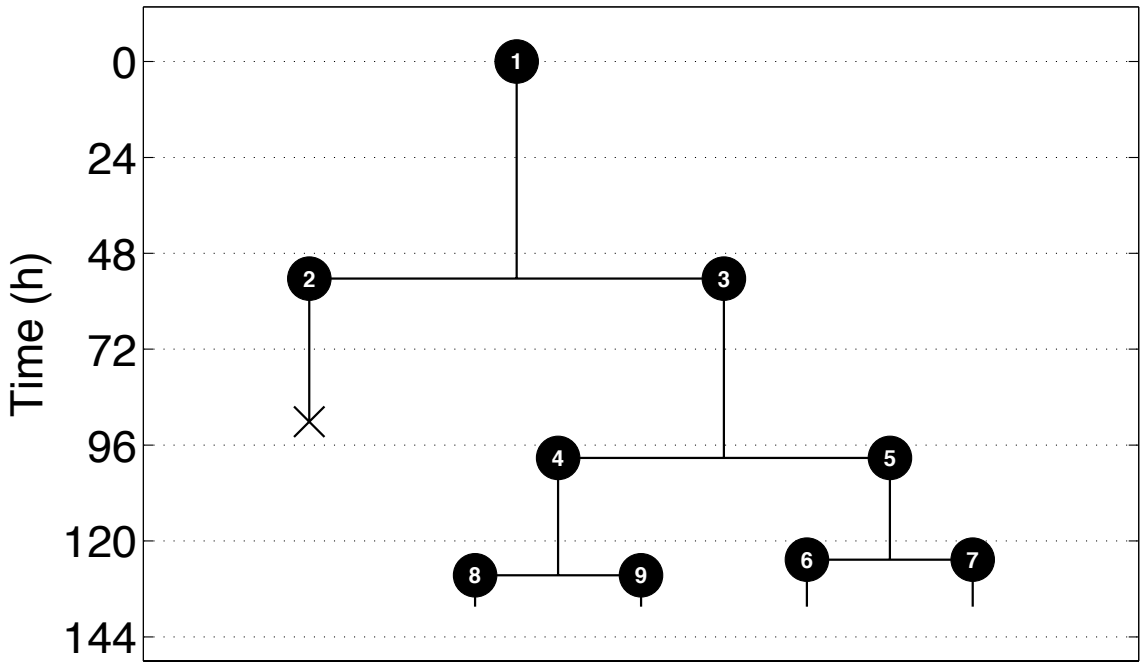

| Frame | Well | Clone rank | Population | EPCR intensity | Repopulating activity |
|---|---|---|---|---|---|
| 47 | 1 | 56 | EPCR$^-$ | 370.2 | N/A |

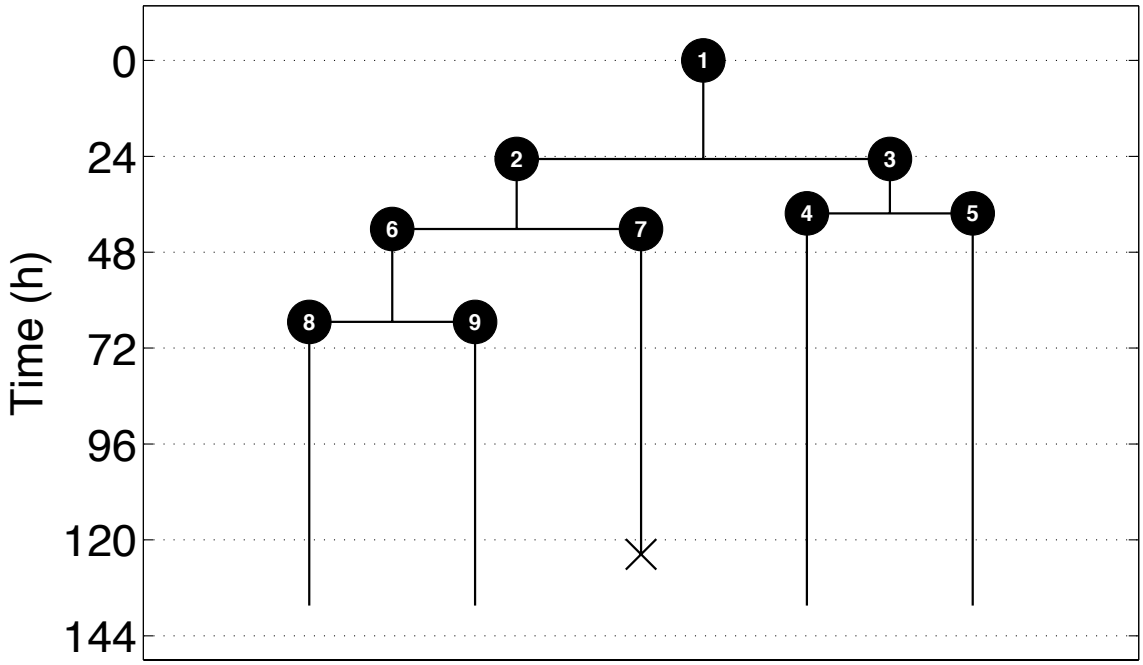


| Frame | Well | Clone rank | Population | EPCR intensity | Repopulating activity |
|---|---|---|---|---|---|
| 41 | 2 | 57 | EPCR$^-$ | 361.6 | N/A |

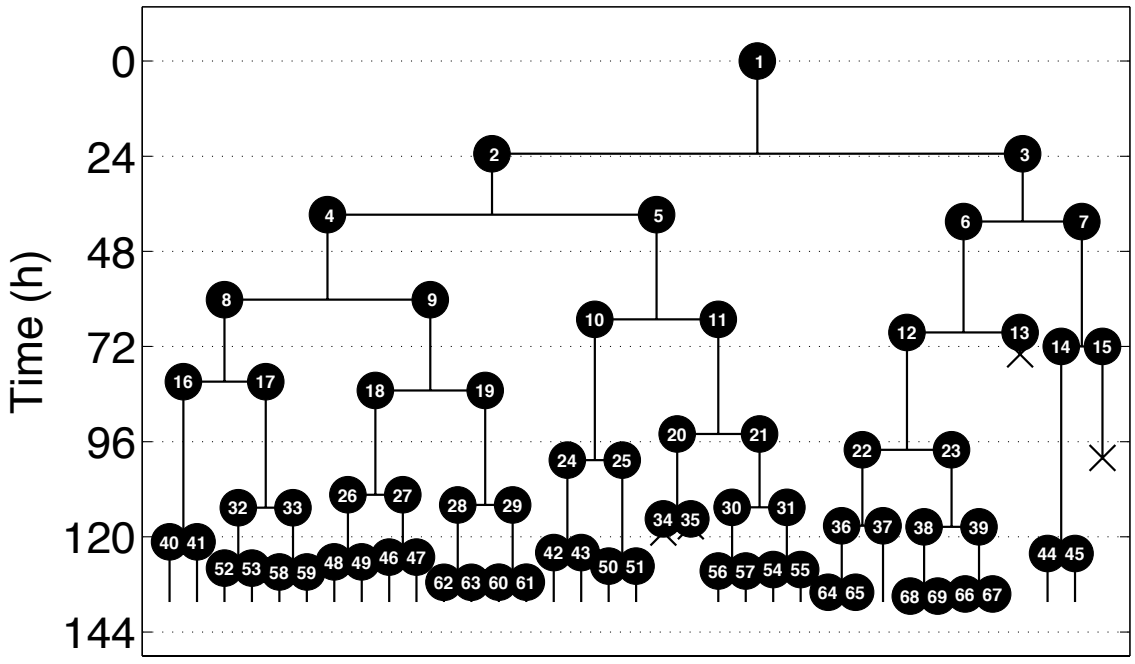

| Frame | Well | Clone rank | Population | EPCR intensity | Repopulating activity |
|---|---|---|---|---|---|
| 41 | 4 | 58 | EPCR$^-$ | 360.4 | No |

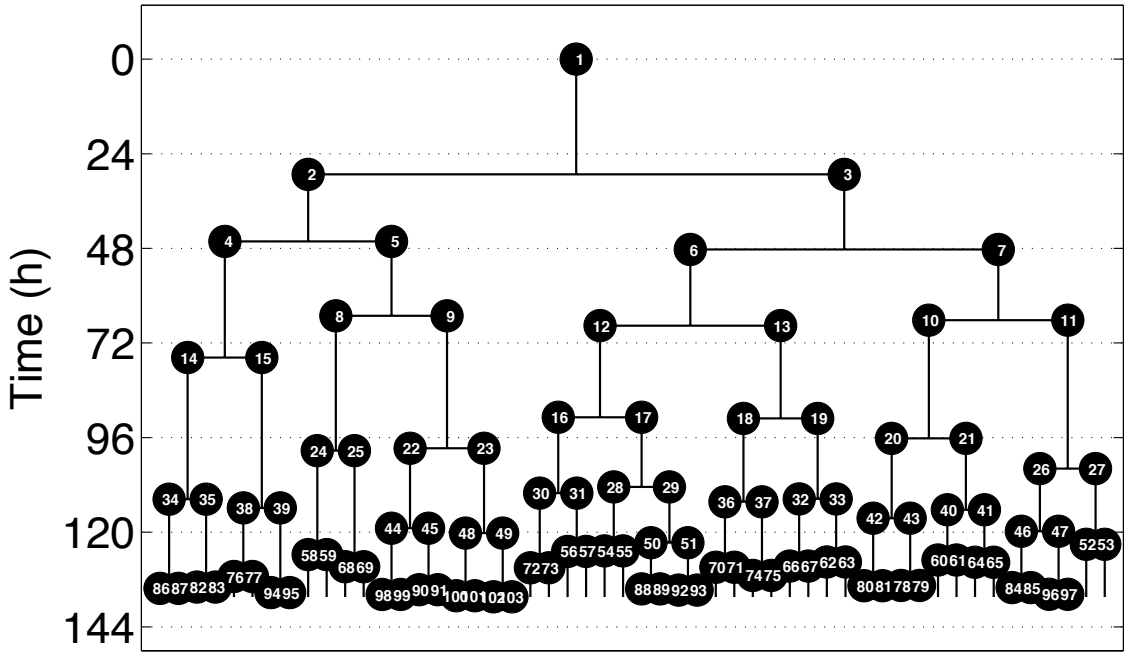


| Frame | Well | Clone rank | Population | EPCR intensity | Repopulating activity |
|---|---|---|---|---|---|
| 43 | 4 | 59 | EPCR$^-$ | 358.9 | No |

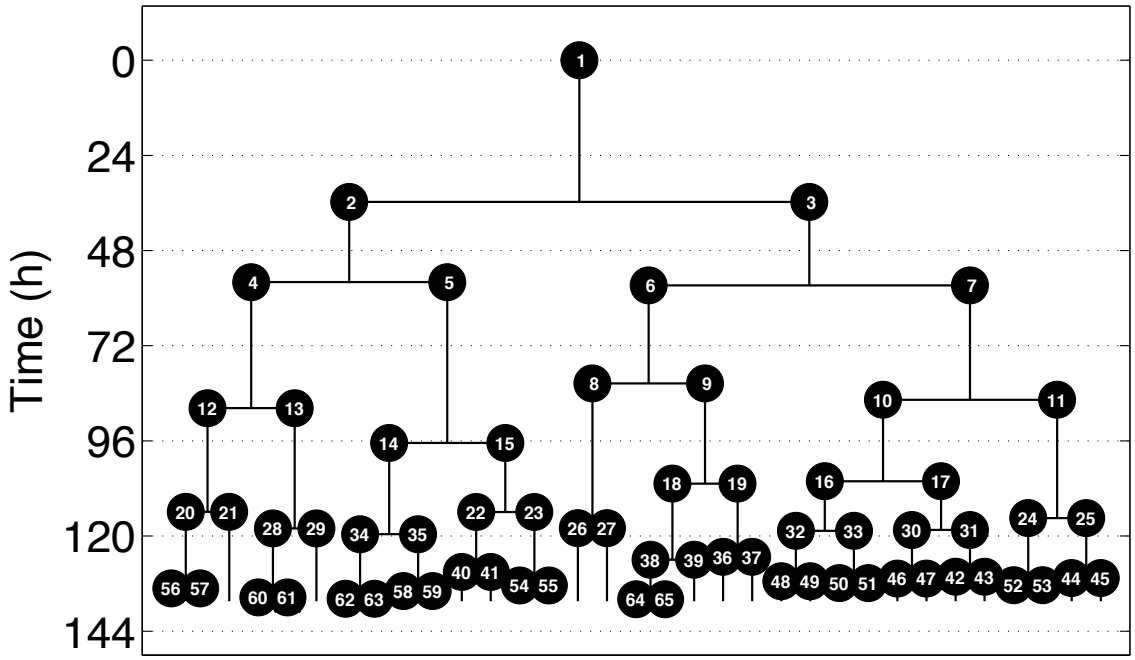

| Frame | Well | Clone rank | Population | EPCR intensity | Repopulating activity |
|---|---|---|---|---|---|
| 33 | 3 | 60 | EPCR$^-$ | 358.7 | N/A |

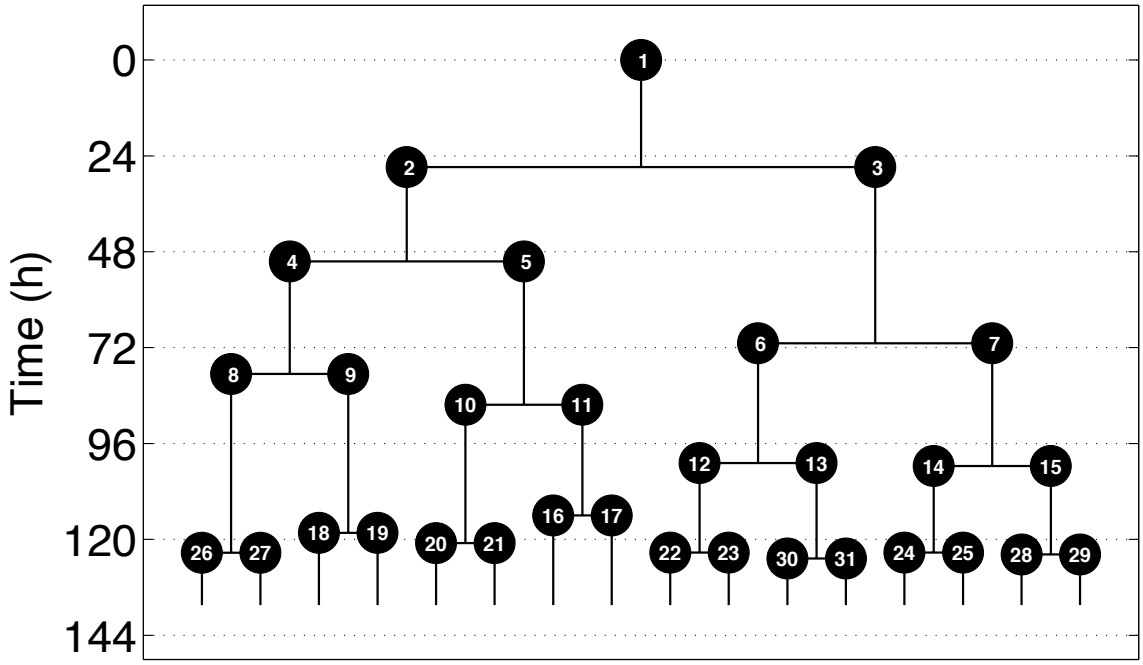


| Frame | Well | Clone rank | Population | EPCR intensity | Repopulating activity |
|---|---|---|---|---|---|
| 36 | 1 | 61 | EPCR$^-$ | 358.4 | N/A |

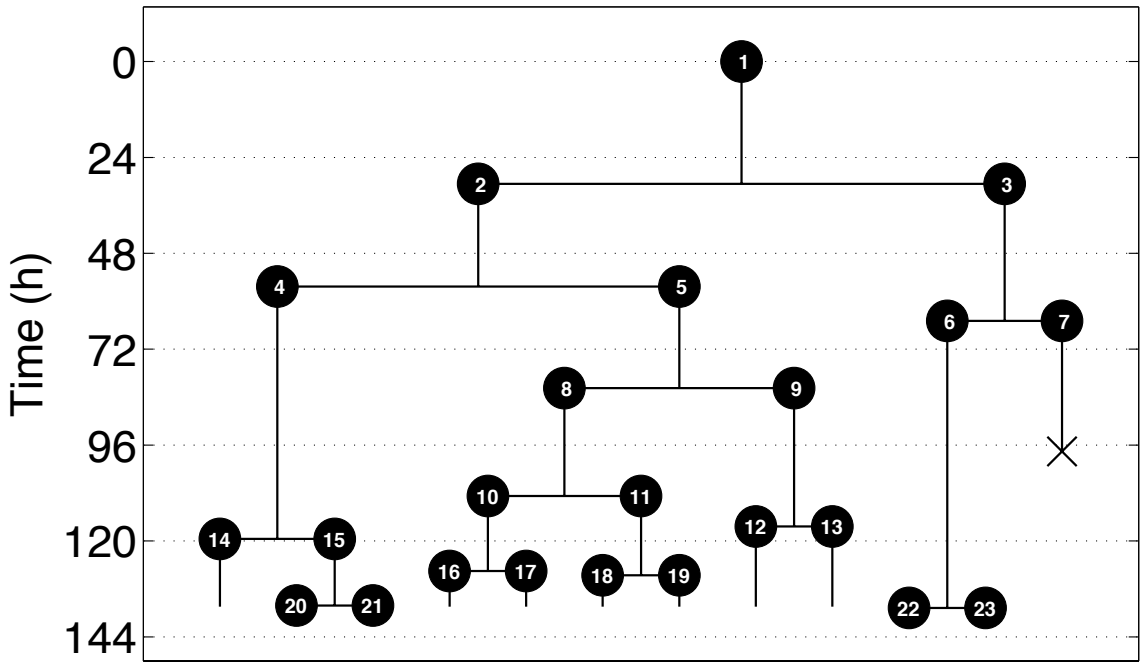

| Frame | Well | Clone rank | Population | EPCR intensity | Repopulating activity |
|---|---|---|---|---|---|
| 17 | 3 | 62 | EPCR$^-$ | 355.0 | N/A |

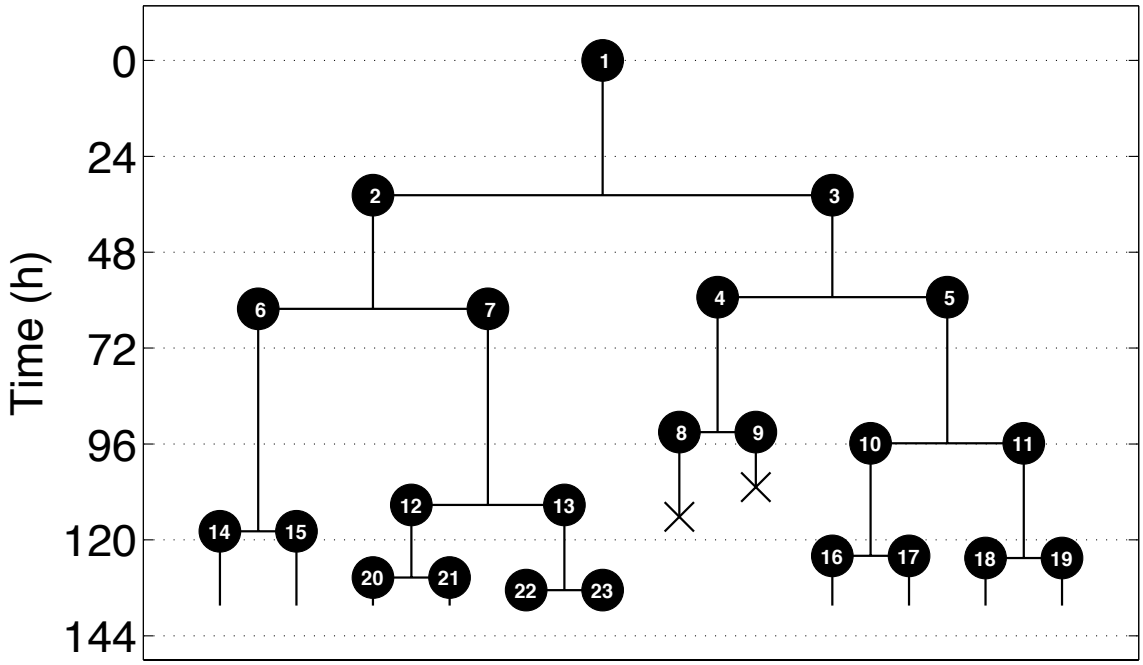


| Frame | Well | Clone rank | Population | EPCR intensity | Repopulating activity |
|---|---|---|---|---|---|
| 21 | 1 | 63 | EPCR$^-$ | 348.5 | N/A |

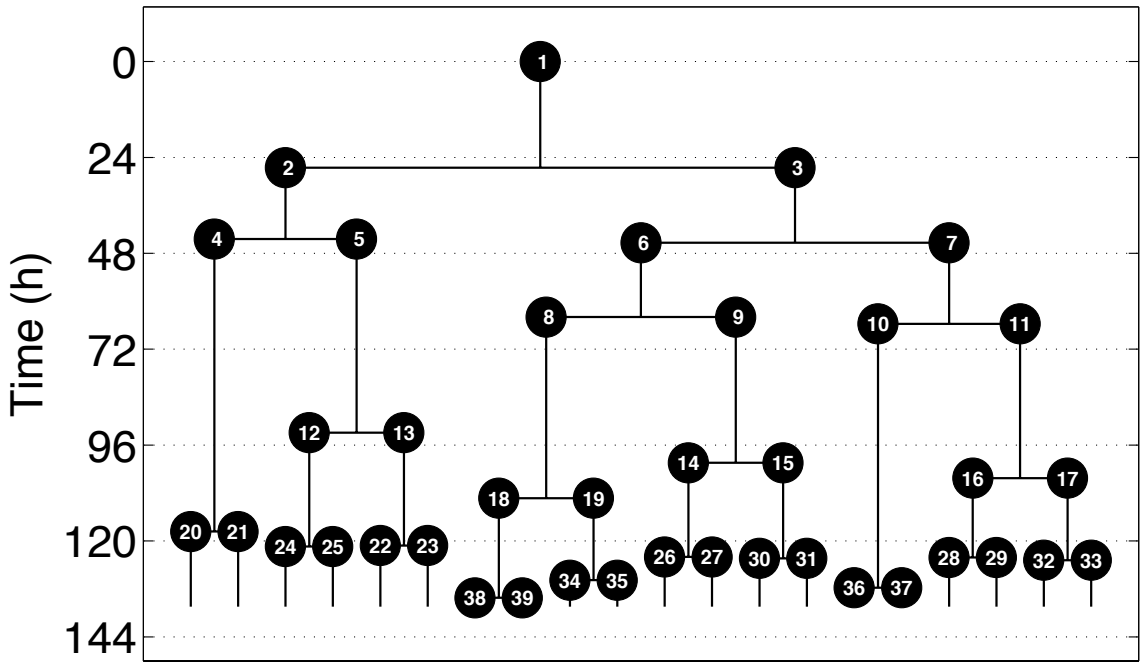

| Frame | Well | Clone rank | Population | EPCR intensity | Repopulating activity |
|---|---|---|---|---|---|
| 34 | 4 | 64 | EPCR$^-$ | 345.4 | N/A |

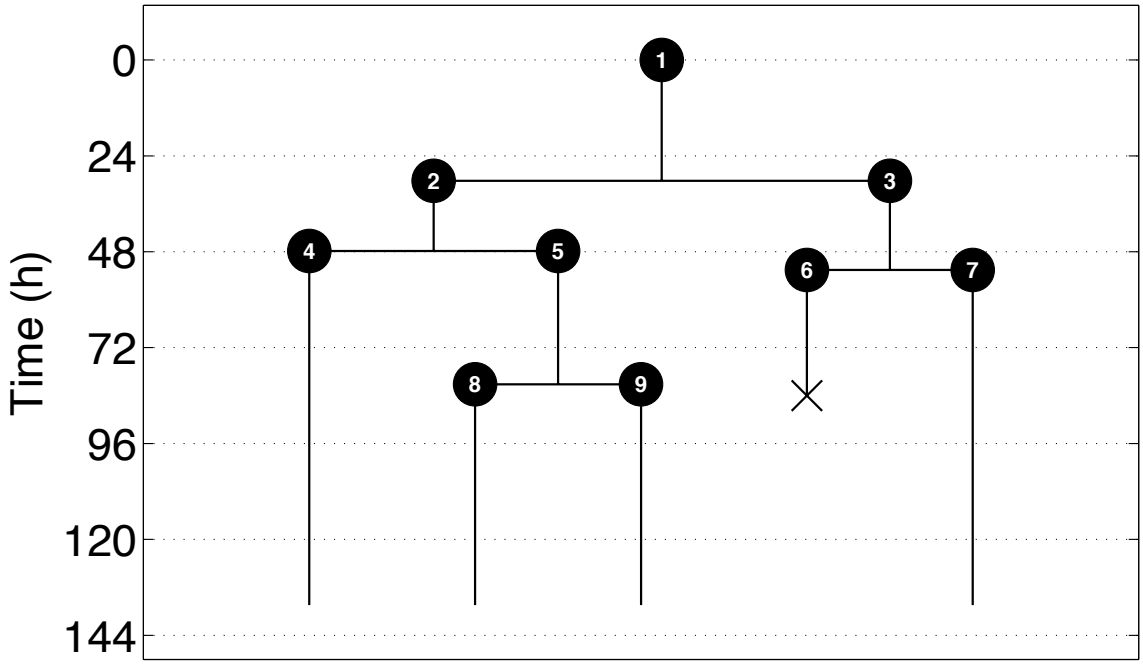


| Frame | Well | Clone rank | Population | EPCR intensity | Repopulating activity |
|---|---|---|---|---|---|
| 7 | 3 | 65 | EPCR$^-$ | 344.8 | No |

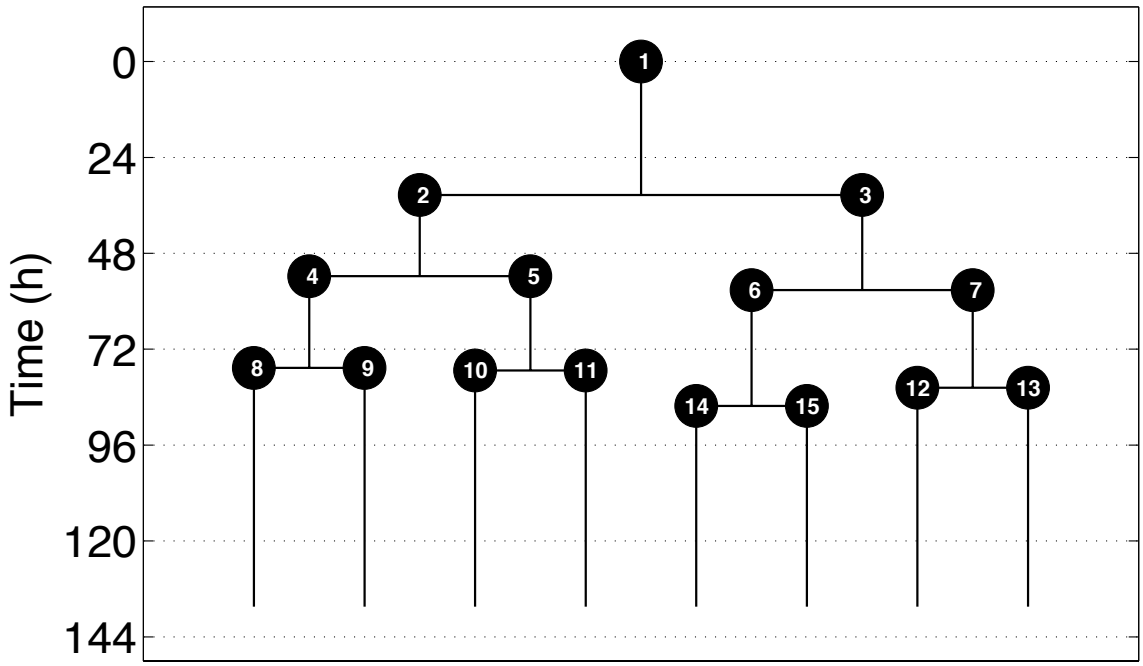

| Frame | Well | Clone rank | Population | EPCR intensity | Repopulating activity |
|---|---|---|---|---|---|
| 20 | 2 | 66 | EPCR$^-$ | 339.9 | No |

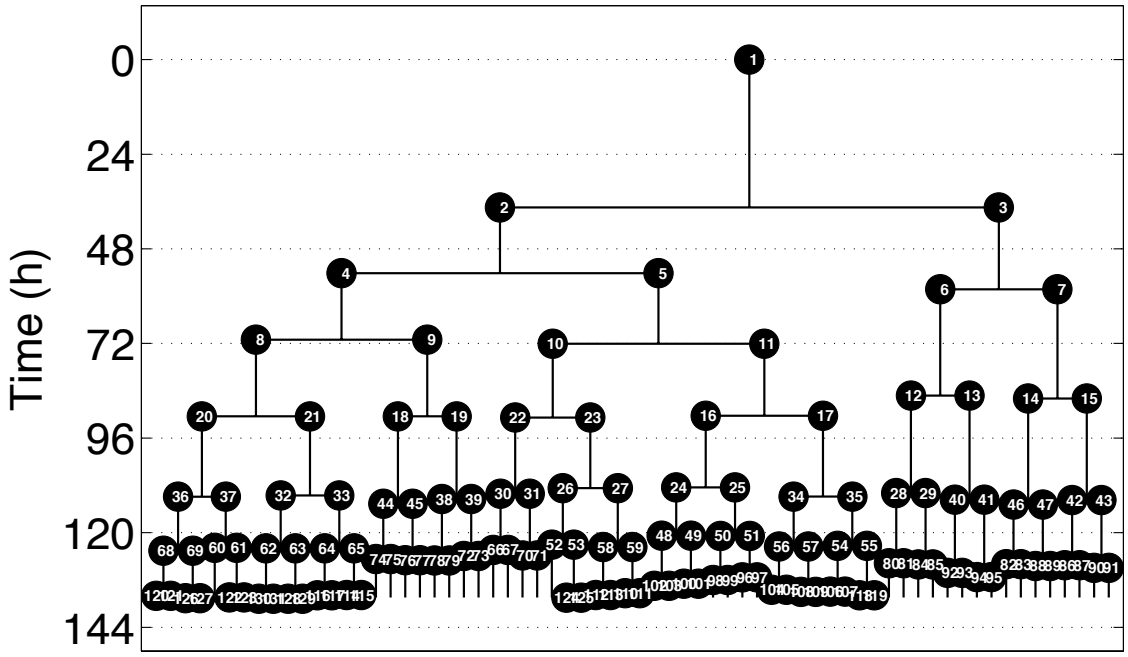


| Frame | Well | Clone rank | Population | EPCR intensity | Repopulating activity |
|---|---|---|---|---|---|
| 6 | 1 | 67 | EPCR$^-$ | 335.3 | No |

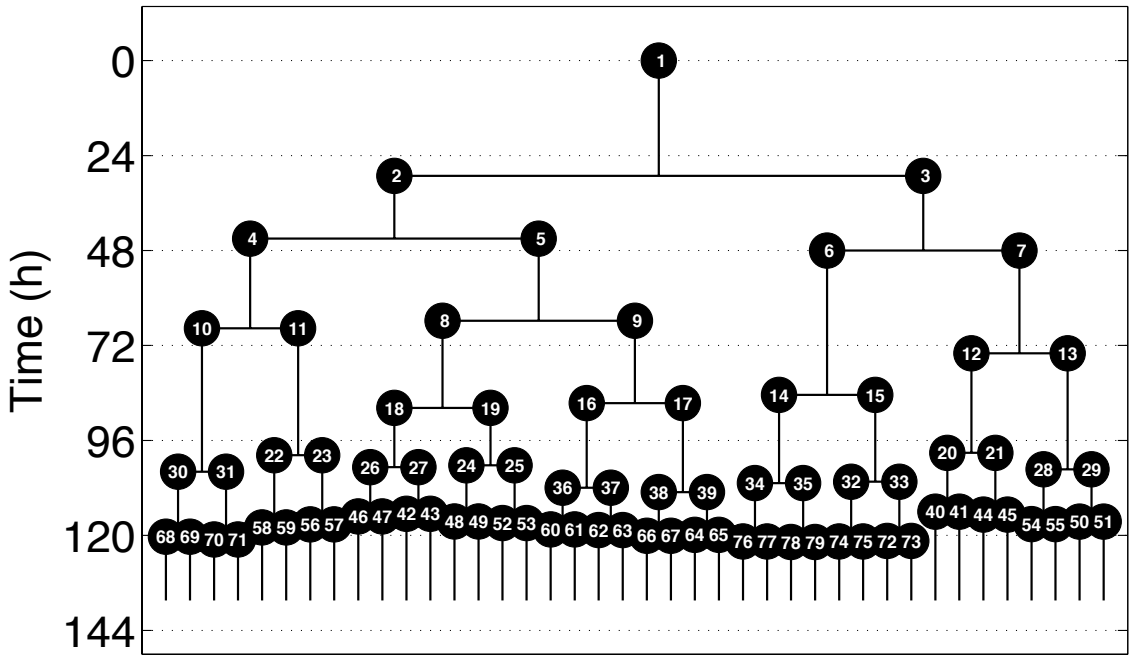

| Frame | Well | Clone rank | Population | EPCR intensity | Repopulating activity |
|---|---|---|---|---|---|
| 29 | 2 | 68 | EPCR$^-$ | 335.2 | No |

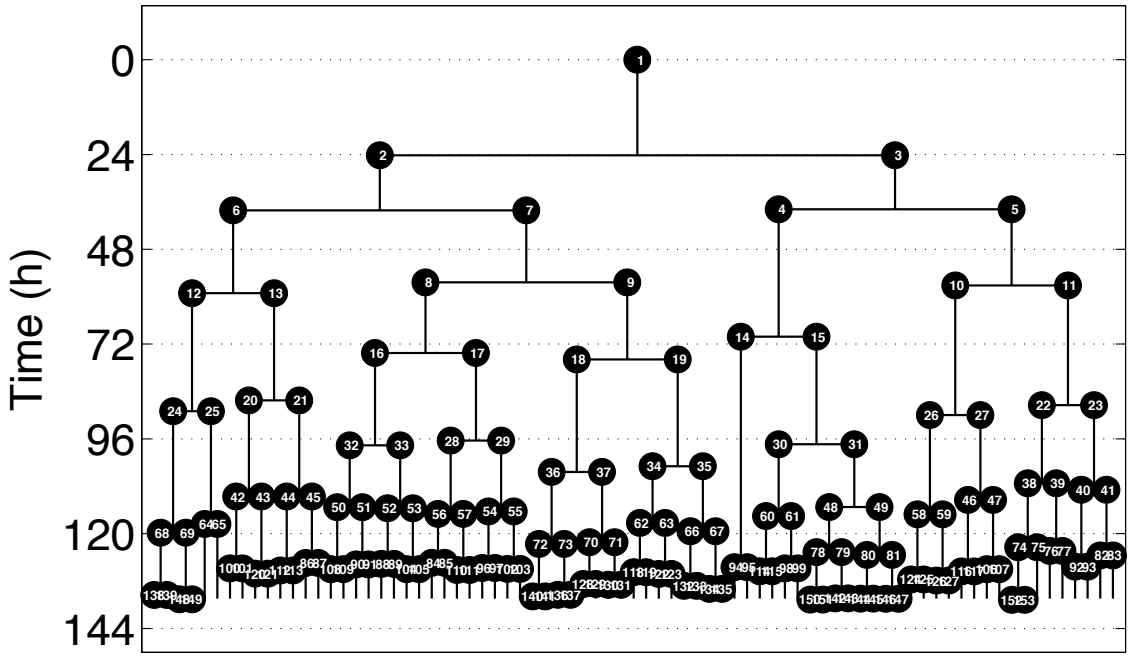


| Frame | Well | Clone rank | Population | EPCR intensity | Repopulating activity |
|---|---|---|---|---|---|
| 29 | 3 | 69 | EPCR$^-$ | 328.8 | No |

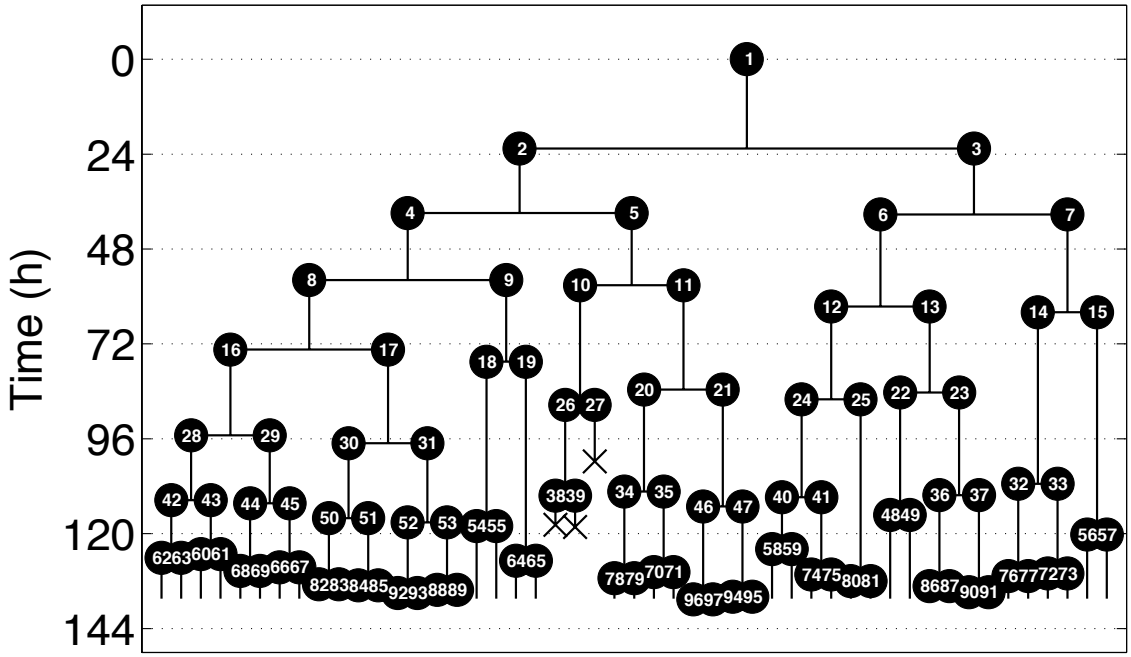

| Frame | Well | Clone rank | Population | EPCR intensity | Repopulating activity |
|---|---|---|---|---|---|
| 32 | 1 | 70 | $EPCR^-$ | 302.0 | N/A |

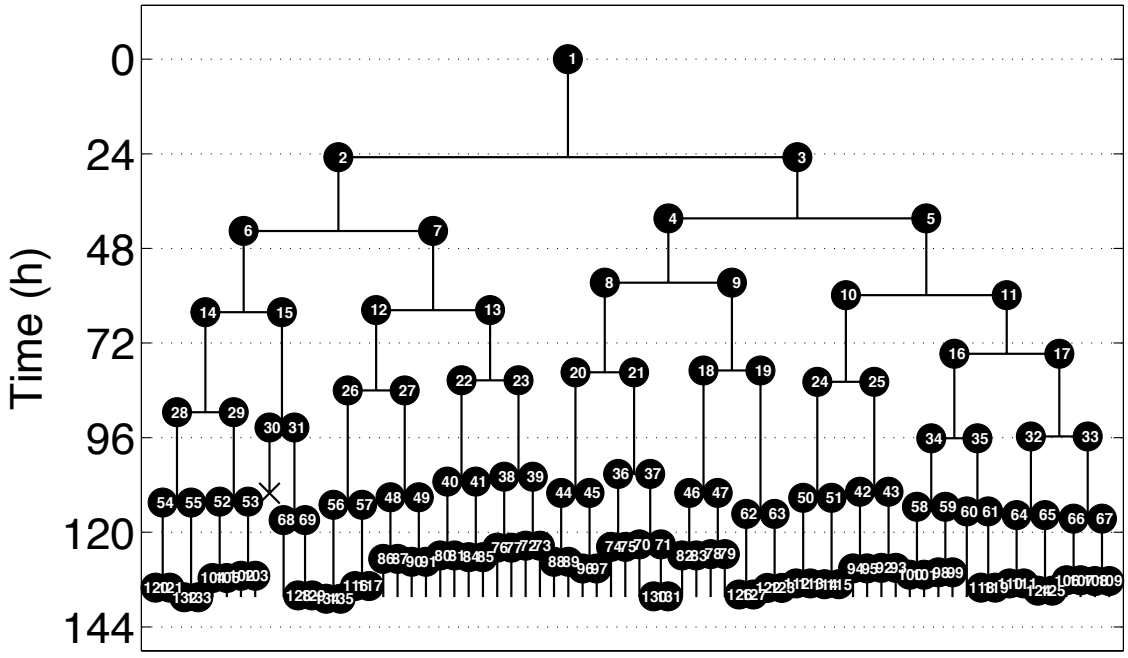


| Frame | Well | Clone rank | Population | EPCR intensity | Repopulating activity |
|---|---|---|---|---|---|
| 37 | 2 | N/A | N/A | N/A | N/A |

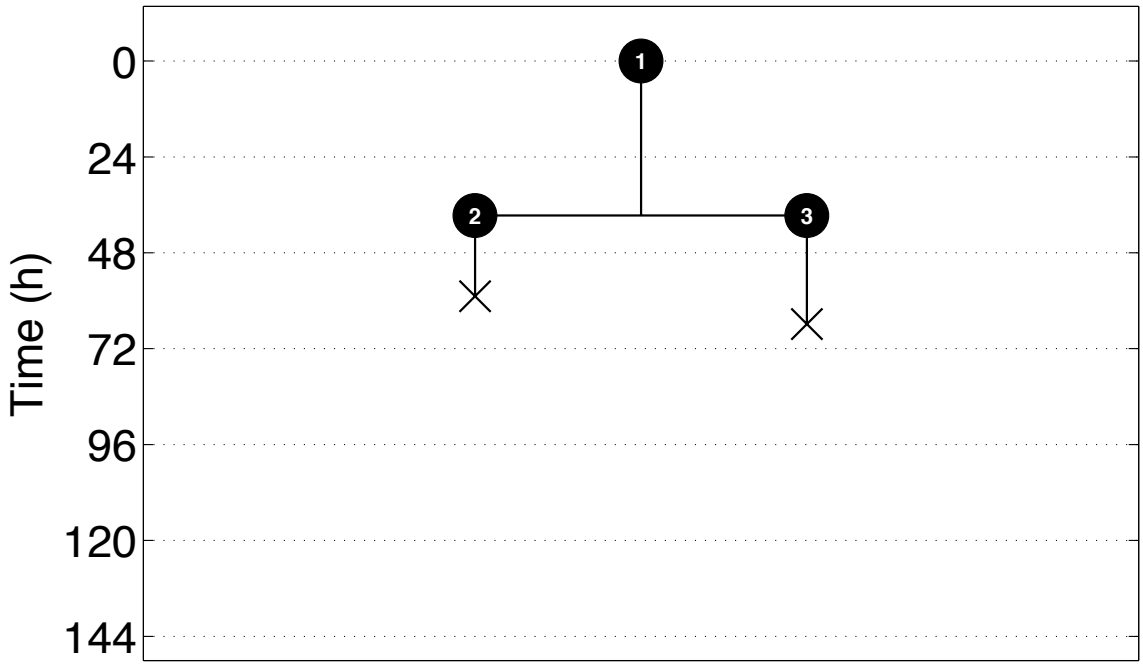

# Appendix E Estimation of Maximum Time Constant for Bead Antibody Capture

The maximum time constant for antibody capture can be estimated by modeling a single bead in a chamber containing a homogeneous concentration of mAb. Assuming infinite association and no dissociation, the flux for antibody diffusion to a bead can be estimated using Fick's law.

$$J = -D\nabla C \tag{E.1}$$

where $D$ is the diffusion constant of a human IgG antibody molecule in a 10% serum solution ($4.4 \times 10^{-11}$ $m^2$ $s^{-1}$)[322] and $C$ is the antibody concentration in the culture medium.

A region of depletion can be estimated to be one radius larger than the bead, whereby the distance travelled by molecules in the region of depletion correspond to the bead radius $a$ ($2.45 \times 10^{-6}$ m). Assuming that all antibody molecules are captured when they reach the surface of the bead, the antibody concentration around the bead ($r = a$) is zero. The antibody concentration at the boundary of the region of depletion ($r = 2a$) is assumed to be the same as the concentration in the chamber $C(t)$. Therefore, the rate of diffusion $I$ to one bead can be estimated by the following equation:

$$I = -4\pi DC(t)a \tag{E.2}$$

Assuming a constant initial antibody concentration in the chamber $C_0$, the concentration at time $t$ ($C_t$) can be calculated by the following equation:

$$C_t = C_0 e^{-\frac{4\pi Da}{V}t} \qquad \text{(E.3)}$$

where $V$ is the volume of the chamber ($4.1 \times 10^{-12}$ m$^2$). Therefore, the time constant ($\tau$) can be calculated as:

$$\tau = \frac{V}{4\pi Da} \qquad \text{(E.4)}$$

For one bead only, this corresponds to a time constant of 50 min. In a typical assay, a chamber would contain on average 130 beads, which would yield a time constant well below the 2-hour incubation period of the assay.